Masaryk University

Faculty of Science

What Drives the Lability of Glass-Forming Liquids to Crystallize?

Applications in Electronic, Structural and Optical Materials

Habilitation Thesis

Brno, 2021

Ing. Jiří Orava, Ph.D.

This thesis is dedicated to all my supervisors, mentors, collaborators, friends, and family for their support driving me continuously forward and towards interesting new topics.

I would like to thank namely

Prof. Tomas Wagner
Prof. A. Lindsay Greer

for their inspirational mentoring during different stages of my career.

I would especially dedicate this thesis to the memory of

Prof. Miloslav Frumar
(1936–2021)

for his enthusiastic guidance and encouragement during my studies at the University of Pardubice.

Contents

Preface

Glassy materials prepared by cooling the melt have been known to human civilizations for millennia. According to archaeological evidence, the first man-made glasses date back to around 3000–4000 BC with findings in Mesopotamia and Egypt.[a] Comprehensive empirical knowledge had been collected to form glasses of different properties, colours and shapes over centuries.

In the second half of the 20th century with the rigorous scientific understanding of non-crystalline solids of how and why they can form, and how the macroscopic properties relate to the atomic arrangement, glasses became of significant advanced technological importance. Around the 1960s and 1970s, among others, Turnbull, Kolomiets, and Sir Nevill F. Mott answered possibly the most puzzling and fundamental questions about non-crystalline materials of that time: i) *How does a glass form?* and ii) *How can there exist a transparent glass when it lacks the long-range order?* The questions laid the foundation for the new physics and chemistry of non-crystalline materials. The former question is now understood in terms of kinetically-driven exiting from the frustrated thermodynamically metastable state, which can be scientifically quantified in Figure I. In other words, nature dictates that any glass, whose state can be pictured as a frozen liquid, should transform to crystal. But it is the sluggish atomic diffusion that prevents that, and many natural glasses (vulcanic or lunar glass) exist which have not transformed since they formed. This fundamental property of glasses and its application in advanced technologies is the main focus of the commentary. The second question can be reasoned via the structure of glasses. Although glasses are amorphous, their atomic structure is not completely random and the short-range and medium-range order exists in glasses, while lacking the long-range order. The short-range order can be represented by the existence of specific structural motifs, for example, tetrahedral, octahedral or icosahedral structural units, often distorted, in the glass. This means that the nearest-neighbour atomic distances and angles between the corresponding crystal and glass can be very similar. The units interconnectivity represents the medium-range order and leads to some characteristic structural “ordering” in the frozen liquid.

Our research interest is multi- and inter-disciplinary, yet the focus has always been materials-oriented and based around chalcogenide (amorphous semiconductors) and metallic glasses. In this commentary, which is far from being comprehensive, we will summarize and convey our contribution to the understanding of crystallization in glasses (Ch. 1), and the role of kinetic fragility and the reduced-glass-transition temperature in crystallization kinetics (Ch. 2), mostly represented by crystal-growth rate (Ch. 3). We will show that the significant difference in crystal-growth rate exceeding 12 orders of magnitude and the principal difference in propensity for crystallization of glass-forming liquids is kinetic, not thermodynamic. The temperature at which the maximum in crystal-growth rate occurs can be described by a correlation between two parameters, namely the reduced-glass-transition temperature and kinetic fragility of a liquid thus evolving from the fundamental problem addressed by Turnbull. For the first time, pure-metal glasses will be shown to also follow different glass-forming correlations, mostly suggested for traditional glass-forming liquids, bridging the gap between collision-limited and diffusion-limited models for crystal growth.

[a] D. Whitehouse, *Glass: A Short History*, Smithsonian Books, Washington, DC, (2012).

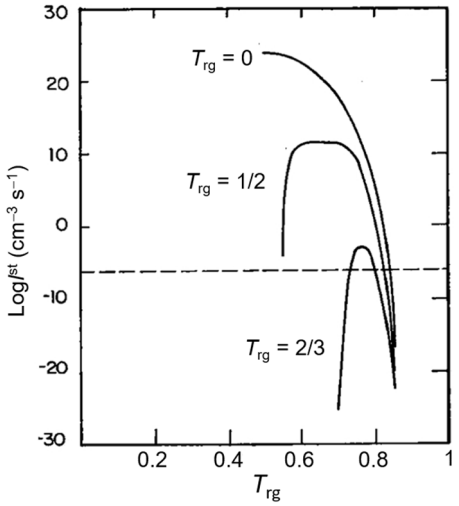

Fig. I Turnbull's seminal work on "*Under what conditions can a glass be formed*" published in 1969 brought the first quantitative definition of the glass-forming ability based on nucleation theory by assuming steady-state nucleation kinetics. The horizontal dashed line at $I^{\mathrm{st}} = 10^{-6}$ cm^{-3} s^{-1} indicates the nucleation rate below which the liquid volume is too small, and the time-scale is too long to be practically measured and therefore glasses are formed. This is characteristic for systems with $T_{\mathrm{rg}} > 2/3$, the so-called "$2/3$-rule". He also noted that the dependence would be greatly influenced by what is now termed as *kinetic fragility*, reflecting the temperature dependence of viscosity, and we will present this in detail in the main text of the thesis. [I^{st} – steady-state nucleation rate; ΔT_{rg} – reduced-glass-transition temperature: $T_{\mathrm{rg}}\left(= T_{\mathrm{g}}/T_{\mathrm{m}}\right)$, T_{g}: glass-transition temperature, T_{m}: melting point.] *Adapted and modified from Ref.*[b]

In chapter 4, we will describe details of the nanosecond time-scale crystallization in the supercooled liquid of phase-change chalcogenides which are used as the active layer in phase-change random-access memory. The crystallization kinetics in the entire region of the existence of the supercooled liquid is obtained and correlated with the liquid fragility (viscosity) by using novel ultrafast-heating calorimetry. Two types of phase-change chalcogenide glasses are identified: i) single-fragility liquids – the temperature-dependent viscosity of the liquid can be described by (super)-non-Arrhenius kinetics; and ii) liquids showing a fragile-to-strong crossover on cooling. Implications of both types of kinetics on the memory performance, in terms of writing, erasing rates and long-term stability, are discussed. The two types of kinetics can also explain the different crystallization mechanisms of two types of phase-change chalcogenides, i.e., nucleation- and growth-dominated. We will theoretically calculate that by tuning the size and population of subcritical nuclei, the memory writing speed can be enhanced by several orders of magnitude, and the calculated improvements agree with experimental data.

Chapter 5 focuses on describing the non-equilibrium phase-selection mechanism of fast heating and cooling in metallic-glass-forming liquids. By combining a unique set of *in-situ* experimental techniques, including synchrotron radiation, the conditions and mechanism under which metal-glass–crystal composites form are defined on millisecond time-scale between the glass-transition and melting temperature. Composites improve the glass plasticity and a critical heating rate to achieve the beneficial property lies in a range of heating rate ~10^2–10^3 K s^{-1}.

Enhanced by the lacking long-range order and the presence of strong electron-phonon coupling, chalcogenide glasses dynamically respond to illumination, and their structure and properties can actively be controlled. Unlike in the above cases, we will address some fascinating features of

[b] D. Turnbull, Under what conditions can a glass be formed? *Contemp. Phys.* **10**, 473 (1969).

reversible *athermal* transitions (amorphous-to-amorphous and amorphous-to-crystalline) in Chapter 6, those without an effective heat transfer, induced by lasers. Although the origin of the transitions is electronic not thermal, it bears some resemblance with thermal effects which is discussed. We show that when the glass contains the right amount and type of structural defects the transitions are fully reversible and cyclable.

In this commentary, it is not intended to offer full and detailed background and mathematical treatment of individual problems – these can be found in the published papers. The aim is to describe the processes underlying thermal crystallization/solidification and athermal transitions and relate them to on-demand macroscopic properties of functional glasses in selected applications and performance of electronic (phase-change random-access memory – Chapter 4), structural (metallic glasses – Ch. 5) and optical (chalcogenide glasses – Ch. 6) materials.

It is my great honour to dedicate this thesis to Prof. Miloslav Frumar, who passed away in February 2021. I was fortunate to study and work in Frumar's laboratory at the *University of Pardubice* between 2004–2009. He dedicated his professional life to glass science, and although he spent a major part of his career 'isolated' in the Czechoslovak Socialist Republic, Frumar became a worldwide respected and leading expert in the field. Frumar was completely driven by his passion for science, and he was known for detail and critical thinking at a level I keep trying to reach.

In the experimental work and in writing this thesis, I have been greatly inspired and motivated by two mentors of mine, namely Tomas Wagner (*University of Pardubice*) and A. Lindsay Greer (*University of Cambridge*). I have greatly benefited from their support, and I would like to thank them for the inspiring discussions which have been constantly bringing new ideas and driving me forward even in writing this commentary.

I thank all my friends, colleagues, and co-workers without whom most of the papers would never get published.

I would like to thank the *Faculty of Chemical Technology* (University of Pardubice), *Department of Materials Science and Metallurgy* (University of Cambridge), *Advanced Institute for Materials Research* (Tohoku University), *Leibniz Institute for Solid State and Materials Research Dresden* (IFW Dresden), *Deutsches Elektronen–Synchrotron* (DESY, Hamburg) facility and *Faculty of Environment* (J. E. Purkyne University in Usti nad Labem) for providing me with the access to their research facilities.

I thank my family, wife Lucie, and sons Krystof and Martin for their great support.

Symbols

Symbol	Definition
$A_{\mathrm{CG}}, B_{\mathrm{CG}}, C_{\mathrm{CG}}, T_0^{\mathrm{CG}}$	fitting parameters of Cohen-Grest model of $\eta(T)$
a	effective molecular diameter
B, C	fitting parameters in MYEGA model of $\eta(T)$
C_{c}	crystallographic-dependent constant in a collision-limited U model
C_1, C_2, W_1, W_2	fitting parameters in generalized-MYEGA model of $\eta(T)$
D	diffusivity
D_0	pre-exponential factor in D
f	fraction of active growth sites at the crystal-liquid interface
E	photon energy
$E_{\mathrm{g}}^{\mathrm{opt}}$	optical bandgap energy
E_{U}	Urbach energy
F	dimensionless parameter for glass-forming ability
G	Gibbs free energy
H	enthalpy
I^{st}	steady-state nucleation rate
K	kinetic coefficient in Johnson-Mehl-Avrami kinetics
k_{B}	Boltzmann's constant
k^+	forward flux to grow *n* to $n+1$
k^-	backward flux to dissolve *n* by $n-1$
m	kinetic fragility of supercooled liquid
m'	kinetic fragility of a high-temperature end of a fragile-to-strong crossover
$m_{\mathrm{str.}}$	structural fragility index
M	molar mass
n	**Sections 1–5**: number (size): of atoms of formula units; *monomers* in CNT terminology; **Section 6**: refractive index
n^*	critical nucleus size
n_{A}	Avrami exponent
N	nuclei density in Johnson-Mehl-Avrami kinetics
N_{A}	Avogadro's number
N^{eq}	equilibrium cluster population
N^{st}	steady-state cluster population
q	latent heat of crystallization per molecule
Q	wave vector
Q_D^{eff}	thermally-compensated activation energy for diffusion
Q_I	activation energy for steady-state nucleation rate
Q_{K}	activation energy from Kissinger analysis
Q_U	activation energy for crystal growth

Q_η	activation energy for viscous flow
R	universal gas constant
r^*	critical radius of a nucleus
r_1, r_1	positions of the first- and second-coordination shells in the pair-correlation function
S_{ex}	excess entropy of the interface
$S(Q)$	X-ray total structure factor
$S(Q_1)$	height of the first peak in $S(Q)$
t	time
t_{x}	crystallization onset time
T	temperature (typically in absolute units)
T_{e}	eutectic-melting temperature
T_{f}	fictive temperature
T_{g}	glass-transition temperature
T_{K}	Kauzmann temperature
T_{s}	solidus temperature
T_{l}	liquidus temperature (typically in absolute units)
T_{m}	equilibrium melting temperature (typically in absolute units)
T_{p}	crystallization peak temperature
T_{x}	crystallization onset temperature
T_{max}^{U}	temperature at which U_{max} occurs $(= 1.48T_{\mathrm{g}})$
T_{gu}	fragility-corrected reduced-glass-transition temperature: $T_{\mathrm{gu}}(= T_{\mathrm{rg}} - m/505)$
T_{rg}	reduced-glass-transition temperature: $T_{\mathrm{rg}}(= T_{\mathrm{g}}/T_{\mathrm{m}})$
T_{FTS}	temperature of a fragile-to-strong crossover
T_{LL}	temperature of liquid-to-liquid transition
U	crystal-growth rate
U_{kin}	kinetic coefficient of crystal-growth rate
U_{max}	maximum in crystal-growth rate
v	atomic or monomer volume
V_{m}	molar volume
W	reversible work of clusters formation
x	volume fraction of crystalline phase
x_{M}	molar fraction
α^{l}	activity coefficient of an element in the liquid
α_{m}	crystal-structure-dependent geometrical factor
γ	molecular jump frequency
ΔH_{m}	latent heat of melting/enthalpy of melting
ΔH_{x}	latent heat of crystallization/enthalpy of crystallization
ΔS_{m}	entropy of melting
ΔS_{r}	reduced entropy of melting $(= \Delta S_{\mathrm{m}}/R)$

ΔT_{c}	curvature supercooling
ΔT_{k}	kinetic supercooling
ΔT	used in general discussion; if not specified then it mostly refers to ΔT_{m}
ΔT_{m}	supercooling $(= T_{\mathrm{m}} - T)$
ΔT_{l}	supercooling $(= T_{\mathrm{l}} - T)$; typically used in solidification studies
ΔT_{s}	solutal supercooling
ΔT_{t}	thermal supercooling
$\Delta\mu$	driving force for crystallization per molecule
ζ_0^{λ}	temperature-dependent coefficient of an element in the liquid
η	shear viscosity
η_∞	high-temperature limit of viscosity
θ_{n^*}	time-lag (incubation time, transient time)
κ	adiabatic bulk modulus
λ	wavelength
ξ	decoupling constant
ρ	density
σ	crystal-liquid interfacial energy (the energy per unit area of the interface between the crystal and the supercooled liquid)
Φ_{c}	cooling rate
Φ_{h}	heating rate
χ_{n^*}	number of critical nuclei
Ψ	thermodynamic factor of crystal-growth rate

Abbreviations and acronyms

Acronym	Meaning
AATs	amorphous-to-amorphous transitions
AFM	atomic-force microscopy
AIST	(Ag,In)-doped Sb_2Te alloys, predominantly $Ag_{5.5}In_{6.5}Sb_{59}Te_{29}$ (at.%)
CAGR	compound annual growth rate
CB-RAM	conductive-bridging random-access memory
CCT	continuous-cooling-transformation (diagram)
ChGs	chalcogenide glasses
CG	Cohen-Grest (model of $\eta(T)$)
CHT	continuous-heating-transformation (diagram)
CNT	classical nucleation theory
CS	corner-sharing (tetrahedra)
DESY	Deutsches Elektronen-Synchrotron
DFT	density-functional theory
DSC	differential scanning calorimetry
EDX	energy dispersive X-ray (analysis)
ES	edge-sharing (tetrahedra)
FDSC	ultrafast DSC (alternatively known as flash DSC, ultrafast-heating DSC)
FSC	fragile-to-strong crossover
GFA	glass-forming ability
GST	$Ge_2Sb_2Te_5$
HAADF	high-angle annular dark-field (scanning)
JMA	Johnson-Mehl-Avrami (kinetics)
LEAPT	local-electrode atom-probe tomography
MD	molecular-dynamics
MOF	metal-organic framework
MGs	metallic glasses
MYEGA	Mauro-Yue-Ellison-Gupta-Allan (model of $\eta(T)$)
OTP	*o*-terphenyl
PC	phase change
PCM	phase-change memory
PLD	pulsed-laser deposition
PMC	programmable metallization cell
ROY	5-methyl-2-[(2-nitrophenyl)amino]-3-thiophenecarbonitrile
SAED	selected area electron diffraction (imaging)
SBs	shear bands
SEM	scanning electron microscopy
STEM	scanning transmission electron microscopy
TE	thermal evaporation
TEM	transmission electron microscopy
TTT	time-temperature-transformation (diagram)
XPS	X-ray photoelectron spectroscopy
XRD	X-ray diffraction

List of publications included in the thesis

Following the Masaryk University habilitation rules, Table I lists my quantitative and content contribution to the papers and book chapters included in the thesis (**Appendix I**).

Table I Chronological list of published papers and book chapters in Appendix I, and my quantitative (%) and author's contribution to each publication.

#	Publication	Share	Author's contribution	Page
	2012			
1	Letter: **J. Orava**, A. L. Greer*, B. Gholipour, D. W. Hewak, and C. E. Smith, Characterization of supercooled liquid $Ge_2Sb_2Te_5$ and its crystallization by ultrafast-heating calorimetry. *Nat. Mater.* **11**, 279 (2012). https://doi.org/10.1038/nmat3275	60%	Thin-film deposition; ultra-fast calorimetry measurements and data analysis; numerical modelling, writing.	-1-
2	**J. Orava**, A. L. Greer*, B. Gholipour, D. W. Hewak, and C. E. Smith, Ultra-fast calorimetry study of $Ge_2Sb_2Te_5$ crystallization between dielectric layers. *Appl. Phys. Lett.* **101**, 091906 (2012). https://doi.org/10.1063/1.4748881	70%	Thin-film deposition; fast calorimetry measurements and data analysis; numerical modelling; conceptualization & writing.	-1-
	2013			
3	M. Kalyva§, **J. Orava**§, A. Siokou*, M. Pavlista, T. Wagner, and S. N. Yannopoulos*, Reversible amorphous-to-amorphous transitions in chalcogenide films: Correlation changes in structure and optical properties. *Adv. Funct. Mater.* **23**, 2052 (2013). https://doi.org/10.1002/adfm.201202461	30%	Thin-film deposition; spectroscopic ellipsometry; conceptualization & writing	-2-
	2014			
4	**J. Orava** and A. L. Greer*, Fast and slow crystal growth kinetics in glass-forming melts. *J. Chem. Phys.* **140**, 214504 (2014). https://doi.org/10.1063/1.4880959	50%	Data analysis and calculations; conceptualization & writing.	-2-
5	Book chapter: **J. Orava**, T. Kohoutek, and T. Wagner, Deposition techniques for chalcogenide thin films, in: *Chalcogenide Glasses: Preparation, Properties and Applications*, J. L. Adam & X. Zhang (Eds.), Woodhead Publishing Ltd., Cambridge, UK, 2014, pp. 265–309. https://doi.org/10.1533/9780857093561.1.265	70%	Lead author; conceptualization & writing.	-3-
	2015			
6	**J. Orava**, D. W. Hewak, and A. L. Greer*, Fragile-to-strong crossover in supercooled liquid Ag-In-Sb-Te studied by ultrafast calorimetry. *Adv. Funct. Mater.* **25**, 4851 (2015). https://doi.org/10.1002/adfm.201501607	60%	Thin-film deposition; ultrafast calorimetry measurements, data analysis, numerical modelling, conceptualization & writing.	-3-
7	**J. Orava*** and A. L. Greer*, Kissinger method applied to the crystallization of glass-forming liquids: Regimes revealed by ultra-fast-heating calorimetry. *Thermochimica Acta* **603**, 63 (2015). https://doi.org/10.1016/j.tca.2014.06.021	50%	Modelling, data analysis, conceptualization & writing.	-4-

8	**J. Orava**[*], M. N. Kozicki, S. N. Yannopoulos, and A. L. Greer, Reversible migration of silver on memorized pathways in Ag-$Ge_{40}S_{60}$ films. *AIP Advances* **5**, 077134 (2015). http://dx.doi.org/10.1063/1.4927006	60%	Conductive atomic-force microscopy and Raman spectroscopy measurements and analysis; conceptualization & writing	-4-
	2016			
9	**J. Orava**[*], H. Weber, I. Kaban, and A. L. Greer[*], Viscosity of liquid Ag–In–Sb–Te: Evidence of a fragile-to-strong crossover. *J. Chem. Phys.* **144**, 194503 (2016). https://doi.org/10.1063/1.4949526	60%	Thin-film deposition; ultrafast calorimetry measurements; data analysis; numerical modelling; conceptualization & writing.	-5-
10	Review: **J. Orava**[*] and A. L. Greer[*], Fast crystal growth in glass-forming liquids, *J. Non-Cryst. Solids* **451**, 94 (2016). https://doi.org/10.1016/j.jnoncrysol.2016.06.007	50%	Conceptualization & writing.	-5-
	2017			
11	**J. Orava**[*] and A. L. Greer[*], Classical-nucleation-theory analysis of priming in chalcogenide phase-change memory. *Acta Mater.* **139**, 226 (2017). https://doi.org/10.1016/j.actamat.2017.08.013	50%	Calculations; data analysis; conceptualization & writing.	-6-
12	V. Benekou[*], L. Strizik, T. Wagner, S. N. Yannopoulos, A. L. Greer, and **J. Orava**[*], *In-situ* study of athermal reversible photocrystallization in a chalcogenide glass. *J. Appl. Phys.* **122**, 173101 (2017). https://doi.org/10.1063/1.5003575	30%	Conceptualization & writing.	-6-
13	**J. Orava**[*], Y. Wen, J. Prikryl, T. Wagner, N. A. Stelmashenko, M. W. Chen, and A. L. Greer[*], Preferred location for conducting filament formation in thin-film nano-ionic electrolyte: Study of microstructure by atom-probe tomography. *J. Mater. Sci.: Mater. Electron.* **28**, 6846 (2017). https://doi.org/10.1007/s10854-017-6383-y	70%	Thin-film deposition; atom-probe tomography measurements and data analysis; conceptualization & writing.	-7-
	2018			
14	H. Weber, **J. Orava**[*], I. Kaban[*], J. Pries, and A. L. Greer, Correlating ultrafast calorimetry, viscosity, and structural measurements in liquid GeTe and $Ge_{15}Te_{85}$. *Phys. Rev. Mater.* **2**, 093405 (2018). https://doi.org/10.1103/PhysRevMaterials.2.093405	50%	Data analysis; conceptualization and writing.	-7-
15	Book chapter: **J. Orava** and A. L. Greer, Chalcogenides for phase-change memory, in: *Handbook of Thermal Analysis and Calorimetry: Recent Advances, Techniques and Applications*, 2nd Edition, S. Vyazovkin, N. Koga & C. Schick (Eds.), Elsevier, Amsterdam, Netherlands, 2018, pp. 685–734. https://doi.org/10.1016/B978-0-444-64062-8.00014-0	50%	Conceptualization & writing.	-8-
	2019			
16	S. Balachandran[*], **J. Orava**, M. Köhler, A. J. Breen, I. Kaban, D. Raabe, and M. Herbig, Elemental re-distribution inside shear bands revealed by correlative atom-probe tomography and electron microscopy in a deformed metallic glass. *Scr. Mater.* **168**, 14 (2019). https://doi.org/10.1016/j.scriptamat.2019.04.014	20%	Atom-probe tomography data interpretation; writing.	-8-

17	Review: **J. Orava**[*], I. Kaban, M. Benkocka, X. Han, I. Soldatov, and A. L. Greer, Fast-heating-induced formation of metallic-glass/crystal composites with enhanced plasticity. *Thermochimica Acta* **677**, 198 (2019). https://doi.org/10.1016/j.tca.2019.03.029	80%	Conceptualization & writing.	-9-
	2020			
18	**J. Orava**[*], K. Kosiba[*], X. Han, I. Soldatov, O. Gutowski, O. Ivashko, A.-C. Dippel, M. v. Zimmermann, A. Rothkirch, J. Bednarcik, U. Kühn, H. Siegel, S. Ziller, A. Horst, K. Peukert, R. Voigtländer, D. Lindackers, and I. Kaban, Fast-current-heating devices to study in situ phase formation in metallic glasses by using high-energy synchrotron radiation. *Rev. Sci. Instrum.* **91**, 073901 (2020). https://doi.org/10.1063/5.0005732	40%	Device manufacturing; calibrations; high-energy X-ray diffraction measurements and data analysis; conceptualization & writing.	-9-
19	Q. Cheng, X. Han, I. Kaban, I. Soldatov, W. H. Wang, Y. H. Sun[*], and **J. Orava**[*], Phase transformations in a Cu–Zr–Al metallic glass. *Scr. Mater.* **183**, 61 (2020). https://doi.org/10.1016/j.scriptamat.2020.03.028	50%	Data analysis; conceptualization & writing; supervision.	-10-
	2021			
20	Letter: Q. Cheng, P. F. Wang, H. Y. Jiang, L. Gu, **J. Orava**[*], Y. H. Sun[*], H. Y. Bai, and W. H. Wang, Effect of high-temperature up-quenching on stabilizing off-eutectic metallic glasses. *Phys. Rev. B* **103**, L100302 (2021). https://doi.org/10.1103/PhysRevB.103.L100203	30%	Conceptualization & writing; supervision.	-10-
21	**J. Orava**[*], S. Balachandran[*], X. Han[*], O. Shuleshova, E. Nurouzi, I. Soldatov, S. Oswald, O. Gutowski, O. Ivashko, A.-C. Dippel, M. v. Zimmermann, Y. P. Ivanov, A. L. Greer, D. Raabe, M. Herbig, and I. Kaban[*], In situ correlation between metastable phase-transformation mechanism and kinetics in a metallic glass. *Nat. Commun.* **12**, 2839 (2021). https://doi.org/10.1038/s41467-021-23028-9	50%	Lead author; device construction; *in-situ* synchrotron XRD measurements and data analysis; electromagnetic levitation measurements and data analysis; atom-probe-tomography-data interpretation; conceptualization & writing.	-11-
22	Book chapter: **J. Orava**, T. H. Lee, S. R. Elliott, and A. L. Greer, Crystallization of phase-change chalcogenides, in: *The World Scientific Reference of Amorphous Materials, Volume 1: Amorphous Chalcogenides: Structure, Properties, Modeling and Applications*, K. Shimakawa & A. V. Kolobov (Volume Eds.), Elsevier, World Scientific, 2021, pp. 367–402. https://doi.org/10.1142/9789811215575_0012	30%	Lead author; conceptualization & writing.	-11-

* Corresponding author(s)
§ These authors contributed equally to the work

1. INTRODUCTION

In this chapter, we give a short overview of crystallization in glasses to facilitate the understanding of the presented results. The background text is far from being comprehensive, and more details, also covering different topics of the commentary can be found in: *Nucleation in Condensed Matter: Applications in Materials and Biology* by Kelton & Greer [1]; *Solidification and Crystallization* by Herlach [2]; *Metastable Solids from Undercooled Melts* by Herlach, Galenko & Holland-Moritz [3]; *Phase Transformations in Metals and Alloys* by Porter & Easterling [4]; *Solidification of Containerless Undercooled Melts* by Herlach & Matson (Eds.) [5]; *Bulk Metallic Glasses* by Suryanarayana & Inoue [6]; *Chalcogenide Glasses: Preparation, Properties and Applications* by Adam & Zhang (Eds.) [7]; *Phase Change Materials: Science and Applications* by Raoux & Wuttig (Eds.) [8]; *Molecular Dynamics Simulations of Disordered Materials: From Network Glasses to Phase-Change Memory Alloys* by Massobrio, Du, Bernasconi & Salmon (Eds.) [9]; and *The World Scientific Reference of Amorphous Materials: Structure, Properties, Modeling and Applications – Vol. 1* by Kolobov & Shimakawa (Eds.) [10].

1.1. Manipulating glassy states

Upon cooling the liquid, a range of glassy states can be achieved reflecting the liquid thermal history controlled by cooling rate, Φ_c, which can exceed 17 orders of magnitude (**Fig. 1.1**). The corresponding enthalpy range, H, of the glassy states achieved is remarkably wide, up to $\sim 0.9\Delta H_m$ – the latent heat of melting – at a given homologous temperature. The schematic of $H(T)$ in Fig. 1.1 is based on that for metallic glass (MG) $Zr_{52.5}Cu_{17.9}Ni_{14.6}Al_{10.0}Ti_{5.0}$ (here and throughout the text in at.%) with a critical cooling rate of ~1 K s^{-1} [11]. The standard Φ_c is defined at ≈10–20 K min^{-1} (0.16–0.33 K s^{-1}), corresponding to the rates typical in conventional calorimetry, and is used for defining the glass-transition temperature, T_g, which conventionally adopts value of viscosity $\eta = 10^{12}$ Pa s [12]. The range of experimental or predicted (modelled) values of T_g is very wide. It can be represented by the variation of the reduced-glass-transition temperature $T_{rg}\left(= T_g/T_m\right)$, T_m is the melting point, ranging from $T_{rg} \approx 0.32$ for very bad-glass-forming-supercooled pure metals (Ir, Pd) [13,14] to $T_{rg} \approx 0.84$ for ultrahigh glass-forming metal-organic-framework (MOF) glasses (ZIF-62) [15]. At the standard rate, the typical heat of crystallization, ΔH_x, is $\sim 0.4\Delta H_m$ for metallic-glass-forming systems.

Relaxation (ageing) refers to states of lower energy, while *rejuvenation*, the inverse of relaxation, terms states of higher energy. Highly relaxed glassy states corresponding to $\Phi_c \approx 10^{-14}$ K s^{-1} and lower are possibly achieved for ultrastable amorphous films deposited at the elevated substrate temperature of $(0.75 - 0.9)T_g$, for example, in molecular glasses [16,17]. Highly unrelaxed states may be reached at Φ_c as high as 10^{14} K s^{-1}, which is readily studied in molecular-dynamics (MD) simulations [9], in Joule-heated pure-metal glassy nanobridges [18] or in laser surface melting [19]. For any glass, the details of the transition to the supercooled-liquid state depend on heating rate, Φ_h, (inset in Fig. 1.1). During slow heating relative to the cooling of the liquid, the glass can undergo true relaxation, potentially erasing its thermal history, and, in that case, the crystallization is generally considered to be unaffected by the prior glassy state.

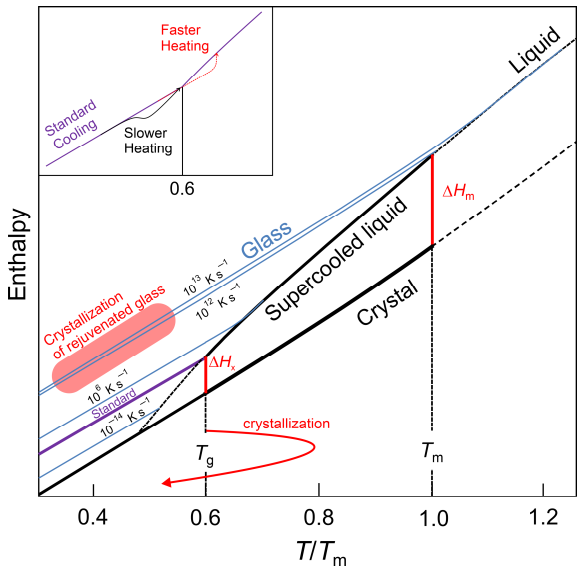

Fig. 1.1 Schematic showing the representation of the temperature dependence of relative enthalpy H on cooling a metallic-glass-forming liquid $Zr_{52.5}Cu_{17.9}Ni_{14.6}Al_{10.0}Ti_{5.0}$ also known as Vitreloy 105. Potential isoconfigurational states which can be reached are from 10^{-14} (ultrastable amorphous films) to 10^{13} K s^{-1} (a glass formed upon rapid quenching in computer simulations). The inset shows the typical relaxation behaviour near T_g on heating at different rates; the temperature indicated in the figure is for $\Phi_h = 0.33$ K s^{-1} (20 K min^{-1}). (ΔH_x – enthalpy of crystallization; ΔH_m – enthalpy of melting). *Reproduced from Orava & Greer [20] (**publication #10 – Appendix I**).*

The relaxation spectrum, often bimodal but also of higher order, can be detected as a complex exotherm spreading over a range of temperatures (related to the α-, β-relaxation processes [21]) just below or overlapping with T_g, and certainly before crystallization. On relatively fast heating of the glass, an endothermic peak overlapping with T_g is observed reflecting the development of structural changes on heating the slowly cooled liquid.

It becomes apparent that manipulating the isoconfigurational states in Fig. 1.1 gives access to a wide range of energetic systems with new and/or enhanced functional properties. For typical thermal treatments, relaxation is achieved by annealing below T_g. Rejuvenation necessitates going through the supercooled-liquid state by reheating the glass, a temperature of a few percent above T_g may be enough [22], followed by fast quenching. In general, **relaxation** gives harder glasses with high resistance to creep and crystallization and having fewer structural defects ensuring long-term structural stability. **Rejuvenation** gives heterogeneous glassy structure and chemical inhomogeneities on the nanometre length-scale and glasses with greater plasticity and faster crystallization. Nevertheless, structural drift in unrelaxed glasses, especially for low-T_g systems, becomes the limiting factor for glasses used in electronics [23]. For rejuvenated (high-H) glasses, crystallization may proceed even below T_g (Fig. 1.1) at very low temperature, for example, for amorphous Bi films deposited at ~2 K crystallization already starts at 15 K upon heating [24].

In this commentary, which aims to summarize and provide an overview of the results published in the enclosed papers in **Appendix I**, we will mostly focus on three exemplary study cases covering our research interest.

i) For fast-crystallizing phase-change (PC) chalcogenides used in phase-change memory (PCM), presented in Ch. 4 in detail, contradictory requirements bridging the material's property of the two extreme energy states in Fig. 1.1 must be met. The PC glass atomic structure must be stable at room

and at slightly elevated temperatures up to ~100 °C – low-H state ensuring data stability – while the crystallization rate, specifically crystal-growth rate $U(T)$, must be high, preferably as high as in the supercooled liquid pure metals $U(T)\sim 10-100$ m s^{-1} – high-H state – providing short writing times. The maximum in $U(T)$, $U_{\max}$, should ideally be controlled in a narrow temperature range – practical for intermediate-H state (such as for SiO_2 represented by $T_{\mathrm{rg}}=2/3$ in Fig. I – *Preface*). All these requirements are difficult to be achieved with a single material, and which is prototyped by single-fragility $Ge_2Sb_2Te_5$ (Sect. 4.1.). We will demonstrate that the existence of a *fragile-to-strong crossover* (FSC) in the temperature-dependent viscosity, $\eta(T)$, upon cooling the supercooled liquid can be one of the strategies to fulfil such a contradictory criterion (Sect. 4.2.). Tuning the population and size of subcritical nuclei in the liquid can represent another way of improving PCM device performance, and this is discussed in Sect. 4.3.

ii) In metallic glasses, except for a few cases such as $Cu_{50}Zr_{50}$ and some Pd–Ni–P-based systems, phase transformations are mostly not polymorphic during conventional heating, $\Phi_{\mathrm{h}}<100$ K min^{-1}. On the other hand, when the heating rate exceeds a certain critical value, solute partitioning is kinetically suppressed, crystallization becomes congruent and metastable phases, not being possible to obtain during conventional heating, can be formed. Some metastable phases can have beneficial influence on materials properties, such as enhancing plasticity (deformation in compression) and ductility (deformation in tension), which is exploited in MGs–crystal composites. Equilibrium phases might be brittle but can provide, for example, hardness [25] thus representing a trade-off between the two mechanical properties. The critical heating rate depends on the glass composition. In our case, the interest will be in the archetype CuZr-based family of MGs, the critical rate needed is $>10^2$ K s^{-1} and it can be achieved, among other methods, by resistive heating, so-called *flash-annealing* (Ch. 5).

iii) Thermal cycling through the supercooled liquid and below-T_{g} are the most traditional ways of tuning glass' properties, and they are limited by the range of experimentally practical Φ_{h} and Φ_{c}; fasters rates are achievable for smaller-size samples limiting the potential use in some applications. A wide range of glassy states can also be accessed by other methods such as mechanical processing (plastic and elastic deformation induced by various methods) [26], irradiation (this can induce one of the largest relative changes in H, although limited to small surface volumes) [26], or through cryogenic cycling [26]. These methods do not necessitate the supercooled liquid state and are beyond the scope of this commentary. Details can be found either in our papers [27–29] or in the literature [26,30,31]. Here, will demonstrate a specific case of illumination which promotes *amorphous-to-amorphous transitions* (AATs) in a chalcogenide glass (ChG) by targeting 'defective' bonding (Sect. 6.1.), and a unique effect of *athermal photoinduced rejuvenation* followed by *reversible athermal crystallization*, where the photocrystallization is the exit strategy from the highly unrelaxed state of a ChG (Sect. 6.2).

1.2. Crystallization/solidification in glass-forming liquids

The kinetic and thermodynamic factors underlying some of the processes discussed in Fig. 1.1 are introduced in **Fig. 1.2**. In general, crystallization (phase transformations on heating) and solidification (phase transformations on cooling) of the supercooled liquid are represented by the temperature-dependent steady-state nucleation rate, $I^{\mathrm{st}}(T)$, and $U(T)$ mostly occurring: i) close to T_{g}, at large supercooling (defined either as $\Delta T_{\mathrm{m}}=T_{\mathrm{m}}-T$ or as $\Delta T_{\mathrm{l}}=T_{\mathrm{l}}-T$); or ii) just below T_{m} corresponding to small supercooling, respectively. Crystal-growth rate is easier to analyse than I^{st} because of the quantitatively unknown role of the crystal-liquid interfacial energy, σ, which is associated with the

energy formation of a new interface between a crystal nucleus and the supercooled liquid or the glass matrix in which it forms per unit area.

The above definition of ΔT is derived from the following simplification. In general, crystallization is not polymorphic (the composition of a crystal is different from the supercooled liquid), and phase formation involves the transport of one or more solutes in the liquid. The latent heat released at the newly-forming interface between the liquid and a crystal involves the transport of heat, and the interface might be curved changing locally the supercooling through the Gibbs-Thomson effect [3].

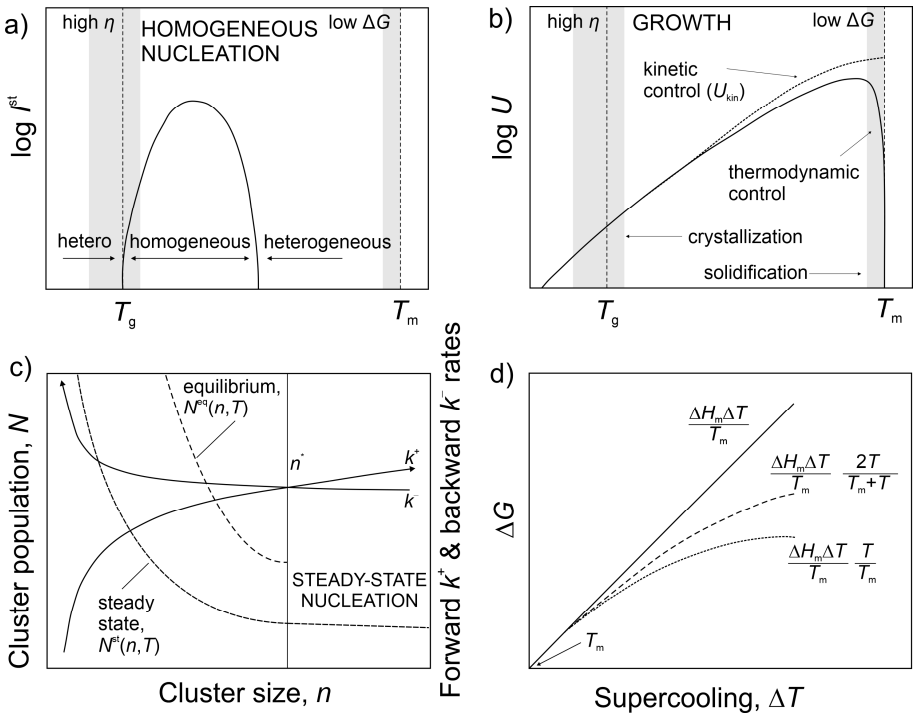

Fig. 1.2 Schematics representing the a)–b) kinetic and c)–d) thermodynamic factors driving phase transformations in glass-forming liquids. a) The temperature-dependent steady-state nucleation rate, $I^{\mathrm{st}}(T)$. The arrows mark a temperature range of the dominant heterogeneous and homogeneous nucleation. The glass-transition temperature, T_{g}, the melting point, T_{m} , viscosity, η, and the difference between the crystal and liquid Gibbs free energy, ΔG, are shown. **b)** Crystal-growth rate, $U(T)$, with the controlling kinetic, U_{kin} (Eq. 1.10), and thermodynamic factors (see details in the main text, Sect. 1.2.2.). The shading in parts a and b highlights the regions of conventional crystallization and solidification of glass-forming liquids. **c)** The steady-state population, $N^{\mathrm{st}}(n,T)$, (strictly, it represents a quasi-steady-state distribution because monomers are depleted over time) and the equilibrium population, $N^{\mathrm{eq}}(n,T)$, Eq. 1.5, of clusters (per mole) as the function of cluster size, n, (no. of molecules) are shown by the *dashed lines*. The forward, $k^{+}(n)$ and the backward, $k^{-}(n)$, rates of respectively adding and removing molecules/formula units to/from nuclei are shown as the solid lines. **d)** Examples of various Gibbs free energy approximations used for glass-forming liquids: *Solid line* shows the simplest linear Turnbull's equation which was derived by assuming that the difference between the specific heats of the two phases, such as the liquid and a solid, is $\Delta C_{\mathrm{p}} = 0$, and it works well for pure metals [32]. The *long-dashed line* is the approximation by Thompson and Spaepen [33] assuming that $\Delta C_{\mathrm{p}} = \mathrm{const.}$ and non-zero, and that the entropy difference, ΔS, between the two phases vanishes close to the Kauzmann temperature, T_{K}, which lies somewhat below T_{g} – this approximation works well for metallic-glass-forming systems and is used in Chapter 4. The short-dashed line is after Hoffman [34]; it also assumes that $\Delta C_{\mathrm{p}} = \mathrm{const.}$ and works for some organics, for example, *o*-terphenyl. (ΔH_{m} – enthalpy of melting). *Parts a and b are re-drawn from Cahn & Greer [35]; the figure is reproduced from Orava & Greer [36] (**publication #15 – Appendix I**).*

All of these factors contribute to the total ΔT, which is then sum of predominantly four fundamental contributions [3,13]:

$$\Delta T = \Delta T_{\mathrm{s}} + \Delta T_{\mathrm{t}} + \Delta T_{\mathrm{c}} + \Delta T_{\mathrm{k}}, \tag{1.1}$$

where ΔT_{s} is the solutal term accounting for the interface composition being different from that of the bulk liquid; ΔT_{t} is the thermal term accounting for the temperature difference between the interface and the bulk; ΔT_{c} is the curvature effect via Gibbs-Thomson; and ΔT_{k} represents the actual supercooling, difficult to measure directly, at the interface driving $U(T)$, and in practice, it can be considered that $\Delta T \approx \Delta T_{\mathrm{k}}$, and that ΔT_{s}, ΔT_{t}, and ΔT_{c} are negligible [13,37–39]. For example, another contribution to ΔT could be due to the shift of the equilibrium slope of the liquidus line [40].

Both, $I^{\mathrm{st}}(T)$ and $U(T)$ have a maximum between T_{g} and T_{m} originating from the interplay between the kinetic and thermodynamic factors (Fig. 1.2a and b). For crystallization of metallic-glass-forming liquids, $I^{\mathrm{st}}(T)$ typically shows a maximum at a homologous temperature of $\sim 0.6T_{\mathrm{m}}$ [41,42], and the temperature, T^{U}_{max}, at which a maximum in $U(T)$ occurs lies at $T^{U}_{\mathrm{max}} = (1.48 \pm 0.15)T_{\mathrm{g}}$ [13] (see Fig. 2.3a in Chapter 2) for polymorphic (congruent) crystallization in different families (molecular organics, oxides, metallic glasses, metals, chalcogenides) of glass-forming liquids, and, maybe surprisingly, also holds for eutectic transformations [13,43,44].

1.2.1. Nucleation

Here, we use the nomenclature and formalism of Kelton & Greer [1,45] (please note that different nomenclature has been used in the literature which can result in confusion). In the view of *classical nucleation theory* (CNT) the freezing is considered to be polymorphic, and the crystal nucleation of spherical clusters is taken to be homogeneous in the supercooled liquid. The reversible work of clusters formation of a new phase (a crystal in the supercooled liquid) depends on the cluster size, n, representing the number of molecules (atoms of formula units; *monomers* in CNT terminology) can be described as [1]:

$$W(n,T) = n\Delta\mu + (36\pi)^{1/3} v^{1/3} n^{2/3} \sigma, \tag{1.2}$$

and the work shows a maximum at the critical nucleus size, n^*:

$$n^*(T) = \frac{32\pi v^2 \sigma}{3|\Delta\mu|^3}, \tag{1.3}$$

where, σ is the crystal-liquid interface, $\Delta\mu(T)$ is the driving force for crystallization per molecule related to the change in the Gibbs free energy per unit volume $\Delta G = \Delta\mu(T)/v$, where $\Delta G = G_{\mathrm{l}} - G_{\mathrm{c}}$, G_l and G_{c} are the Gibbs energies of the liquid and the crystalline states, and v is the atomic volume. Both σ and v are weekly dependent on temperature. It is difficult to obtain σ experimentally especially for fast-crystallizing systems used in PCM. It has been suggested, based on observations, that the product $\sigma \times V_{\mathrm{m}}^{2/3} \times N_{\mathrm{A}}^{1/3}$ (V_{m} – molar volume, N_{A} – Avogadro's number) scales with ΔH_{m} [46]. Because

σ can be treated as mainly of entropic origin [47,48], and energy associated with creating the new interface, it can be expressed using the Spaepen-Mayer expression [49]:

$$\sigma = \alpha_{\mathrm{m}} \frac{\Delta S_{\mathrm{m}}}{V_{\mathrm{m}}^{2/3} \times N_{\mathrm{A}}^{1/3}} T, \tag{1.4}$$

where ΔS_{m} is the entropy of melting ($= \Delta H_{\mathrm{m}}/T_{\mathrm{m}}$), and α_{m} is a crystal-structure-dependent geometrical factor with values $\alpha_{\mathrm{m}} = 0.71$ for bcc, and $\alpha_{\mathrm{m}} = 0.76$ for fcc and hcp structures. The crystal-liquid interface energy is typically treated to be constant, but it weakly increases with temperature as $\mathrm{d}\sigma/\mathrm{d}T = -S_{\mathrm{ex}}$, where the latter parameter is the excess entropy of the interface [50,51]. For the prototype CNT system lithium disilicate, the temperature dependence is $\sigma = 0.094 + (7\times10^{-5})T$ by fitting the measured $I^{\mathrm{st}}(T)$ [52].

The first term in Eq. 1.2 is negative, and the second term is positive. Nucleation occurs when $n \geq n^*$, and the critical nucleus size decreases with lower T (**Fig. 1.3a**) roughly proportional to ΔT^{-3} [1]. The equilibrium population of clusters $N^{\mathrm{eq}}(n,T)$ – their size distribution, per mole of a glass, is expressed as:

$$N^{\mathrm{eq}}(n,T) = N_{\mathrm{A}} \exp\left(-\frac{W}{k_{\mathrm{B}}T}\right), \tag{1.5}$$

where k_{B} is Boltzmann's constant. It can be shown that at any given temperature, $N^{\mathrm{eq}}(n)$ shows a minimum at n^* (Fig. 1.2c). For post-critical clusters, $N^{\mathrm{eq}}(n)$ has no physical meaning, represented by the upturn in Fig. 1.3b as clusters are consumed by their growth into macroscopic crystals, and the cluster sizes tend to a steady-state distribution, $N^{\mathrm{st}}(n)$, with lower population on isothermal annealing (Fig. 1.2c). As n approaches one, $N^{\mathrm{st}}(n)$ tends to $N^{\mathrm{eq}}(n)$, and at the critical size at a given temperature $N^{\mathrm{st}}(n^*) = 1/2\, N^{\mathrm{eq}}(n^*)$ (Fig. 1.3b). In Sect. 4.3., will show that nanosecond time-scale *priming* (pre-structural ordering) of PCM may seem to contradict CNT because $N^{\mathrm{st}}(n,T)$, approximated by $N^{\mathrm{eq}}(n,T)$, shows the opposite trend to what can be predicted by CNT for typical oxide glasses. It will be demonstrated that priming, indeed, can be well described by CNT and the effect arises from the unique combination of thermodynamic and kinetic parameters of PC chalcogenides. We will also show that a similar regime can theoretically be found in silicates [42], namely $Li_2O.2SiO_2$, but is physically inaccessible.

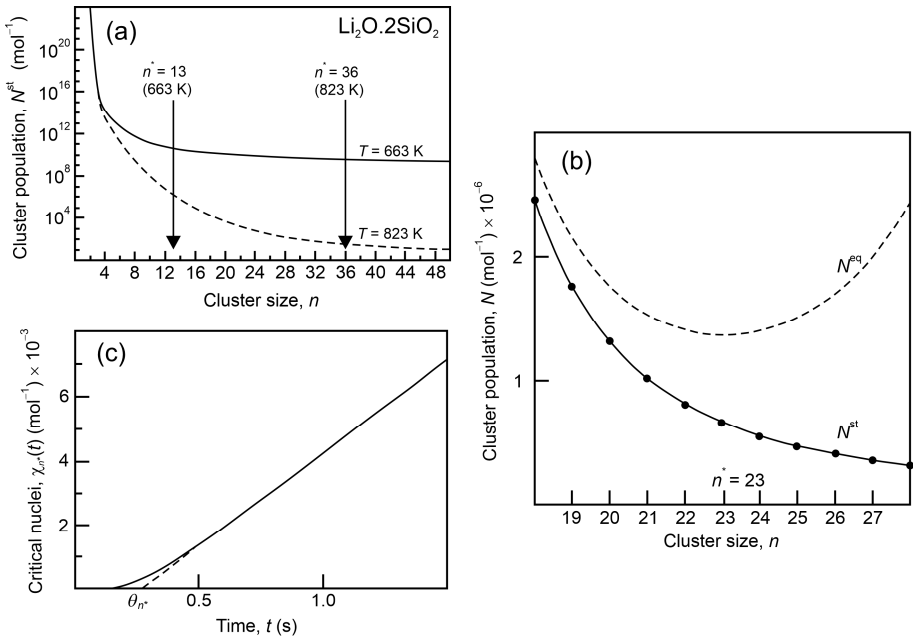

Fig. 1.3 Calculation of the steady-state, $N^{\mathrm{st}}(n,T)$, equilibrium, $N^{\mathrm{eq}}(n,T)$, cluster population, and the time evolution of the number of critical nuclei, $\chi_{n^*}(t)$, in the prototype lithium disilicate glass. a) Steady-state distributions and critical size, n^*, of formula units at 663 K and 823 K. **b)** Numerical simulation of the comparison between N^{st} and N^{eq} in the region of the critical size $n^* = 23$ at 750 K. **c)** The number of critical nuclei evolving on annealing at 820 K. The effective time-lag, θ_{n^*}, (Eq. 1.8) is read by the extrapolation highlighted by the dashed line. The thermodynamic and kinetic parameters used for the calculation can be found in Ref. [42] (see Table 4.2 in Chapter 4). *Reproduced from Orava & Greer [42] (**publication #11 – Appendix I**). Parts a and b are recalculated from the original work of Kelton & Greer [1,45,46]. Part b is re-calculated from Kelton et al. [45].*

For $n > n^*$, $N^{\mathrm{st}}(n)$ continues to decrease with increasing n because the post-critical clusters are effectively removed from the distribution by growing into microscopic crystals. In the steady-state, there is at the same time a forward $k^+(n)$ and backward $k^-(n)$ flux (per second) to form a cluster of size n to size $(n+1)$ and to dissolve a cluster by the same amount, respectively [53]. This leads to time-, t, and cluster-size-dependent nucleation rate given by $I(n,t) = N(n,t)k^+(n) - N(n+1,t)k^-(n+1)$. The Zeldovich factor [45] accounts for $N^{\mathrm{st}}(n,T)$ being smaller than $N^{\mathrm{eq}}(n,T)$, and for the significant $k^-(n)$, and therefore the probability of dissolving post-critical clusters (Fig. 1.2c) [1]. For $k^+(n)$ exceeding $k^-(n)$ by a constant amount, the steady-state rate of *homogeneous nucleation* is established, independent of n, and given by [1]:

$$I^{\mathrm{st}}(T) = N^{\mathrm{eq}}(n^*)\gamma(T)\left(\frac{\sigma}{k_B T}\right)^{1/2} v^{1/3} 4\left(\frac{8}{81\pi^2}\right)^{1/6}, \tag{1.6}$$

where $\gamma(T)$ is the temperature-dependent molecular jump frequency; it is related to diffusivity D [45], and to η through the Stokes-Einstein relation [39]:

$$\gamma(T) = \frac{6D}{a^2} = \frac{2k_{\mathrm{B}}T}{\pi a^3 \eta}, \tag{1.7}$$

where a is an effective molecular diameter (or jump distance), and to be typically taken to correspond to a unit cell distance in our calculations. As we will see further in the text, for practical reasons we will use $\eta(T)$ to express kinetics because it is easier to obtain than the fundamental mobility. Experimental data analysis must relate to $N^{\mathrm{st}}(n,T)$, but there is no straightforward analytical expression for these. Therefore, we typically calculate $N^{\mathrm{eq}}(n,T)$ up to n^*, and $N^{\mathrm{st}}(n,T)$ is closely approximated by $N^{\mathrm{eq}}(n,T)$ to which homogeneous nucleation frequencies are directly proportional [42].

The last fundamental thing we need to consider here is that the steady-state size distribution of crystalline clusters is not established instantaneously upon annealing but takes some time. In most studies, an idealized case is treated as such that there are no pre-existing nuclei prior to isothermal anneal, and the nucleation formally starts when some clusters reach the critical size and $I^{\mathrm{st}}(T)$ is established. Typically, critical nuclei are too small to be experimentally detected, and there is no *in-situ* probe to their population as they form. The $n^*$and the probability of dissolving post-critical nuclei, the rate $k^-(n)$, can now readily be studied in MD simulations [54], and n^* can be inferred experimentally from, for example, fluctuation transmission electron microscopy (TEM) [55]. At a given *T*, it takes time for the critical nuclei to form which is represented as $\chi_{n^*}(t)$ – an example of this evolution is shown Fig. 1.2b. There exists an effective *time-lag*, $\theta_{n^*}(T)$ (relative to the beginning of the anneal), after which $\chi_{n^*}(t)$ depends linearly on time. The time-lag can be approximated by [45]:

$$\theta_{n^*}(T) = k_{\mathrm{B}}T\left(\frac{32\pi v^2}{3}\right)^{1/3}\frac{\sigma}{\gamma|\Delta\mu|^2}. \tag{1.8}$$

The time-lag is closely related to other measured times as the *incubation time* or *transient time* [42]. The forming nuclei (crystals) take some time to be experimentally detected and sizes larger than the critical size are typically observable. Correspondingly, the effective time-lag is longer than the theoretical one in Eq. 1.8, but empirically the difference is no more than one order of magnitude [45], though the relationship may not be simple [56]. In order to be consistent with the used nomenclature, the general form of $\Delta\mu$, for example, due to Thompson and Spaepen [33] (Fig. 1.2d), used for PC chalcogenides in Chapter 4, must be re-calculated per atom (cluster) as [42]:

$$\Delta\mu = \left[\frac{\Delta H_{\mathrm{m}}\Delta T}{T_{\mathrm{m}}}\left(\frac{2T}{T_{\mathrm{m}}+T}\right)\right]\frac{1}{N_{\mathrm{A}}}. \tag{1.9}$$

1.2.2. Crystal growth

Crystal-growth rate is more straightforward to connect to the dynamics in the supercooled liquid because, for ideal planar growth, there is no role of σ. **Fig. 1.4** shows an overview of crystal growth modes observed in glass-forming liquids; part a and b schematically express the modes in terms of a decoupling, discussed in the following paragraphs, and the $U(T)$ shape resembles that shown in Fig. 1.2b. Special cases of $U(T)$ in molecular glasses (part c – *o*-terphenyl, OTP) and pure-metal glasses (part d – silver) are also shown. For $U(T)$, the driving force for crystallization, $\Delta G(T)$, is restricted to the *thermodynamic factor* $\Psi(T)$ (square brackets in Eq. 1.10). The equation is for *continuous diffusion-limited* normal growth (Fig. 1.2b and 1.4a), congruent crystallization with the solutal term $\Delta T_{\mathrm{s}} = 0$, and it is given by the Wilson-Frenkel model [57]:

$$U(T) = U_{\mathrm{kin}}(T)\Psi(T) = U_{\mathrm{kin}}(T)\left[1 - \exp\left(-\frac{\Delta G(T)}{RT}\right)\right], \tag{1.10}$$

where R is the universal gas constant, $U_{\mathrm{kin}}(T)$ is the temperature-dependent *kinetic coefficient*, the limiting value to $U(T)$ at high values of the driving force for crystallization at large ΔT (Fig. 1.2b). The thermodynamic factor, $\Psi(T)$, controls $U(T)$ at small ΔT, i.e., close to T_{m}, where U is low, tending to 0 on approaching T_{m} where $\Delta G_{\mathrm{l}} = \Delta G_{\mathrm{s}}$ because of the lack of thermodynamic driving force. This is the mode we take later to calculate $U(T)$ in phase-change chalcogenides (Ch. 4). When dealing with the crystal-liquid (glass) interface it has to be considered that it has a finite roughness. Nascimento and Zanotto [38] presented modified models of Eq. 1.10, namely *screw-dislocation growth model* (SD) and *2-D surface nucleation growth* in oxide glasses. Both models basically introduce scaling factors that represent either: i) the fraction of active sites at the interface where atoms of the liquid can be preferentially attached/detached in SD model; or ii) the relative size of a secondary crystal to the size of primary crystals in 2-D model, where 2-D refers to two-dimensional crystals growing on a crystal-phase template. Detail analytical analysis is presented in Ref. [38] for oxides, or a case study in slow-crystallizing chalcogenide glasses can be found, for example, in Refs. [58,59]. In practice, it may actually be difficult to theoretically distinguish different modes, especially for fast crystallizing systems for which only limited experimental points with large scatter due to the short nanosecond time-scale as in PCM are available, and long-range diffusion is somewhat limited during fast memory switching (Ch. 4).

The $U_{\mathrm{kin}}(T)$ takes over as ΔT increases on cooling, then the slow-down in $U(T)$ on approaching T_{g} is due to slowing the kinetics; U_{kin} is then taken to be inversely proportional to viscosity as [39]:

$$U_{\mathrm{kin}}(T) \approx \eta(T)^{-\xi}, \tag{1.11}$$

where ξ is the decoupling constant ($\xi \leq 1$) with the classical value, expected from the Stokes-Einstein relation (Eq. 1.7), of 1 for strong liquids which have the Arrhenius kinetics of $\eta(T)$ such as SiO_2 [39]. The experimentally observed *breakdown* in the Stokes-Einstein relation (Eq. 1.7), related to Eq. 1.11, has also been predicted by MD simulations. For example, in supercooled GeTe (PC chalcogenide), a high atomic diffusivity is retained even at low *T* on cooling/reheating, unlike what would be expected from the sharp increase in $\eta(T)$ [60]. Ediger and co-workers [39] suggested a constant value of decoupling between T_{g} and T_{m}, but $U_{\mathrm{kin}}(T)$ and $\eta(T)$ must merge at high temperatures. The authors also observed that the decoupling becomes greater for the liquids with higher value of *kinetic fragility, m,* given by [12]:

$$m = \left.\frac{\mathrm{d}\log_{10}\eta}{d\left(T_{\mathrm{g}}/T\right)}\right|_{T=T_{\mathrm{g}}}. \tag{1.12}$$

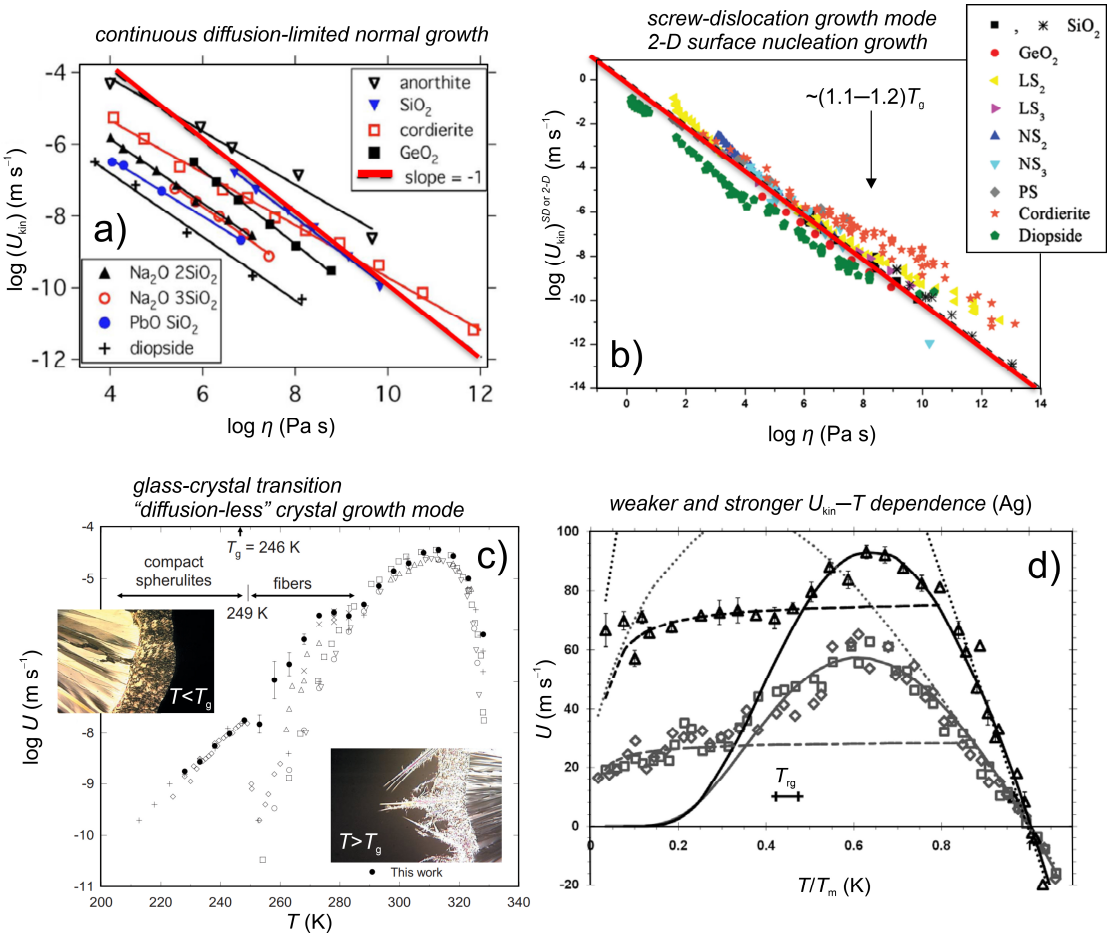

Fig. 1.4 Graphical representation of the (a–b) commonly-described decoupling and (c–d) crystal-growth modes across a wide range of glass-forming liquids. a)–c) *Diffusion-limited modes*, for parts a and b the shape of $U(T)$ resembles that shown in Fig. 1.2b, for which the kinetic part $U_{\rm kin}(T)$ is taken to scale with $\eta(T)^{-\xi}$ Eq. 1.11, or proportional to $D(T)$ through the Stokes-Einstein relation (Eq. 1.7), in the supercooled liquid. *Part a* assumes *continuous growth* (Eq. 1.10) with a constant decoupling over the entire temperature range of the existence of supercooled liquid (Eq. 1.11). Different symbols show experimental data points. *Part b* shows modified $U_{\rm kin}(T)$ by the available active sites in the *screw-dislocation growth* mode (SD) and by the crystal size of the growing phase in the *2-D surface nucleation growth* mode. Different points represent experimental data sets. In both parts a and b, the solid red line plots $\xi = 1$. In part a, Ediger assumed constant decoupling over the entire range of the supercooled liquid state; in part b, $\xi < 1$ between $T_{\rm g}$ and $T \leq (1.1 - 1.2)T_{\rm g}$. *Part c*: So-called "*diffusion-less*" crystal growth arises in some molecular liquids, such as *o*-terphenyl. For large ΔT and below $T_{\rm g}$, $U(T)$ proceeds several orders of magnitude faster than it would be predicted from the bulk liquid $D(T)$. **d)** Kinetic part of crystal growth in pure-metal glasses shows two regimes: a weak $U_{\rm kin} - T$ dependence for $T < T_{\rm g}$, and a significant $U_{\rm kin} - T$ dependence at $T > T_{\rm g}$. Solid points: simulated $U(T)$ for (111) – grey, and (100) – black, crystallographic orientations of Ag crystal. The solid, dashed and dotted lines represent best-fits to different thermally-activated processes [61]. See the main text for an explanation. *Adapted and modified: part a is from Ediger et al. [39]; part b is from Nascimento & Zanotto [38]; part c is from Xi et al. [62]; and part d is taken from Ashkenazy & Averback [61].*

Based on the Ediger's observation, Nascimento and Zanotto, showed that the Stokes-Einstein relation holds well in a wide temperature range for strong liquids, those for which $m < 30$ [38]. On the other hand, there is a clear breakdown in the relationship for fragile liquids represented by the kink in the $U_{\rm kin}(T) \approx \eta(T)^{-\xi}$ which only becomes pronounced in a temperature range of about $(1.1 - 1.2)T_{\rm g}$ of high viscosity towards $T_{\rm g}$ (Fig. 1.4b).

Pure-metal glasses may represent an extreme case of a decoupling, though not of the same origin [63]. The fragility of supercooled metals is unknown. Orava & Greer [13] estimated $m \approx 70-90$ by extrapolating high-temperature viscosity down to corrected T_g from MD simulations, defining T_g at $\eta = 10^{12}$ Pa s, by using a free-volume model of Cohen-Grest given by [64,65]:

$$\log_{10}\eta = A_\mathrm{CG} + \frac{2B_\mathrm{CG}}{T - T_0^\mathrm{CG} + \left[\left(T - T_0^\mathrm{CG}\right)^2 + 4C_\mathrm{CG}T\right]^{1/2}}, \tag{1.13a}$$

and taking into account the decoupling according to Ediger (Eq. 1.11), we can derive:

$$\log_{10}U_\mathrm{kin} = \text{const.} - \xi\left(A_\mathrm{CG} + \frac{2B_\mathrm{CG}}{T - T_0^\mathrm{CG} + \left[\left(T - T_0^\mathrm{CG}\right)^2 + 4C_\mathrm{CG}T\right]^{1/2}}\right), \tag{1.13b}$$

where, A_CG, B_CG, C_CG and T_0^CG are fitting parameters, where the latter was found to be 10–17% higher than the measured T_g in the systems studied by the authors. For metals, the fast U was originally considered by Turnbull in terms of the *collision-limited growth* model (Fig. 1.4d), linked to the thermal velocity of atoms in the liquid [66–68], where U_kin scales with the sound velocity in the liquid $U_\mathrm{kin} \propto (\kappa/\rho)^{1/2}$, where κ is the adiabatic bulk modulus and ρ is the liquid density giving the theoretical $U \approx 10^3 - 10^4$ m s^{-1}. Data from simulations (Fig. 1.4d [61]) and levitation [48] of pure metals show U_kin higher than would be permitted by diffusion-limited case, though they are not as high as would be predicted by the Turnbull's model which fails to fit the available measured data [3,69]. Even at temperatures as low as a few tens of kelvin, pure-metal glasses may retain a high value of U in the range of ~10^1 K s^{-1} as suggested by MD simulations (Fig. 1.4d, [61]). Although experimental work by Zhong *et al.* [18] on pure-metal glass nanobridges suggests that at least for refractory metals, U at room temperature must be much lower. Ashkenazy & Averback revealed two regimes of growth with a transition near T_g [61]. For $T > T_\mathrm{g}$, U_kin is significantly temperature-dependent, indicating thermal process and U shows a maximum (Fig. 1.4d). For $T < T_\mathrm{g}$, U_kin is only weakly thermally-dependent, and the activation energy for crystal growth, Q_U, is effectively 0 as no diffusion is required [66]. For example, thin-film amorphous metals prepared by physical vapour deposition at 4 K typically crystallize on slow heating at 20–30 K, and this crystallization onset temperature, T_x, is higher for thinner films [63]. The U_kin was found by MD simulations to scale as $U_\mathrm{kin} \propto C_\mathrm{c}(R/MT_\mathrm{m})^{1/2}$ for fcc metals [70], where M is the molar mass, and C_c is a constant dependent on crystallographic orientation resulting in a strong growth-rate anisotropy $U_{\mathrm{kin}(100)} > U_{\mathrm{kin}(110)} > U_{\mathrm{kin}(111)}$ [70,71]. Recently, Schottelius *et al.* [68] showed the importance of the thermodynamic factor in collision-limited model and which can account for the fast crystal-growth rates in liquid mixtures of Ar and Kr. The authors modified the collision-limited (CL) rate by a thermodynamic function expressed as: $U_\mathrm{CL}^\mathrm{mod.}(T) = U_\mathrm{CL}(T)\Psi$, and, for example, with $\Psi(x_\mathrm{M}, T) = 1 + x_\mathrm{M}\frac{\partial \ln \alpha_\mathrm{Kr}^\mathrm{l}}{\partial x_\mathrm{M}} = 1 - 2(1 - x_\mathrm{M})x_\mathrm{M}\zeta_0^\mathrm{l}(T)$, where x_M is the molar fraction of the gas (Kr in this case), $\alpha_\mathrm{Kr}^\mathrm{l}$ is the activity coefficient, and ζ_0^l is a temperature-dependent coefficient. This newly-developed model bridges the limitations between the diffusion-limited and collision-limited models, and provides the foundation to develop more rigorous

crystal-growth theories also extending to non-ideal systems; possibly also helping to understand the large difference in the crystal-growth rate of about 8 orders of magnitude observed between metals and, for example, metallic-like $Ge_2Sb_2Te_5$ (GST) at large ΔT (see Fig. 2.1 in the next chapter).

We just briefly comment on the growth mode characteristic for some molecular glass-forming liquids, such as OTP, ROY, and others (Fig. 1.4c) as it complements the modes discussed above. Up to intermediate ΔT, down to $\sim 1.15 T_g$ for OTP in Fig. 1.4c [62], the growth mode is diffusion controlled. For lower *T*, the growth is no longer controlled by the bulk diffusion, thus termed "*diffusion-less*", and U proceeds several orders of magnitude faster than it would be predicted from bulk diffusivity, and the rapid growth continuous even below T_g. The change in the growth mechanism is accompanied by a distinct variation in the forming polymorphs changing from fibres (diffusion-controlled) to spherulites (diffusion-less) in OTP. This mode is of importance for amorphous pharmaceutical systems, and it is beyond the scope of this commentary – details can be found in Refs. [72–75], and therein. A crystal-growth mode conforming to that in molecular glasses was recently revealed in ChG thin-film $Se_{95}Te_5$, ≈1 μm thick, deposited by thermal evaporation [76]; the origin was assigned to the breakdown in the Stokes-Einstein relation (Eq. 1.7) and the growth was controlled by surface diffusion.

2. THE ROLE OF T_{rg} AND KINETIC FRAGILITY m IN THE LABILITY OF THE LIQUID

Here, we describe general behaviour and scaling relationships of U with a special focus on the position of the maximum $U_{\max}$ in crystal growth in a variety of glass-forming liquids (**Fig. 2.1**). The relationships derived below can also be related to the description of glass-forming ability, for which, a vast number of empirical rules exists [43,44,77–84]. We see that the range of U spans over 15 orders of magnitude for different liquids, and that is driven by the interplay between $U_{\mathrm{kin}}(T)$ and the thermodynamic factor $\Psi(T)$ (Eq. 1.10). The latter can be described, to a good approximation, by Turnbull's relation (Fig. 1.2d) $\Delta G = \Delta S_{\mathrm{m}}/\Delta T$ [32]. **Fig. 2.2** shows the temperature-dependent thermodynamic factor calculated by using the Turnbull's expression for a range of glass-forming systems plotted in Fig. 2.1; the reduced entropy of melting $\Delta S_{\mathrm{r}} = \Delta S_{\mathrm{m}}/R$ ranges from ~1 for pure-metal glasses to ~8 for good glass-forming silicates, such as SiO_2 [37]. At very low-*T*, $\Psi = 1$, the thermodynamic driving force is largest, limited by $\eta,\ D$. For the practical temperature range of interest for the labile regime between T_{g} and T_{m}, Ψ changes about 2–(3) orders of magnitude, it varies by the same order among different glass-forming systems, and it changes less than 1 order of magnitude below $0.9\,T/T_{\mathrm{m}}$ [13]. Considering the vast range of U and $U_{\max}$ (Fig. 2.1) in glass-forming liquids, we conclude that the principal difference between the variety of systems is *kinetic* not *thermodynamic* [13]. In other words, to find the relationship(s) governing the wide range of kinetics and, therefore, the glass-forming ability between different liquids, the role of the underlying $\eta(T)$ must be understood – this is the focus of this chapter. Although, as noted in the previous chapter, the thermodynamic factor has to be considered when describing details within the individual systems [68].

As pointed out by Turnbull, the likelihood of crystallization or glass formation depends on T_{rg} (Fig. I in the *Preface*). For lower T_{rg}, the maximum in $I^{\mathrm{st}}(T)$ lies at lower *T* and the maximum itself is much higher. The position of the maximum in crystal-growth rate, occurring at higher *T* than $I^{\mathrm{st}}(T)$, conforms to the Turnbull's finding (Fig. 2.1, and **Fig. 2.3a** – individual points are labelled with the corresponding value of $U_{\max}$). This correlation, though with a great data scatter, was already noted by Fokin *et al.* [37] in oxide glasses. As expected, the lability of the liquid is greater for higher m and lower T_{rg} (Fig. 2.3). Although, from the data available, there seems to be no straightforward correlation between the maximum in crystal-growth rate, m and T_{rg}, the contours in Fig. 2.3a suggest that the crystal-growth rate in diverse glass-forming liquids shows a general trend. The contours show the same value of $U_{\max}$, they are unevenly spaced but, to some extent, having a similar gradient. The similarity in the gradient allowed Orava & Greer to derive a new *fragility-corrected reduced glass-transition temperature* parameter [13]:

$$T_{\mathrm{gu}} = T_{\mathrm{rg}} - \frac{m}{505}. \tag{2.1}$$

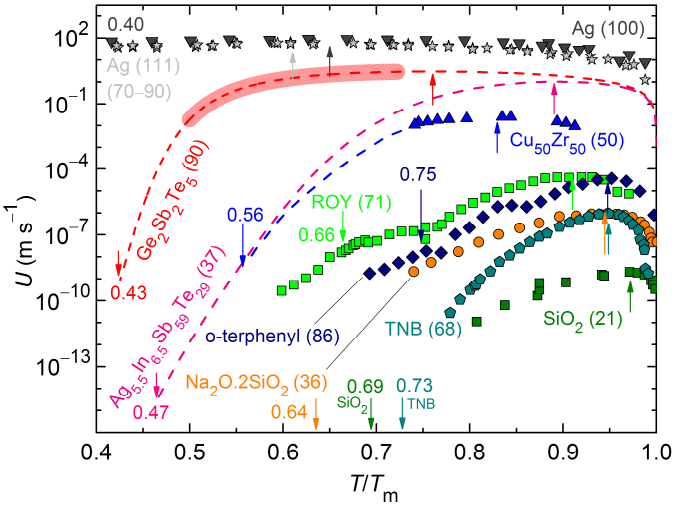

Fig. 2.1. Survey of polymorphic crystal-growth rates, U, as a function of the homologous temperature, T/T_{m}, for different families of glass-forming liquids. The maximum in crystal-growth rate, U_{max}, is marked by the upward arrows, and T_{rg} is marked by the arrows pointing downwards. Symbols show experimental or MD simulation (for Ag) values of U. The lines show $U(T)$ obtained by calculations. The dashed lines for $Ge_2Sb_2Te_5$ (GST) [85] and $Ag_{5.5}In_{6.5}Sb_{59}Te_{29}$ (AIST) [86] are inferred from ultrafast heating calorimetry (FDSC) [87]. The directly measured temperature range, $(0.5-0.72)T_{\mathrm{m}}$, in FDSC for GST is highlighted by the thick line [85]. The *single-fragility* liquid GST and the AIST liquid showing a *fragile-to-strong crossover* are discussed respectively in Sects. 4.1 and 4.2 describing the crystallization in phase-change chalcogenides in detail. The dashed line for $Cu_{50}Zr_{50}$ metallic glass represents the extrapolation of direct measurements during levitation experiments [88] (discussed in Chapter 5). Note the "diffusion-less" transition mode, upward change in U, around T_{g} for ROY and OTP. The values of kinetic fragility, m, are given in the parentheses. *Reproduced from Orava & Greer [36]* (***publication #15 – Appendix I***).

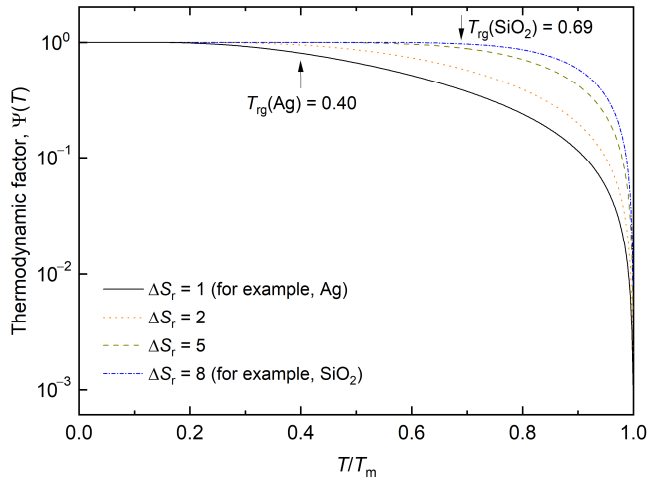

Fig. 2.2 Calculated thermodynamic factor $\Psi(T)$ for a variety of glass-forming systems. Different glass-forming liquids are represented by the reduced entropy of melting $\Delta S_{\mathrm{r}} = \Delta S_{\mathrm{m}}/R$ (*unpublished data*).

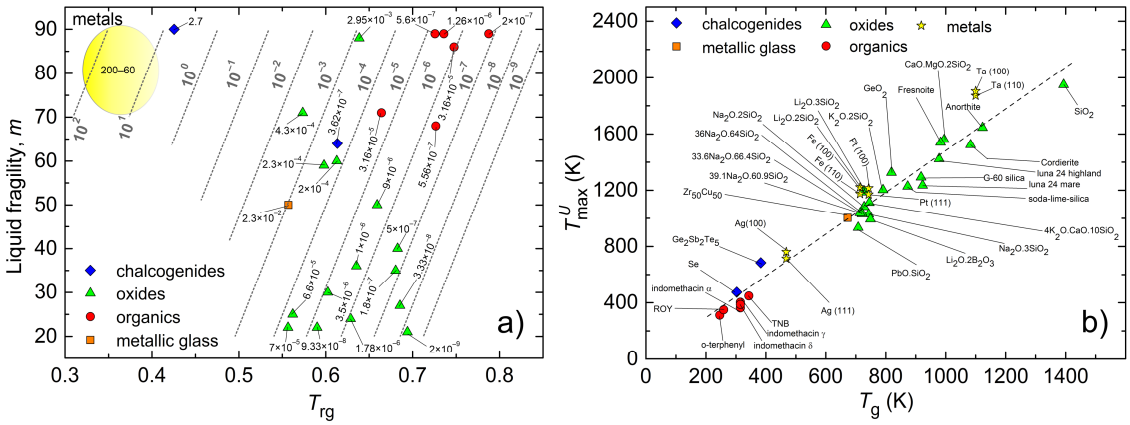

Fig. 2.3 Assessment of different correlations between the maximum in crystal-growth rate, $U_{\max}$, fragility, m, and characteristic temperatures for a variety of glass-forming liquids. a) Relationship between the liquid fragility, m, and the reduced glass-transition temperature, T_{rg}, does not indicate any apparent correlation between the two parameters. Each data point is labelled with the corresponding value of $U_{\max}$ in m s^{-1}. The contours showing $U_{\max}$ are as guides for the eye. **b)** A linear correlation between the temperature $T^U_{\max}$ at which polymorphic $U_{\max}$ occurs and the corresponding T_{g}. The dashed line shows $T^U_{\max}/T_{\mathrm{g}} = 1.48$. *Reproduced from Orava & Greer [13] (**publication #4 – Appendix I**).*

Re-plotting the correlation in Fig. 2.3a with the "corrected" parameter gives a new trend shown **Fig. 2.4a** – for a polymorphic growth over the entire wide range of a variety of glass-forming liquids. By considering a critical diameter of a MG rod as the parameter defining glass-forming ability, Na *et al.* [43] and Johnson *et al.* [44] concluded similar T_{gu} trends for eutectic growth for Ni–Cr–Nb–P–B family of MGs $\left(T_{\mathrm{gu}} = T_{\mathrm{rg}} - m/532\right)$ and for 42 metallic-glass-forming liquids $\left(T_{\mathrm{gu}} = T_{\mathrm{rg}} - m/520\right)$, respectively. Moreover, Johnson and co-workers showed that adding new parameters beyond T_{rg} and m does not improve the quality of the correlation in Eq. 2.1. Senkov [84] suggested for metallic alloys a correlation for glass-forming ability, and defined a dimensionless parameter $F = 2\left[\frac{m}{16}\left(\frac{1}{T_{\mathrm{rg}}} - 1\right) + 2\right]^{-1}$ varying from ~0 for fragile liquids to about 8 for strong liquids. The comparison with Senkov (see details in Ref. [13]) shows that the data coincide better in Fig. 2.3a. This can possibly be interpreted as the Senkov's parameter overemphasizes m relative to T_{rg}. Although the data in Fig. 2.4a show some scatterer, there seems to be no influence of the different growth modes (Sect. 1.2.2.). Schmelzer *et al.* [89] suggested a general correlation between $U_{\max}$ vs. $T^U_{\max}/T_{\mathrm{m}}$ (Fig. 2.4b). There is some data scatter in the figure, perhaps caused by the unknown actual interface temperature, which is not possible to get in some experiments (see the next section), and there also is some influence of the growth mechanism. Nevertheless, the correlation provides a basis for a generalized description of $U_{\max}$ as:

$$U_{\max}(T^U_{\max}) \cong f\frac{D_0}{4a}\left(\frac{\frac{q}{Q_D^{\mathrm{eff}}}}{1+\frac{q}{Q_D^{\mathrm{eff}}}}\right)\exp\left(-\frac{1}{1-\left(\frac{T^U_{\max}}{T_{\mathrm{m}}}\right)}\right)\Bigg|_{T=T^U_{\max}}, \qquad (2.2)$$

where $f \leq 1$ is the fraction of active growth sites at the interface reflecting different growth modes ($f = 1$ for normal growth, $f \approx \Delta T/2\pi T_{\mathrm{m}}$ for a screw-dislocation mode), D_0 is the pre-exponential

factor of $D(T)$, q is the latent heat of crystallization per molecule, and Q_D^{eff} is the thermally-compensated activation energy for diffusion. *The fact that the correlations in Fig. 2.4 appear to be so good, reinforces the importance of the liquid viscosity in comparing diverse glass-forming liquids.* Deviations from the correlation may be useful to understand and discuss the role of interfacial mechanisms [13].

It is of interest to explore whether the characteristic temperature T_{max}^{U} at which U_{max} lies shows any correlation with the glass-forming parameters considered above. Typically, good-glass forming liquids are characterized by a higher value of a parameter $T_{\text{x}} - T_{\text{g}}$ which gives the temperature range of the existence of supercooled liquid prior to the onset temperature of primary crystallization [90]. Adopting a similar strategy, a criterion such as $\left(T_{\text{max}}^{U} - T_{\text{g}}\right)$ vs. $\left(T_{\text{m}} - T_{\text{g}}\right)$ could reveal whether there is a constant and one characteristic tempeture T_{max}^{U} [13]. Detail analysis showed that a gradient of such plots, giving the position of T_{max}^{U} relative to the $\left(T_{\text{m}} - T_{\text{g}}\right)$ temperature range, is not constant for different glass-forming liquids, but suggested a possible link between T_{max}^{U} and T_{g} (Fig. 2.3b) resulting in $T_{\text{max}}^{U}/T_{\text{g}} = 1.48$ with a standard deviation of ± 0.15 (i.e., $\pm 0.10\%$) [13]. Fokin *et al.* [37] suggested a similar correlation, by taking T_{rg}, for oxide systems, only. The data show a correlation but propose a different trend likely due to the limited range of U_{max} available in the oxide systems considered. The correlation shows some noticeable features: i) a single family of glass-forming liquid is not concentrated in any particular temperature range, but rather all individual systems are scattered; ii) the position along the line is not correlated with fast or slow crystal growth or with glass-forming ability; and iii) maybe surprisingly, even pure-metal glasses lie on the single line [13]. The latter also supports the observations that the crystal-growth rates of planar interfaces from simulations of Lennard-Jones liquids [67,68,91] are comparable with data obtained from conventional crystal growth measurements, and systems with a wide range of U can directly be compared.

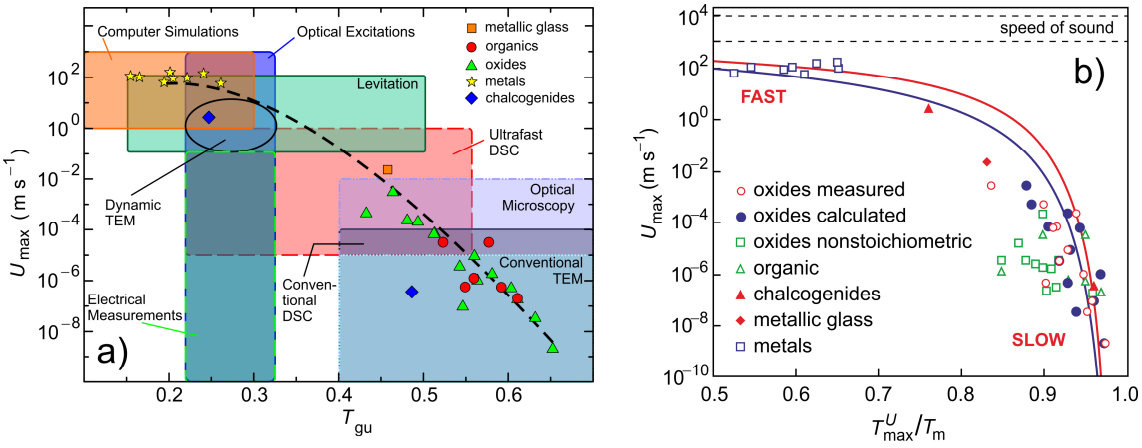

Fig. 2.4 Correlations between the maximum in crystal-growth rate and characteristic temperatures. a) T_{max}^{U} can be correlated with the fragility-corrected reduced glass-transition temperature (Eq. 2.1). The coloured boxes show schematically the typical ranges that are measured by a variety of techniques (see Table 3.1 in Chapter. 3 for details). The dashed line is for guiding the eye only. **b)** Calculated correlation between U_{max} and the homologous temperature $T_{\text{max}}^{U}/T_{\text{m}}$ (Eq. 2.2). The blue and solid lines show calculations for normal and screw-dislocation growth modes, respectively. *Part a is from Orava & Greer [20] (**publication #10 – Appendix I**); part b is from Schmelzer et al. [89].*

3. MEASUREMENT OF CRYSTAL GROWTH

It is evident from the above discussion, that $U(T)$ and $U_{\max}$ span over a wide range of values exceeding 12 orders of magnitude. Fig. 2.4a and **Table 3.1** present an overview of commonly used direct and indirect techniques and their useful range of $U_{\max}$ and T_{gu} in which the measurements are typically carried out [20]. The methods mostly used in our work are highlighted in grey in Table 3.1.

The direct techniques each involve the observation of the advancing crystallization front. There are some uncertainties, such as for higher values of U, the interface temperature may not be well defined exceeding the bulk sample temperature. In optical and electron microscopy, the front is directly observed; in containerless solidification, the position of the interface is inferred from the thermal front that crosses a sample during solidification. Computer simulations are especially useful for fast-crystallizing materials, for example, pure-metal glasses, for which accessing $U(T)$ experimentally is difficult, or techniques are not available. In MD simulations, crystal-growth rates in highly-unrelaxed (rejuvenated) glasses, not supercooled liquids, can be computed because of the high cooling rates applied typically exceeding $>10^{12}$ K s^{-1} (Fig. 1.1).

The indirect techniques mostly measure the overall crystallization rate, and crystal growth must be inferred from the rate by making some approximations of the nucleation rate, the number of active nuclei, the thermodynamic driving force for crystallization and the underlying mobility. By far, a combination of calorimetry techniques offers access to the widest range of $U_{\max}$, and heating and cooling rate from all the common techniques available (Fig. 2.4a and Table 3.1) Our primary focus is on *ultrafast-heating differential scanning calorimetry* (FDSC), also known as flash DSC, and to understand crystallization, especially, in fast-U systems. FDSC has become the pivotal method complementing optical excitations and resistive measurements to understand the fast-switching mechanism, <100 ns, in PCM (Ch. 4). Calorimetric measurements to probe $U(T)$ are done based on varying Φ_{h}. The process of devitrification is difficult to understand with any simple DSC analysis. In the next section, we are going to show that numerical modelling has to be done to recover $U(T)$ from DSC data, especially when the wide range of heating rates as in FDSC is used (Table 3.1). In FDSC, $U_{\max}$ cannot be directly detected as the glass transforms directly to the liquid suppressing crystallization completely before reaching T_{m} on heating [92].

Table 3.1 Survey of various (in)direct methods used to obtain crystal-growth rate, U, in glass-forming liquids. The table summarizes the typical ranges of the maximum rate, $U_{\max}$, the fragility-corrected reduced glass-transition temperature, T_{gu}, [13], heating/cooling rate, $\Phi_{\mathrm{h}}/\Phi_{\mathrm{c}}$, and lists some of the main limitations. The commonly used methods in our work are highlighted in grey (DSC – differential scanning calorimetry; TEM – transmission electron microscopy). FDSC has become the essential tool for understanding crystallization in glass-forming liquids in our research, and, therefore, it is highlighted in red. Graphical representation is shown in Fig. 2.4a. *Adapted and modified from Orava & Greer [20] (**publication #10 – Appendix I**).*

	$U_{\max}$ (m s^{-1})	T_{gu}	$\Phi_{\mathrm{h}}/\Phi_{\mathrm{c}}$ (K s^{-1})	Limitations
INDIRECT TECHNIQUES				
Computer simulations	10^0–10^3	0.10–0.30	10^{11}–10^{15}/10^{11}–10^{15}	Accurate interatomic potentials are needed[a] [69,93]
Conventional DSC	$<10^{-4}$	0.40–0.70	10^{-4}–10^0/10^{-4}–10^{-1}	Arrhenius kinetics[b] [94,95]
Ultrafast DSC (flash DSC)	10^{-5}–10^0	0.22–0.55	10^{-1}–10^6/10^{-1}–10^6	Non-Arrhenius kinetics[c] [85,92,96,97]
Fast optical excitations[d]	$<10^3$	0.22–0.32	10^{10}–10^{11}/up to10^{12}	Temperature simulations; measures crystallized volume fraction[d] [19,98–100]
Electrical measurements	$<10^{-1}$	0.22–0.32	10^0–10^8/—	Complex sample geometry[e] [101,102]
DIRECT TECHNIQUES				
Containerless solidification	10^{-1}–10^2	0.10–0.50	—/10^2	Dendritic growth[f] [5,103]
Dynamic TEM	10^{-1}–10^1	0.20–0.32	10^{10}–10^{11}/10^{10}	[104–106]
Conventional TEM	$<10^{-5}$	0.40–0.70	10^{-4}–10^2/10^3	Sample preparation and e-beam influence [107,108]
Optical microscopy[g]	$<10^{-2}$	0.40–0.70	conventional	[59,76]

[a] For a high U, the temperature of the crystal-liquid interface does not correspond to the bulk temperature.
[b] Because of the limited, conventional, range of Φ_{h}, crystallization occurs in a narrow temperature range in the supercooled liquid very close to T_{g}; the commonly used Kissinger analysis then gives Q_{U} , which is the activation energy for $U(T)$.
[c] Because of the extended Φ_{h}, crystallization has non-Arrhenius kinetics occurring over a wide temperature range in the supercooled liquid. In this case, numerical modelling must be used to calculate $U(T)$ from the Kissinger data (Sect. 3.1.).
[d] Fast optical excitations mean pulsed heating with typically *ps*- and *fs*-pulsed lasers which measure the overall transformation rate, not $U(T)$. There is no direct measure of the temperature at the crystal-liquid interface – has to be estimated by modelling. In Chapter 6, we will demonstrate athermal photoinduced crystallization by using CW lasers.
[e] A thin-film sample is enclosed by electrodes and dielectrics. The mode and kinetics of crystallization can be strongly influenced by stresses in the sample, and by effects such as structural and chemical templating, and possible interdiffusion at the interfaces.
[f] The heat released during the phase transformation gives a negative temperature gradient ahead of the crystal-liquid interface, typically leading to instability of the solidification front and to dendritic-growth mode.
[g] Not using fast-recording cameras.

3.1. Numerical modelling of the crystallization: Regimes revealed by ultrafast calorimetry

Ultrafast-heating calorimetry is a relatively recently commercialized technique originally developed by Schick and co-workers to measure crystallization kinetics in small volumes ranging from ng–μg sample sizes. Technical details of the technique can be found, for example, in books: *Fast Scanning Calorimetry* by Schick & Mathot (Eds.) [87], and *Handbook of Thermal Analysis and Calorimetry, Recent Advances, Techniques and Applications* by Vyazovkin, Koga & Schick (Eds.) [109]. Prior to discussing FDSC results in PCM (Ch. 4) and MGs (Ch. 5), we briefly introduce the principles of kinetic measurements by calorimetry with the focus on regimes revealed by FDSC which are not accessible by conventional DSC for metallic-glass-forming liquids. We need to understand how the Kissinger

analysis reflects non-Arrhenius kinetics over such a wide range of temperatures, especially, when $U_{\max}$ is reached in PCM, by taking the prototype liquid $Ge_2Sb_2Te_5$ (GST) with the input thermodynamic and kinetic parameters found in Refs. [85,92] and Table 4.2 (Ch. 4).

In calorimetry, peak shapes can be fitted [110], but here we will simplify our analysis by using the Kissinger method [111,112] which only considers the crystallization peak temperature, T_{p} – at which the crystallization rate is maximum: $\frac{\mathrm{d}}{\mathrm{d}t}(\mathrm{d}x/\mathrm{d}t) = 0,$ where x is the volume fraction of the crystalline phase. The Kissinger method has widely been studied and used, and what matters specifically is how T_{p} increases with higher Φ_{h}. The nature of the shift gives the activation energy for the overall crystallization process, Q_{K}, through [1,36]:

$$\ln\left(\frac{\Phi_{\mathrm{h}}}{T_{\mathrm{p}}^2}\right) = -\frac{Q}{RT_{\mathrm{p}}} + \mathrm{const.}, \tag{3.1}$$

So far, the Kissinger method has been commonly applied to conventional heating rate ≤100 K min^{-1}, accessible in DSC, which limits the kinetics to narrow temperature range just above T_{g} (for large ΔT) for which Eq. 3.1 gives a straight line because the underlying mobility typically has an Arrhenius kinetics. By using some assumptions, discussed below, the activation energy for crystal growth, Q_U, can be obtained which was demonstrated by Kelton [95] for a traditional silica-based glass (**Fig. 3.1a**).

Polymorphic isothermal phase-transformation can be simplified by Johnson-Mehl-Avrami (JMA) kinetics, in which x varies with time as [113]:

$$x = 1 - \exp[-(Kt)^{n_{\mathrm{A}}}], \tag{3.2}$$

where, $K(T)$ is the temperature-dependent kinetic coefficient (containing both nucleation and crystal growth), t is the elapsed time at a given temperature, and n_{A} is the Avrami exponent which we take for simplicity to be equal to 3 for phase-change chalcogenides; measured values range between 2.5–3 for laser-crystallized GST [114]. The JMA analysis is valid when centres of the growth are randomly dispersed, there is no precipitation, the crystal-growth rate is constant (dependent on T not on t or crystal radius), and I and U are separated. Nevertheless, the nuclei density often saturates on heating, determined by the number density of heterogeneities (insensitive to Φ_{h}), and even when the nucleation fully overlaps with growth, U is still predominant. For an *interface-controlled* 3-D growth (spherical randomly distributed particles) with constant I and U, the above equation adopts the form [1,36,92]:

$$x(t) = 1 - \exp\left(-\frac{\pi I^{\mathrm{st}} U^3 t^4}{3}\right). \tag{3.3}$$

and for growth on constant density of nuclei over time (zero nucleation rate):

$$x(t) = 1 - \exp\left(-\frac{4\pi N U^3 t^3}{3}\right). \tag{3.4}$$

Under non-isothermal conditions, the rate of crystallization at any given moment depends on x and T, but not on thermal history and the kinetic coefficient has the same temperature dependence as crystal growth:

$$K(T) = \left(\frac{4}{3}\pi N\right)^{1/3} U(T), \tag{3.5}$$

and $U(T)$ can be taken from Eq. 1.10 and, for example, Eq. 1.13b for $U_{\mathrm{kin}}(T)$. *By computing the above equations, the Kissinger analysis can give the shape of $U(T)$ but it cannot give its magnitude.* To obtain the absolute values of $\eta(T)$ and $U(T)$, the kinetic term U_{kin}^{-1} can typically be transposed onto the Angell plot – see Chapter 4. Figure 3.1b–d show the correlation between $\ln K(T)$ and $\ln\left(\Phi_{\mathrm{h}}/T_{\mathrm{p}}^2\right)$ for three different liquids: i) GST-like liquid (part b); ii) similar to GST but with strictly Arrhenius kinetics in $K(T)$; and ii) the GST-like liquid with much higher $T_{\mathrm{rg}} \approx 0.69$ such as that corresponding to traditional silicates (Fig. 2.1). The simulation reveals three typical regimes in metallic-glass-forming liquids which can be probed by FDSC, and provides the following general observations [92]:

a) Independent of the underlying temperature-dependent kinetics, the dependences of $K(T)$ and $\ln\left(\Phi_{\mathrm{h}}/T_{\mathrm{p}}^2\right)$ do match at low temperatures, low Φ_{h}, and therefore Q_U can be directly obtained from the plot if the above-noted assumptions are fulfilled (please note that N should be obtained independently). That is also the range where T_{p} corresponds to a transformed fraction of $x = 0.63(2)$, by definition [113]. For fast-crystallizing liquids, such as GST being of interest here, the Φ_{h}-range of strictly Arrhenius kinetics is limited up to about ~10^0 K s^{-1}. The early divergence between $\ln K(T)$ and $\ln\left(\Phi_{\mathrm{h}}/T_{\mathrm{p}}^2\right)$ is mostly due to the high kinetic fragility of the liquid, $m \approx 90$ [85] (Fig. 3.1b). For liquids with strictly Arrhenius kinetics in the entire range between T_{g} and T_{m}, the validity of the analysis extends up to extremely high temperatures, as high as $\sim 0.9T_{\mathrm{m}}$ (Fig. 3.1c), when U becomes thermodynamically suppressed.
b) For intermediate Φ_{h} of about ~10^0–10^5 K s^{-1} in GST (Fig. 3.1b), the slope of the kinetic coefficient and Kissinger analysis do not match anymore. The curvature in $K(T)$, reflecting the kinetic fragility, is systematically overestimated by the analysis (dashed line in Fig. 3.1b). Similar divergence was also shown for the metallic-glass-forming liquid $Au_{49.0}Ag_{5.5}Pd_{2.3}Cu_{26.9}Si_{16.3}$ [115]. The temperature dependence of Q_U $[U(T), U_{\mathrm{kin}}(T)]$ can still be obtained, but only by detailed numerical simulation of the evolving DSC peaks through the equations given above.
c) At high heating rates of >10^6 K s^{-1}, the maximum in crystallization rate is reached as the growth rate becomes thermodynamically limited on approaching T_{m}, and the Kissinger plot has the curvature of the opposite sign to $K(T)$. This is the regime which cannot be experimentally accessed by FDSC because upon such fast heating, the glass transforms directly into the liquid and crystallization is suppressed. Therefore, this regime can be exploited, for example, in the moulding of metallic-glass-forming liquids [116]. The crystallization gets suppressed at effectively lower Φ_{h} for liquids with higher T_{rg} (Fig. 3.1d).

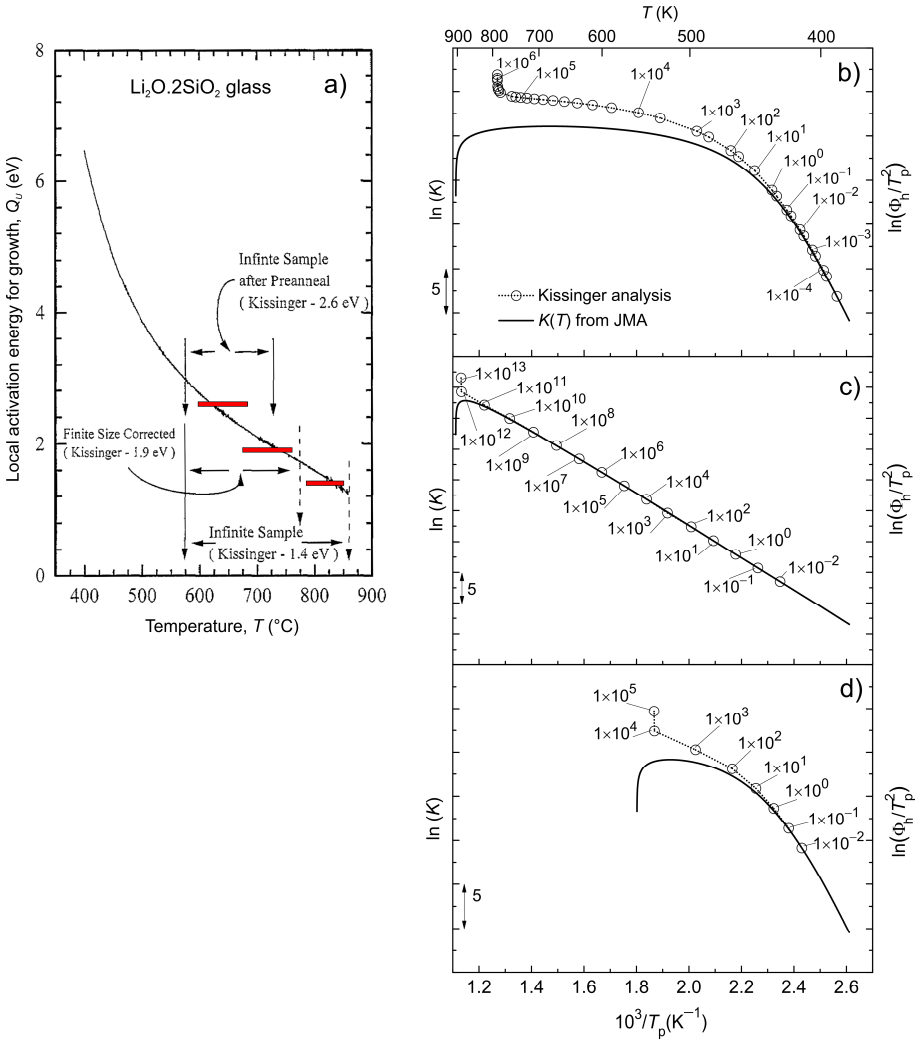

Fig. 3.1 Computational test of the Kissinger analysis for a range of glass-forming liquids, represented by the diverse values of T_{rg}, m and underlying viscosity, over a theoretical range of heating rate exceeding 17 orders of magnitude for polymorphic growth. a) The original work by Kelton showing that the analysis can obtain the activation energy for crystal growth, Q_U, roughly corresponding to the average value (represented by the red rectangles) of the local Q_U in a given temperature range in $Li_2O.2SiO_2$ glass. The average value greatly depends on the glass thermal history, and on whether surface and finite-size effects are included or not. **b)–d)** Numerical simulation over a wide range of Φ_h, useful in FDSC, of the Kissinger method (*right-hand absicca* – open symbols and dashed lines) compared with the underlying kinetic coefficient $\ln K$ (*left-hand absicca* – solid lines). The corresponding heating rates are labelled in K s^{-1}. Different theoretical glass-forming liquids are simulated: i) the liquid with high fragility, low T_{rg} and high K representing a metallic-glass-forming liquid, such as $Ge_2Sb_2Te_5$ ($T_{rg} = 0.43$ and $m \approx 90$ [85])[a)] discussed in Sect. 4.1. in detail; ii) similar to the previous one but K is taken to have strictly Arrhenius kinetics between T_g and T_m; iii) the same input as in part b but with much higher T_{rg}. T_p is the crystallization peak temperature. An ideal (F)DSC performance is assumed for the modelling (no thermal-lag, no limit on heating/cooling rate and maximum temperatures, no temperature gradients within the sample,). *Part a is from Kelton [95]; part b–c is from Orava & Greer [92] (**publication #7 – Appendix I**).*

[a)] The exact value of T_g for fast-crystallizing phase-change chalcogenides, such $Ge_2Sb_2Te_5$ and (Ag,In)-doped Sb_2Te is still in dispute in the literature [117,118] – discussed in Sect. 4.1.1.

There is an additional important difficulty to be considered in the numerical modelling. So far, we have ignored that the underlying temperature-dependent viscosity in U_{kin} can be expressed by different models. For intermediate liquids, in terms of their kinetic fragility, the curvature in the Kissinger plot may be rather weak. Chen *et al.* [97] analysed such a system represented by a thin-film $Sb_{93}Ge_7$ in FDSC (**Fig. 3.2**), and used two typical models to express $\eta(T)$ in PC chalcogenides: i) Cohen-Grest [64,65] (Eq. 1.13), and ii) MYEGA [119] model – this is introduced in Sect. 4.2.1. when describing viscosity in Ag-In-Sb-Te chalcogenide; here we limit ourselves to describing its implications for the modelling without giving further details about the model itself. Both models were able to fit the weak curvature in the obtained Kissinger method giving $m \approx 86$, $\xi = 0.97$ from the Cohen-Grest model, and $m = 65$, $\xi = 1$ from the MYEGA model. But most crucially, the MYEGA model could reproduce the experimental growth rates by introducing a decoupling of $\xi = 0.9$ starting at temperature $\sim 1.2T_{\mathrm{g}}$ on cooling (related to the breakdown in the Stokes-Einstein relation [38]) – inset in Fig. 3.2. The Cohen-Grest model overestimated the growth rate by as much as 2–3 orders of magnitude. This shows the limitation of the numerical analysis and highlights the importance of comparing any modelled $U(T)$ with experimental data if they are available.

It should be noted that for molecular liquids, such as OTP with $T_{\mathrm{rg}} = 0.75$ and $m \approx 86$ [62,120], the three regimes are not so well distinguished as for metallic-glass-forming liquids, and the Kissinger analysis may not provide unambiguous information about the underlying crystallization kinetics [92]. With all the above being established, we now proceed with describing the fast crystallization in PC chalcogenides.

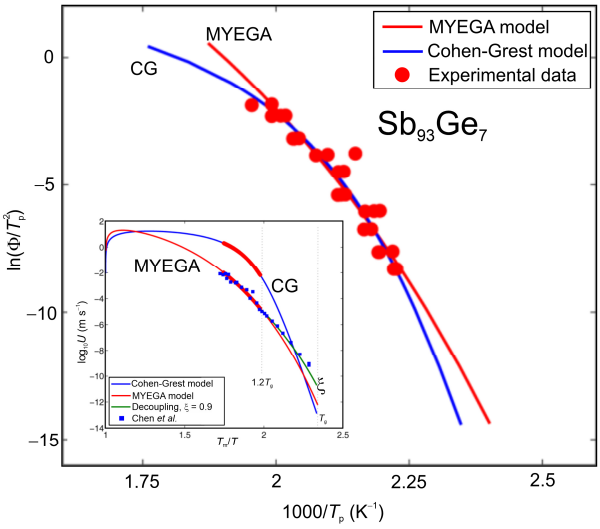

Fig. 3.2 The Kissinger analysis of crystallization in liquid $Sb_{93}Ge_7$ by ultrafast calorimetry highlighting the importance of the used underlying model for viscosity. Two $\eta(T)$ models, Cohen-Grest [64,65] (CG, the blue curves) and MYEGA [119] (the red curves), are used to fit the curvature in the analysis and to reproduce the experimental $U(T)$ (blue full squares in the inset) [121]. The red full circles show T_{p} obtained by FDSC in the range of heating rate 50–40,000 K s^{-1} (450–504 K). Film thickness was ~200 nm. *Reproduced from Chen et al. [97].*

4. FAST CRYSTALLIZATION IN PHASE-CHANGE CHALCOGENIDES: TOWARDS UNIVERSAL MEMORY

Phase-change memory (PCM), using PC chalcogenides as the active layer in the device, is a storage-class memory with the operating parameters (capacity, latency, endurance, and non-volatility) balanced between a fast and volatile CPU with extremely low storage capacity and a non-volatile high-capacity but slow SSD (**Fig. 4.1a**). Connecting to the internet is from various devices (Fig. 4.1b), the relatively low-writing energy (<100 pJ [122]) of PCM is of interest especially for portable devices. The reversible PC of interest is between glass-to-crystal – the forward step corresponds to writing (SET), and the backward step represents erasing (RESET) operations of PCM. Crystallization (writing) is the rate-limiting step and is typically ≈10–100 ns [123]; preferably switching time should be faster than that in DRAM. Re-melting followed by rapid quenching with a critical cooling rate of ~10^9–10^{12} K s^{-1} [42] is the most energy-consuming step of the memory operation.

In PCM operation, two contradictory requirements must be met. Crystallization whether occurring, preferably, in the supercooled liquid or in the glass, must be fast, and any drift (data retention), the stability of the glassy phase against long-term structural relaxations at elevated temperatures, should be minimized. The origin of the existence of the fast-crystallization-rate window in the archetype *nucleation-dominated* $Ge_2Sb_2Te_5$ (GST) is revealed by FDSC in Sect. 4.1. In Sect. 4.2., we will show that the needs for the memory operation could be fulfilled, among other methods, by a so-called *fragile-to-strong crossover* (FSC) occurring on cooling the supercooled liquid of *growth-dominated* (Ag,In)-doped Sb_2Te (AIST). Such a crossover can also explain the different crystallization mechanisms of the two types of PC chalcogenides, i.e., aforementioned nucleation- and growth-controlled. We will demonstrate that crystallization mechanism, its kinetics, temperature-dependent viscosity, and a temperature shift in the X-ray structure factor, $S(Q)$, can all be correlated in the prototype *single-fragility* GeTe and *FSC* $Ge_{15}Te_{85}$ liquids hinting at a close link existing between these properties.

To improve the crystallization rate and fulfil the above requirements, several other strategies than exploiting a crossover can be adopted. Newly emerging superlattice-structure technology combines two types of materials [124], one with a high crystallization speed (Sb_2Te_3) and the other with good data retention (GeTe) – also being explored for the application in spintronics [125]. A new class of materials has constantly been developed. This is experimentally tedious, but with the recently-developed machine-learning computing, a large scale of compositions with defined properties can be probed [126]. In general, the active material should have high crystallization temperature which ensures data retention at room temperature, crystallization, ideally congruent, should be fast, and T_{m} must be low to ensure energy efficiency. As seen in Figs. 2.1 and 2.4a, $U_{\max}$ is higher for low-T_{rg} and kinetically fragile liquids which tend to be unstable at room and somewhat elevated temperatures. Alternatively, one can use the existing materials and exploit new physical principles to improve the memory performance. By modifying the pulsing protocol for writing, switching on the picosecond time-scale has been demonstrated in PCM by so-called "*priming*" method [127,128] by applying an auxiliary low-energy pulse prior the main one, and the mechanism is analysed in Sect. 4.3.

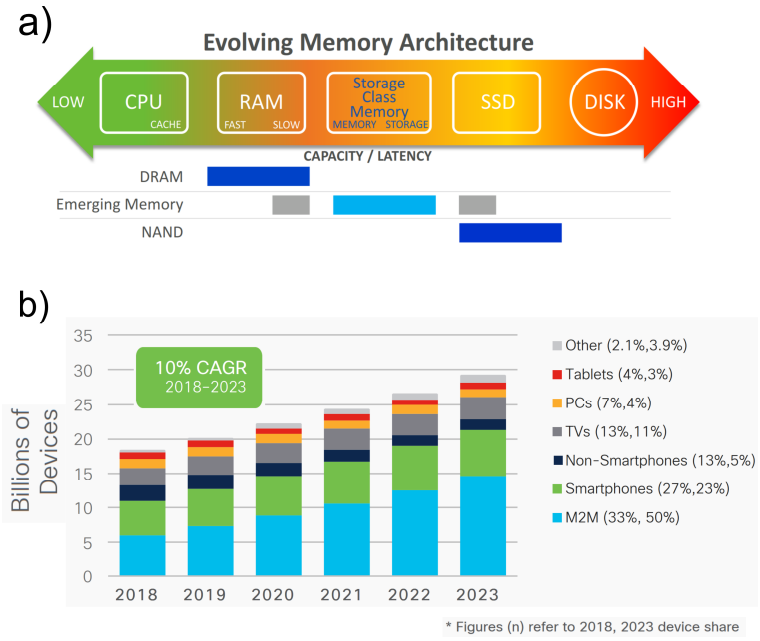

Fig. 4.1 Evolution of memory architecture and the type of the global device connections. a) The place of any emerging storage-class element, such as phase-change memory, will depend on the trade-off between capacity, speed (latency), endurance, non-volatility, and cost. **b)** M2M connections (also referred to IoT) are predicted to be the fastest-growing connection category (forecasted to grow 30% CAGR – compound annual growth rate –between 2018–2023) and to become ~50% of all connections by 2023 followed by smartphones growth of 7% CAGR in the same period. The overall growth of connections and devices is 10% CAGR (CAGR – compound annual growth rate). *Part a is reproduced from Pellizzer et al. [129]; part b is reproduced from Cisco white paper [130].*

4.1. Single-fragility liquid $Ge_2Sb_2Te_5$

Before FDSC and femtosecond time-scale X-ray diffraction [100] were available, crystallization kinetics and dynamics in the supercooled liquid were limited to measurements close to T_g (large $\Delta T \geq 450$ K), or to T_m (small $\Delta T = 40 - 80$ K under B_2O_3 flux [131]), and the observed crystallization (solidification) kinetics was always nearly Arrhenius for the characteristic temperatures <440 K (**Fig. 4.2b** – open symbols). FDSC clearly evidenced, for the first time, a super non-Arrhenius temperature dependence of crystallization in single-film GST in a wide temperature range of $\sim(0.5 - 0.72)T_m$ (Fig. 4.2b – full circles) by analysing the calorimetry traces up to $\Phi_h = 40{,}000$ K s^{-1} (Fig. 4.2a) through the Kissinger method [85]. Later measurements of crystallization directly in PCM devices also confirmed strong non-Arrhenius kinetics [101,102,132] over a wide temperature range of the existence of the supercooled liquid, which is important for understanding and for predicting memory writing performance. Numerical simulations of FDSC traces were performed, as detailed in Sect. 3.1, to recover $K(T)$ dependence by adjusting the absolute value of $N^{1/3}U(T)$, i.e., the simulated values of T_p are matched with those obtained experimentally (Fig. 4.2a). It is assumed that nucleation precedes growth, indeed for very high Φ_h, such as those in FDSC, a much lower effective nuclei density is needed to trigger the crystallization. When nucleation overlaps with growth during the transformation, the kinetic coefficient from Sect. 3.1. can be approximated as $K(T) \propto I^{1/4}U^{3/4}$, and the activation energy obtained from Kissinger analysis is then weighted average of those for nucleation and growth $Q_K = \frac{1}{4}Q_I + \frac{3}{4}Q_U$ [85]. Russo *et al.* [133] showed that at lower temperature, <450 K, the activation energies of $I^{st}(T)$ and $U(T)$ are similar, meaning that the overall temperature dependence of crystallization

rate is not strongly affected, and by taking the measured activation energies Q_{K} (the slope of the black dashed line in Fig. 4.2b) is reduced by about 9% as measured from Kissinger when influenced by nucleation. The combined DSC data (FDSC + conventional DSC) span a wide temperature range of $0.59 < T_{\mathrm{g}}/T < 0.93$ (410–650 K). For obtaining $U_{\mathrm{kin}}(T)$, a functional form based on Cohen-Grest free theory was used Eq. 1.13b, which gives best-fit parameters to the experimental data in Fig. 4.2 as: $B_{\mathrm{CG}} = 121 \pm 2$ K, $C_{\mathrm{CG}} = 1.71 \pm 0.02$ K, and $T_0^{\mathrm{CG}} = 427 \pm 1$ K [85], which is about 11.5% higher than T_{g} (= 383 K) lying within the expected range (10–17%) from Cohen-Grest theory [64]; the parameter A_{CG} is irrelevant because we only fit the shape of $U_{\mathrm{kin}}(T)$, not the absolute values.

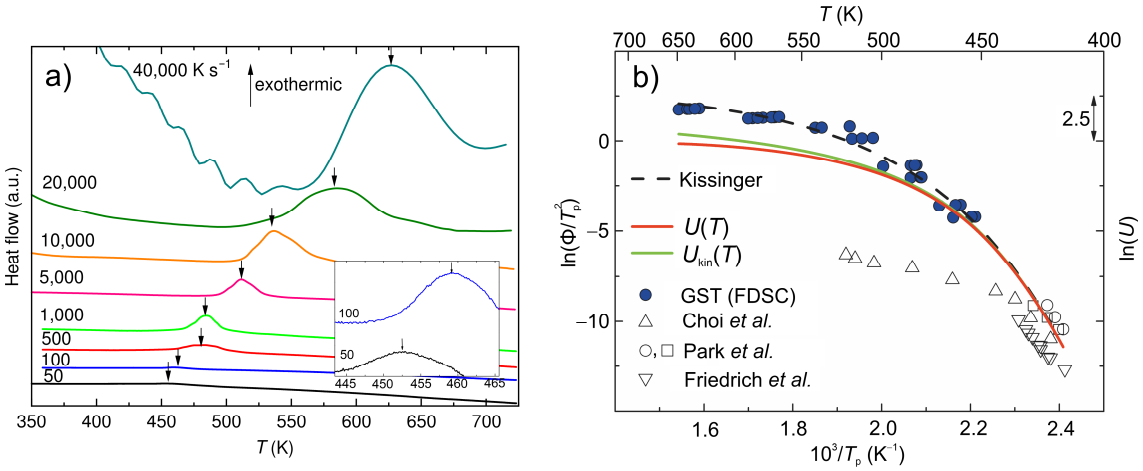

Fig. 4.2 Ultrafast-heating-calorimetry study of single-fragility single-film $Ge_2Sb_2Te_5$ (~80 nm thick). a) Measured FDSC (power-compensated Mettler-Toledo DSC 1; Multistar UFS1 chip with the upper temperature limit of about 800 K) traces – labelled with Φ_{h} in K s^{-1}. The downward arrows mark T_{p}. The estimated sample mass of flakes ~50–100 ng. The inset shows FDSC traces at lower Φ_{h}. The instability at high Φ_{h} likely arises from a larger sample mass being used. **b)** A Kissinger plot (the coloured symbols show FDSC data, and the best-fit to the lowest T_{p}, representing the best thermal contact at a given Φ_{h}, is represented by the black dashed line) for the crystallization of the liquid from part a. The literature data for $Ge_2Sb_2Te_5$ are from Choi *et al.* (electrical resistometry, $\Phi_{\mathrm{h}} = 0.05 - 8.33$ K s^{-1}, 250 nm thick); Park *et al.* (conventional DSC, $\Phi_{\mathrm{h}} = 0.08 - 0.33$ K s^{-1}, 80 nm thick); and Friedrich *et al.* (electrical resistometry, $\Phi_{\mathrm{h}} = 0.009 - 0.09$ K s^{-1}, 80 nm thick). The apparently underestimated value of the activation energy at $\Phi_{\mathrm{h}} > 0.8$ K s^{-1} (>430 K) by Choi *et al.* is difficult to interpret by the expected liquid kinetics. The red curve represents $U(T)$ related to the Kissinger analysis by the numerical modelling of DSC curves introduced in Sect. 3.1. The kinetic coefficient $U_{\mathrm{kin}}(T)$ (green line) relates to the growth via Eq. 1.10, where the thermodynamic driving force, whose strength is shown by the difference between the red and green lines, was approximated by Thompson and Spaepen (Fig. 1.2d; $\Delta H_{\mathrm{m}} = 12.13$ kJ mol^{-1}, $T_{\mathrm{g}} = 383$ K, and $T_{\mathrm{m}} = 900$ K [85]). A thermal lag in FDSC was estimated to be ≈1–10 K (see Supplementary Information in Ref. [85]), which is *comparable with the data spread in measured* T_{p}. *Reproduced from Orava et al. [85] (**publication #1 – Appendix I**).*

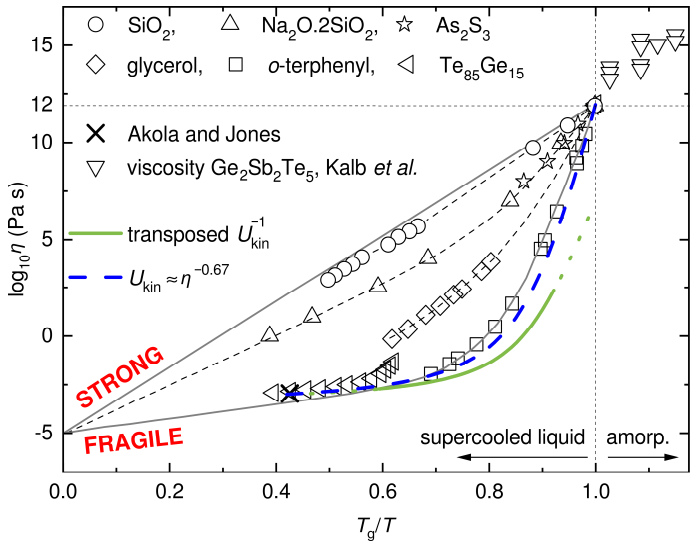

Fig. 4.3 Angell plot of $\eta(T)$ for a variety of glass-forming systems ranging from strong to fragile liquids. The curves for SiO_2, $Na_2O.2SiO_2$, As_2S_3, glycerol and *o*-terphenyl are from Angell [12]. The isoconfigurational viscosity data for single-film amorphous $Ge_2Sb_2Te_5$ (30 nm thick), below the estimated $T_g = 383$ K, are from Kalb *et al.* [134] obtained by atomic-force microscopy growth-rate measurements. The solid green line shows U_{kin}^{-1} of $Ge_2Sb_2Te_5$ transposed from Fig. 4.1b through the numerical modelling presented in Sect. 3.1. and assuming the viscosity shape of that expressed by Eq. 1.13b (the green dashed line shows extrapolated FDSC measurements). The kinetic coefficient for crystal growth is scaled to superpose on MD simulation $Ge_2Sb_2Te_5$ data of Akola and Jones at $T_m = 900$ K [135]. The measured viscosity of $Ge_{15}Te_{85}$ equilibrium liquid is by Neumann *et al.* [136].The U_{kin} data do not extrapolate to the commonly defined value of $\eta = 10^{12}$ Pa s at T_g revealing a decoupling, based on the Ediger's assumption in Eq. 1.11, of $\xi = 0.67$, which gives the calculated shape of $\eta(T)$ shown by the blue dashed line. *Modified from Orava et al. [85] (**publication #1 – Appendix I**).*

Fig. 4.3 shows the transposed $U_{kin}^{-1}(T)$ (green line) on the Angell plot by taking Eq. 1.11. Because $\eta(T)$ is generally unknown for GST, MD simulation data of Akola and Jones (the cross in Fig. 4.3) were used and $U_{kin}^{-1}(T)$ was set to match the viscosity of 1.1–1.2 mPa s [135] at T_m (=900 K). It could be scaled over the entire temperature range of the existence of the supercooled liquid, and it does not cross $\eta = 10^{12}$ Pa s at T_g. The effective temperature-dependent viscosity of GST could be calculated by introducing $\xi = 0.67$ (the blue dashed line in Fig. 4.3). The gradient of the line on approaching $T_g/T = 1$ gives the liquid kinetic fragility $m \approx 90$, and GST can be described as a *high-fragility liquid* contrary to a typical strong glass-forming liquid SiO_2 ($m \approx 21$) [38]. The discrepancy between $\eta(T)$ and $U_{kin}(T)$ is expected according to the decoupling. Fig. 1.4a can be replotted in terms of a broad correlation between ξ and m analysed by Ediger *et al.* [39], and that is shown in **Fig. 4.4**. GST has fragility similar to some of the organics (OTP and indomethacin), and the decoupling conforms to the general observations in a variety of glass-forming liquids including oxides and metallic glasses.

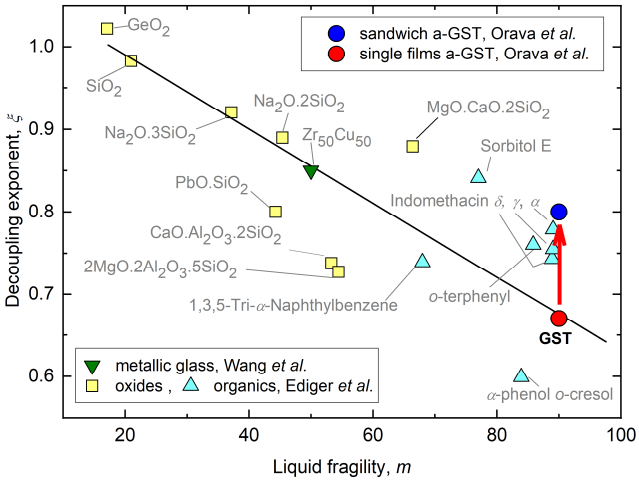

Fig. 4.4 The extent of decoupling between crystal growth and viscosity for a variety of glass-forming liquids increases with increasing kinetic fragility. The survey of data on oxides and organics is from Ediger *et al.* [39], and $Cu_{50}Zr_{50}$ metallic glass is taken from Wang *et al.* [88]. The single-film $Ge_2Sb_2Te_5$ ($\xi = 0.67$, $m \approx 90$) fits the correlation [85], but sandwiched $Ge_2Sb_2Te_5$ [ZnS:SiO_2 (80:20 mol.%; 10 nm thick)/$Ge_2Sb_2Te_5$ (60 nm thick)/ZnS:SiO_2 (10 nm thick)] has higher coupling indicated by the arrow [137]. The line is a guide to the eye only. *Reproduced from Orava et al. [137] (**publication #2 – Appendix I**).*

With all the parameters established, by correcting for thermodynamic effects and using the Stokes-Einstein relation, the absolute values of U can be calculated and its temperature dependences is shown by the red dashed line in Fig. 2.1 (the thicker line highlights the range measured by FDSC) giving $U_{\max} \approx 2.7$ m s^{-1} at a homologous temperature of $0.76T_m$ [85], which conforms to later measurements of $U_{\max} \approx 0.5$ m s^{-1} at $\sim 0.85T_m$ for GST from electrical measurements [101], and compares to experimentally obtained values in other PC chalcogenides: $U_{\max} \approx 3.3$ m s^{-1} at $\sim 0.85T_m$ for liquid GeTe from dynamic TEM [138]; and $U_{\max} \approx 15$ m s^{-1} at $\sim 0.95T_m$ for Ge_8Sb_{92} obtained indirectly by FDSC [121]. The values of $U_{\max}$ in PC chalcogenides are close to those of pure glassy metals $U_{\max} \sim 10^1 - 10^2$ m s^{-1} [61] which are preserved far below T_g ($\sim 0.4T_m$ for Ag). The growth rate of GST has been modelled by a variety of MD simulations typically at the homologous temperature of $\sim 0.67T_m$ (600 K), that lies in the fast-crystallizing window (Fig. 2.1). The absolute values are box-size dependent [139], U calculated for small DFT (density-functional theory) models of 180 atoms were found to be 3.0–5.6 m s^{-1} [139]; and slightly lower $U \approx 0.3 - 0.9$ m s^{-1} were reported for large DFT models (460 atoms) by Kalikka *et al.* [140]. Ronneberger *et al.* [141] calculated U through metadynamics and templated-growth methods, yielding ~1 m s^{-1} for GST. Majority of simulations signify the role of medium-range order, represented by structural four-fold rings motif with the correct chemical order [142–145], in the fast crystallization – there exist active transitions among structural units (also with transient units) with short lifetimes <100 fs [146]. This easy transformation stems from the existing lone pairs and weak axial bonds, which are unique to most of PC chalcogenides [139] (details of the understanding of atomistic origin of the fast crystallization can be found, for example, in Refs. [135,146]). All reported values of $U_{\max}$ are 3 orders of magnitude higher than 2.3×10^{-2} m s^{-1} at $\sim 0.83T_m$ described for congruent growth in $Cu_{50}Zr_{50}$ [88] (details of the mechanism(s) and kinetics of non-equilibrium crystallization and solidification in CuZr-based MGs are discussed in Chapter).

In their News & Views article [147], Wuttig and Salinga comment on the above-discussed results highlighting their importance for understanding the mechanism of fast crystallization (writing) in PCM: "*The work by Orava and colleagues certainly marks the beginning of more systematic studies of fast-crystallization processes. At present, the authors make a number of crucial assumptions to analyse their data that ought to be thoroughly checked in future work.*", and "*Nevertheless, the findings reported by Orava and colleagues encourage further quantum-mechanical calculations of the nucleation and growth phenomena in phase-change materials.*"

For PCM, the high crystal-growth rate which spans over a wide temperature range of $(0.6-0.9)T_{\mathrm{m}}$ (Fig. 2.1) is the underlying mechanism of fast writing (crystallization). On the other hand, the theoretically large decoupling, in other words, the fact that the crystal-growth rate can proceed $10^5\times$ faster than it would be predicted from viscosity at T_{g} could potentially remain the main drawback influencing the long-term data stability. It is now recognized that the original magnitude of decoupling suggested in single-film GST in Fig. 4.3 can probably be overestimated mostly due to the lacking knowledge of the calorimetrically-evidenced glass-transition temperature in fast-transforming chalcogenides (see the next section).

In devices, the GST active layer is capped between dielectrics, for example, ZnS-SiO_2, upon which stresses greatly impede the crystallization process (accompanied by a shrinkage of ~6.5% in layer thickness inducing stresses as high as 1.7 GPa in the absence of relaxation [148]), which becomes pronounced with decreasing GST thickness below ~10 nm [149–151]. Because the critical nucleus is more confined by the dielectrics, the effective crystal-glass interfacial energy increases due to screening effects from the oxide. The screening length was found to be ~0.64 nm, so the strongest effect, ultimately prohibiting any crystal nucleation, is only for ultrathin films <2 nm[152]. By using FDSC [137], we have shown that the crystallization proceeds in two distinct regimes in capped GST. i) At low Φ_{h} (<1,000 K s^{-1}; $T_{\mathrm{p}} < 520$ K), the dielectric layers inhibit crystallization, the activation energy increases from 216±1 kJ mol^{-1} (uncapped) to 261±19 kJ mol^{-1} (capped) [153], which is exhibited by a higher coupling between crystal growth and viscosity giving $\xi = 0.80$ (Fig. 4.4 – the blue point). The change can be attributed to the forming stresses induced by the crystallization itself which increases the effective viscosity in the active layer [154] – a coupling effect expected to be greater in thinner layers. It can be estimated, in the lack of relaxation, that in uncapped GST stresses fall to zero at about 500 K [148], and that corresponds to a transition temperature above which a second crystallization regime in capped GST was observed [137]. ii) At higher Φ_{h} (=5,000–40,000 K s^{-1}; $T_{\mathrm{p}} > 520$ K), the sandwich layers seed the crystallization and enhance the overall crystallization rate contrary to the uncapped films. Both effects are certainly beneficial for improving device reliability and scalability, although obtaining quantitative information about the nucleation and crystal-growth rate in ultrathin sandwiched layers at extremely high heating rates and relate them to the evolving/relaxing stresses remain challenging.

4.1.1. Uncertainty over T_{g} and ξ in fast-crystallizing phase-change chalcogenides

The above analysis of crystallization kinetics and $\eta(T)$ must assume a 'standard' value of T_{g} [85], which was derived from the onset of an endothermic peak in DSC [155]. Nevertheless, there is an ongoing debate about the uncertainty over T_{g} (overlapping with T_{x} at conventional heating rates), and whether crystallization observed close to the estimated T_{g} is in the glass or in the supercooled liquid forming on heating [156]. Typically, on fast heating T_{g}, can be separated from T_{x} because the activation energy

of the latter is about 2× of the former. In other words, for example, on the homologous scale of T/T_{m}, T_{g} may increase by 0.1, while T_{x} increases by as much as 0.4 upon faster heating for a Cu-based metallic-glass-forming liquid before the crystallization is mostly suppressed [116]. In our FDSC, no sign of T_{g} could be evidenced in GST (Fig. 4.2) and in AIST [86] which is typical for PC chalcogenides. The knowledge of T_{g} is important for transposing the data on the Angell plot (Fig. 4.3) – strictly all liquids should be compared with erased thermal history at a standard cooling rate of 0.33 K s^{-1} (20 K min^{-1}). This is especially important for metallic liquids and challenging for pure-metal glasses for which T_{g} in only known from MD simulations with typical cooling rates ~10^{12}–10^{15} K s^{-1}. For metals, Orava and Greer estimated corrected values of T_{g}, with an error ±15%, and are much lower than those obtained by MD simulations [13] (used to plot metals in Fig. 2.4a).

Conventional DSC study of pre-annealed thin-film GST suggested $T_{\mathrm{g}} = 455$ K, to be just ~10 K below T_{x} [155]. Atomic-force-microscopy study of crystal-growth rate [134], in the range temperature range of 388–418 K calculated an effective activation energy of 227±5 kJ mol^{-1}, which is much higher than that for the isoconfigurational viscosity 170±5 kJ mol^{-1} between 333–373 K [157] (downward-facing triangles $T_{\mathrm{g}}/T \geq 1$ in Fig. 4.3), and it was concluded that the measured U must be in the supercooled liquid above T_{g}. The characteristic existence of the two distinct low-(glassy-like) and high-(liquid-like)-activation-energy regimes upon heating/cooling is the basis of the ongoing argumentation. In AIST, Salinga *et al.* [98] estimated $T_{\mathrm{g}} = 550$ K based on optical reflectance measurements of $U(T)$ between 418–553 K with an effective activation energy of 261 kJ mol^{-1}, similar to value of 280±5 kJ mol^{-1} from direct $U(T)$ measurements between 413–458 K [134]. These values contrast with the activation energy for the viscosity of 128±9 kJ mol^{-1} between 343–353 K [157]. Recent study by Pries *et al.* [117], by using FDSC estimated $T_{\mathrm{g}} = 473$ K at 20 K min^{-1} for GST. The authors suggest that for $\Phi_{\mathrm{h}} < 10{,}000$ K s^{-1}, GST crystallizes from the glass, and it crystallizes from the supercooled liquid at higher heating rates. The same authors suggested $T_{\mathrm{g}} = 456$ K for AIST with the transition in the crystallization from the glass to the supercooled liquid at a heating rate of about 5,000 K s^{-1} [118]. On the other hand, Chen *et al.* [158] estimated $T_{\mathrm{g}} \approx 378$ K for GST by FDSC, which conforms to that used in Fig. 4.3. The ongoing dispute over T_{g} must be kept in mind when evaluating fragility of PC chalcogenides. For example, a higher value of T_{g} for GST would imply smaller decoupling effects than presented in Fig. 4.3, and somewhat more sluggish kinetics on approaching the glass-transition temperature. Indeed, we will see in Sect. 4.3 that there exists some discrepancy between the modelled and experimentally obtained crystallization kinetics data at low temperatures likely originating from the errors in T_{g} and the extrapolated viscosity down to T_{g}; kinetics in a high-temperature region can be modelled accurately.

4.2. Fragile-to-strong crossover

So far, in our description, we have assumed single-fragility PC chalcogenide liquids. Some liquids can undergo a fragile-to-strong crossover (FSC) on cooling (**Table 4.1**). A crossover also termed as a first-order liquid-to-liquid transition in the literature and firstly used to explain crystallization of water [159] is of fundamental and also of considerable technological importance as it can improve data retention of the glassy phase while maintaining fast writing speeds in PCM device. It should be noted that a kinetic (dynamic) and structural crossover (transition) do not necessarily appear at the same temperature. The crossover can be described by two values of fragility on either side of the temperature, m represents the strong regime as defined by Eq. 1.12, and m' represents the high-

temperature fragile side. The ratio m'/m describes the strength of FSC and it ranges from 1 (no FSC) to about ~8 for $Pr_{55}Ni_{25}Al_{20}$ metallic glass [160]. The existence of a crossover has recently been evidenced for single-film $Ag_{5.5}In_{6.5}Sb_{59}Te_{29}$ [86,161] – the first fast PC chalcogenide reported by Orava, Hewak & Greer [86] and discussed in detail here, $Ag_4In_3Sb_{67}Te_{26}$ [100], $Ge_{15}Sb_{85}$ [100], $Sc_{0.2}Sb_2Te_3$ [158]; in nanoparticles of $Ge_2Sb_2Te_5$ (~16 nm in diameter) [162] and of GeTe (~10 nm in diameter) [163]; and in non-PCM single-film $Ge_{15}Te_{85}$ [164–166]. Crystallization in $Ge_{15}Te_{85}$ is sluggish and not of technological importance in PCM, but, as we will see, it can actually provide useful insights into the crystallization mechanism of fast PC chalcogenides. In the following paragraphs, we will predominantly focus on liquid $Ag_{5.5}In_{6.5}Sb_{59}Te_{29}$ (AIST) and Ge–Te.

FDSC studies of fast PC-chalcogenide liquid AIST [86] and non-PCM liquid $Ge_{15}Te_{85}$ [166] revealed a wide temperature range of Arrhenius crystallization kinetics. For AIST, the range is up to $T_\mathrm{p} \approx 490$ K ($\sim 0.6 T_\mathrm{m}$) for $\Phi_\mathrm{h} < 200$ K s^{-1} giving single $Q_\mathrm{K} = 276 \pm 5$ kJ mol^{-1} (**Fig. 4.5a**). For $Ge_{15}Te_{85}$, the regime was measured in a wide range of the existence of the supercooled liquid, i.e., between T_p $\sim 460 - 600$ K, $(0.70 - 0.91) T_\mathrm{e}$, where T_e is the eutectic-melting temperature, for $\Phi_\mathrm{h} \leq 2{,}000$ K s^{-1} with $Q_\mathrm{K} = 165 \pm 4$ kJ mol^{-1} (Fig. 4.5b). The Arrhenius kinetics indicates that U_max has not been reached yet, which would yield higher Q_K with the opposite sign to $U(T)$ in the Kissinger plot (Fig. 3.1b).

Table 4.1 Known parameters of a fragile-to-strong crossover described by the fragile (high-temperature) and the strong (low-temperature) ends of the crossover, m' and m, respectively, and the ratio of these values, m'/m, in a variety of glass-forming liquids, including chalcogenides, metallic glasses, and supercooled water. The glass-transition temperature, T_g, is given for comparison. $Ge_2Sb_2Te_5$ is listed as an example of a single-fragility liquid. *Modified from Orava & Greer [36] (**publication #15 – Appendix I**).*

Composition	T_g (K)	m	m'	m'/m	Refs.
$Ge_2Sb_2Te_5$	383	90	—	—	[85]
$Ag_{5.5}In_{6.5}Sb_{59}Te_{29}$	378	37	74	2.0	[86,161]
$Ge_{15}Te_{85}$	404	50	90(98)	1.8(2.0)	[164,166]
$Ge_{30}Se_{70}$	579	28	92	3.3	[167,168]
$Sc_{0.2}Sb_2Te_3$	371	64	170[a)]	2.7	[158]
$Pr_{55}Ni_{25}Al_{20}$	484	19	156	8.2	[160]
$Cu_{50}Zr_{50}$	673	32(50)	127	4.0(2.5)	[88,169]
$Cu_{46}Zr_{46}Al_8$	701	130	53	2.5	[169]
water	136	22	98	4.5	[160,170]

[a)] The reported value of m' is at the physical limit of Angell plot and has to be treated with caution – see the main text discussing the complexity of overestimated kinetic-fragility values by incorrectly assuming single-fragility $\eta(T)$ models (Sect. 4.2.1.).

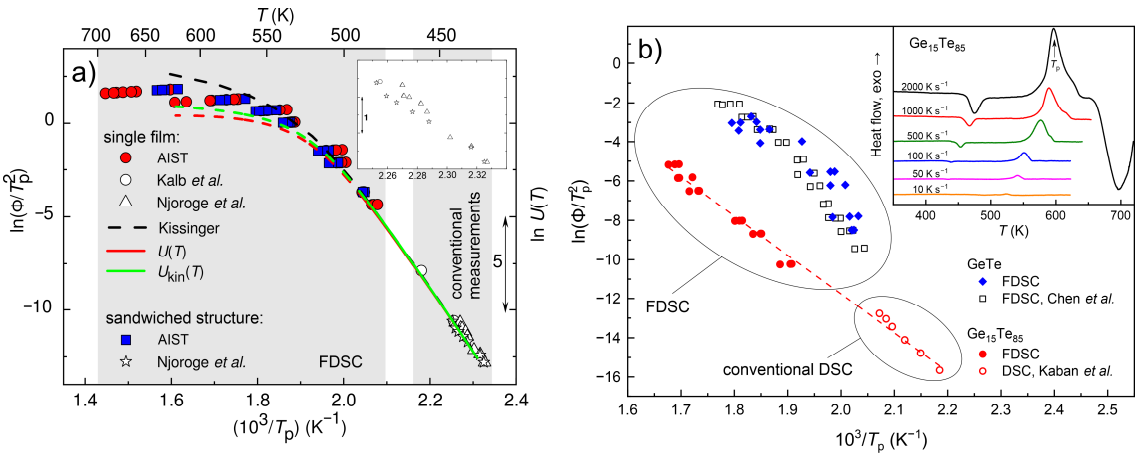

Fig. 4.5 The signature of the Kissinger analysis showing a wide range of Arrhenius crystallization kinetics due to a fragile-to-strong crossover in the chalcogenides. a) Crystallization kinetics of as-deposited single-film and sandwiched $Ag_{5.5}In_{6.5}Sb_{59}Te_{29}$ (AIST; ≈60 nm thick as-deposited films, capped between ≈10 nm thick ZnS:SiO_2 layers). The solid data points (circles – single film; squares – sandwiched structures) are from FDSC measurements (Φ_h = 50–40,000 K s^{-1}; sample mass is less than 100 ng) by Orava *et al.* [86]. The lines are modelled temperature-dependent parameters (*right-hand abscissa*: $U(T)$ – red line; $U_{kin}(T)$ – green line) as in Sect. 3.1 to achieve a Kissinger best-fit (*left-hand abscissa*: black dashed line). The open symbols are from Kalb *et al.* [171] obtained by conventional DSC ($Ag_{5.5}In_{6.5}Sb_{59}Te_{29}$, as-deposited 7 μm-thick films), $\Phi_h = 0.083$ and 1.3 K s^{-1}, and from Njoroge *et al.* [172] ($Ag_5In_6Sb_{59}Te_{30}$ single 100 nm film and capped AIST (100 nm)/ZnS:SiO_2 (5 nm)) measured by resistometry, $\Phi_h = 4.5 \times 10^{-3} - 5.7 \times 10^{-2}$ K s^{-1}. The inset shows a zoom-in view of the low-temperature data. **b)** Crystallization-kinetics data of non-PCM $Ge_{15}Te_{85}$ (<10 μm thick glassy flakes) and single-fragility single-film GeTe (≈5.6 μm thick films) liquids obtained by FDSC measurements (red solid circles cover a range of $\Phi_h = 10 - 2{,}000$ K s^{-1} for $Ge_{15}Te_{85}$; blue solid diamonds cover a range of $\Phi_h = 50 - 20{,}000$ K s^{-1} for GeTe) [166]. The inset shows the FDSC traces of $Ge_{15}Te_{85}$ – on heating faster than 2,000 K s^{-1}, T_p overlaps with the low eutectic-melting temperature $T_e = 658$ K. The open symbols show data of Chen *et al.* [173] (as-deposited single-film GeTe, 1.4 μm thick) measured by FDSC ($\Phi_h = 20 - 40{,}000$ K s^{-1}). The conventional DSC ($\Phi_h = 0.033 - 0.667$ K s^{-1}) data are from as-spun $Ge_{15}Te_{85}$ ribbons by Kaban *et al.* [174] – only the temperature of the first crystallization peak is considered in the analysis. The typical FDSC sample mass was <75 ng. A thermal lag in FDSC for Ge–Te liquid was measured to be <5 K by using the known value of T_e for $Ge_{15}Te_{85}$. Only FDSC data of $Ge_{15}Te_{85}$ are used to infer viscosity in Sect. 4.2.2. because crystallization upon conventional heating is complex and cannot be described by the simulation in Sect. 3.1. *Part a is reproduced from Orava et al. [86] (**publication #6 – Appendix I**); part b is reproduced from Weber et al. [166] (**publication #14 – Appendix I**).*

4.2.1. Crossover in liquid Ag–In–Sb–Te

What is the origin of the wide Arrhenius kinetics? For AIST, Salinga *et al.* [98] observed similar wide Arrhenius temperature regime between 418–553 K by optical reflectometry, and they concluded that even after subtracting relaxation, such dependence cannot be explained by decoupling or by liquid-like behaviour – the crystallization was assigned to a highly-energetic isoconfigurational glassy state of very high T_g. Ab-initio MD simulations of diffusivity suggested that there may be a nearly-Arrhenius regime at $T > 500$ K [175]. Unfortunately, on further cooling, the diffusivity diverges from the MD simulations, the latter is overestimated than those inferred from the crystal-growth rate. This divergence was assigned to different cooling rates of MD ($\Phi_c \sim 10^{13}$ K s^{-1}) and experimental ($\Phi_c \sim 10^{10}$ K s^{-1}) glasses. However, for isoconfigurational states, the low-temperature diffusivity should lie on parallel, not divergent, Arrhenius lines. Orava, Greer & Hewak concluded, for the first time, that *the Arrhenius kinetics reflects a weak FSC* (Table 4.1) shown by respectively the thick blue and red lines in **Fig. 4.6**, part a and b [86]. Although the existence of an FSC was originally inferred

indirectly from FDSC [86], the authors clearly showed that the numerical modelling of the curvature in the Kissinger analysis in Fig. 4.5 to infer $U_{\mathrm{kin}}(T)$ cannot be done by assuming a single-fragility $\eta(T)$, for example, the Cohen-Grest model (Eq. 1.13) – the model is only applicable to low temperatures (heating rates) (red solid line). This is in stark contrast to the single-fragility liquid GST in Fig. 4.2a.

The Arrhenius kinetics is further explored and discussed in the Angell plot in Fig. 4.6 by taking $T_{\mathrm{g}} = 378$ K [86], 5 K lower than for GST. The transposed U_{kin}^{-1} inferred from FDSC is shown by the green line in Fig. 4.4a, $T_{\mathrm{g}}/T \leq 0.77 - 0.87$. As for GST, there was no directly measured $\eta(T)$ for supercooled liquid AIST in the original work of Orava *et al.* [86]. Only intermediate-temperature viscosities, $T_{\mathrm{g}}/T \leq 0.82 - 0.91$ of AIST inferred from crystal-growth rate measured by AFM in as-deposited single-film $Ag_{5.5}In_{6.5}Sb_{59}Te_{29}$ [134] and MD data at 850 K were available [176] (Fig. 4.4a). Later, Orava *et al.* [161] obtained $\eta(T)$ of the equilibrium liquid AIST directly in the temperature range 829–1254 K (Fig. 4.6b – open circles) by using an oscillating-crucible viscometer [177]. The authors showed that the measured viscosity of $\log_{10}\eta\,(\mathrm{Pa\ s}) = -2.64$ (error in the measured value is <10%) at $T = 850$ K is close to the value of $\log_{10}\eta\,(\mathrm{Pa\ s}) = -3.11$ obtained by MD simulations for $Ag_{3.5}In_{3.8}Sb_{75.0}Te_{17.7}$ [176].

Let's firstly assume that AIST behaves a single-fragility liquid, which can be described by using a model based on Adam-Gibbs theory [178] and proposed by Mauro *et al.* [119]. This MYEGA (**M**auro-**Y**ue-**E**llison-**G**upta-**A**llan) equation can, unlike traditional Vogel-Fulcher-Tammann [119], fit a variety of glass-forming liquids with m ranging between 20 and 90, and it is given as:

$$\log_{10}\eta(T) = \log_{10}\eta_{\infty} + \left(\frac{B}{T}\right)\exp\left(\frac{C}{T}\right), \tag{4.1}$$

where η_{∞} is the high-temperature limit of viscosity, and B and C are adjustable parameters.

Let us initially inspect the FDSC and AFM combined data in the intermediate temperature range $T_{\mathrm{g}}/T = 0.77 - 0.91$ by implementing two fitting approaches [161]. In the first approach, T_{g} is fixed at 378 K and the fit to Eq. 4.1 is forced to take the conventional value $\log_{10}\eta\,(\mathrm{Pa\ s}) = 12$; the best-fit is shown by the black dotted line in Fig. 4.6b. The second approach, commonly applied in the literature, treats T_{g} as an adjustable parameter and the best fit gives $T_{\mathrm{g}} = 400$ K (Fig. 4.4b, grey dashed line); such value appears high (compared to 378 K) and the fragility near T_{g} is overestimated (the grey dashed line in Fig. 4.6b corresponds to $m \approx 70$). Similar fitting problems near T_{g}, by assuming single-fragility liquid, may account for high fragility values reported: $m \approx 130$ for melt-quenched films [98], and $m \approx 104$ and 217 for as-deposited and melt-quenched films [99]. Detail analysis of the high-temperature region (**Fig. 4.7**) reveals that when T_{g} is set at the constant value 378 K, the best-fit curve (Fig. 4.7 – black dotted line) has ~2.5 higher slope than the measured $\eta(T)$ (symbols in Fig. 4.7). For T_{g} being an adjustable parameter, the best-fit grey dashed line also does not reproduce the measured $\eta(T)$, its slope is ~1.7× greater than of the experimental values and the fit on approaching T_{g}, as noted above, is worsened (Fig. 4.6). It can be concluded that although the single-fragility models and measured $\eta(T)$ match at $T_{\mathrm{g}}/T = 0.364$ (1,038 K) and both approaches can reproduce the slope of the viscosities in the intermediate range, *the single-fragility approach fails to reproduce the shape of* $\eta(T)$ *in the entire temperature range* $T_{\mathrm{g}}/T = 0.3 - 1.0$ (Fig. 4.6b) – the temperature dependences are irreconcilably different [161].

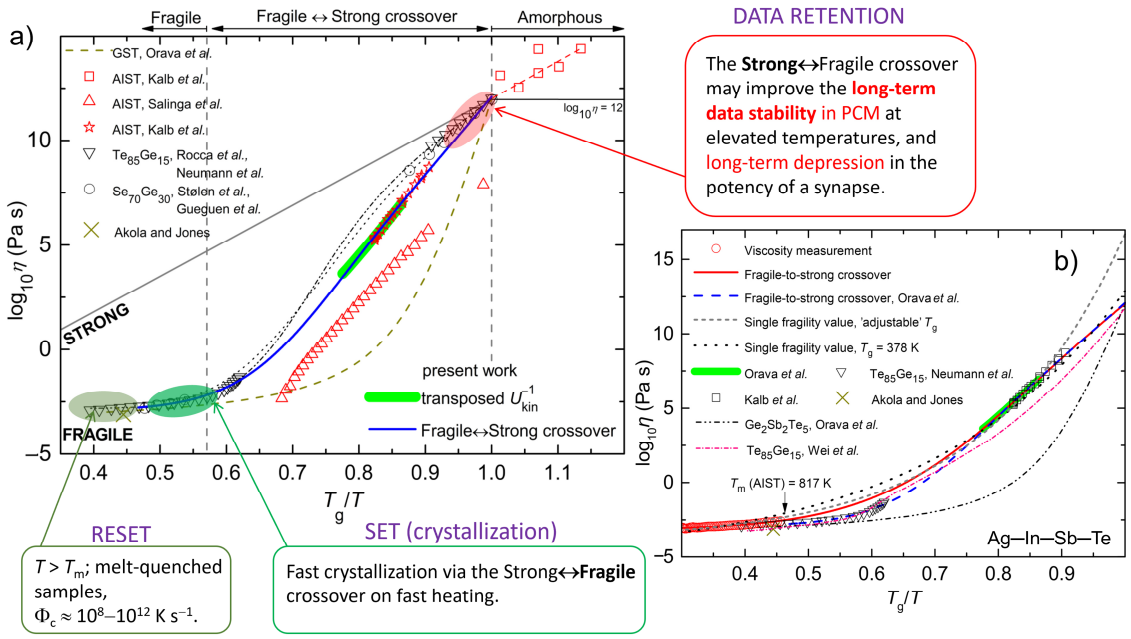

Fig. 4.6 Angell plot showing the existence of a fragile-to-strong crossover (FSC) upon cooling the liquid $Ag_{5.5}In_{6.5}Sb_{59}Te_{29}$ and the implications for the performance of phase-change memory. In both parts, liquid $Ge_2Sb_2Te_5$ (GST) is the only single-fragility liquid shown ($m \approx 90$) and it is inferred from FDSC by Orava *et al.* [85]. The other data do not fit single-fragility forms and are all interpreted in terms of a crossover modelled by a generalized-MYEGA model (Eq. 4.2) [160]. **a)** For AIST, the *blue solid line* shows a best-fit to data covering the intermediate temperature range from the transposed U_{kin}^{-1} curve (green line) from Fig. 4.5a, viscosity derived from AFM-based growth-rate measurements (stars) by Kalb *et al.* [134] (single-film $Ag_{5.5}In_{6.5}Sb_{59}Te_{27}$, 30 nm thick), and to the value for η at 850 K (cross) calculated from modelled diffusivities in $Ag_{3.5}In_{3.8}Sb_{75.0}Te_{17.7}$ by Akola and Jones [176]. The data of Salinga *et al.* [98] (triangles) are derived from reflectometry measurements ($Ag_4In_3Sb_{67}Te_{26}$, 30 nm thick and sandwiched between ZnS:SiO_2 layers). The viscosity data derived for thin-film $Ag_{5.5}In_{6.5}Sb_{59}Te_{29}$ by Kalb *et al.* [157] are for an amorphous film ($T_g/T > 1$). The data for $Ge_{15}Te_{85}$ are from viscosity measurements by Neumann *et al.* [136] (refined data are shown in Fig. 4.9 [166]) and recalculated from a Kissinger analysis of conventional DSC measurements ($\Phi_h = 0.083 - 1.3$ K s^{-1}) by Rocca *et al.* [179]. The data for $Ge_{30}Se_{70}$ are from viscosity collected by Stølen *et al.* [167] and indentation creep measurements by Gueguen *et al.* [168]. The dashed lines show generalized-MYEGA fits of these two liquids as suggested in the original work in Ref. [86] based on the limited data available at that time. A newly defined FSC in $Ge_{15}Te_{85}$ based on direct viscosity measurements is presented in Fig. 4.9 and discussed in the corresponding parts of the main text. The implications of the existing FSC for the performance of PCM are schematized by the rectangles for SET (crystallization) and RESET (melt-quenching) operations, and DATA RETENTION (drift of the glassy phase – unwanted relaxation) – discussed in Sect. 4.2.3. **b)** Refined shape of the FSC (red line) by Orava *et al.* [161] by including directly measured viscosities (circles) of the equilibrium liquid AIST in the generalized-MYEGA fit. The blue dashed line shows a FSC originally suggested by Orava *et al.* [86] (part a) without the high-temperature viscosity data. The black and grey dashed lines show the best single-fragility fits, using Eq. 4.1: i) by setting $T_g = 348$ K in MYEGA fitting, at $\Delta\log_{10}\eta\,(\mathrm{Pa\ s}) = 12$, or ii) by taking T_g as an adjustable parameter. The pink dot-dashed line shows a FSC suggested for $Ge_{15}Te_{85}$ by Wei *et al.* [164] by combining viscosity data of Neumann *et al.* [136] with conventional calorimetry measurements. The remaining displayed data have same references as in part a. *Part a is modified from Orava et al. [86]; part b is reproduced from Orava et al. [161] (**publications #6 and #9, respectively – Appendix I**).*

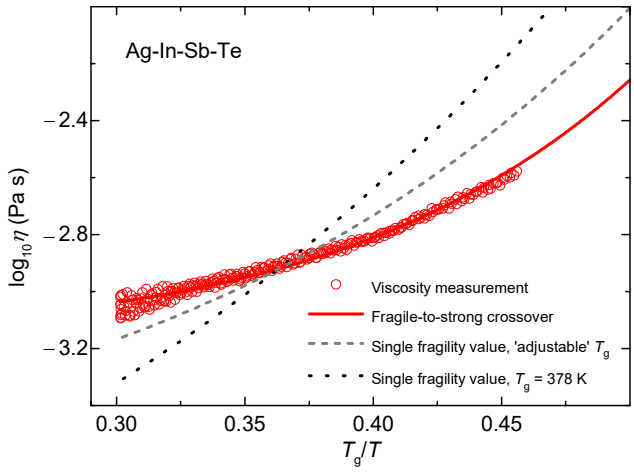

Fig. 4.7 Close-up view of the experimental high-temperature viscosity of liquid $Ag_{5.5}In_{6.5}Sb_{59}Te_{29}$ in the range of $T_g/T = 0.30 - 0.50$. The viscosity (open symbols) was obtained by an oscillating-crucible viscometer technique on cooling the liquid at a rate of 1 K min^{-1} in the temperature range 829–1,254 K (±5 K) – the onset of solidification was observed at ≈817 K (the best-fit of the measured $\eta(T)$ to Eq. 4.1 gives $\log_{10}\eta_\infty(\text{Pa s}) = -3.31 \pm 0.02$, $B = 100 \pm 16$ K, and $C = 1{,}487 \pm 112$ K with the quality of the fit $R^2 = 0.9872$) [161]. The black dotted and grey dashed lines are best-fits, details of which are described in the main text, to Eq. 4.1 and yielding respectively $\log_{10}\eta_\infty(\text{Pa s}) = -4.31 \pm 0.06$, $B = 617 \pm 36$ K, $C = 890 \pm 23$ K, $R^2 = 0.9919$; and $\log_{10}\eta_\infty(\text{Pa s}) = -3.64 \pm 0.03$, $B = 198 \pm 11$ K, $C = 1{,}382 \pm 24$ K, $R^2 = 0.9980$. The full extent of the fragile-to-strong crossover (red line) is shown in Fig. 4.6b and discussed in the main text. *Reproduced from Orava et al. [161]* ***(publication #9 – Appendix I)***.

All the above indicate the possible presence of a fragile-to-strong crossover (Fig. 4.6), which, in metallic-glass-forming liquids, can be described by the generalized-MYEGA model [160]:

$$\log_{10}\eta(T) = \log_{10}\eta_\infty + \frac{1}{T\left[W_1\exp\left(-\frac{C_1}{T}\right) + W_2\exp\left(-\frac{C_2}{T}\right)\right]}, \tag{4.2}$$

where W_1, C_1, W_2, C_2 are fitting parameters, and η_∞ has the same meaning as in Eq. 4.1. By fitting the indirectly inferred data, Orava *et al.* [86] suggested the first shape of an FSC, and the fitted parameter values for the *blue solid line* in Fig. 4.6a are: $\log_{10}\eta_\infty(\text{Pa s}) = -2.95 \pm 0.04$, $W_1 = 5.3 \pm 2.2$ K^{-1}, $C_1 = 5{,}334 \pm 231$ K, $W_2 = (5.79 \pm 0.71) \times 10^{-4}$ K^{-1}, $C_2 = 459 \pm 45$ K, and $R^2 = 0.9997$. By including the directly measured high-temperate $\eta(T)$ [161], a corrected shape of the FSC shown by the *red solid line* in Figs. 4.6b and 4.7 was derived [161]: $\log_{10}\eta_\infty(\text{Pa s}) = -3.16 \pm 0.01$, $W_1 = (6.4 \pm 0.3) \times 10^{-2}$, $C_1 = 2{,}949 \pm 34$ K, $W_2 = (1.59 \pm 0.14) \times 10^{-4}$ K^{-1}, $C_2 = 27 \pm 29$ K, and $R^2 = 0.9999$. The high uncertainty of 100% in C_2 is due the wide temperature range of the Arrhenius kinetics on approaching T_g. For the range of greatest curvature in the Angell plot, $T_g/T = 0.46 - 0.77$, experimental $\eta(T)$ is still lacking. Both forms show a significant difference over $T_g/T = 0.5 - 0.7$ with the largest deviation of $\Delta\log_{10}\eta(\text{Pa s}) \approx 0.8$ at $T_g/T = 0.6$ (630 K) [161]. They show a wide range of Arrhenius kinetics corresponding to a moderately strong "intermediate" liquid giving $m \approx 37$ at T_g. The fragile regime yields $m' \approx 74$ by the latter fit giving the strength of the FSC: $m'/m \approx 2$ [161]. Generally, PC chalcogenides have the weakest FSC reported in a variety of glass-forming liquids, so far (Table 4.1).

So far, the evidence about the FSC in AIST has been based on data inferred from indirect measurements (FDSC & AFM) in the key region of the intermediate temperatures (Fig. 4.6). A direct structural fingerprint of a crossover has been missing because of the fast liquid dynamics which obscures any measurements due to crystallization. A crossover is usually accompanied by a change in specific heat capacity, compressibility, sound velocity, thermal expansion etc. reflecting a phase transition between two liquids of different properties [180–184]. It has been suggested that the transition in AIST is between high-temperature metallic to low-temperature semiconducting liquids [86], such as observed at $\sim 1.05 T_{\mathrm{m}}$ upon cooling the sluggish equilibrium liquid $Ge_{15}Te_{85}$ [100,165,166,182]. Recently, Zalden and co-workers [100] provided the first direct structural evidence for the existence of a crossover (liquid-to-liquid transition) in liquid AIST and $Ge_{15}Sb_{85}$ from pump-probe femtosecond X-ray diffraction experiments (**Fig. 4.8**), and the structural evolution could be correlated with kinetic data. The authors defined two temporal intervals $\{t_{\mathrm{a}}\} \approx 10^1$–$10^2$ ps and $\{t_{\mathrm{b}}\} \approx 10^4$–$10^5$ ps in which the temperature of PC chalcogenides was stable within 10% and could, therefore, be accurately calculated. The evolution of temperature-dependent structural ordering, defined by a ratio of $R = r_2/r_1$ (r_1 and r_2 are the positions of the first- and second-coordination shells obtained from the calculated pair-correlation function), revealed the occurrence of a liquid-to-liquid transition at $T_{\mathrm{LL}} = 660 \pm 20$ K $[(0.81 \pm 0.01) T_{\mathrm{m}}$ and 610 ± 20 K $[(0.71 \pm 0.01) T_{\mathrm{m}}]$ for AIST and $Ge_{15}Sb_{85}$ (Fig. 4.8a), respectively. These temperatures are higher than the crossover temperatures, T_{FTS} (vertical dashed lines in Fig. 4.8), reported from the experimental measurements which are subject to errors and unresolved assumptions. The structural transition was also observed in the temperature-dependent intensity of a pre-peak (I_{pp}), located at $\approx 2 \times r_1$, i.e., at 5.8 Å (AIST) and 5.9 Å ($Ge_{15}Sb_{85}$), which reflects the formation of alternating long and short bonds of a central atom in octahedral coordination and being the fingerprint of a *Peierls distortion* [100], which was concluded to be the predominant structural mechanism underlying the liquid-to-liquid transition. A tendency for a pseudogap opening in the density of states was reported with increasing distortion hinting at the above-suggested metallic-to-semiconductor transition upon cooling. The temperature dependence of diffusivity, obtained from the literature and represented by its effective activation energy, is shown in Fig. 4.8, part c and d. Although the dispute over T_{g} remains unresolved, the strong end of AIST is shown for $T_{\mathrm{g}} = 450$ K (the dashed-dotted line in Fig. 4.8d), unlike $T_{\mathrm{g}} = 378$ K in Fig. 4.6, the temperature dependence of the structural parameters clearly correlates with the increasing apparent activation energy of diffusivity on cooling, especially with the kinetic measurements of melt-quenched AIST by Salinga *et al.* [98] (shown also in Fig. 4.6 by the triangles).

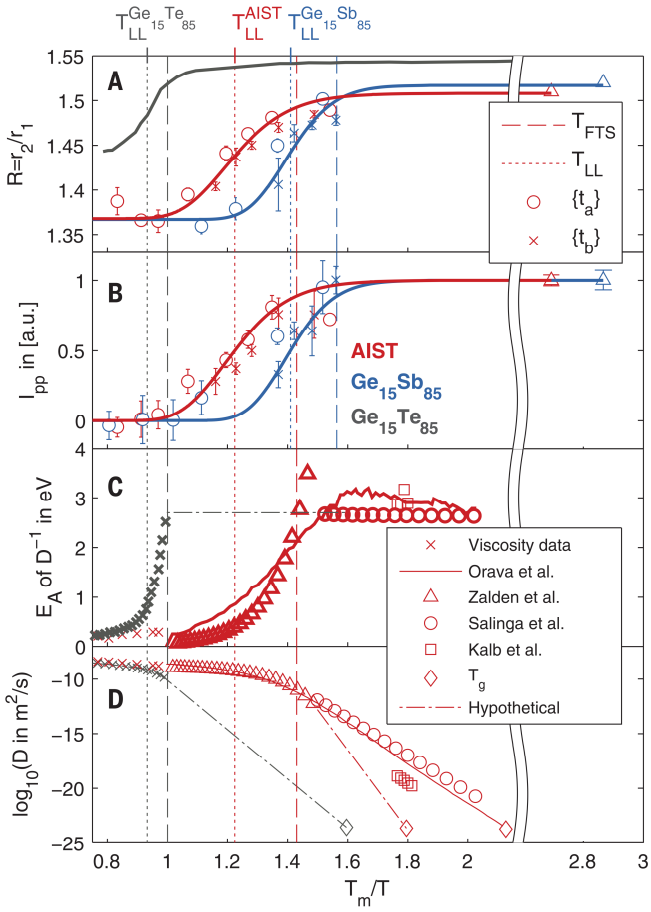

Fig. 4.8 Structural signature of a fragile-to-strong crossover in the supercooled liquid $Ag_4In_3Sb_{67}Te_{26}$, $Ge_{15}Te_{85}$, and $Ge_{15}Sb_{85}$. Each composition is depicted in different colour: AIST – red, $Ge_{15}Sb_{85}$ – blue, both obtained by pump-probe femtosecond X-ray diffraction experiments, and $Ge_{15}Te_{85}$ is shown as grey (data are taken from Wei *et al.* [165]). Two different temperatures correlate with the apparent activation energy for diffusivity and structural evolution. The vertical dotted lines highlight the structural 'liquid-to-liquid' transition temperature, T_{LL}, defined by the inflection points of the corresponding curves. The vertical dashed lines show the crossover temperature, T_{FTS}, reported from kinetic data previously, and correspond to the present data at which ~90% of the low-temperature structure is reached for AIST and $Ge_{15}Te_{85}$; a fragile-to-strong crossover temperature is taken by Zalden *et al.* [100] to be 570 K (AIST) and 550±20 K ($Ge_{15}Sb_{85}$ – derived from the plot). **a)** The temperature evolution of a ratio R of the distances in the second-, r_2, and the first-coordination, r_1, shells. **b)** Temperature dependence of the intensity of a pre-peak from the structural factor and which is related to a Peierls distortion. The solid lines in part a and b show a best fit to an error function for guiding the eye only. **c)** and **d)** Diffusivity data obtained from viscosity measurements above T_{m} for $Ge_{15}Te_{85}$ [185], from crystal-growth rate Zalden *et al.* [99], Salinga *et al.* [98], and Kalb *et al.* [134]. The glass-transition temperature T_{g} is shown for $Ge_{15}Te_{85}$ ($T_{\mathrm{g}} \approx 411$ K) and AIST ($T_{\mathrm{g}} \approx 450$ K) [100]. The solid line in part d describes a fragile-to-strong crossover as suggested in Fig. 4.6 by Orava *et al.* [86]. *Reproduced from Zalden et al. [100].*

4.2.2. Crossover in liquid Ge–Te

In this section, we describe the kinetics in fast single-fragility fast PC liquid GeTe and compare it with the occurring crossover in non-PCM liquid $Ge_{15}Te_{85}$. The FSC can be correlated with the experimentally obtained crystallization by FDSC, viscosity, and temperature evolution of liquid structure.

We start by describing the *single-fragility* liquid GeTe, and later compare it with $Ge_{15}Te_{85}$. Liquid GeTe was reported to be a high-fragility liquid with $m \approx 131$ inferred from FDSC [173] (only the

thermodynamic without the Kissinger correction was applied), and $m \approx 104-111$ by MD simulations [60]. High fragilities conform to the observed non-Arrhenius crystallization kinetics by FDSC (Fig. 4.5b) as concluded in Fig. 3.1, and to generally high crystal-growth rate in the liquid, $U_{\max} \approx 3.3$ m s^{-1} at $0.85T_{\mathrm{m}}$ [138] (from TEM), but the absolute values somewhat do not reflect well to the fact that liquid GeTe has lower activation energy for crystal growth $Q_U = 171$ kJ mol^{-1} [186] in comparison to liquid $Ge_2Sb_2Te_5$ $Q_U = 227$ kJ mol^{-1} [186]. A best-fit of the measured viscosity (blue solid squares measured in the temperature range $T_{\mathrm{g}}/T = 0.332-0.444$, and described by a single value of the activation energy for viscous flow $Q_\eta = 28$ kJ mol^{-1}) (**Fig. 4.9**), combined with the transposed U_{kin}^{-1} from FDSC ($T_{\mathrm{g}}/T = 0.75-0.86$, Fig. 4.5b) to the MYEGA model (Eq. 4.1) provides a *new value of fragility* $m \approx 76$ (thick blue line in Fig. 4.9) [166], which contrasts with the values reported so far. Rather surprisingly, Chen *et al.* [163] derived $m \approx 78$, conforming to single-film GeTe, for a crossover in GeTe nanoparticles. The newly derived viscosity (blue solid line) differs from the early one proposed by Chen *et al.* [173] (dashed line) by up to 3 orders of magnitude in the intermediate temperature range $T_{\mathrm{g}}/T = 0.7-0.8$. Assuming the continuous diffusion-limited normal growth (Eq. 1.10) and no decoupling, the new $\eta(T)$ gives $U_{\max} \approx 0.8$ m s^{-1} at $0.89T_{\mathrm{m}}$ which is close to the value reported by Santala *et al.* [138], noted just above, by using dynamical TEM.

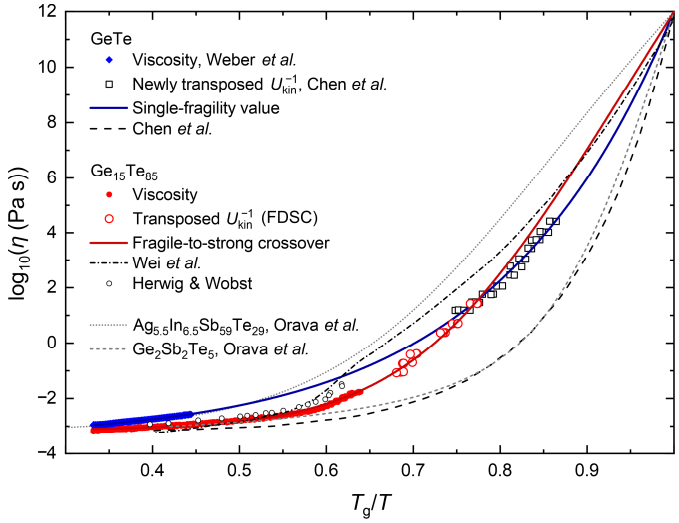

Fig. 4.9 Angell plot of the temperature-dependent viscosity for the non-PCM liquid $Ge_{15}Te_{85}$ showing a crossover and the single-fragility fast PC liquid GeTe. The measurements of the temperature-dependent dynamic viscosity of GeTe (diamonds), from Weber *et al.* [187], and $Ge_{15}Te_{85}$ (full circles) were carried out with an oscillating-crucible viscosimeter at a cooling rate of −1 K min^{-1}. For *single-fragility liquid* GeTe ($T_{\mathrm{g}} = 423$ K), the open squares show the newly transposed U_{kin}^{-1} obtained from FDSC measurements (Fig. 4.5b) and the crystallization data conform to the FDSC measurements by Chen *et al.* [173]. The originally proposed $\eta(T)$ [173] is shown by the black dashed line. The newly derived temperature dependence of viscosity is shown by the thick blue line with the best-fit parameters to the MYEGA model: $\log_{10}\eta_\infty\,(\mathrm{Pa\ s}) = -3.317 \pm 0.008$, $B = 126 \pm 3$ K, $C = 1{,}666 \pm 8$ K, $R^2 = 0.9995$ by combining the experimental $\eta(T)$ and the newly transposed U_{kin}^{-1} [166]. A *fragile-to-strong crossover* in $Ge_{15}Te_{85}$ ($T_{\mathrm{g}} = 406$ K) is represented by the red solid line – the best-fit to the generalized-MYEGA (Eq. 4.2) by combining experimental $\eta(T)$ (full circles) and transposed U_{kin}^{-1} (red open circles) from FDSC (Fig. 4.5b) [166]. A crossover predicted by Wei *et al.* [164] based on Adam-Gibbs theory [178] and the best-fit to combined data of conventional calorimetric measurements and viscosity from Neumann *et al.* [136] is shown by the dash-dotted line. The early measurements of $\eta(T)$ by Herwig & Wobst [188] are shown by the black open circles. The viscosity of single-fragility $Ge_2Sb_2Te_5$ [85] (Fig. 4.3) and the crossover in AIST [161] (Fig. 4.6b) obtained by Orava *et al.* are shown for comparison. *Reproduced from Weber et al. [166] (**publication #14 – Appendix I**).*

In several metallic-glass-forming liquids, Mauro *et al.* [189] (later reviewed by Kelton [190]) demonstrated that the temperature evolution in the height of the first peak $S(Q_1)$ of the total structure factor $S(Q)$ can be correlated with the liquid fragility. The authors suggested a new *structural fragility index* defined as:

$$m_{\mathrm{str.}} = \left(\frac{S(Q_1)_{\mathrm{glass}} - S(Q_1)_{\mathrm{liquid\ extrapolation}}}{S(Q_1)_{\mathrm{glass}}} \right) \times 100\%. \tag{4.3}$$

The structural fragility index increases with m, and implies that for glass-forming systems of a greater $m_{\mathrm{str.}}$ at T_{g}, the liquid must undergo more severe structural ordering on cooling in order to achieve the configurational state of the glass, and therefore, more pronounced super non-Arrhenius dependence of $\eta(T)$ is to be expected giving higher m. Although metallic glasses and PC chalcogenides are structurally different, the concept of structural fragility also seems to provide a useful insight into the temperature-dependent structural evolution of glassy and liquid chalcogenides (**Fig. 4.10**).

The Arrhenius temperature-dependent $S(Q_1)$ for liquid GeTe (data are taken from Weber *et al.* [187] – equilibrium liquid, and Piarristeguy *et al.* [191] – for the glassy state) on cooling between $(1 - 1.2)T_{\mathrm{m}}$ is shown in Fig. 4.10. The large structural discrepancy between the extrapolated liquid (dashed line) and the glass indicates a fragile liquid with $m_{\mathrm{str.}} = 12.9$. A comparison to $m_{\mathrm{str.}} = 16.5$ ($m \approx 90$) for GST (Weber *et al.* [166] – the liquid; Jóvari *et al.* [192] – the glass) implies that the kinetic fragility of GeTe must be smaller than that for the liquid GST and that is supported data in Figure 4.9, again contradicting the overestimated reported values of kinetic fragility in the literature [60,173].

The *liquid $Ge_{15}Te_{85}$ anomaly*, also known in other Te-rich alloys, above T_{e} has experimentally been described in the literature by measuring heat capacity, thermal expansion, resistance, compressibility, molar volume, density (Fig. 4.10) etc. [180–184,193,194]. Structural measurements showed that the addition of about 15–20 at.% of Ge into Te stabilizes the low-temperature liquid structure [195], the liquid $Ge_{15}Te_{85}$ may be characterized of being heterogeneous containing higher mobility clusters [196], and there is a distinct evolution of the short-range and medium-range order, represented by a pre-peak at ~1.1 $Å^{-1}$ (the length-scale of ~8 Å in the real space) in $S(Q)$, underlying the crossover [165].

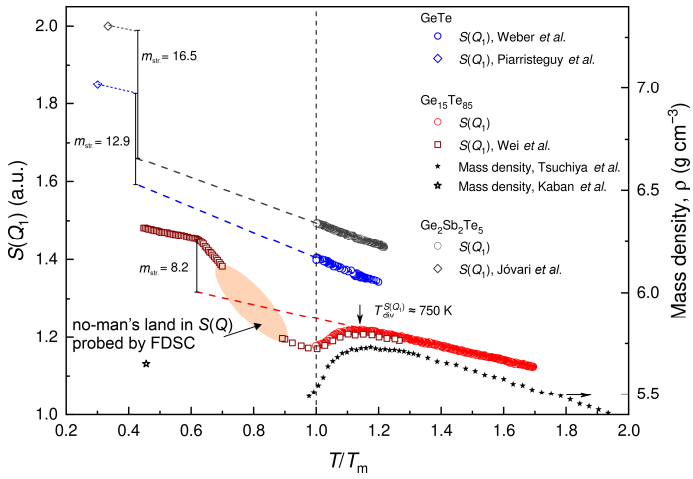

Fig. 4.10 Temperature evolution of the height of the first peak $S(Q_1)$ of the X-ray structure factor in phase-change liquid GeTe, $Ge_2Sb_2Te_5$ and non-PCM $Ge_{15}Te_{85}$. *Left-hand absicca*: *In-situ* $S(Q_1) - T$ dependences. Single-fragility GeTe ($T_m = 998$ K): high-temperature liquid data (blue open circles) are from Weber *et al.* [187] (bulk alloy, a cooling rate –5 K min^{-1}, carried out at the P07 beamline, PETRA III, DESY, Hamburg, Germany). The structure of the glass (blue diamond) is taken from Piarristeguy *et al.* [191] (as-deposited 1–3 μm thick film; measurements were carried out at the original X-ray BW5 wiggler beamline of the DORIS III positron storage ring operated at the HASYLAB, DESY, Hamburg, Germany – shut down in January 2013) and extrapolated to T_g. A crossover in $Ge_{15}Te_{85}$ ($T_e = 658$ K): The data points are vertically displayed by –0.2 for clarity. The present X-ray measurements (red open circles) were carried out at the ID11 beamline at the European Synchrotron Radiation Facility (ESRF, Grenoble, France), and the data were obtained by cooling the alloy at a rate of –5 K min^{-1} (experimental details can be found in Ref. [187]) The data (open squares) of Wei *et al.* [165] are for the glass (measured on heating at a rate of 20 K min^{-1}), and for the high-temperature and supercooled liquid (obtained on cooling at –20 K min^{-1}); carried out at the X-ray P02.1 beamline, PETRA II, DESY, Hamburg, Germany. The shaded area highlights a temperature range of "no-man's land" at $\approx (0.70 - 0.91)T_m$ in which $S(Q)$ measurements of the liquid are hindered by crystallization that can readily be probed by ultrafast calorimetry giving the Arrhenius kinetics in Fig. 4.5b. Single-fragility liquid $Ge_2Sb_2Te_5$ ($T_m = 900$ K): The liquid was measured at the ID11 beamline, ESRF, Grenoble using similar conditions as for $Ge_{15}Te_{85}$ [166,187]. The glass (as-deposited 1–3 μm thick film) is taken from Jóvari *et al.* [192] (measured at the BW5 high energy beamline at HASYLAB, DESY, Hamburg, Germany) and extrapolated to T_g. The solid vertical lines show the structural fragility index $m_{str.}$. *Right-hand absicca:* The temperature-dependent mass density, ρ, of $Ge_{15}Te_{85}$ (stars) is taken from Tsuchiya [197] for the liquid and from Kaban *et al.* [198] for the glass. *Adapted from Weber et al. [166] (**publication #14 – Appendix I**).*

On cooling the liquid, the newly obtained viscosity data (Fig. 4.9) start to diverge at ~750 K from the early data obtained by Herwig & Wobst [136,188] – these have been used in the literature, so far, and can result in a somewhat exaggerated crossover. The temperature-dependent viscosity of $Ge_{15}Te_{85}$ cannot be fitted with single-fragility models, and a wide range of Arrhenius kinetics similar to that of AIST can be distinguished. By invoking a crossover, $\eta(T)$ is described via the generalized-MYEGA model (Eq. 4.2), and restricting the data to the new measured $\eta(T)$, the transposed U_{kin}^{-1} from FDSC ($T_g/T \approx 0.68$–0.78, Fig. 4.5b) and $m = 50$ obtained from conventional calorimetry [164] gives: $\log_{10}\eta_\infty(\text{Pa s}) = -3.130 \pm 0.006, W_1 = (3.1 \pm 0.5) \pm 10^{-4}, C_1 = 330 \pm 60$ K, $W_2 = 0.56 \pm 0.06$ K^{-1}, $C_2 = 4{,}060 \pm 80$ K, and $R^2 = 0.9996$ (red solid line in Fig. 4.9) [166]. The fragility of the high-temperature regime is $m' = 98$, reiterating the ratio of $m'/m \approx 2$ [166] also suggested by Wei *et al.* [164] $m'/m \approx 1.8$ (Table 4.1). It can immediately be understood that the sluggish crystallization in the eutectic non-PCM $Ge_{15}Te_{85}$ contrary to the fast GeTe [199] stems from the strong behaviour of the supercooled liquid in the range of $T_g/T = 0.75 - 1$. Although the liquid $Ge_{15}Te_{85}$ viscosity is lower

than that of the liquid GeTe at $T_g/T \approx 0.65 - 0.70$, it already falls into the regime of very low thermodynamic driving force, tending to zero, for crystallization, resulting in sluggish kinetics.

The temperature-dependent structural factor in $Ge_{15}Te_{85}$ shows a complex behaviour. Unlike for GeTe, some amount of supercooling can be achieved $\Delta T_m \approx 70$ K (down to $0.9T_e$) [165]. On cooling the liquid, a divergence of $S(Q_1) - T$ from Arrhenius kinetics occurs at $\sim 1.1T_e$ which reflects the same divergence observed in the viscosity dependence (see Fig. 2 in Ref. [166] – publication #9), and it lies in the temperature range ~600–800 K in which the occurrence of the liquid anomaly is known [180–184,193,194]; represented by the density change in Fig. 4.10. The structural fragility index by extrapolating the liquid data is $m_{str.} = 8.2$ or 10.2 by using the present work (red dashed line) or Wei *et al.* [165] data, respectively, indicating that $Ge_{15}Te_{85}$ is effectively stronger liquid relative to GeTe, and $Ge_2Sb_2Te_5$ (see kinetic fragilities in Table 4.1). Upon further cooling, the low-temperature liquid is stabilized, and the diffraction measurements are hindered by the onset of crystallization at $T < 0.9T_m$. Although this region cannot be accessed by *in-situ* XRD, it is readily probed by FDSC (Fig. 4.5b). *The wide temperature range of the Arrhenius crystallization kinetics* $\sim(0.70 - 0.91)T_m$ *superimposes on the "no-man's land" region in the X-ray scattering data providing a strong experimental evidence of a clear correlation between crystallization kinetics, temperature evolution of structure, and viscosity in PC chalcogenides* [166].

Just to note that a similar correlation between the temperature evolution of structure and viscosity could also be seen in $Zr_{60}Cu_{30}Al_{10}$ metallic glass by Georgarakis *et al.* [200]. They could experimentally distinguish two structural regimes, i.e., a strong (at large supercooling) and a fragile end (above T_m) on cooling the liquid, and the interplay between the two fragility ends correlated with a sharp increase in measured viscosity. This not only hints at the possible existence of a crossover in that liquid but reiterates the correlation between $S(Q_1) - T$ and $\eta(T)$ possibly being generally applicable to a variety of glass-forming liquids.

4.2.3. Role of a crossover in nucleation- and growth-dominated crystallization and implications for memory operation

The effects of liquid fragility on the crystallization kinetics, predominantly on crystal-growth rate, have been studied for a wide range of glass-forming liquids (Ref. [13] and references therein), but understanding the role of a fragile-to-strong crossover has been limited to a few systems up to now with water being probably the most thoroughly studied liquid [170,201].

The different crystallization mechanism of *nucleation*- (prototyped by GST) and *growth*-dominated (prototyped by AIST) PC chalcogenides has practical implications for memory operation, especially data recording. In optical disk, Zhou [202] showed that the family of nucleation-dominated systems is faster for erasing larger glassy marks by stochastic nucleation within the amorphous spot. The growth-dominated systems are more suited for erasing smaller glassy spots by growing crystals inwards from the glass/crystal interface. This categorization is the foundation for materials selection in PCM applications [203]. Yet, a new category of PC materials may have been emerging recently, represented by the discussed AIST or Sc-doped Sb–Te alloys [158], those with an FSC on cooling and combining the advantages of the aforementioned categories.

We will show in the next Section 4.3. that the maximum in steady-state homogeneous nucleation rate in AIST is up to ~18 orders of magnitude lower than in GST – nucleation is suppressed in the strong liquid; the temperature at which I^{st} reaches its maximum is at $\sim 0.65T_m$ in AIST and $\sim 0.59T_m$ in GST

[42]; the temperature at which U reaches its maximum is $\sim 0.89 T_{\mathrm{m}}$ in AIST [86] (it is shifted to higher relative temperature than it would be expected for single-fragility fast-transforming systems because the maximum is reached in the fragile regime of the crossover) and $\sim 0.76 T_{\mathrm{m}}$ in GST; while $U_{\max}$ is about the same and high ~1 m s^{-1} in AIST [86] and ~2.7 m s^{-1} in GST [85] (Fig. 2.1). The three distinct regimes on cooling AIST liquid, i.e., fragile regime, Arrhenius kinetics, and moderately strong liquid conform to the observations of $U(T)$ and $\eta(T)$ during a crossover in water [201]. All those differences could account for the different crystallization mechanisms in these two PC chalcogenides.

The presence of a crossover upon cooling the PC liquid may also help to meet the contradictory requirements on PCM (Fig. 4.6a). By taking AIST as an example [86,161], the moderately strong liquid ($m \approx 37$, without any role of a decoupling) has a lower propensity for crystallization because of the lower mobility, and, therefore, this can lead to improved long-term data stability in memory and long-term depression in the potency of a synapse [204]. Simultaneously, fast crystallization (SET, writing operation) is maintained because it occurs well within the fragile regime of the crossover ($m' = 74$) at $T_{\mathrm{g}}/T \approx 0.52$ in AIST [86] – a relative temperature at which viscosity of AIST and GST is similar. At $T < T_{\mathrm{m}}$, the viscosity in both systems is low corresponding to that in pure metals [205], and melt-quenching (RESET operation) remains unaffected by the underlying crossover. On the other hand, the presence of a crossover may prevent to use priming for improving PCM performance and this is discussed in the following section.

4.3. Priming of phase-change memory: Classical-nucleation-theory description

In their seminal work, Loke *et al.* [127] demonstrated that by priming PCM device, applying a low-power auxiliary pulse before the main SET pulse, the crystallization speed can be significantly enhanced, and ~500 ps writing time was achieved (cf. ~10–100 ns typical switching time in PCM [206]). They suggested that the improved rate is due to much higher nucleation and growth rates in GST primed layer. In the following paragraphs, we will show that it is the nucleation, not growth, which is greatly enhanced, and provide a quantitative assessment of priming in the view of classical nucleation theory (CNT) – referring to the theoretical background introduced in Sect. 1.2.

Multiple-pulse interactions in PCM are not limited to priming only and are of general interest including the parallel writing of memory arrays [18], and the possibility of undesirable read-disturb [37]. Lee *et al.* [207] showed that priming pulses can reduce not only the duration of the SET pulse necessary for switching but also the total duration of the priming + shortened SET pulses is by up to 33% shorter than for using a single SET pulse. Priming is also beneficial to the total energy consumed which is up to 43% less [18] (**Fig. 4.11b**). The crystallization in primed devices has been considered to be analogous to two-stage heat treatment to calculate nuclei density upon devitrification [18,19,34], and to be of purely thermal origin, arising from Joule heating [207]. The priming pulse must be energetic and long enough to generate subcritical nuclei, but short enough to avoid their growth. Most intriguingly, Lee and co-workers [207] noted that the priming *fades* (substantially, but not totally) if the time delay between the priming and SET pulse is too long; they found a relaxation time of ~1 μs (Fig. 4.11a). In other words, there is a finite time to apply the SET pulse for the priming to be beneficial for PCM performance. The fading was concluded to be intrinsic property of the PC chalcogenide [207], although other effects, such as a raised base temperature, especially for larger memory cells used in Ref. [207], may not be completely ruled out. At the end of the priming pulse, the temperature falls, and fundamental questions arise which are addressed in this section: *What happens to the population of subcritical nuclei?* and *Does the evolution go to lower population (as required to explain the fading)*

or to higher population as predicted by CNT? The evolution of cluster population is understood from the extensive quantitative measurements and modelling of oxide glasses (Fig. 1.3a), and higher steady-state population has been associated with lower temperature, so far. The latter scenario would enhance rather than weaken the effect of priming, and thus, the observed fading during priming appears to contradict the predictions of CNT of the existing glass-forming systems represented by oxide glasses (here we present $Li_2O.2SiO_2$ for comparison).

The thermodynamic and kinetic parameters used for the calculations are presented in **Table 4.2.** Before proceeding with the results of the calculations, the unknown value of σ has to be established, and this can predominantly be done for GST for which several microstructural experimental/modelling studies exist, and $\sigma = 0.03 - 0.1$ J m^{-2} has been indirectly derived and agreed in the literature [133,208–210]. Direct observations of nucleation kinetics, unlike *ex-situ* microstructural studies, are very rare in PC chalcogenides. Kalb *et al.* [131] showed that GST can be supercooled up to $\Delta T = 42.5$ K under a B_2O_3 flux, the nucleation may be heterogenous, and they derived a lower-boundary estimate of $\sigma = 0.04$ J m^{-2}. Burr *et al.* [211] fitted the observed polycrystalline grain size distributions, obtained by TEM, to CNT and obtained $\sigma = 0.06$ J m^{-2}. The energy can also be estimated if the size of the critical nucleus, n^*, is known, which can be suggested by MD simulations. As noted by Lee & Elliott [145], the probabilities of cluster growth and dissolution are roughly equal for clusters composed of 5–10 connected cubes (22–33 atoms for GST at 600 K). By taking the radius of a sphere with volume matching of 8 cubes as the critical radius and noting that $r^* = 2\sigma v/\Delta\mu$ yields $\sigma = 0.05$ J m^{-2}; although the value depends on the defined size of crystallites including or not quasi-crystalline regions in the simulations (larger sizes yield greater σ). We use a value estimated from Eq. 1.4 $\sigma = 0.075$ J m^{-2} [42], which lies inside the expected region, and the calculated I^{st} fits the experimental data by Privitera *et al.* [212] (Fig. 4.13b), for which a best-fit yields $\sigma = 0.077$ J m^{-2} [42]. By taking the constant value of σ and the thermodynamic driving force, Eq. 1.9, the minimum in the nucleation barrier to form a critical nucleus $W(n^*)/k_BT$ occurs at $0.54T_{\mathrm{m}}$ [42].

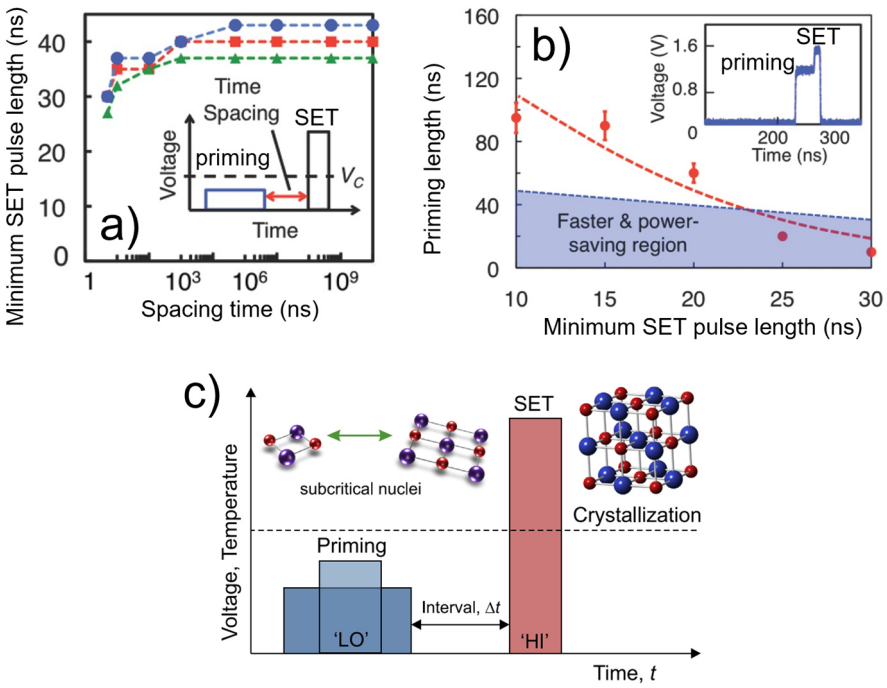

Fig. 4.11 Priming of phase-change memory: The observed fading of the priming effect appears, at first glance, to contradict the predictions of classical nucleation theory. a) Experimental dependence of the minimum SET (1.5 V) electrical pulse length on the time delay, Δt, between the priming pulse (0.9 V & 900 ns) and the SET pulse, in PCM device (the active layer is a 30 nm thick nitrogen-doped $Ge_2Sb_2Te_5$ film [207]). **b)** A combination of priming and the minimum SET pulses to get a fast and power-efficient device. **c)** Schematic illustration of priming mechanism highlighting that the priming pulse generates subcritical (metastable) crystalline clusters that aid the nucleation of the ultimate crystalline structure during SET pulse. 'HI' and 'LO' stand for high and low-power pulses representing SET and priming, respectively. *Parts a and b are reproduced from Lee et al. [207]; part c is from Orava & Greer [42] (**publication #11 – Appendix I**).*

Table 4.2 Thermodynamic and kinetic parameters used for the calculations of the glass-forming systems: $Li_2O.2SiO_2$, $Ge_2Sb_2Te_5$ (GST) and $Ag_{5.5}In_{6.5}Sb_{59}Te_{29}$ (AIST). (T_m– melting point; T_g – glass-transition temperature; T_{rg} – reduced-glass-transition temperature ($= T_g/T_m$); ΔH_m – latent heat of melting per mole; v – monomer volume (i.e., per atom for GST and AIST, and per formula unit for $Li_2O.2SiO_2$); σ– crystal-liquid interfacial energy; $\gamma(T)$ – temperature-dependent atomic jump frequency (calculated by using the Stokes–Einstein relation Eq. 1.7. The theoretical background of the calculations is introduced in Sect. 1.2. *Reproduced from Orava & Greer [42] (**publication #11 – Appendix I**).*

	$Li_2O.2SiO_2$	GST	AIST
T_m (K)	1300 [213]	900 [209]	810 [171]
T_g (K)	728 [13,52,213]	383 [85]	378 [86,161]
T_{rg}	0.56	0.42(6)	0.46(7)
ΔH_m (kJ mol^{-1})	52 [213]	12.13 [209]	16.1 [171]
v (m^3)	9.96×10^{-29}	3.06×10^{-29}	3.08×10^{-29}
σ (J m^{-2})	0.15 [213]	0.075	0.11[a]
	$0.094 + (7 \times 10^{-5})T$ [52][b]		
$\gamma(T)$ (s^{-1})	Refs. [52,214]	$\eta(T), U_{kin}(T)$ [85]	$\eta(T)$ [86]

[a] Kalb *et al.* [171] showed that σ of AIST is greater than for GST, and this is consistent with the relative values of ΔH_m [46].
[b] Here, σ is taken to be constant. Its temperature dependence for GST is unknown. The derived dependence is for lithium disilicate, and its influence on the nucleation barrier in GST is discussed in Ref. [42].

Thermodynamic description. The calculated N^{eq} (a close approximation to N^{st}) in $Li_2O.2SiO_2$ and which is consistent with the earlier work Greer and Kelton [52] – extending the calculation from Fig. 1.3 – is shown in **Fig. 4.12a**. The supercooled liquid region starts at $T_{\mathrm{rg}} = 0.56$, and therefore, the cluster population (by extension, steady-state) associated with priming effects, i.e., higher population at higher temperature (red curves), can only be reached theoretically at temperatures well-below T_{g} ($\leq 0.4T_{\mathrm{m}}$ – a temperature regime not previously considered) and for unphysically small clusters $n < 6$ [42], and can be deemed impossible in $Li_2O.2SiO_2$.

Figure 4.12b shows N^{eq} for GST, and there exists a physically accessible regime in the supercooled liquid state, not available in $Li_2O.2SiO_2$, in which cluster populations can increase as much as ~1–2 orders of magnitude as the temperature is increased from $T_{\mathrm{rg}} = 0.43$ to $0.55T_{\mathrm{m}}$ and vice versa, which is also consistent with the fading of the priming effect when the time delay between the priming and set pulses increases (Fig. 4.11). Indeed, Burr *et al.* [211] may already hint at the existence of such a regime (the inset of Fig. 6 in Ref. [211]), although it is not easy to separate the effects of Φ_{h} and T. By taking $N^{\mathrm{st}} \approx \frac{1}{2}N^{\mathrm{eq}}$ at n^* [1] and considering simple JMA kinetics (Sect. 3.1), already yields theoretical enhancement in the overall crystallization rate by ~0.5–1 orders of magnitude. For AIST (not shown here), the corresponding window relevant for priming/fading is between $(0.47 - 0.54)T_{\mathrm{m}}$, a relative temperature range consistent with GST due to the similar thermodynamic parameters.

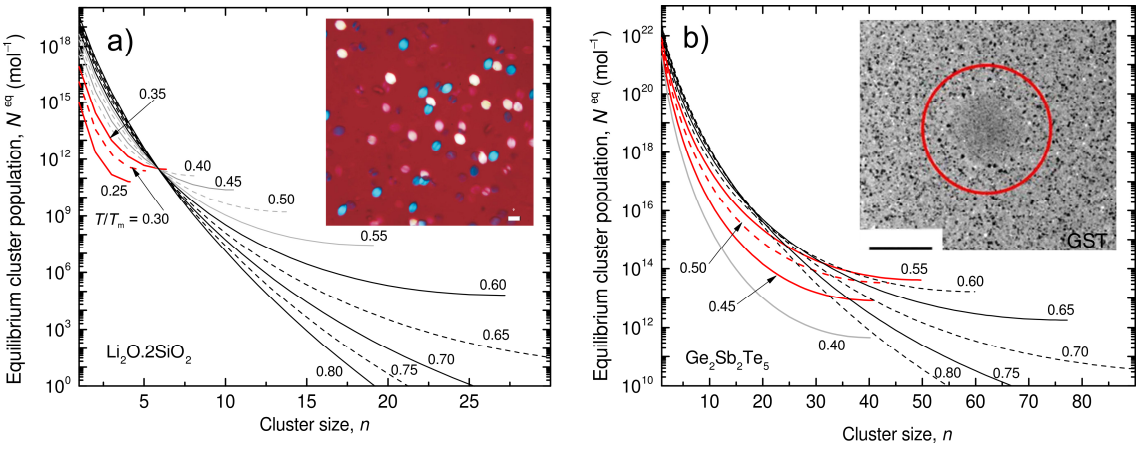

Fig. 4.12 Thermodynamic description of priming (fading) in single-fragility liquids. Calculated equilibrium subcritical cluster size distribution (Eq. 1.5) for crystallites at different homologous temperature (T_{m}/T) is shown for: **a)** $Li_2O.2SiO_2$ ($T_{\mathrm{rg}} = 0.56$); and **b)** $Ge_2Sb_2Te_5$ ($T_{\mathrm{rg}} = 0.43$) liquids. The end points, where visible, of each curve correspond to the critical cluster size, n^*, at a given reduced temperature. The grey curves are for temperatures below T_{g} (Table 4.2), and the distribution is considered to be physically inaccessible – certainly true for lithium disilicate. *The red curves indicate the regime in which lower populations N^{eq} can be associated with lower temperature – priming and fading are possible.* The insets show a comparison of the characteristic microstructure of $Li_2O.2SiO_2$ glass (single-heat isothermal annealing above T_{g}, optical microscopy, polarized transmitted light, the scale bar is 50 μm, *reproduced from Zanotto* [215]), and GST (recrystallized glass at 493 K – highlighted by the red circle – on the background of as-made crystalline phase, the scale bar is 200 nm, *reproduced from Salinga et al.* [98]). *The main figures are reproduced from Orava & Greer [42] (**publication #11 – Appendix I**).*

Kinetic description. In the above paragraphs, we have defined the temperature range in which priming (fading) is physically accessible in GST by controlling the nuclei population, and now, we will consider whether it is kinetically feasible or impractical by calculating the time-scale of the thermodynamic changes. Firstly, we explore whether the temperature-dependent molecular jump frequency $\gamma(T)$ is simply related to viscosity by the Stokes-Einstein relation (Eq. 1.7), or, as for crystal growth, there is some role of decoupling, and $\gamma(T)$ scales somehow with $U_{\mathrm{kin}}(T)$, although in both cases $\gamma(T)$ is matched at T_{m}. **Figure 4.13a** shows the calculated time-lag θ_{n^*} (Eq. 1.8) for the two cases, and their comparison with experimental measurements of isothermally annealed samples, from the first detection of crystallization in transmission electron microscopy (TEM) [57], in reflectometry [13], or in resistometry [58] (all of these data times must principally be longer than the fundamental θ_{n^*}, and have been measured near T_{g} in the range 390–420 K), and from molecular-dynamics simulations [19,55,56] at 600 K and 700 K (the time-lags obtained can be considered to be those at n^*). It should be noted that θ_{n^*} very weakly depends on σ in the studied range ~0.066–0.1 J m^{-2} (not shown here); the magnitude of the difference is comparable to the MD simulation data spread at 700 K ($\sim 0.78 T_{\mathrm{m}}$) shown in Fig. 4.13b. It can be seen, by considering all limitations in experiments and calculations, that there are some difficulties in interpreting the effective activation energy between the calculated data and experiments in the low-temperature region near T_{g}, which also arises from the T_{g} uncertainty. The high-temperature data obtained by computer modelling can be well interpreted by CNT. We strictly consider crystallization from the supercooled liquid, while low-temperature long-anneal data might represent crystallization from the glass – an ongoing dispute about their origin. Nevertheless, taking $\gamma(T) \propto 1/\eta$ spans a wide range matching all literature values, and it is clear that in the process of nuclei formation, unlike in the growth, decoupling does not play any role, although the breakdown in the Stokes-Einstein relation and its role in nucleation deserves further study. In GST, the temperature at which I^{st} reaches its maximum is around $0.59 T_{\mathrm{m}}$ (~530 K) [42] (Fig. 4.13b), which is a characteristic value for metallic-glass-forming systems [35]. The maximum nucleation rate is ~$10^{15}\times$ faster, and $U_{\max}$ is ~$10^{5}\times$ [85] faster than in $Li_2O.2SiO_2$ [38]. Correspondingly the microstructure is ~2–3 orders of magnitude finer in GST than in the oxide glass because it scales as $(U/I)^{1/4}$, and therefore requires TEM to be resolved (refer to the insets in Fig. 4.12 showing the different microstructure).

It is experimentally difficult to directly observe the evolution of subcritical nuclei – possibly fluctuation TEM [216–218] might hint at some early distribution of ordered incipient crystal-like regions in PC chalcogenides. Lee *et al.* [54] studied by MD simulation the atomistic origin of the sluggish crystallization in N-doped GST. Among other effects of N-doping, they highlighted that nitrogen reduces the incidence of nucleation due to topological mismatch effectively increasing the incubation time. Most intriguingly, they provided the first-ever evidence for the formation and dissolution of subcritical clusters (transient states) upon anneal at 700 K (Fig. 4.13c) –this fundamental assumption of CNT is accounted for by the Zeldovich factor (Sect. 1.2.1.).

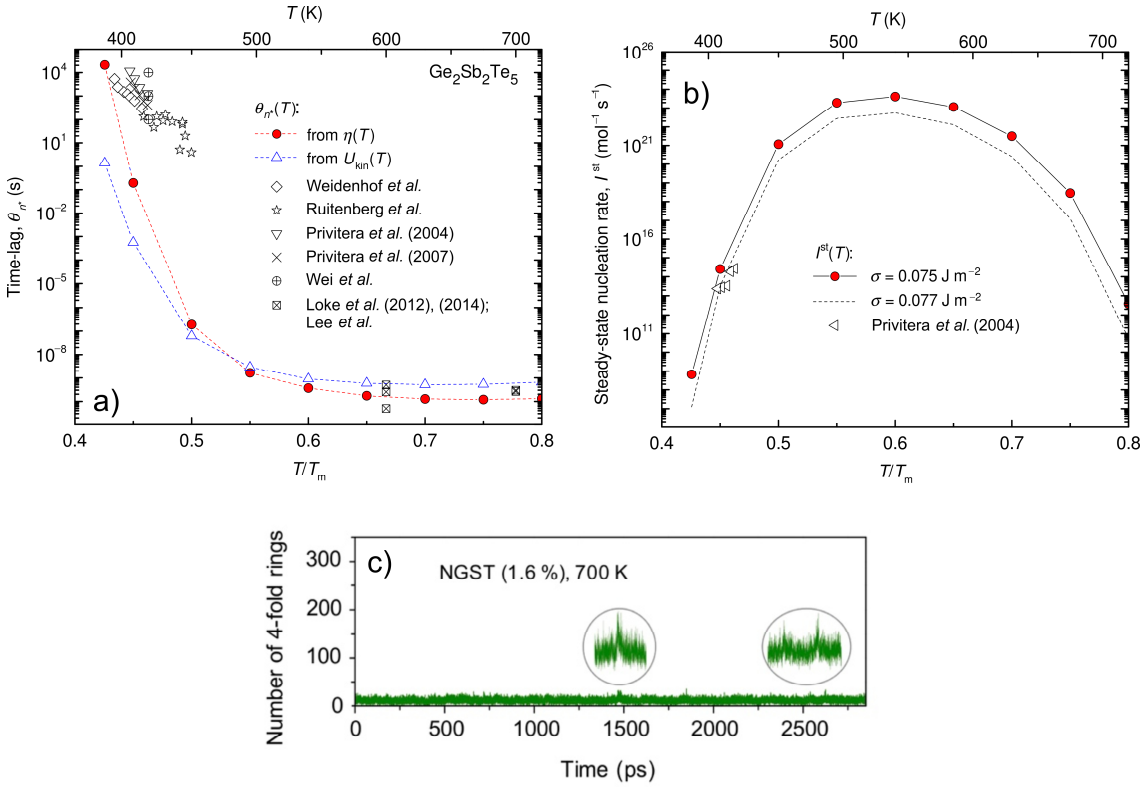

Fig. 4.13 Kinetic description of priming (fading) in single-fragility supercooled liquid $Ge_2Sb_2Te_5$. Nucleation is represented by **a)** the nucleation time-lag, θ_{n^*} (Eq. 1.8), and **b)** steady-state homogeneous nucleation rate, I^{st}, as a function of the homologous temperature (T_m/T). *Part a*: The atomic jump frequency, $\gamma(T)$ – Eq. 1.7, is derived either from the viscosity $\eta(T)$ or from the kinetic coefficient $U_{kin}(T)$ (the inputs are from Ref. [85]) to test the fundamental underlying mobility, and the former one is used for further calculations (see the main text for details). Details of the experimental data are: Weidenhof *et al.* [114] – as-prepared single film, 85 nm thick, optical reflectometry; Ruitenberg *et al.* [219] – as-prepared film, 25 nm thick, sandwiched between Si_3N_4 layers (2 nm thick), *in-situ* TEM; Privitera *et al.* [212,220] – chemically-etched GST, deposited thickness of 50 nm, *in-situ* TEM; Wei *et al.* [149] – as-prepared GST, different thickness 3.5, 10 and 100 nm, sandwiched between ZnS:SiO_2 (50 nm thick) measured by electrical resistometry; Loke *et al.* [127], and Lee *et al.* [54,145] – *ab initio* MD simulations (180 atoms). *Part b*: Using $\gamma(T)$ derived from viscosity, $I^{st}(T)$ is calculated for σ = 0.075 J m^{-2} (Table 4.2); fitting the $I^{st}(T)$ (the black dashed line) to the measured data by Privitera *et al.* (open triangles [212]) yields the crystal-liquid interfacial energy σ = 0.077 J m^{-2}. Considering the experimental errors in σ, the estimated value 0.075 J m^{-2} from Eq. 1.4 is taken to be a good approximation in this work. **c)** *Ab initio* MD simulations of the evolution of the number of four-fold rings during anneal at 700 K in N-doped (1.6 at.%) $Ge_2Sb_2Te_5$. The spike events provide the evidence for the formation and dissolution of subcritical nuclei. *Parts a and are reproduced Orava & Greer [42] (**publication #11 – Appendix I**). Part c is reproduced from Lee et al. [54].*

Implications of priming (fading) and the overall transformation kinetics of on memory performance. Lee *et al.* [207] computed that the rate of crystalline ordering in GST is fastest at 500 K, slower at 400 K and 700 K, and suggested that this must coincide with the maximum in nucleation rate. Fig. 4.13b supports the observations by the authors as similar trends are predicted by CNT. The temperature range at which priming/fading is possible is between 383 K and 490 K in GST. Loke *et al.* [127] estimated the associated temperature rise to be up to ~100 K and take a temperature of 420 K for their MD simulations, which lies in the temperature regime predicted by CNT. The work of Lee *et al.* [207] does not provide any information about the possible temperature rise during priming. Nevertheless, by taking the priming effect which was achieved for ~60 ns long pulse and taking the cluster distribution from Fig. 4.12b, we get a temperature of ~470 K $(0.52T_m)$. That is exactly in the

range where upon ceasing the priming pulse fading would be expected on cooling. The present CNT calculation does not and cannot provide any quantitative information about the origin of the relaxation time ~1 μs [207]. Just for comparison, the required priming times, if physically feasible, in $Li_2O.2SiO_2$ would be ~10^{11} s and longer, which can be estimated by extending the Arrhenius dependence of the time-lag [45] down to the temperature range $(0.25 - 0.35)T_{\mathrm{m}}$ – the theoretical thermodynamic priming region predicted in Fig. 4.12a. Although there are very limited experimental data on the priming effects and the CNT calculations are based on several assumptions, we can conclude that the effects of priming can be qualitatively and quantitatively well described by CNT theory. The early apparent contradiction stems from the fact that such temperature range with the combination of the thermodynamic properties of GST has not been considered before, and likely more systems can possess such a region, possibly, also on the time-scale to be practically studied by conventional techniques.

We can consider the crystallization kinetics in PCM device by taking GST as the active layer. **Figure 4.14** shows the calculated time-temperature-transformation (TTT) and continuous-cooling-transformation (CCT) diagrams based on the data obtained in the preceding sections. Isothermal crystallization data (symbols) obtained from PCM mushroom-type device are from Ciocchini *et al.* [132]. Two theoretical limiting cases are shown in the TTT plot. i) The black part shows device operation assuming that the SET (writing) operation is only growth-dominated, i.e., it does not require nucleation, and the crystallization time should be minimum at the crystal-growth rate maximum at $0.76T_{\mathrm{m}}$ [85]. The minimum measured value of ~100 ns is longer than ~30 ns estimated from purely $U(T)$ by assuming a constant propagating crystal front at a rate of about 1 m s^{-1} across the 60 nm thick active layer. At higher temperatures, the crystallization time should diverge to infinity, but this is not seen in the real device, presumably because the calculated temperature in the device measurements is overestimated [132]. ii) The red part in Fig. 4.14 shows the time-lag obtained from Fig. 4.13a. The device operation is assumed to be predominantly nucleation-driven, and the minimum time-lag is less than 0.1% of the minimum measured crystallization time in PCM. Upon nucleation, many growth centres are generated in the device, thereby reducing the growth distances, and crystallization time, required for writing operation. Alternatively, both scenarios can be considered in terms of the RESET operation (melt-quenching) – the region enclosed by the two curves. The CCT (inset) is calculated from TTT curves, and it predicts critical cooling rate between ~6×10^8 K s^{-1} and ~2×10^{12} K s^{-1} for the PCM cell and θ_{n^*}, respectively [42]. This can also quantitatively explain why the incubation time in melt-quenched samples (higher population of larger quenched-in nuclei) is much shorter than in as-deposited GST films (fewer and smaller frozen-in nuclei) [42,221].

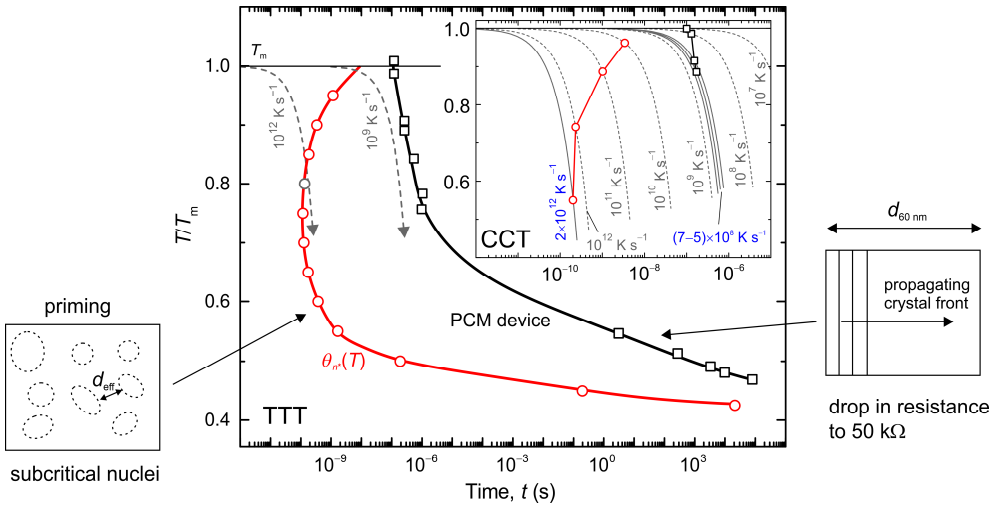

Fig. 4.14 Calculated time-temperature-transformation (TTT) and continuous-cooling-transformation (CCT) – inset – diagrams of supercooled liquid $Ge_2Sb_2Te_5$. *Red part*: The calculated nucleation time-lag $\theta_{n^*}(T)$ is derived from $\eta(T)$ in Fig. 4.13. *Black part*: The PCM device data (squares) are for the SET operation of a cell with a 60 nm thick GST layer by Ciocchini *et al.* [132] and show isothermal crystallization times (defined by the resistance of the memory cell decreasing to 50 kΩ). The microstructure schematics on each side of the main part show the theoretically considered dominant crystallization mechanism, i.e., when the SET operation is nucleation-driven (only spherical nuclei are considered by the calculation) or controlled by the propagating crystal front (no effective nucleation is assumed). For the two scenarios, the calculated CCT diagram indicates critical cooling rate ~2×10^{12} K s^{-1} and ~6×10^{8} K s^{-1}, respectively. The main figure shows traces for constant cooling rate from T_m. *Adapted and modified from Orava & Greer [42]* (***publication #11 – Appendix I***).

The potential role of a crossover in priming (fading), prototyped by AIST. The equivalent of priming in AIST has been demonstrated in optical tester experiments [216,222], but quantitative data on time-lags and nucleation rate are missing. Therefore, we present CNT calculated data in **Fig. 4.15** taking the parameters listed in Table 4.2. The feasible thermodynamic range for priming is up to $0.54T_m$ (~437 K, $T_g/T \approx 0.86$) and falls into the strong side of the crossover. Therefore, the time-lag in the regime of priming with possible fading is ~6–8 orders of magnitude longer, the maximum in I^{st} is up to about 18 orders of magnitude lower, and it is shifted to higher homologous temperature $\sim 0.65T_m$ ($T_g/T \sim 0.72$) than in GST and corresponding to the fragile side of the crossover. It can be concluded that priming in AIST is still possible, but the presence of a crossover, giving it much slower kinetics, is unlikely to be useful in reducing the switching time and the energy consumed in PCM. Priming could still be potentially used in systems with either weaker crossover or where subcritical nuclei may be provided by heterogenous structure, for example, via doping. The calculations again reinforce the distinction between the two crystallization mechanisms, nucleation- (GST) and growth-dominated (AIST) – discussed in Sect. 4.2.3. Just to add to the complexity, Yeo *et al.* [223] observed shorter incubation time in AIST (~50 ns) than GST (~120 ns), when integrated in the memory cell. A complex interplay between many factors, not only the role of the fundamental mobility, has to be understood in detail by considering, for example, chemical (TiN, Al_2O_3 dielectrics cause increase in T_x, while ZnS:SiO (85:15) was shown to have negligible effect on the crystallization temperature in GST [224]) and topological templating, interdiffusion between the active layer and surrounding dielectrics, the active layer thermal history (pre-annealing generates higher population and larger subcritical nuclei and the effect is greater for AIST than for GST [218]), the role of stresses [224] (thickness

decrease of ~5.5% in AIST vs. ~6.5% for GST upon crystallization, and the extrapolated stress in AIST tends to fall to zero at much higher relative temperature than in GST on heating [148]), etc.

It may be concluded that future work exploiting computer-modelling predictions of crystallization behaviour, the size and distribution of subcritical clusters and their kinetics, including modifications of CNT by considering the influence of the electrical field [225] may be useful in guiding materials selection and for quantitative assessment of PCM device operations.

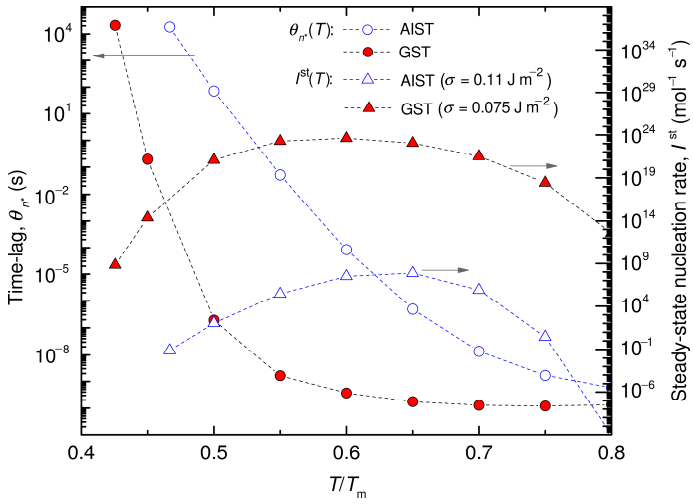

4.15 Comparison of crystallization kinetics in single-fragility liquid GST and liquid AIST with a crossover. a) Nucleation time-lag, θ_{n^*} (*left-hand absicca*), and **b)** steady-state homogeneous nucleation rate, I^{st}, (*right-hand absicca*) as a function of the homologous temperature (T_{m}/T). The fragile-to-strong crossover is taken from [86] (Fig. 4.6a); the data for GST are from Fig. 4.13 Ref. [42]. *Reproduced from Orava and Greer [42]* (***publication #11 – Appendix I***).

Before closing this chapter, let us just briefly comment on another type of emerging solid-state memory which is variously known as nano-ionic, programmable metallic cell (PMC), and **conductive-bridging random-access memory** (CB-RAM) [226]. CB-RAM contains Ag-photodoped thin-film Ge–S ChG as the active layer, and a bipolar switching mechanism is based on nanosecond time-scale reversible conductive filament (CF) formation/dissolution upon the application of a voltage across two electrodes giving the ON/OFF states, respectively. The metallic-filament growth bears some resemblance with the mechanism in PCM, though the CF growth is a purely electronic effect (it remains unclear if any heat is involved). The focus of papers #8 [227] and #13 [228] by Orava *et al.* (**Appendix I**) was to answer the following questions: "*What are the scaling relations, role of stresses, compositional non-uniformity and therefore preferential pathways for CFs formation?*"; and "*How do CFs grow and to what extent do they depend on morphology, branching, electron efficiency etc.*?" These have direct implications for memory performance, such as endurance, retention, writing/erasing currents, and electron efficiency.

By using conductive atomic-force microscopy (AFM) and local-electrode atom-probe tomography (LEAPT), electrical and microstructural properties in lateral and vertical CB-RAM devices were studied. Based on the current characteristics in a lateral device, it was found that Ag migration pathways are structurally "memorized" in the material after the first writing cycle (**Fig. 4.16a**), and the CF formation is then easier in the subsequent cycles [227]. Along the memorized pathways, it was concluded that erasing is ~6–7× faster than the filament growth, and the CF formation has a low electron efficiency of ~9% [227], most current is superfluous. The LEAPT study of a vertical device revealed that the microstructure of the active layer consists of two types of regions, type-I and type-II which are Ag-rich and relatively Ag-poor, respectively [228]. Type-I regions typically extended beyond the LEAPT sampling volume of ~40×40×80 nm^3, and type-II regions were typically ~10–20 nm wide. The Ag-rich parts contain vertically oriented nanocolumns (Fig. 4.16b), ~5 nm wide, with excess Ag existing inside type-I regions and these may represent the preferential pathways for Ag^+ ions migration in CB-RAM. The pathways are inherited from sputtering, and rather unexpectedly are preserved after optically-induced dissolution and diffusion of silver [229], a method of activating the host thin-film Ge–S matrix. The microstructure consisting of the nanometre length-scale highly-oriented nanocolumns is also responsible for the ultra-high resolution of silver-doped ChGs used as inorganic resists in optical lithography [230]. More details about the studies can be found in Refs. [227,228].

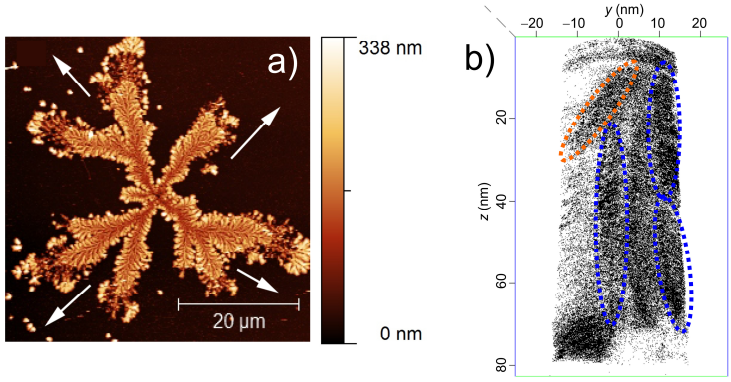

Fig. 4.16 Structurally-memorized pathways in Ag-doped thin-film $Ge_{40}S_{60}$ – an active layer in CB-RAM. a) Atomic-force microscopy image of a re-writing step upon an applied voltage of +7 V on the surface of a lateral device. The conductive filament is established in a first writing cycle, and then it grows along the same memorized pathways which facilitates reversibility. The film is ~300 nm thick and contains about 16 at.% of photodoped Ag. **b)** LEAPT 3-D atomic map of Ag (only 10% of the total detected Ag content is shown) highlighting with the ellipses the oriented nanocolumns with excess Ag existing inside Ag-rich regions in a vertical device (~80 nm thick film containing >10 at.% of Ag). *Part a and b are reproduced respectively from Refs. [227] and [228] (**publication #8 and #13 – Appendix I**).*

5. METASTABLE PHASE TRANSFORMATIONS IN METALLIC GLASSES

5.1. Origins of the high propensity of a metallic glass for metastable phase formation

Metallic glasses (MGs) are of fundamental and technological interest because of their mechanical properties such as large reversible elastic energy storage, high hardness giving excellent wear resistance and high toughness [231]; low-energy-loss soft-magnetic properties [232]; biocompatibility for (non)-degradable implants [233]; or as a spacecraft shielding absorbing the high kinetic energy of debris [234]. Generally, monolithic MGs suffer from poor compressive plasticity and tensile ductility; the elastic strain limit is universally ~2.67±0.02% [26]. Metallic glasses lack atomic periodicity and the microstructure, consisting of structural and chemical inhomogeneities, in MGs cannot be controlled in the same way as in polycrystalline materials, at least not in the standard view of grains, grain boundaries and defects. Typically room-temperature plastic flow in MGs is inhomogeneous [235] and is localized into thin shear bands (SBs) with the initial deformation thickness of ~10–20 nm [236]. The fundamental mobility in SBs can increase up to 8 orders of magnitude [236]. When initiated in locally communicating shear-transformation zones, a single SB can readily propagate via a self-promoting mechanism [236,237] leading to a crack formation and resulting in catastrophic failure of MGs (**Fig. 5.1a**). This limits their application as structural materials [231]. The critical length of an SB is about tens of nanometres and therefore most methods of improving plasticity/ductility rely on inhibiting nucleation and controlling consequent propagation of SB by generating regions forcing shear-band branching and multiplications.

Many techniques have been developed to improve MGs formability [29,31,238–241], among those, methods exploiting the inherent heterogeneities in MGs [242] such as cryogenic thermal cycling [28,29], i.e., manipulation of the glassy states (Fig. 1.1) via non-affine thermal strains, and the formation of MG–crystal composites via flash-annealing [243–245] have been studied by the author – the latter method is the focus of this chapter.

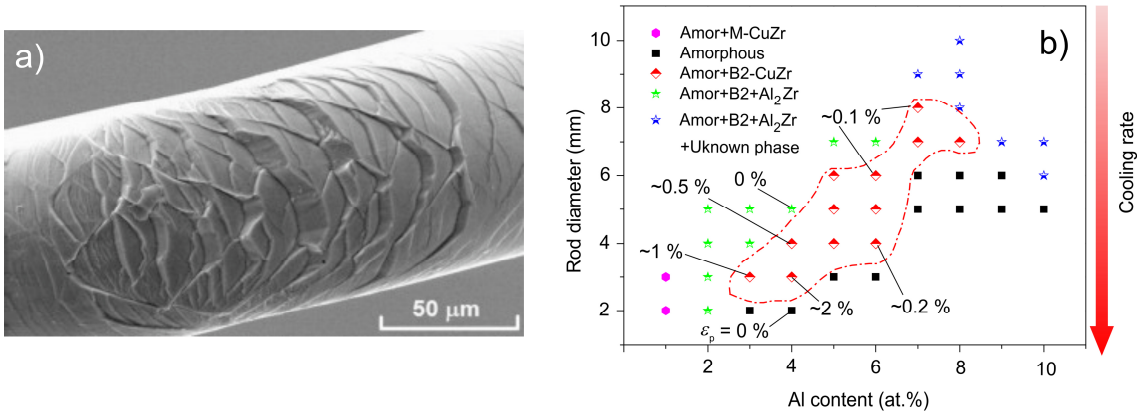

Fig. 5.1 Improving the formability of metallic glasses. a) Surface pattern created by shear bands propagating to the tensile side of a bent Fe-based MG wire (diameter of 100 μm). **b)** Evolution of microstructure in a ternary $(Cu_{0.5}Zr_{0.5})_xAl_{100-x}$ bulk MG after cooling during suction casting. The increasing cooling rate is achieved by decreasing the rod diameter, and the estimated Φ_c is ~200–250 K s^{-1} and ~30 K s^{-1} for 2-mm and 5-mm diameter [246]. The beneficial region to ductility (outlined by the red dashed line) is achieved by the formation of MG–B2 CuZr composite (diamonds); symbols are labelled with the corresponding plastic strain. *Part a is reproduced from Greer et al. [236]; part b is published from Orava et al. [238] (**publication #17 – Appendix I**), which is modified from Wu et al. [247].*

Here, we use $Cu_{47.5}Zr_{47.5}Al_{5.0}$ metallic-glass ribbons, a ternary composition belonging to the entire family of archetype CuZr-based MGs (Fig. 5.1b) used to study the effects of composite type and microstructure on the mechanical properties. A combination of complementary *in-situ* techniques represented by high-energy X-ray diffraction, containerless solidification during electromagnetic levitation (EML), TEM and FDSC, complemented by *ex-situ* LEAPT analysis, allows probing hitherto inaccessible phase evolution in the glass upon fast heating and cooling up to the range of ~10^4 K s^{-1}. In other words, the entire temperature range of the existence of the supercooled liquid could be directly studied, and the kinetic and chemical conditions of the high propensity of the glass for the formation of phase(s) beneficial to the plasticity could be formulated for the first time.

The composite formation (type, size, and fraction of the crystals) is better controlled on heating MGs, giving access to a wide range of heating rates spanning over 8 orders of magnitude, rather than the solidification process on cooling the liquid (Figure 5.1b). Composites formed during fast resistive (Joule) [25] and inductive heating [248], so-called flash-annealing because of high $\Phi_h > 100$ K s^{-1}, contain the metastable B2 CuZr phase (space group $Pm\bar{3}m$ and a prototype CsCl structure) which is *beneficial to the plasticity* [240]. Such composites can achieve a compressive strain of about 10% (crystals: ~10 μm in diameter and ~15 vol.% of B2 phase) for CuZr-based bulk MGs [248]. The B2 phase formation takes place on a millisecond time-scale on heating translating to Φ_h up to the range of ~10^2 K s^{-1}. The B2 CuZr phase can already form on isothermal annealing at 671 K for 20–30 minutes, or upon conventional heating at $\Phi_h \leq 60$ K min^{-1} where $T_x = 706$ K lies far below the forming temperature of ~900 K of the B2 phase in the equimolar CuZr glass [249–251]. So far, the Φ_c range for *in-situ* experimental studies of composite formations has been limited to conventional rates, which are ~2–3 orders of magnitude lower than the Φ_h required and be practical for the low-temperature equilibrium phases, mainly $Cu_{10}Zr_7$ (space group C2ca) and $CuZr_2$ (space group I4/mmm), being hard and brittle, to be suppressed on heating – the critical heating rate was suggested to be ~700 K s^{-1} for $Cu_{47.5}Zr_{47.5}Al_{5.0}$ [25]. Flash-annealing may introduce small crystals ~1.5–2 nm, which is at the theoretical limit of the critical nucleus, that can promote crystallization in MGs upon deformation, thereby also improving plasticity when an optimum grain-size range is reached [252,253]. Here, we do not intend to discuss the relationship between the phase-transformation mechanism therefore the final microstructure and improved ductility, carried out *in-situ* by high-resolution XRD, because this is still an ongoing study – more details are in Refs. [254–261].

The aim is to understand the kinetic and chemical conditions of the high propensity of the glass for the B2 phase formation. At this stage, it is not intended to prepare composites with defined microstructure, phase type and volume content (fraction of the remaining glass and crystals). The goal is to understand the basic phase-transformation principles in a full cycle of heating (re-melting) and cooling. So far, the crystallization (solidification) mechanism, its kinetics and the phase equilibria have been derived for the binary systems, especially $Cu_{50}Zr_{50}$ glass, which represents a too simplified approach. Understanding of phase transformations in more technologically important MGs is needed to clearly define the conditions under which composites with multifaced on-demand properties can be obtained, such as for low-energy-loss soft-magnetic Fe-based-MG–crystal composites [232]. Full details of the results briefly discussed in the following paragraphs can be found in Refs. [238,243–245] (publications #17–19 and #21 by Orava *et al.* **– Appendix I**).

We limit ourselves to demonstrate the phase-transformation mechanism upon **sub and supercritical Φ_h** in vacuum represented by *in-situ* TEM (**Fig. 5.2**) and *in-situ* high-energy XRD (**Fig. 5.3**), respectively. The regime of subcritical Φ_h is dominated by $Cu_{10}Zr_7$ phase formation (Fig. 5.2a and b).

A distinct two-step crystallization with $T_{x1} = 750$ K ($t_{x1} = 2.06$ s) and $T_{x2} = 850$ K ($t_{x2} = 2.35$ s) corresponding respectively to $Cu_{10}Zr_7$ and the B2 (coarsening on continuous heating) phases was revealed (Fig. 5.2a – SAED patterns). Also, the presence of two minor phases could be distinguished from the SAED patterns: i) $CuZr_2$ (the equilibrium low-temperature phase) was mostly detected at the initial stages of heating; and ii) the ternary Cu_2ZrAl was detectable at the cooling onset. On cooling, unlike on heating, predominantly $Cu_{10}Zr_7$ phase coarsening without noticeable B2 growth was observed. The trends in the crystallization mechanism correspond to those obtained by *in-situ* high-energy XRD [243] and FDSC [245], but the kinetics and absolute values are slightly different due to the confined environment; for example, the onset temperature of the primary crystallization is suppressed by about 100 K compared to the crystallization in free-standing ribbon [245].

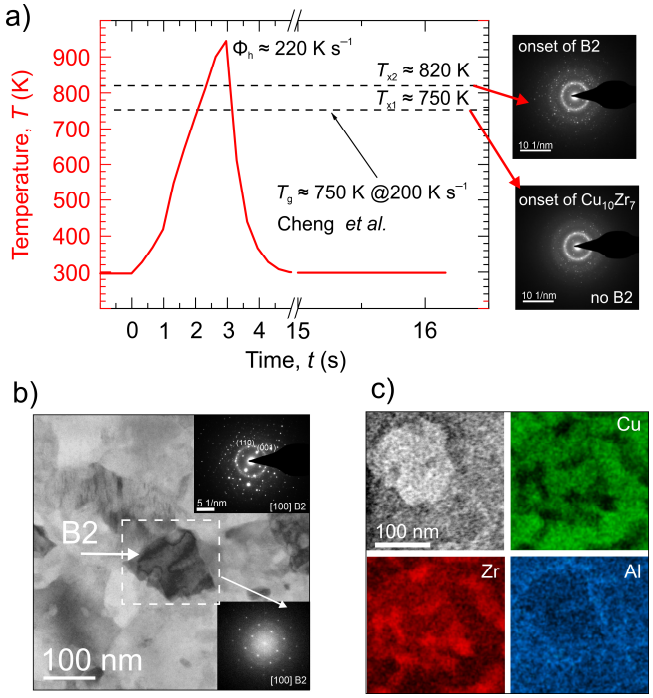

Fig. 5.2 *In-situ* TEM revealing the crystallization mechanism and the final microstructure at a subcritical heating rate of ~220 K s^{-1} in a vacuum. a) Temperature profile of a thin foil (thickness ~50–100 nm) upon phase transformation in a confined volume of ~16×0.05 μm³ (area×thickness) heated in DENSsolutions holder. Two crystallization temperatures T_{x1} and T_{x2} corresponding respectively to the onset of $Cu_{10}Zr_7$ and B2 phase formation – confirmed by the SAED (selected area electron diffraction) patterns shown on the right-hand side – can be identified. The value of the glass-transition temperature, T_g, at the corresponding Φ_h are taken from Cheng *et al.* [245] (Fig. 5.4 – obtained by FDSC; publication #19). The maximum temperature reached on heating is ≈944 K, followed by cooling at ~1,090 K s^{-1}. No thermal drift was observed as in Ref. [108]. **b)** Bright-field STEM (scanning transmission electron microscopy) micrograph SAED (top-right inset) of the final microstructure from part a. A B2 CuZr grain, an area highlighted by the white rectangle and processed by fast-Fourier-transformation in the right-bottom inset, is mostly surrounded by the low-temperature $Cu_{10}Zr_7$ phase. **c)** HAADF (high-angle annular dark-field scanning) image and the corresponding elemental distribution (measured by EDX analysis – energy dispersive X-ray) of the area from part b (Cu: green; Zr: red; and Al: blue). *Reproduced from Orava et al. [243]* ***(publication #21 – Appendix I)***.

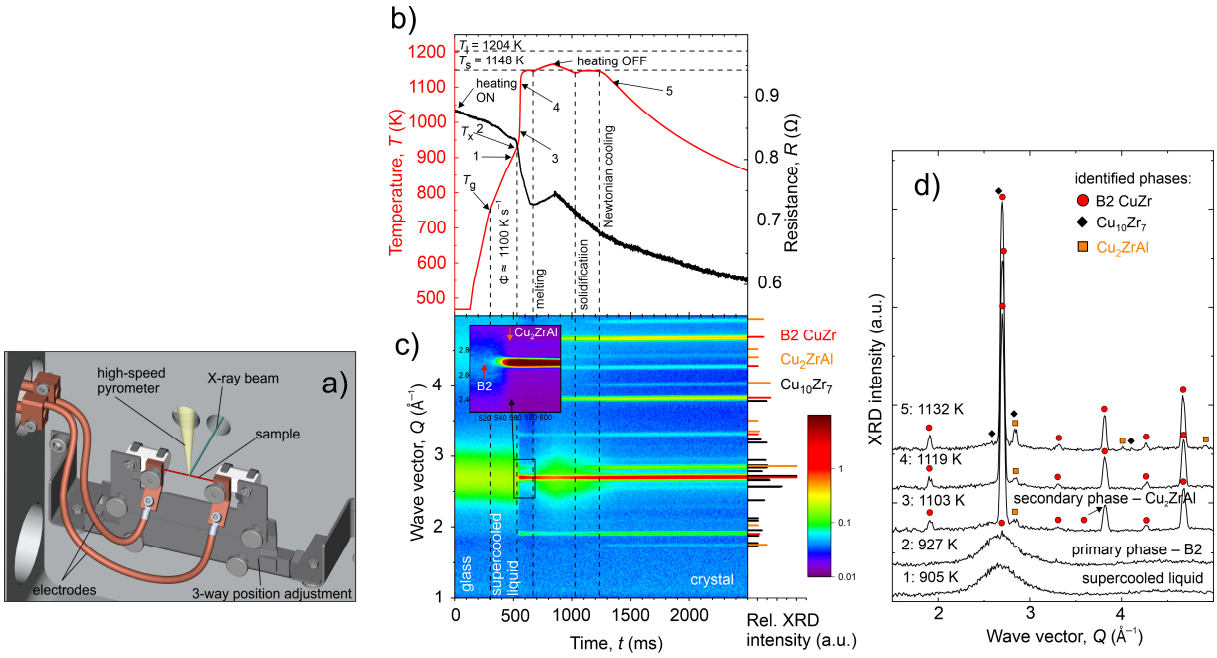

Fig. 5.3 Flash-annealing and *in-situ* high-energy X-ray diffraction of metallic-glass $Cu_{47.5}Zr_{47.5}Al_{5.0}$ at a supercritical heating rate of 1,100 K s^{-1} in a vacuum. a) Schematic of the custom-built flash-annealing device [244] placed at the P21.1 beamline DESY (wavelength of 0.1204 Å), Hamburg, Germany. A constant-current mode resistive heating is synchronized with the beam, and X-ray scattered intensities are captured by using a hybrid pixel Dectris PILATUS3 X CdTe 2M detector (pixel size 172×172 μm²) operated at 250 Hz (cooling is done either in vacuum or in a chamber flushed with He). The ribbon is ≈30 μm thick and ~2 mm wide. **b)** Time evolution of temperature (red) and resistance (black) upon flash-annealing. (T_s – solidus temperature; T_l – liquidus temperature). The vertical dashed lines mark different transitions and stages during heating and cooling. The initial cooling rate is ~300 K s^{-1} in a vacuum. **c)** The correlated temporal evolution of high-energy X-ray patterns on heating and cooling. The inset shows a close-up of the crystallization onset around T_x for B2 (red arrow) and Cu_2ZrAl (orange arrow) phases. *Right-hand part*: The relative X-ray intensities are normalized to the highest-intensity peak. For clarity, only selected $Cu_{10}Zr_7$ diffraction peaks are plotted. The patterns are taken as: ICDD PDF number 00-047-1028 for $Cu_{10}Zr_7$ phase; ICSD collection code 103163 for B2 phase; and ICSD collection code 656062 for Cu_2ZrAl phase. **d)** Selected XRD patterns showing the different stages of crystallization and phase transformations. The brittle equilibrium low-temperature $Cu_{10}Zr_7$ and $CuZr_2$ (not identified in the patterns) phases are suppressed and the B2 phase becomes dominant on supercritical heating giving enhanced plasticity. Full symbols label the position of the most pronounced peaks of the corresponding phases identified by Rietveld refinement The labelled points correspond to the overall time of 1: 489 ms; 2: 520 ms; 3: 552 ms; 4: 566 ms; and 5: 1,300 ms. Source data of the XRD patterns are freely accessible on https://doi.org/10.24435/materialscloud:nn-38. *Part a is published from Orava et al. [238] (**publication #17 – Appendix I**); parts b–d are reproduced from Orava et al. [243] (**publication #21 – Appendix I**).*

On supercritical heating (Fig. 5.3), the $Cu_{10}Zr_7$ crystallization is suppressed, and B2 is the primary phase. Because of the high temperature reached the ternary high-temperature Cu_2ZrAl phase (τ_4, space group $Fm\bar{3}m$) forms as the secondary phase (it can be obtained on isothermal annealing at temperatures between 1,000 K and 1,100 K [262,263], or at $T_x = 861$ K on heating $Cu_{46}Zr_{46}Al_8$ glass at 20 K min^{-1} [264]). The appearance of the ternary phase is not driven kinetically, but by the temperature reached, and the lowest temperature at which the ternary phase formation could be resolved by the high-energy XRD was about 890 K [243]. This lower limit also conforms to the Cu_2ZrAl detected by *in-situ* TEM at >900 K. Upon re-melting and cooling, $Cu_{10}Zr_7$ formed at $T = 1{,}132$ K and B2 continuous growth was observed until ~1,100 K. Independent of heating, cooling rate and achieved supercooling ΔT_l (details of solidification studied by EML are discussed in Ref. [243]), no eutectoid

reaction $Cu_{10}Zr_7 + 3CuZr_2 \rightarrow 13CuZr$ [265] could be detected as would be expected from the $Cu_{50}Zr_{50}$ glass phase equilibrium; all phases formed directly from the supercooled liquid.

The **correlation between kinetics and crystallization mechanism** mapped by the multi-technique approach combining conventional and fast DSC, flash-annealing (resistive heating), and *in-situ* high-energy X-ray diffraction is summarized and represented by a CHT diagram in **Fig. 5.4**. For subcritical heating rate $\Phi_h < 500$ K s^{-1}, the primary crystallization is predominated by $Cu_{10}Zr_7$ phase formation. When $\Phi_h > 500$ K s^{-1} and higher, the formation of the low-temperature $Cu_{10}Zr_7$ and $CuZr_2$ (not unambiguously resolved on heating, but clearly identified by *in-situ* XRD during cooling in EML) is suppressed, and the metastable B2 becomes the primary phase up to the measured $\Phi_h \sim 1{,}500$ K s^{-1} by *in-situ* XRD, and likely extends up to the critical heating rate of 10,000 K s^{-1} to avoid crystallization obtained by the flash-annealing [245]. The critical heating rate is about 2 orders of magnitude higher than a critical cooling rate of ~100 K s^{-1} of this glass [245]. The asymmetry is typical for glass-forming liquids and arises from a higher $N^{\mathrm{eq}}(n, T)$ (Eq. 1.5) in a glass than in a liquid [266], in other words, more and larger frozen-in nuclei are present in the glass than in the liquid increasing the propensity for crystallization on heating. The nose around 1,000 K corresponds to the position of polymorphic $U_{\max}$ at $T_{\max} \approx 1{,}025$ K $(0.89T_m)$ estimated by using the empirical relation presented in Fig. 2.3b, and to $T_{\max} \approx 1{,}000$ K $(0.87T_m)$ calculated by computer simulations for the B2 growth in the supercooled liquid [267]. This suggests the crystallization to be growth-dominated in $Cu_{47.5}Zr_{47.5}Al_{5.0}$ bearing the similarity with the mechanism in the binary $Cu_{50}Zr_{50}$ glass [265]. FDSC data in Ref. [245] do not provide any evidence about the formation of the ternary Cu_2ZrAl phase. Nevertheless, an FDSC trace at $\Phi_h \approx 1{,}500$ K s^{-1} (see Figure 2a in Ref. [245]) reveals a possible two-step phase-transformation scenario, and by deconvoluting the peak into two gives a potential second onset temperature around 950 K, which coincides with ~960 K at ~1,100 K s^{-1} in Fig. 5.5, and thus, feasibly hints at the presence of the ternary phase in the FDSC traces as well.

Fast DSC allows to readily study isothermal annealing, and a TTT diagram of the glass is constructed in **Fig. 5.5**. The TTT plot has two noses at ~850 K $(0.74T_m)$ and ~950 K $(0.83T_m)$ (the measurement is limited up to about 1,000 K, a temperature above which the MEMS sensor breaks). For $T \leq 843$ K, primary, T_{x1} (solid symbols), and secondary, T_{x2} (open symbols), transformations are observed. FDSC does not provide any evidence about the phase evolution, but based on the *in-situ* study above [243], we can conclude that this temperature regime corresponds to the dominant formation of the low-temperature equilibrium $Cu_{10}Zr_7$ as the primary phase followed by the growth of the B2 phase. For $T > 850$ K only one transformation event is observed, and the temperature of the second nose falls into the region of $U_{\max}$ in the B2 phase growth.

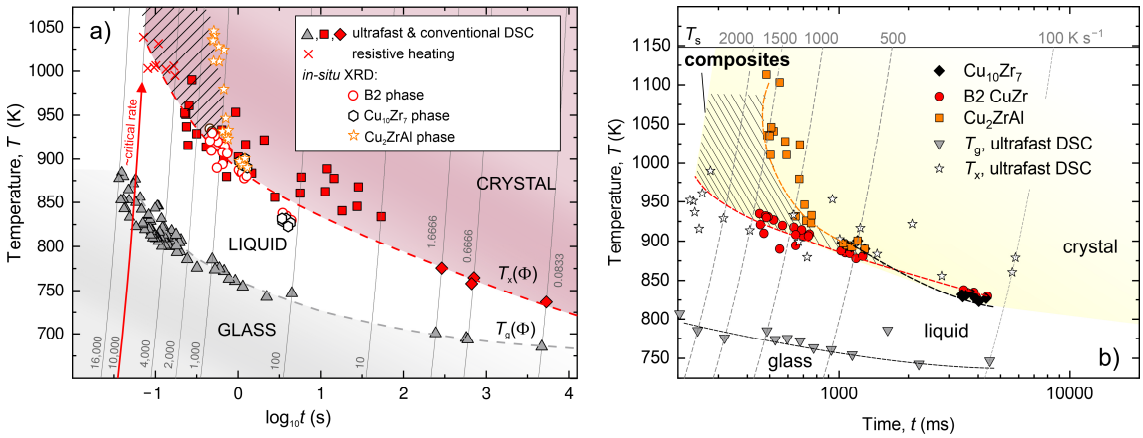

Fig. 5.4 Correlation between the kinetics and mechanism of phase transformation represented by a continuous-heating-transformation (CHT) phase diagram in the supercooled liquid $Cu_{47.5}Zr_{47.5}Al_{5.0}$. The CHT plots are constructed by combining the experimental data obtained by FDSC, *in-situ* high-energy XRD and flash-annealing (resistive heating). Only the glass-transition temperature, T_g, obtained by FSDC are shown because this can be measured more accurately than by flash-annealing. Part b shows a close-up view of the temperature region corresponding to the range of heating rate of 100–2,900 K s^{-1}. The hatched area highlights the range of heating rates beneficial to the plasticity/ductility, a range dominated by the B2 phase growth by suppressing the low-temperature $Cu_{10}Zr_7$ and the high-temperature ternary Cu_2ZrAl phase on heating. The plotted heating rates are in K s^{-1}. *Part a is modified from Cheng et al. [245] (**publication #19 – Appendix I**), and part b is reproduced from Orava et al. [243] (**publication #21 – Appendix I**).*

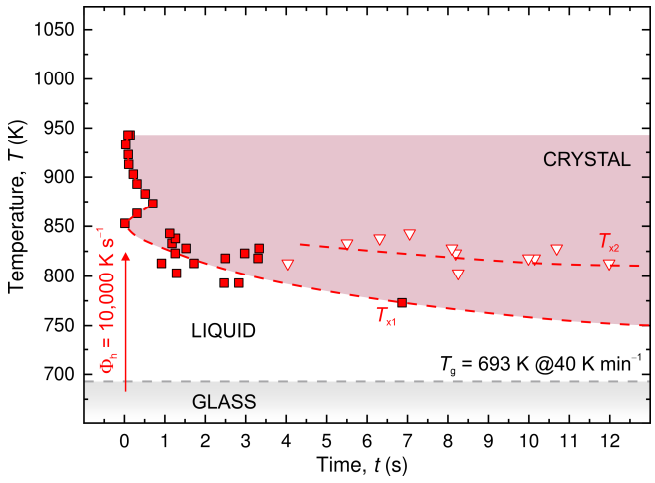

Fig. 5.5 A double-peak time-temperature-transformation (TTT) diagram for the crystallization of supercooled liquid $Cu_{47.5}Zr_{47.5}Al_{5.0}$ measured by ultrafast calorimetry. The temperature of the primary, T_{x1}, and secondary, T_{x2}, (detectable below $T < 850$ K, only) crystallization are shown by the solid and open symbols, respectively. Prior to isothermal anneal, the glass was rapidly heated at a rate of 10,000 K s^{-1}. The dashed lines are to guide the eye only. *Reproduced from Cheng et al. [245] (**publication #19 – Appendix I**).*

The **microstructure** and **composition** of the glass–crystal composites were studied by TEM (Fig. 5.2) and LEAPT (**Fig. 5.6** – the glass thermal history conforms to that in Fig. 5.3). Representative microstructure obtained under supercritical-heating condition is shown in Fig. 5.6a. Both TEM and LEAPT showed that only B2 phase composition corresponds to the expected 1:1 atomic ratio. All the remaining phases crystallographically correspond to the phases noted above, but the local composition is different – for simplicity, the stoichiometric compound nomenclature has been used.

The *in-situ* TEM (SAED in Fig. 5.2b, top-right corner) and Kikuchi mapping (Fig. 5.6b – spheroidal B2 crystals containing $Cu_{10}Zr_7$ dendrites in the centre) show that the final microstructure, even after the heating conditions which should result in fully-crystalline samples, remained partially amorphous. In TEM, these amorphous regions probably separate B2 crystals from $Cu_{10}Zr_7$ grains. The surface-nuclei density, calculated *in-situ* from a high-speed video camera [244] was nearly constant ~(0.2 to 1.2)×10^5 m^{-2} in the range of $\Phi_h = 50 - 950$ K s^{-1} [243] which conforms to the observed tendency of independent surface-nuclei density on isothermal annealing in some oxide glasses [268]. On the other hand, the volume-nuclei density decreased from 1.23×10^{17} to 2.63×10^{16} m^{-3} with increasing Φ_h [243], which contrasts with the usual trend, at least within the range of conventional Φ_h, but is similar to the dependence reported by Kosiba *et al.* [248] for flash-annealed $Cu_{44}Zr_{44}Al_8Hf_2Co_2$ bulk MG, who suggested a lower effective nucleation rate during flash-annealing than for steady-state conditions. A small amount of $CuZr_2$ phase could be identified by Kikuchi mapping – highlighted in blue Fig. 5.6a – together with the commonly-found $Cu_{10}Zr_7$ and B2 phases. Different microstructural features were resolved by LEAPT. Two types of Zr-rich precipitates were found in the B2 matrix: i) spheroidal particles up to ~20 nm in diameter with Cu:Zr atomic ratio of ≈0.36 (Fig. 5.6b); and ii) in same LEAPT samples eutectoid-like structures (lamella thickness of ~5 nm) of alternating lamellae with nearly equiatomic CuZr and Cu:Zr ≈ 0.67 ratio. The latter is close to that in Cu_5Zr_8 and whose existence is still unclear in CuZr glass [249]. Zr-rich precipitates (Cu:Zr ≈ 0.73) could be identified at the interface between B2 phase and $Cu_{10}Zr_7$ dendrites (Fig. 5.6c). The Cu-rich phase at the interface has a ratio of about 1.21, which suggests a slight Cu-deficiency of the nominal $Cu_{10}Zr_7$ phase with the ratio of 1.43. The LEAPT microstructure analysis revealed that there is a tendency to the equilibrium phases formation, namely $Cu_{10}Zr_7$ and $CuZr_2$, but because of the fast heating/cooling the frozen-in phases represented some transient (metastable) compositions. Both TEM and *in-situ* XRD only hint on the presence of $CuZr_2$, but its absence on heating would contradict, for example, FDSC measurements evidence the eutectoid reaction in a thin-film CuZr glass for Φ_h as high as 21,000 K s^{-1} [265,269].

Most importantly and intriguingly, precipitation of Al around the B2 crystals was detected by both microstructural studies, i.e., by TEM in Fig. 5.2c – bottom-right image, and by LEAPT in Fig. 5.6d. In TEM, the Al-enrichment was observed around the nanoconfined B2 crystal and the thickness of the enriched regions was <10 nm. LEAPT revealed Al-enriched precipitates with a diameter <10 nm containing up to ~12 at.% of Al and these were typically found at the internal boundaries within the B2 phase.

Under what conditions does the metastable B2 form? For the binary CuZr glass, Cullinan and Kalay [249–251] suggested the crystallization mechanism at conventional Φ_h or under isothermal conditions. They suggest that once the primary $Cu_{10}Zr_7$ grows, accompanied by a solute partitioning giving Zr-enriched glass, then $CuZr_2$ (<20 nm thick) can form around the $Cu_{10}Zr_7$ crystals and templates the B2 phase growth already during the primary crystallization event at temperatures far below 900 K. For ternary glasses and flash-annealing, the suggested mechanism has limited validity and the *in-situ* high-energy XRD did not reveal any eutectoid transformation [243]. To obtain a maximized fraction of the B2 phase on heating, a minimum Φ_h of ~1,500 K s^{-1} has to be applied, giving a relatively narrow temperature range of ~200 K before melting the crystals (Fig. 5.4).

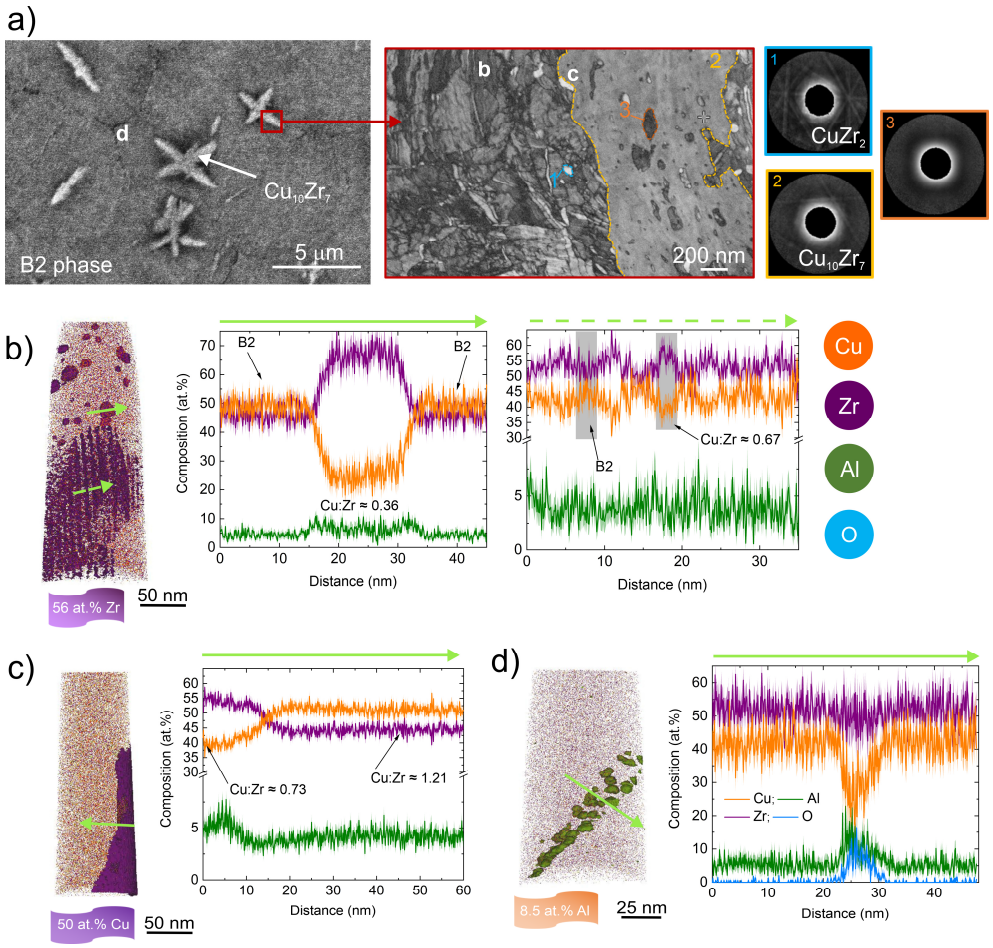

Fig. 5.6 Local-electrode atom-probe tomography (LEAPT) reconstruction of the local microstructure after flash-annealing a supercritical heating rate of ~900 K s^{-1} in a vacuum. a) From *left-to-right*: i) SEM micrographs of an area from which LEAPT samples were obtained. ii) Transmission Kikuchi diffraction image map of an interface between $Cu_{10}Zr_7$ (the region enclosed by the yellow borderline) and B2 phase (uncoloured) containing a small fraction of $CuZr_2$ phase (the region enclosed by the blue line). The letters indicate different regions of LEAPT samples and whose reconstructions are shown in the corresponding figure parts b–d. iii) Kikuchi patterns taken from the mapping in the middle ($CuZr_2$: blue; $Cu_{10}Zr_7$: yellow; amorphous regions: orange). Some regions contained unindexed crystallization phases because mapping with extremely low confidence indexing was excluded. **b)** Reconstructed 3-D atom map and the corresponding 1-D concentration profiles showing a local eutectoid microstructure. **c)** 3-D atom map and the corresponding 1-D concentration profile of a local microstructure dominated by $Cu_{10}Zr_7$ phase. **d)** Reconstruction and 1-D concentration profile evidencing the presence of aluminium precipitation within the B2 crystal. The LEAPT was operated in a laser pulse mode, a repetition rate of 125 kHz, pulse energy of 40 pJ, and sample temperature 60 K. *Reproduced from Orava et al. [243] (**publication #21 – Appendix I**).*

The high propensity of the glass for the B2 phase formation originates from the following conditions: i) kinetics – higher Φ_h suppresses partitioning and promotes polymorphic crystallization; ii) chemistry – on the other hand, a kinetic mechanism of very local nanometre length-scale Al partitioning facilitates the B2 phase growth, which is the only crystallization product composition corresponding to the equilibrium; iii) atomic-packing density – there is effectively no difference in the number density between CuZr B2 crystal (0.0576 $Å^{-3}$) and $Cu_{47.5}Zr_{47.5}Al_{5.0}$ glass (0.0577 $Å^{-3}$) unlike the density different for $Cu_{10}Zr_7$ (0.0609 $Å^{-3}$) and $CuZr_2$ (0.0518 $Å^{-3}$) phases which are ≈5.5% and ≈10.2% smaller, respectively [270], and whose growth might be accompanied by a significant rise in local stresses; iv) atomic structure – a structural study by Kaban *et al.* [270] showed that there is a close

resemblance for the Cu–Zr atomic pairs in the first-coordination shell of the glass and the B2 phase. The idea of the high propensity can also be supported by the work of Guo *et al.* [271] who showed that nanocrystalline B2 phase can be obtained through thermal cycling of the ternary glass between room and liquid-nitrogen temperature, in other words, enough mobility is gained to promote B2 growth.

5.2. Compositional changes accompanying shear bands formation in a metallic glass

So far in our discussion, we have ignored any potential compositional changes in MGs associated with strain localization due to shear bands formation and propagation. This is because, in the flash-annealed glass studied above, no SBs could be identified due to the very high-volume fraction of crystals (Fig. 5.6a), and the ribbons were not plastically deformed – the latter is an ongoing study.

It is known, mostly by STEM-HAADF, by synchrotron X-ray tomography and by nanobeam X-ray fluorescence that there exist periodic spatial fluctuations in density along SBs as shown, for example, for Al-based [272], Pd-based [273,274], Zr-based [273,275,276], and Mg-based [273] MGs. Our focus here is on e-beam techniques; dark-field intensity corresponds to a resultant atomic contract, and the fluctuations originate from the combination of local compositional changes and mass-density variations. Therefore, correlative LEAPT experiments were carried out to distinguish the two contributions. An $Al_{85.6}Y_{7.5}Fe_{5.8}$ (the bulk composition measured by LEAPT; the remaining ~1.1 at.% accounts for trace elements) MG is chosen because the intensity fluctuations have been well-studied by TEM, though the corresponding composition has not been analysed except an attempt by Rösner *et al.* [276] by using STEM-EDX resulting in high inaccuracy. The composition is not complex making the LEAPT analysis straightforward for the comparison with TEM measurements. For example, mass-density changes of −9% and +6% with an average wavelength of ~50−100 nm in <10 nm thick SB were observed in $Al_{88}Y_7Fe_5$ ribbon cold-rolled to about 72% of its original thickness [272].

A STEM-HAADF imaging of a plastically-deformed ribbon revealed a network of interconnected SBs (**Fig. 5.7a**). The variation in bright (higher atomic contrast; brown arrows) and dark (lower atomic contrast; yellow arrows) regions of a length >50 nm in a ~10 nm thick SBs conforms to the previous reports by STEM-HAADF [272,274,276]. A correlative LEAPT (Fig. 5.7b) reveals that the dark and bright regions are predominantly associated with Al-rich (red coloured) and Al-depleted (blue coloured) regions. The Al content changes to ~91.7±0.4 at.% and ~81.0±0.8 at.% in the rich and depleted regions, respectively (Fig. 5.7c and d). Al-based MGs are prone to form nanocrystalline fcc Al upon plastic deformation even at room temperature [277,278]. No crystalline phases could be identified, although Al-rich clusters, a volume of ~15 nm^3, with the Al content up to about 95 at.% could be resolved [279]. No interdiffusion between the SBs and the adjacent glassy matrix was detected. All compositional changes were localized into SBs illustrating the enhanced atomic mobility within the bands. The effective-diffusion coefficient, the fundamental mobility resulting from the volumetric strain originating from an interplay between the shear-strain driven disordering and thermally-activated relaxation, was estimated by using Fick's first law to be in the range of 10^{-8}–10^{-12} m^2 s^{-1} [279]. The upper limit corresponds to Al self-diffusion coefficient in the melt at 730 °C [280], while the lower bound is for solid-state diffusion slightly above 200 °C [281]! Just to note that a recent work showed that the binary equimolar CuZr glass studied in Sect. 5.1 tends to interestingly form the equilibrium low-temperature $Cu_{10}Zr_7$ and $CuZr_2$ phases in SBs on deformation at room and nominal 80 K temperature [282].

Maybe surprisingly and for interest, another LEAPT sample analysis revealed the presence of two nearly parallel SBs of the opposite Al regions separated by the glass of ~5 nm thick (**Fig. 5.8**).

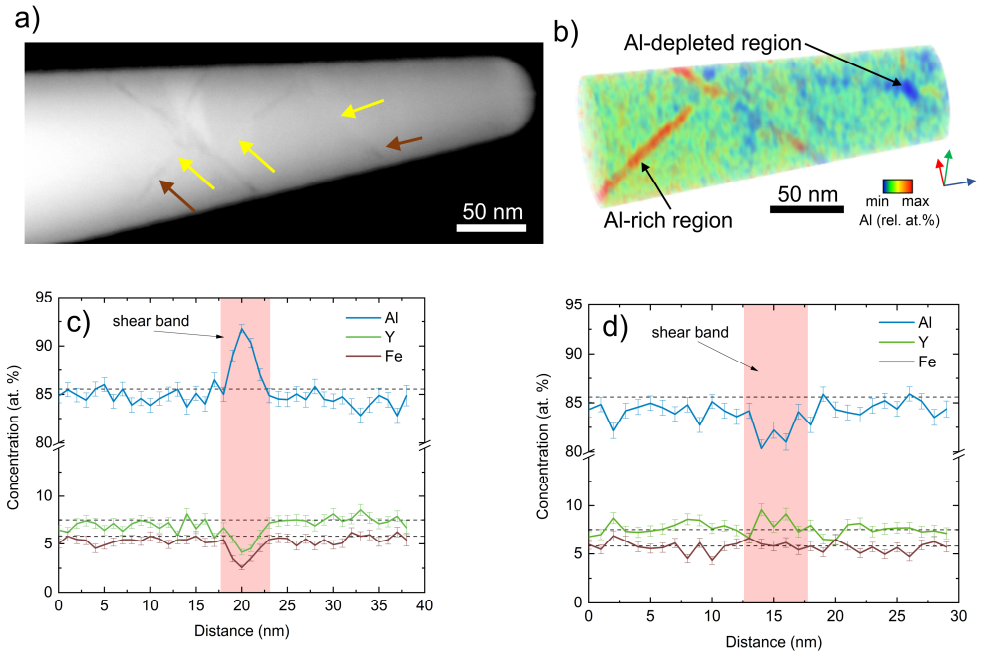

Fig. 5.7 Correlative TEM and LEAPT analysis of shear bands formation in plastically-deformed $Al_{85.6}Y_{7.5}Fe_{5.8}$ metallic-glass. a) A STEM-HAADF micrograph from a bent region of a ribbon. The arrows mark a network of shear bands with a spatial variation of higher (brighter) and lower (darker) atomic-contrast regions inside SBs. **b)** Correlative-LEAPT 3-D map of the Al concentration fluctuations inside shear bands from the TEM micrograph in part a. **c)** 1-D concentration profile across an Al-rich region inside SB. **d)** 1-D concentration profile across a plane of an Al-depleted region inside SB. The horizontal dashed lines mark the bulk composition The plastic deformation was induced by displacing a free end of a cantilever (2 μm thick, 2 μm wide and 20 μm long prepared by focused-ion beam milling) by 1.12 μm inside SEM equipped with a micro-cantilever test unit. LEAPT sample was taken from a compressive site. *Reproduced from Balachandran et al. [279] (**publication #16 – Appendix I**).*

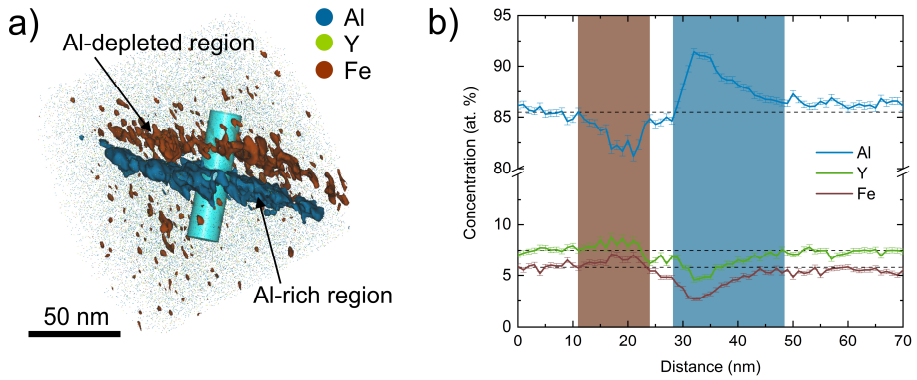

Fig. 5.8 LEAPT reconstruction of two nearly parallel-running shear bands. a) The edge-on perspective of isoconcentration surfaces of Al-depleted (brown volume – Al isosurface volume concentration 84 at. %) and Al-rich (blue volume – Al isosurface concentration of 89 at.%) regions of SBs. **b)** The mean concentration profile across the shear bands by ROI. The horizontal dashed lines show the bulk composition. An $Al_{85.6}Y_{7.5}Fe_{5.8}$ ribbon was plastically deformed by a Vickers nanoindentation method. *Reproduced from Balachandran et al. [279] (**publication #16 – Appendix I**).*

6. REVERSIBLE *ATHERMAL* PHOTOINDUCED EFFECTS IN CHALCOGENIDE GLASSES

Due to the lacking long-range order and a strong electron-phonon coupling at structural defects, chalcogenide glasses are prone to many photoinduced effects, for example, photodarkening, photodissolution of metals, photoplastic effects, and others – see Refs. [7,229,283–289], and references therein. The classification different photoinduced effects is summarized in **Table 6.1**. Many of the photoinduced effects in ChGs are naturally of electronic origin, especially light-driven photoplasticity, although the magnitude and the direction of a change depend on temperature – and appears to be effectively thermally activated, and it becomes difficult to separate the two contributions. There exists only a limited number of studies that have attempted to systematically separate and reveal the role of thermal and electronic contributions and the underlying structural mechanism in photoinduced effects in ChGs. The optical activity of ChGs is facilitated by the presence of so-called valence alternation pairs (VAPs), which are typical defect pairs of under- and over-coordinated atoms, for example, chalcogens and pnictides, with low formation energy. VAPs can easily transform between each other via bond re-orientation, creation and breaking mediated via a self-trapped exciton. The density of the intrinsic VAPs defects in ChGs is ~10^{18}–10^{20} cm^{-3} [284], which is several orders of magnitude higher than, for example, the vacancy concentration in Czochralski-grown monocrystalline silicon [290].

Table 6.1 Classification of the main photoinduced effects observed in chalcogenide glasses (bulks and thin films). The red-highlighted cells emphasize the effects discussed in detail in this chapter. *Adapted from Yannopoulos [284].*

PHOTOINDUCED EFFECTS		
PERMANENT		TRANSIENT
Reversible	Irreversible	
Photodarkening	Photovaporization	Photoviscous effect
Photobleaching	Photopolymerization (*thermally-evaporated films*)	Photopolymerization (*bulk S-rich glasses*)
Photoinduced anisotropy (*birefringence, dichroism, gyrotropy*)	Photomelting	Photoconductivity
Photocrystallization[a)]	Photoexpansion/contraction	Photostructural changes
Photoamorphization[a)]	Photodissolution of metals (*doping, diffusion*)	Optical stopping effect
Photoconductive degradation	Photosegregation of metals	
Polyamorphism	Photoplastic effects (*softening, hardening, deformation*)[b)]	
	Photochemical changes (*oxidation, decomposition*)	

[a)]Also has irreversible part (see Sect. 6.2.)
[b)]Can be (ir)reversible.

In general, structural changes in glasses, induced by light, annealing, thermomechanical processing, implantation etc., can be understood in terms of changing the glass energy (**Fig. 6.1** [26]). Depending on the initial state of the glass, bulks – relaxed systems of low energy, and thin films – unrelaxed system of high energy (excluding ultrastable glasses [291] here), external stimuli (mostly light and annealing in our case) can give either rejuvenation or relaxation. A steady-state condition is reached after a long time of stimulation. For high stimulation rates, such as pulsed lasers or low temperature, the steady-state (enthalpy, entropy, and volume) is higher, and vice versa on low-rate stimulation and high temperature. The energy of the final state depends on the interplay between illumination-induced damage (can also give relaxation) and the amount of repair/relaxation (typically achieved by annealing). The region of intermediate states is most prone to go in either energy direction depending on the details of an external stimulus applied. Although as we will see, the illumination can give more complex states as the energy provided by the light can exceed that of the as-deposited glass giving glassy states corresponding to effectively high cooling rates exceeding 10^{12} K s^{-1}, similar to isoconfigurational glassy states with high mobility mostly studied by computer simulations, providing completely new structural environments which cannot be achieved by standard melt-quenching techniques or even thin-film deposition.

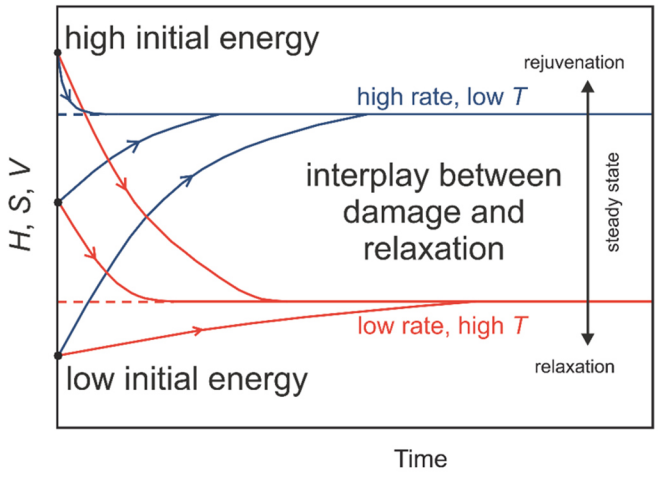

Fig. 6.1 Schematic of energetic stimulation of glasses represented by the change in enthalpy, H, entropy, S, and volume, V, over time upon application of an external stimulus. The solid symbols at the starting time represent glassy states of different initial energy. *Reproduced from Sun et al. [26].*

In the following sections, we will discuss two intriguing reversible photostructural changes, namely, *amorphous-to-amorphous transitions* (AATs) in Section 6.1., although the reversibility necessitates soft annealing, and *athermal photocrystallization* (Sect. 6.2.). Especially the latter one bears some similarity with photoplasticity which is perhaps the most spectacular photoinduced effect in ChGs because it is accompanied by a variety of large shape-changes [292]. Although the early studies on reversible photoinduced changes in ChGs date back to 1970's, the origin and the underlying mechanism of athermal effects remain still poorly understood. We will show that some aspects of the effects may appear to contradict received opinion, yet the apparent challenges (contradictions) can be explained by the unique bonding features in the glasses giving the exciting macroscopic responses. Such photoactivity is of interest in designing active photonic devices [293] exploiting the high-infrared

transparency of chalcogenide glasses extending up to ~27 μm [294], high optical non-linearity (both second- and third-order) [295], and photon up- and down-conversion in rare-earth-ions-doped ChGs [296].

6.1. Amorphous-to-amorphous transitions

Polyamorphism (reversible and hysteretic first-order transition below T_g), analogous to polymorphism in crystals, in glasses is a newly-emerging field and the presence of AATs has now been reported in a variety of glass-forming liquids, such as in oxide glasses [297–299] , metallic glasses [300,301], chalcogenide glasses [302,303], phase-change chalcogenides [304,305], organic glasses [306,307], and water [308]. Unlike in crystals, where both T and pressure are commonly used to control the crystalline phase(s), reversible AATs in glasses have predominantly been reported upon high-pressure (de)compression upon which the short-range and medium-range order changes dramatically. The different low- and high-density phases have mostly been evidenced by a variety of *in-situ* scattering experiments (X-ray, Raman etc.). Recently, thermomechanical processing of metallic glasses provided a new route for controlling and switching between different glassy states and, unlike in complex high-pressure experiments, AATs can readily be detected by observing a shift in the fictive temperature, T_f, by using conventional calorimetry technique [26].

There are very few studies on well-documented photoinduced AATs in ChGs [284], and it remains controversial whether such transitions can actually be true AATs. Usually, there is no direct measurement of changes in density, enthalpy upon transitions in ChGs. In typical effects such as photodarkening and photobleaching, the change in optical functions can be large, though the fraction of atoms involved is rather small ≈2% [309]. In sulphur-rich binary As–S bulk glasses, the fraction of atoms involved in photopolymerization can be extraordinarily high ~20%, represented mainly by the scission of S_8-rings and their polymerization to S_n-chains [310,311]. Those transitions are athermal but are transient (**Table 6.1** – in bulk glasses) and therefore not termed as AATs. It has been suggested that systems exhibiting nanometre length-scale heterogeneity of closely related atomic configurations might be good candidates for AATs because the actinic light could induce transitions between two different atomic configurations with low system energy cost. Yannopoulos, co-workers, and the author of this thesis [312,313] showed by X-ray photoelectron spectroscopy (XPS) that thin-film binary $As_{50}Se_{50}$ glass prepared by pulsed-laser deposition (PLD) has strong nanoscale structural non-uniformity. The unique structure of thin-film $As_{50}Se_{50}$ is also manifested by the appearance of two strong exothermic sub-T_g peaks in glasses deposited by thermal evaporation (TE) [314]. Rather unexpectedly, this highly unrelaxed as-deposited system can further be rejuvenated on illumination or on soft annealing (near T_g) – the dependence on the external stimulus is complex, and both external stimuli give structurally different glasses of higher enthalpy. This composition has become the prototype system for studying athermal reversible photostructural effects.

A comparison between the favourable presence of structural heterogeneities in PLD $As_{50}Se_{50}$ films and the irreversible structural motifs in TE films is demonstrated by the XPS spectra in **Fig. 6.2**. The As3d peaks are characterized by three components [310,311,315] located at the binding energy of: i) ≈41.6±0.05 eV labelled as As^{I}; ii) ≈42.1±0.05 eV termed as As^{II}; and iii) in the range of 44–45.5 eV, denoted as As^{III} that originates from As in AsO_x [312,313]. The former two components are of importance in AATs. The structure of PLD films As_xSe_{1-x}, where $x > 0.4$, consists mainly of $AsAs_{3-i}Se_i$ (i = 0, 1, 2 and 3) pyramidal units. As^{I} then represents As_4 (i = 0) and As_3Se (i = 1) pyramids classified as

the *elemental-like domains* (the instrumental resolution did not allow to separate those two components). The fraction of As atoms contributing to the elemental-like domains was calculated to be between 15% and 20% (of the peak area). As^{II} originates from As_2Se_2 (i = 2) and $AsSe_3$ (i = 3) pyramids forming *stoichiometric-like domains*. The Se3d peak of the PLD films (Fig. 6.2b) consists of a doublet peak at ≈54.1±0.05 eV, labelled as Se^a environment, that represents Se atoms bonded to As in the glassy As–Se matrix. On the other hand, for TE films (Fig. 6.2d), the Se3d peak can be analysed into two components ≈54.1±0.05 eV (Se^a) and ≈54.6±0.05 eV (Se^b) where the latter originates from Se in Se-rich units [310], it forms about 50% of the total Se3d peak area and enhances the fraction of As^I type units resulting in TE films up to ≈30%. *The thermally-evaporated films are more heterogenous than the corresponding pulsed-laser-deposited films, but maybe surprisingly, that does not promote AATs but enhances irreversibility* which we reason below.

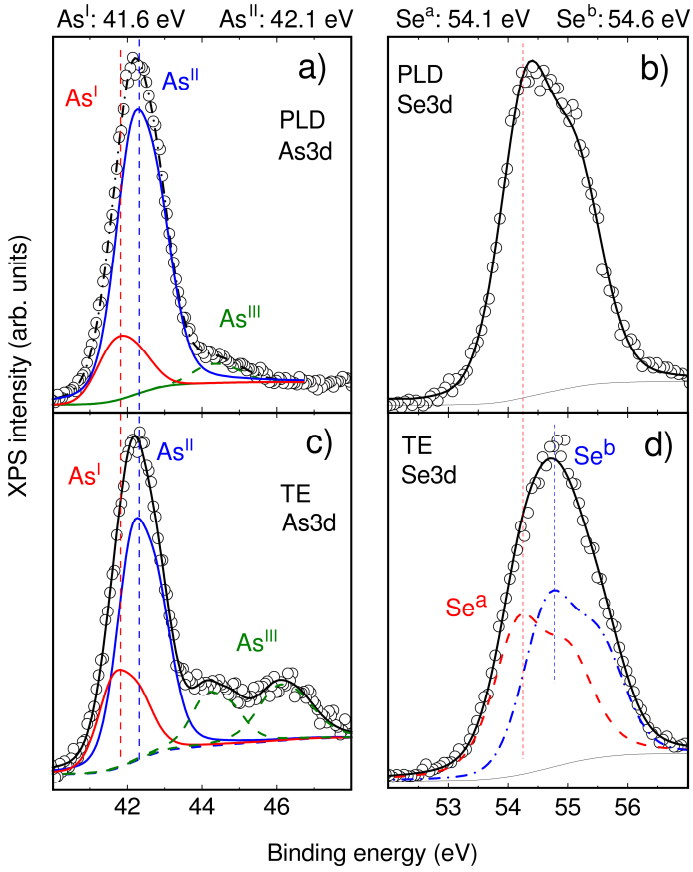

Fig. 6.2 Representative XPS spectra of as-deposited $As_{50}Se_{50}$ films prepared by pulsed-laser deposition, PLD, (top panels a and b) and thermal evaporation, TE (bottom panels c and d). XPS data (open symbols) show peaks deconvolution into Gaussian–Lorentzian peaks (solid and dashed curves) after subtracting a Shirley-type background for As3d (part a and c) and Se3d (part b and d) peaks. Each component of the analysed spectra is the sum of the 3d5/2 and 3d3/2 contributions; the values of binding energy given in the main text correspond to the 3d5/2 peak. *Reproduced from Kalyva et al. [315] (**publication #3 – Appendix I**).*

Here, we explore two types of switching cycles represented by a different order of the initial external stimulus applied: 1) illumination → annealing, 2) annealing → illumination, and correlate the optical responsiveness and structural changes between PLD and TE films during cycling. In this case, unlike for photocrystallization in Sect. 6.2., the AATs are not fully of photoelectronic origin and reversibility necessitates soft annealing near T_g (**Fig. 6.3**).

For PLD films (Fig. 6.3a), the transitions are fully *reversible* irrespective of the initial type of stimulus. Illumination gives rise to $f(\mathrm{As^I})$ creating As–As homonuclear bonds in As_4 and As_3Se structural units. Annealing reduces the fraction by the scission of As–As bonds enhancing the formation of $AsSe_3$ and As_2Se_2 pyramids. A nearly constant value of $f(\mathrm{As^I})$ is reproduced after each stimulation resulting in ≈30% and ≈10% in post-illuminated and post-annealed states, respectively. These values oscillate between the intermediate value of $f(\mathrm{As^I}) \approx 20\%$ in the as-deposited film. A reproducible and strong transient state (film state 1 and 5 in Fig. 6.3a) can be seen resulting in a remarkably high fraction of As–As bonds amounting for ≈40%; exceeding that in the highly disordered as-deposited TE films (Fig. 6.3b). Although the present work does not provide any direct evidence about polyamorphism, we want to emphasize that the exceptionally large change in the participating atoms, i.e., ≈15−20% or more (cf. ~2% in typical photoinduced effects [309]), may suggest the existence of two long-term stable amorphous configurations and therefore the switching is termed as AATs.

For TE films, the initial concentration of As–As "defective" bonds is high ≈30%, and the switching is *irreversible* (Fig. 6.3b). The high fraction of the As homonuclear bonds is inherited from the gas phase which is enriched with As–As molecular structures during TE [316]. In the first cycle, irrespective of the order of the stimulus applied, the trends conform to those in PLD films, yet the magnitude is different. The change in $f(\mathrm{As^I})$ upon illumination is just about ½ of that in PLD, likely because As–As bonds in the as-deposited TE films have already reached their saturation. Annealing results in more severe relaxation than in PLD, although the final fraction of As^I units is the same in both types of films. Upon continuous cycling, the TE films are optically and thermally inactive, even illumination gives relaxation at film state 4, and the elemental As bonds saturate at the level of the as-deposited film independent of the stimulus. This direct comparison reveals that the right content of structural defects is a prerequisite for successful reproducible switching behaviour reflected by the changes in the short- and medium-range order. Such an initial state can be pictured as to lie at the intermediate energy point in Fig. 6.1, while the TE films are already of high energy and only soft annealing results in appreciable changes quickly reaching steady-state condition. It remains unclear why highly defective metalloid-enriched structures are stabilized. Hard annealing to fully erase the thin-film thermal history was not studied as the focus was on understanding and maximizing the magnitude and reversibility of AATs.

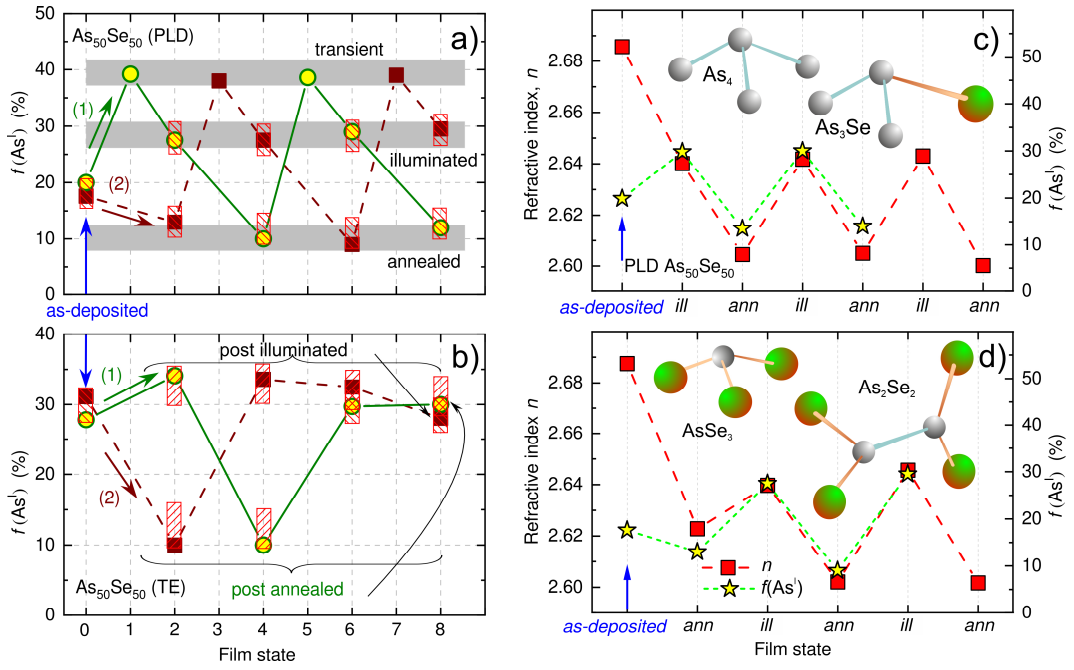

Fig. 6.3 Amorphous-to-amorphous transitions in thin-film $As_{50}Se_{50}$ upon above-bandgap illumination and after soft annealing cycles. a) Reversible transitions in PLD films (≈1,500 nm thick). **b)** Irreversible transitions in TE films (≈1,050 nm thick). The switching is expressed by the change in the fraction of As^{I}-type atoms, which is calculated from the fractional peak area (A) as: $f(\mathrm{As^I}) = A(\mathrm{As^I})/\left(A(\mathrm{As^I}) + A(\mathrm{As^{II}})\right)$. The film-state values correspond to: 0 – as-deposited and 1–8 different steps of illumination (circles) and annealing (squares) cycles. Route #1 shows the illumination, and route #2 shows the annealing as the first stimulus applied, respectively. The shading in part a) highlights three different states: transient (laser ON), post-illuminated, and post-annealed. The dashed rectangles show the reproducibility of $f(\mathrm{As^I})$. The corresponding correlation between $f(\mathrm{As^I})$ and refractive index n, taken at 1,500 nm (Table 6.2 – best-fit to Cauchy model from ellipsometry measurements) for PLD films after imposing external stimuli in **c)** cycle illumination → annealing (part c) and **d)** annealing → illumination. The atomic structures show schematically mixed $AsAs_{3-i}Se_i$ (i = 0, 1, 2 and 3) structural units, where elemental-like (i = 0, 1) and stoichiometric-like (i = 2, 3) structures give rise to respectively As^{I} and As^{II} XPS peaks. Illumination was carried out by using a diode-pumped solid-state laser operating at $\lambda = 671$ nm ($E = 1.85$ eV, a power density of ≈300 mW cm^{-2}) in an ultra-high vacuum for 2 h; reversibility was achieved on soft annealing at 150 °C, 30 °C below the crystallization onset, under N_2 atmosphere for 1.5 h. *Reproduced from Kalyva et al. [315] (**publication #3 – Appendix I**)*.

The reproducible structural changes in PLD films can be correlated with their optical properties (Fig. 6.3c – initial illumination, and Fig. 6.3d – initial annealing). Spectroscopic ellipsometry was used to obtain the optical functions dispersion, and the experimental data were fitted with Cauchy [317], Tauc-Lorentz [318,319], and Cody-Lorentz models [320] which are known to be appropriate approximations for optical functions in ChGs, for example, in thin-film binary As–S [321], bulk ternary As–S–Se [322,323] and thin-film $Ge_2Sb_2Te_5$ [323,324]. The calculated parameters of interest are summarized in **Table 6.2**. Illumination and annealing cause only negligible thickness change of about 0.3% [315], which is much lower than the shrinkage of about 6.5% upon crystallization in PCM [148]. Illumination always increases the value of the refractive index to about $n \approx 2.64$ (at the telecommunication wavelength of 1,500 nm), while n decreases to ≈2.60 on soft annealing giving a reproducible change of $\Delta n \approx 0.04$. The change follows the evolution of As–As fraction, and elemental amorphous arsenic has $n \approx 3.45$ at λ = 1500 nm [325]. According to the Moss rule [326], the product of the optical bandgap energy, E_g^{opt}, and n is constant, and the present data give $E_g^{\mathrm{opt}} \times n^4 \approx 88$

(Table 6.2) [315]; the constant varying between ≈77−100 eV has been reported for ChGs [295,327]. The Cody-Lorentz model allows to qualitatively hint at the "disorder" (chemical rather than topological in this case) in a studied system. A weak absorption tail represented by the Urbach energy, $E_{\mathrm{U}} \approx 100$ meV was found for the as-deposited films (Table 6.2). The tails states are predominantly governed by the energy states in the tops of the valence band in many amorphous semiconductors [328,329], not water [330]. Many non-crystalline systems have a threshold value of $E_{\mathrm{U}} > 50$ meV, which reflects the inherent thermodynamical density fluctuations at the estimated nanoscale of ≈1−2 nm (medium-range order) of glasses [329]. Reflecting the "degree of disorder" upon applying the external stimuli, E_{U} systematically increases (more disorder higher-energy state) and decreases (less disorder lower-energy state) upon illumination and annealing, respectively. The Urbach energy is difficult to be assigned to any specific bonding here.

For TE films, the optical properties could not systematically be correlated with the structural changes (see Fig. S2 in Supplementary Information of Ref. [315]). The refractive index did not level off at As–As bonding saturation (Fig. 6.3b) and it suggests a decoupled correlation between the optical functions and saturated $f(\mathrm{As^I})$. It is the complex densification and Se-rich nanoregions which could become the predominant factors controlling optical properties after the 1st cycle. The as-prepared TE films are more disorder $E_{\mathrm{U}} \approx 110 - 130$ meV $(\pm 10\ \mathrm{meV})$ than the corresponding PLD films.

A schematic topological view of the switching is shown in an energy landscape diagram (**Fig. 6.4**). For PCM erasing (crystal-to-glass transition – state "1" to "5" transition), a high energy to melt the material, energy-limiting step in PCM data recording, followed by rapid quenching (>10^{10} K s^{-1}), must be provided. State "2" can be reached by PLD or TE, although the two are profoundly different in As–As bonds fraction, and followed by illumination or annealing recurring switching between amorphous states with alike, albeit discrete, bonding features is achieved. The transient state "3" corresponds to an amorphous phase upon constant illumination with the highest fraction of As–As bonds (Fig. 6.3a), and it is depicted as a shallow minimum that tends to relax to a post-illuminated state "4" on ceasing the actinic light. Soft annealing causes the switching in a direction of "4" → "5", while the reversal is achieved on illumination by passing through state "3".

Table 6.2 Values of best-fit models to ellipsometric data calculated by the Cauchy (C) [317] **Tauc-Lorentz (TL)** [318,319]**, and Cody-Lorentz** [320] **dispersion models in two types of switching cycles: 1) illumination → annealing, and 2) annealing → illumination in PLD films.** Refractive index, n, is given at the telecommunication wavelength of $\lambda = 1{,}500$ nm in the transparent region of the glass, the optical bandgap energy, $E_{\mathrm{g}}^{\mathrm{opt}}$, is calculated by TL model and the Urbach energy, E_{U}, is calculated by CL model. The errors in the calculated values are $n \pm 0.002$, $E_{\mathrm{g}}^{\mathrm{opt}} \pm 0.01$ eV, and $E_{\mathrm{U}} \pm 6$ meV. *Adapted from Kalyva et al. [315] (**publication #3 – Appendix I**).*

illumination → annealing	n_{C}	n_{TL}	$E_{\mathrm{g}}^{\mathrm{opt}}$ (eV)	E_{U} (meV)	annealing → illumination	n_{C}	n_{TL}	$E_{\mathrm{g}}^{\mathrm{opt}}$ (eV)	E_{U} (meV)
as-deposited	2.686	2.687	1.69	100	*as-deposited*	2.688	2.689	1.68	100
illuminated	2.640	2.648	1.80	88	*annealed*	2.623	2.626	1.80	83
annealed	2.605	2.609	1.82	76	*illuminated*	2.640	2.645	1.76	108
illuminated	2.642	2.647	1.79	101	*annealed*	2.602	2.605	1.79	60
annealed	2.605	2.607	1.82	54	*illuminated*	2.646	2.652	1.76	91
illuminated	2.643	2.647	1.86	98	*annealed*	2.602	2.607	1.78	58
annealed	2.600	2.611	1.79	73	—	—	—	—	—

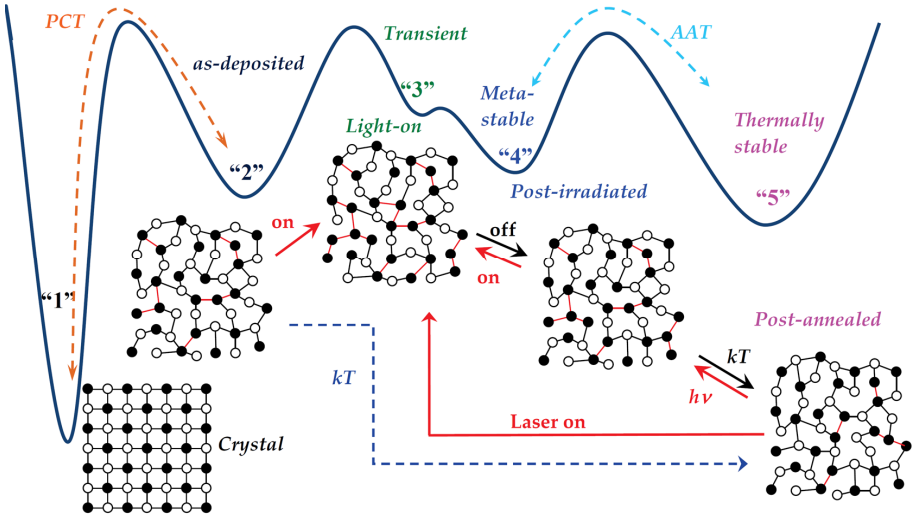

Fig. 6.4 Schematic of potential energy landscape of the various structural states which pulsed-laser deposited thin-film $As_{50}Se_{50}$ was shown to adopt on continuous illumination and on annealing. The deepest energy minimum "1" represents the crystalline state (the depicted structure does not represent the true atomic structure of $As_{50}Se_{50}$ crystal). The structure of the as-deposited state "2" consists of homonuclear As–As (red lines between the black solid circles) and heteronuclear As–Se bonds (red lines between the black solid circles). On illumination, more As–As bonds form and state "1" transforms into the transient state "3" which has a very shallow minimum. The transient state can relax into the post-illuminated state "4" on ceasing the laser light, only. State "4" is thermally metastable and upon annealing, it relaxes to the thermally stable state "5" with the lowest density of homonuclear As–As bonds from all the metastable states shown. Reversible switching occurs between states "4" and "5" upon illumination/annealing. Transition to state "5" can be accelerated through annealing of state "2". PCT – phase-change transition; AAT – amorphous-to-amorphous transition. *Published from Kalyva et al. [315] (**publication #3 – Appendix I**).*

The reproducible switching and the zero-induced stress on applying the stimuli make the effect of interest for application in active photonic devices. The change of Δn is about 2× lower than that achieved in thin-film $Ge_2Sb_2Te_5$ upon (de)vitrification in DVD disk [203] (operating at $\lambda = 633$ nm). Switching in AATs, unlike in PCM for which all atoms are involved during the transitions, involves only a fraction of atoms which can theoretically give more precise control of the optical response and its magnitude. Another advantage is that such structural transformations make take place at relatively low-cost energy upon illumination, which is hard to estimate but the bond energies of homonuclear As–As (~200 kJ mol^{-1}) and heteronuclear As–Se (~230 kJ mol^{-1}) are close to each other [331]. Yet, the endurance, data retention (amorphous phase drift), kinetics, unlikely to be shorter than hundreds of seconds, and other compositions must further be explored. For example, concerning the composition, another study showed that photoinduced changes in PLD $As_{48}S_{52}$ are irreversible [332].

6.2. Athermal photocrystallization and photoamorphization

Photocrystallization can be more readily realized than photoamorphization, supported by the rules of thermodynamics leading to a more stable phase, and, therefore, much fewer papers exist on the latter transition. Possibly the most known studies of photocrystallization and photoamorphization were done by Ovshinsky and co-workers in Ge_xTe_{1-x} system [333,334]; yet the authors did not separate optical and thermal contributions to the phase transitions observed. Nevertheless, the study gave the foundation to the optical-disk technology exploiting a large optical contrast in GeTe–Sb_2Te_3 alloys on thermally-induced phase transition via laser as studied by Yamada and co-workers [206], and

discussed in Chapter 4. Important aspects of optically-induced transitions were possibly not fully realized until the work of Griffiths *et al.* [335,336] and Frumar *et al.* [337]. Griffiths *et al.* observed athermal reversible photocrystallization in $GeSe_2$ glass, and they noted its reversibility in the dark within several hours. The authors referred to the detection of quasi-crystalline configurations, incipient crystal-like ordering, which when grown into micrometre-sized crystals makes the transition permanent. Unfortunately, the Raman peaks elucidation was ambiguous not allowing to understand the underlying mechanism. Frumar *et al.* realized that photocrystallization in Ge–Sb–S glass is accompanied by photobleaching. Based on the clues above, we may speculate about the possible existence of preceding structural changes templating and/or providing mobility for photocrystallization/photoamorphization. A quite few studies have dealt with the photocrystallization of a-Se and its dependence on light polarization – summarized by Yannopoulos [284].

Elliott & Kolobov [338] demonstrated reversible and cyclable white-light photoamorphization of thermally-crystallized thin-film $As_{50}Se_{50}$, but the crystallization step necessitated thermal annealing. The equimolar compound is the only composition exhibiting the transition in the As–Se system [339–343] – possibly arising from the nanometre-lengthscale heterogeneity as discussed in the previous section. Frumar *et al.* [344] studied optically-induced amorphization of c-As_2S_3 (orpiment) owing to the stability of the supercooled liquid to crystallization and induced disorder promoting the phase transformation. They considered that light can provide enough energy to rise the Gibbs free energy of the defected (metastable) crystal above that of the amorphous phase.

Our recent study [345]*, is essentially the first work to report in-situ an all-optical reversible photocrystallization where the complete cycle does not necessitate going through the supercooled liquid state for the reversal.* Well-annealed $Ge_{25.0}Ga_{9.5}Sb_{0.5}S_{65.0}$ bulk glass, where glassy GeS_2 is the main constituent (75 mol.%), doped with 0.5 at.% of Er^{3+} was chosen due to its optical activity. Prior to studying the kinetics and mechanism of photocrystallization, reliable Raman peak assignment must be done to avoid ambiguous structural interpretation, and that is based on Ref. [346]. Adding erbium into the host matrix does not cause any observable changes to the Raman peaks, which are composed of six main vibration peaks (**Fig. 6.5a** – bottom spectrum): ~343 cm^{-1}, $v_1(A_1)$ mode – symmetric stretching mode of corner-sharing (CS) $GeS_{4/2}$ tetrahedra with the contribution of $GaS_{4/2}$ tetrahedra; ~373 cm^{-1}, the companion line A_1^c – symmetric stretching mode of edge-sharing (ES) tetrahedra; ~408 cm^{-1} and ~440 cm^{-1} – antisymmetric stretching mode, $v_3(F_2)$, of A_1 and A_1^c, respectively; ~290 cm^{-1} – a weak band may be originate from the bending/deformation modes of $Ge(Ga)S_{4/2}$ tetrahedra and $SbS_{3/2}$ pyramids, although Sb-content is low, Sb–S bonds are highly Raman active; and lower frequencies at ~230–250 cm^{-1} – account for (semi)metallic M–M (M: Ge, Ga) bonds in ethane-like units, for example, $Ge_2(S_{1/2})_6$ [346–348]. It will become apparent in later paragraphs that the largely 3-D glassy network, due to the high population of CS tetrahedra over the ES tetrahedral bridges, of the well-equilibrated glass, resembling the structure of the 3-D low-temperature β-GeS_2 crystal [349], is the prerequisite for the observed athermal photocrystallization (amorphization).

The *in-situ* Raman spectra (Fig. 6.5b – high-fluence illumination, and 6.5c – low-fluence illumination) revealed a *three-step mechanism* of the photoinduced structural changes: i) photoassisted lowering of the glassy-network dimensionality; ii) photocrystallization; and iii) photoassisted re-amorphization – all of which bear a strong fingerprint in the dominant frequency region between 200 cm^{-1} and 400 cm^{-1}.

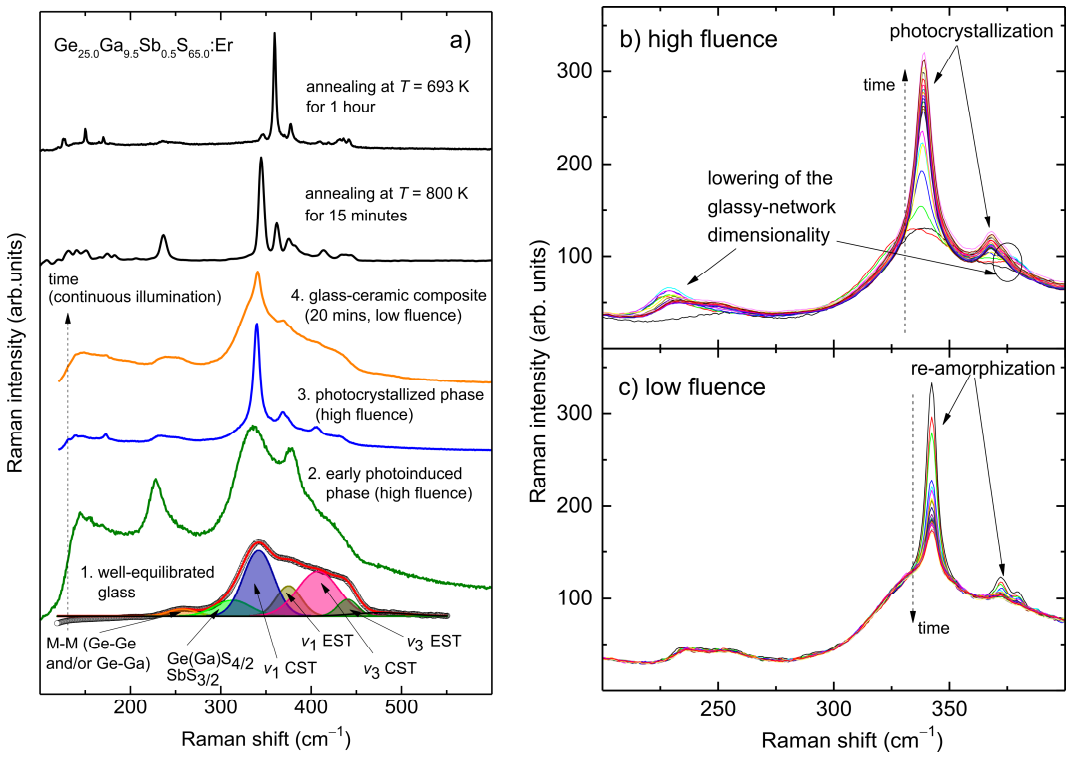

Fig. 6.5 Raman spectra of athermal photocrystallization/photoamorphization in bulk-glass $Ge_{25.0}Ga_{9.5}Sb_{0.5}S_{65.0}$ doped with 0.5 at.% of Er^{3+}. a) Different stages of athermal photocrystallization under continuous-above-bandgap illumination with a He-Cd laser, $\lambda = 441.6$ nm (E = 2.41 eV; E_g^{opt} of the glass is ≈2.4 eV [296]), and the Raman spectra of glasses annealed above $T_g = 683$ K are shown. The starting glass was well-annealed at 20 K below T_g for 3 hours. Raman spectra of the well-equilibrated glass is deconvoluted to Gaussian lines, keeping the least possible number of fitted lines (the best-fit to the measured data is shown by the red solid curve. CST and EST stand for corner-sharing and edge-sharing tetrahedral units, respectively. This reference spectrum was measured at low fluence to avoid any photostructural changes. The intensity is rescaled, and all spectra are vertically displayed for clarity. See the main text for the Raman assignment discussion. **b)** *Photocrystallization* is initiated by lowering the glassy-network dimensionality – *rejuvenation* – represented by the saturation of the bands at ~235 and at ~375 cm^{-1}. The photocrystallization is predominantly characterized by the growth of the A_1 mode ~338–340 cm^{-1} intensity at high fluence ~10^4 W cm^{-2}. **c)** *Re-amorphization* under low-fluence illumination, ~10^3 W cm^{-2}, in ~17.5 min. The spectra in parts b and c are normalized with the respect to the broad spectrum of the glass. *Reproduced from Benekou et al. [345] (**publication #12 – Appendix I**).*

Stage I: lowering of the glassy-network dimensionality. Photostructural changes are initiated by the onset of two bands at ~235 cm^{-1} and ~375 cm^{-1} (Fig. 6.5b and c), where the former is the fingerprint of the glassy-network-dimensionality modifications; compare spectra 1 (well-equilibrated glass) and 2 (early stages of photostructural changes) in Fig. 6.5a. The extra Ge atoms needed to form the ethane-like units originate from the bond disruption either of CS or ES tetrahedra network substructures. It is evident that the increase in the ES/CS ratio of the tetrahedral units upon illumination precedes any photocrystallization, and we term this stage also as an incubation period. As the result of the *glassy*-network lowering dimensionality from predominantly 3-D to a mixture of 2-D/1-D, the low-dimensional structures (ES tetrahedra and ethane-like units) predominate, and more free volume is created providing higher effective mobility of atomic displacements and bond formation/breaking in the *optically-rejuvenated glass* (conforming to the schematical energetic processing of a low-energy glass in Fig. 6.1). This rejuvenation saturates in about 50–150 s (**Fig. 6.6a**), where also the increase in the ES tetrahedra peak at 375 cm^{-1} vanishes, not its contribution to the

overall spectra, and seeds the photocrystallization step represented by the increasing A_1 mode at ~338–340 cm^{-1} (Fig. 6.5b). The lowering dimensionality follows the usual understanding of defect-driven photostructural changes in chalcogenide glasses [350].

Before proceeding with the description of the photocrystallization stage, we have to estimate any potential temperature rise during the illumination by observing a frequency shift of the temperature-sensitive A_1 mode. By taking the mode to be temperature-dependent as $\sim 1.7\times10^{-2}$ cm^{-1} K^{-1} [349] and the small observed shift of ~1–2.5 cm^{-1} (Fig. 6.5b; and its reversal under dark conditions) gives an estimated temperature rise between 60 K and 150 K which corresponds to a small fraction of $(0.52 - 0.65)T_g$ – the starting glass was already equilibrated by annealing at ≈97% of T_g and the glass is photostable (spectrum 1 in Fig. 6.5a). The process appears to be "weakly" thermally activated, and the apparent activation energy for photocrystallization is ~0.16 eV (15.4 kJ mol^{-1} – in this section, activation energy is quoted in *eV* as this is more common in optical studies); it can be calculated by taking the incubation time to follow an Arrhenius kinetics (Fig. 6.6). This value seems to be characteristic for athermal processes in general, and, for example, Elliott and Kolobov showed a value of ~0.15 eV (14.5 kJ mol^{-1}) for athermal photoamorphization of thermally crystallized $As_{50}Se_{50}$ films [338]. Thermally-activated processes in GeS_2, the main constituent of the glass for which all parameters are well known in the literature are: the activation energy for viscous flow is $Q_\eta \approx 4.8$ eV (462±15 kJ mol^{-1}) [351], for crystallization ~1.91 eV (184±2 kJ mol^{-1}) obtained by DSC at large ΔT [352], and $Q_U = 2.53$ eV (244±13 kJ mol^{-1}) and $= 4.43$ eV (427±9 kJ mol^{-1}) for the low-temperature β-GeS_2 phase growth respectively on the bulk glass surface and in the bulk obtained by direct growth-rate measurement at large ΔT [353]. We can conclude that the photoinduced changes are mainly governed by photoelectronic process in the glass and can be termed as being effectively athermal. Certainly, no step involving the supercooled liquid state is needed which would involve large heat. The origin of such very weak temperature dependence, characteristic for the early stages of photostructural transformations, remains unknown.

Stage II: photocrystallization. The photocrystallization is predominantly detected by the intensity change around ~338–340 cm^{-1} representing the A_1 mode of the glass (cf. the resemblance with crystal). Maybe there is a minor contribution from a second phase, the high-temperature 2-D GeS_2 phase, observed around ~369 cm^{-1} (Fig. 6.6b). Photocrystallization stops around 20 min (Fig. 6.5b) giving a glass-ceramic composite with the total crystallized fraction of about 80 vol.% (spectra 3 and 4 in Fig. 6.5a). The composite is characterized by the band at ~405 cm^{-1} of the photomodified glass and nanocrystals dominated by a 3-D phase. The photocrystallized phase has characteristic bands of A_1 and A_1^c at respectively at ~339 cm^{-1} and ~369 cm^{-1}. Surface modifications are shown in Fig. 6.6d–f. Low fluence does not effectively induce any changes to the microstructure of the photostable glass (Fig. 6.6d). Upon high-fluence illumination, photoinduced mass transport takes place giving a columnar-porous structure along the actinic light direction, and this may be one of the possible origins of the weak thermal activation prior to photocrystallization, although this cannot be resolved in our study, especially because the effect has a complex non-monotonic dependence on temperature [285]. Upon reaching the saturation in stage II, nanocrystalline spheroidal particles are formed with a typical diameter of ~1.1–1.5 μm (Fig. 6.6f).

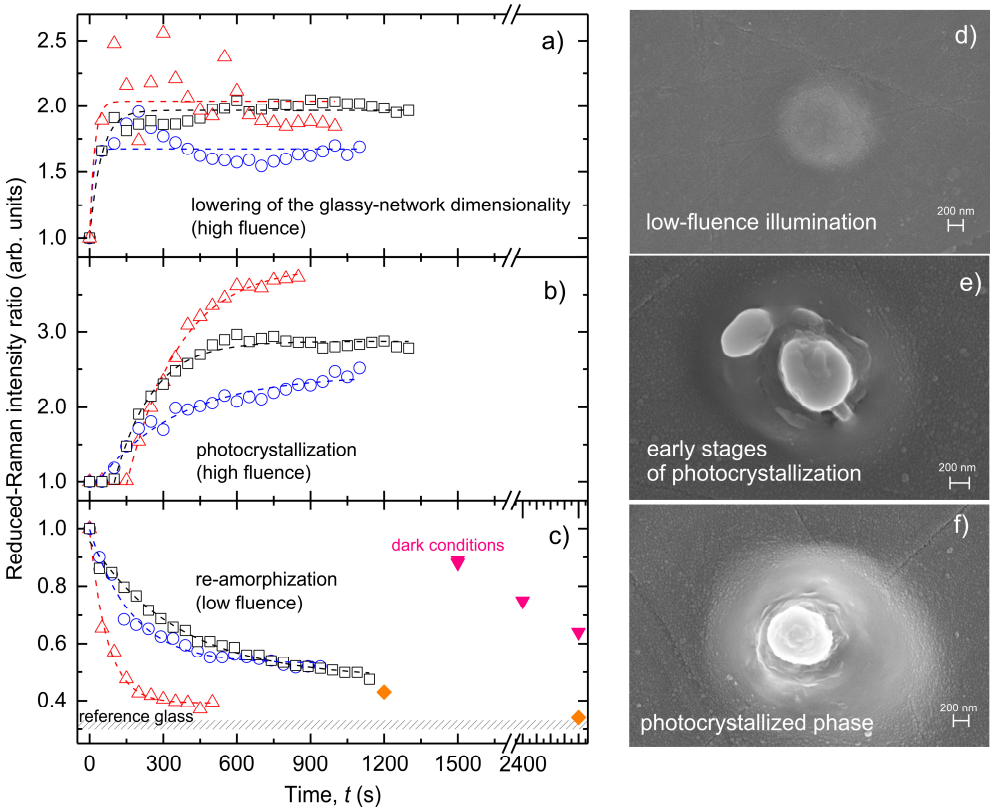

Fig. 6.6 Temporal evolution of the reduced-Raman intensity ratio upon illumination (a–c) and representative SEM micrographs (d–f) showing different stages of the athermal photostructural changes. a) *Stage I*: lowering of the glassy-network dimensionality through optical rejuvenation probed at ~235 cm^{-1}. **b)** *Stage II*: photocrystallization monitored at ~340 cm^{-1}. Stage I and II are induced on high fluence of ~10^4 W cm^{-2}. **c)** *Stage III*: re-amorphization on low fluence ~10^3 W cm^{-2} and under dark conditions observed by the lowering A_1 mode intensity. In all parts, the open symbols represent three independent measurements from different spots on the glass. Dashed lines are exponential fits for guiding the eye only. The solid symbols in part c show slow re-amorphization in dark (pink triangles) and nearly complete re-amorphization in 60 min under low-fluence conditions (orange diamonds). SEM micrographs show: **d)** stability of the well-equilibrated glass during low-fluence illumination; **e)** the early stages of crystal growth; and **f)** the photocrystallized phase with a particle diameter of ~1.1 μm. The small nanoparticles show the applied Au coating for SEM imaging. *Adapted and modified from Benekou et al. [345] (**publication #12 – Appendix I**).*

It is worth comparing the athermal photocrystallization with traditional isothermal and isokinetic annealing experiments. The Raman spectrum of the photocrystallized phase bears some similarity with that of thermally-annealed glass at 800 K for 15 minutes (Fig. 6.5a), which resembles that of a low-temperature 3-D phase with its main mode at ~344 cm^{-1} and with some contribution of the A_1 mode of a 2-D phase at ~362 cm^{-1} [348]. Our early results indicate that the 3-D thermal phase can be photoamorphized. On the other hand, the glass crystallized at 683 K just above T_g has the dominant bands of ~360 cm^{-1} and ~377 cm^{-1} which resemble modes in a high-temperature 2-D crystalline phase A_1 (~363 cm^{-1}) and the A_1^c (~382 cm^{-1}) [348], respectively. Details about the assignment of the complex Raman spectra of thermally-crystallized phases can be found in Ref. [345]. The photoinduced crystal-growth rate can be estimated to be in the range of ≈10^{-3} μm s^{-1} on the glass surface at room temperature ($\sim 0.27T_m$). This is high and comparable to thermally-activated U_{max} achieved in the supercooled liquid state of very good glass-forming oxides (Fig. 2.4), and to the growth of the low-temperature β-GeS_2 phase at high temperatures $U = 7.5 \times 10^{-3}$ μm s^{-1} at $T = 672$ K

($0.60T_{\mathrm{m}}$; $T_{\mathrm{m}} = 1{,}116$ K [354]) in thin-film GeS_2 [355], $U = 1.7 \times 10^{-3}$ μm s^{-1} at $T = 754$ K ($0.68T_{\mathrm{m}}$) on the bulk GeS_2 surface [353], and $U = 2.2 \times 10^{-3}$ μm s^{-1}, at $T = 704$ K ($0.63T_{\mathrm{m}}$) in the bulk GeS_2 [353]. Indeed, thermal crystallization can be photoaccelerated [356–358]. For example, the incubation time for isothermal annealing of the formation of the low-temperature $GeSe_2$ phase can be reduced by 1–2 orders of magnitude [358]. The onset of the photoassisted temperature of thermal crystallization in glassy $GeSe_2$ depends on the liquid thermal history. More relaxed slowly cooled glasses, as the starting glass here, start to crystallize at a much lower temperature than unrelaxed glasses upon illumination. This can be understood in the context of classical nucleation theory, such that slow cooling gives a higher density of frozen-in nuclei in the glass, I^{st} is higher, and its maximum is shifted to lower homologous temperatures in contrast to a fast-quenched glass. These arguments support the observation that illumination enhances the rate of structural re-ordering of favourable units (stage I), and the overall photoassisted/photoinduced crystallization time is shorter than the annealing time required to crystallize the supercooled liquid. Because of the resemblance between photo- and thermally-induced crystallization, though the nature is different, the optical excitations look like the reversibility of the transient-nucleation effect observed in the supercooled liquid of phase-change chalcogenides presented in Sect. 4.3. (Fig. 4.12.) [42]; an effect that can extend into the glassy state when enough kinetics is provided by light.

Stage III: photoassisted re-amorphization. On low-fluence illumination, re-amorphization with Arrhenius kinetics takes place immediately after reducing the laser power (Fig. 6.6c – open symbols). The Raman peak evolution of the composite which is largely formed of a 3-D photocrystallized phase, and the remaining glassy matrix partially preserves 2-D/1-D network dimensionality, contrary to the 3-D network of the starting glass (Fig. 6.5a), and shows a predominant reversal during fast re-amorphization up to about 20 min of illumination. Nearly complete reversal can be achieved in ~60 min. When stored in the dark, the composite is unstable, and about 17 vol.% of the photocrystallized phase reverses in ~25 minutes, and ~50 vol.% in 60 min; the same converted fractions can be achieved respectively in 45 s and 300 s under the low-fluence illumination. The composite dark-condition stability is about ~175 hours before nearly full re-amorphization is achieved, although possibly 100% conversion cannot be completed in the dark. On prolonged illumination, the structure relaxes towards an equilibrated glassy state, substantially but not fully similar to the well-equilibrated glass. This suggests that there is a possibility for cycling the phase transitions (**Fig. 6.7**). Our early results, investigation ongoing, suggest that the glass-to-crystal photoinduced athermal phase transformation can be cycled. Fig. 6.7. shows an example of a 2$^{\mathrm{nd}}$ cycle for photocrystallization and re-amorphization. Clearly, the photocrystallization step is different from the first cycle, which can originate, among technical reasons such as a laser defocus, from the fact that the re-amorphized glassy structure does not fully correspond to the well-equilibrated glass because of the *irreversible* part of the cycling represented by the mass transport in stage I. Although the study is still ongoing, we may speculate that the irreversible part will be the limiting factor for the maximum number of cycles which can be achieved. On the other hand, the re-amorphization process is well reproducible and shows similar kinetics as in the 1$^{\mathrm{st}}$ cycle independent of previous steps; it does not necessitate stage I.

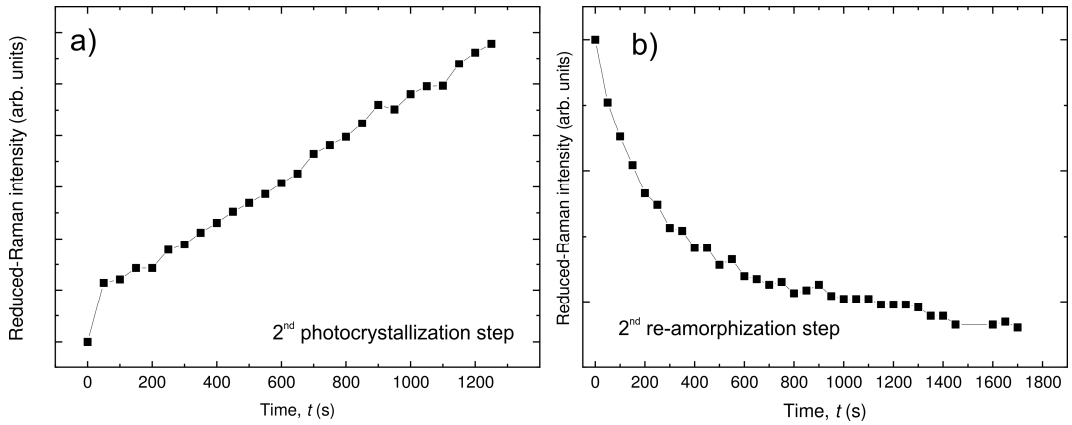

Fig. 6.7 Proof-of-concept of the athermal photocrystallization cyclability showing the A_1 mode temporal evolution during 2nd step of a) photocrystallization (high fluence) and b) re-amorphization (low fluence). Only the re-amorphization step is qualitatively similar to that in the 1st cycle – Fig. 6.6c (*unpublished data*).

Further systematic investigations are ongoing to understand the athermal effect in detail. As noted by Griffiths *et al.* [336], the phase transformation can also be achieved at liquid-nitrogen temperature. The interplay between light-induced "damage" and relaxation can be balanced towards the former one giving higher magnitude of changes, which is the case for reversible photodarkening [359] and photoplastic [360] effects. Maybe, surprisingly pure GeS_2, the main constituent of the studied glass, does not exhibit such athermal effects. It is therefore of interest to study the role of Sb/Ga ratio in the glass to understand the structural/chemical conditions under which athermal effects can(not) be stimulated. It has been suggested in Ge–As–S glass upon femtosecond time-scale illumination, that photostructural changes are faster and more likely optically reversible, although the overall magnitude of an effect is smaller, for over-constrained rather than for under-constrained glassy networks [361]; the former is the case of the studied composition with its mean-coordination number of 2.6. Contrary, Calvez *et al.* [362] demonstrated an optically-reversible, on higher laser power of continuous illumination, giant photocontraction in under-constrained $GeAsSe_{13}$ glass. Such provoking results, probing different parts of the structural dynamics spectrum in both studies, further support the need for detail and clear understanding of the relationship between photoinduced effects, atomic structure, and its dynamics in chalcogenide glasses. As possibly in $As_{50}Se_{50}$, it may be that the right amount of local structural heterogeneous environment provides the activity.

We may therefore conclude that the reversible photocrystallization/re-amorphization stems from: i) athermal effects; ii) high effective mobility for atomic displacement which is provided by the optically-rejuvenated glass; iii) photocrystallization of a low-temperature phase favours reversibility (supported by the possibility of photoinduced re-amorphization of a similar phase not of thermal origin); and iv) the power density must be below a certain threshold to promote the formation of metastable (subcritical) nuclei and to avoid the growth of high-temperature phases.

7. CONCLUSION

We have shown that the understanding of crystallization in glasses has not only strong implications in fundamental science, but it is of great technological importance in electronics, optics, and applications as structural materials. Crystallization and supercooling are also of direct importance for animal species survival, for example, to avoid ice formation in living species during winter, or to form the toughest natural material such as spiders silk fibres formed of amorphous-crystalline composite. Clear empirical rules can be derived correlating the liquid lability and propensity for crystallization, specifically crystal-growth rate, in a variety of glass-forming liquids including, maybe surprisingly, also pure-metal glasses whose kinetic fragility and reduced-glass-transition temperature have been derived indirectly, so far. The reason for such rules to exist is that crystal growth, spanning many orders of magnitude among different glass-forming liquids, is predominantly kinetically driven which can be represented by the temperature dependence of fundamental mobility. This allows studying and comparing different liquids experimentally and also with those obtained from computer simulations.

Classical nucleation theory, with all its limitations and assumptions, seems to be still an adequate and powerful theory to describe crystallization qualitatively and quantitatively in phase-change chalcogenides. This helps to correlate memory performance with materials property and to predict and design new types of materials to be used as the active layer in the device. Moreover, because of the unique thermodynamic properties of phase-change chalcogenides, a new thermodynamic regime of a temperature-dependent subcritical-size nuclei formation could be revealed by the theory and which has been unknown to exist in oxide glasses, so far. The crystallization mechanisms of the archetype phase-change chalcogenides, namely nucleation- and growth-dominated, could be correlated with their viscosity being represented by a single value of kinetic fragility or the occurrence of a fragile-to-strong crossover on cooling the liquid, respectively. Although ultrafast-heating calorimetry is an indirect technique to infer viscosity of a liquid, it can be extremely useful to probe fast kinetics in a wide temperature range of the existence of the supercooled liquid, which is otherwise inaccessible by other techniques, especially for fast-crystallizing liquids

By combining fast calorimetry with other *in-situ* techniques (high-energy X-ray diffraction, containerless levitation, and TEM), the crystallization mechanism and its kinetics can readily be correlated in metallic-glass-forming liquids upon flash-annealing. The propensity of a metallic glass for the metastable phase formation could be understood in terms of kinetic, chemical, and structural requirements. The condition under which ductile composites can be formed can then be defined giving a clear technological and operating window to produce composites with desired crystalline phases.

Although athermal transitions are induced by optical excitations they bear some similarities with thermal annealing, but the kinetics of the former one is typically much faster. We have demonstrated different reversible athermal phase transitions, amorphous-to-amorphous and amorphous-to-crystalline and correlated them with the underlying structural changes in the glasses.

We have shown that the topic of crystallization in glasses and stability of their liquids is a thriving field, and many new phenomena are yet to be discovered, such as liquid-to-liquid transitions above the liquidus temperature, which potentially could lead to obtaining new glassy phases.

References

[1] K. F. Kelton and A. L. Greer, *Nucleation in Condensed Matter, Applications in Materials and Biology*, Elsevier, Oxford (2010).

[2] D. M. Herlach (Ed.), *Solidification and Crystallization*, WILEY-VCH Verlag GmbH & Co. KGaA, Weinheim, (2004).

[3] D. M. Herlach, P. Galenko, and D. Holland-Moritz, *Metastable Solids from Undercooled Melts*, Elsevier, Oxford, (2007).

[4] D.A. Porter and K.E. Easterling, *Phase Transformations in Metals and Alloys* (2nd edition), Chapman & Hall, London, (1996).

[5] D. M. Herlach and D.M. Matson (Eds.), *Solidification of Containerless Undercooled Melts*, WILEY-VCH Verlag GmbH & Co. KGaA, Weinheim (2012).

[6] C. Suryanarayana and A. Inoue, *Bulk Metallic Glasses*, CRC Press, Boca Raton, (2017).

[7] J. L. Adam and X. Zhang (Eds.), *Chalcogenide Glasses, Preparation, Properties and Applications*, Woodhead Publishing Limited, Oxford, (2014).

[8] S. Raoux and M. Wuttig (Eds.), *Phase Change Materials: Science and Applications*, Springer, Cham, (2009).

[9] M. Massobrio, J. Du, M. Bernasconi, and P.S. Salmon, *Molecular Dynamics Simulations of Disordered Materials*, Springer, Cham, (2015).

[10] A. V. Kolobov and K. Shimakawa (Eds.), Volume 1: *Structure, Properties, Modeling and Applications of Amorphous Chalcogenides,* in: *The World Scientific Reference of Amorphous Materials: Structure, Properties, Modeling and Main Applications* (P. C. Taylor, ed.), World Scientific, New Jersey, (2021).

[11] Z. Evenson, T. Schmitt, M. Nicola, I. Gallino, and R. Busch, High temperature melt viscosity and fragile to strong transition in Zr–Cu–Ni–Al–Nb(Ti) and $Cu_{47}Ti_{34}Zr_{11}Ni_8$ bulk metallic glasses. *Acta Mater.* **60**, 4712 (2012).

[12] C. A. Angell, Formation of glasses from liquids and biopolymers. *Science* **267**, 1924 (1995).

[13] J. Orava and A. L. Greer, Fast and slow crystal growth kinetics in glass-forming melts. *J. Chem. Phys.* **140**, 214504 (2014).

[14] Y.-W. Kim, H.-M. Lin, and T. F. Kelly, Amorphous solidification of pure metals in submicron spheres. *Acta Metall.* **37**, 247 (1989).

[15] A. Qiao, T. D. Bennett, H. Tao, A. Krajnc, G. Mali, C. M. Doherty, A. W. Thornton, J. C. Mauro, G. N. Greaves, and Y. Yue, A metal-organic framework with ultrahigh glass-forming ability. *Sci. Adv.* **4**, eaao6827 (2018).

[16] D. R. Reid, I. Lyubimov, M. D. Ediger, and J. J. de Pablo, Age and structure of a model vapour-deposited glass. *Nat. Commun.* **7**, 13062 (2016).

[17] Y. Z. Chua, M. Ahrenberg, M. Tylinski, M. D. Ediger, and C. Schick, How much time is needed to form a kinetically stable glass? AC calorimetric study of vapor-deposited glasses of ethylcyclohexane. *J. Chem. Phys.* **142**, 054506 (2015).

[18] L. Zhong, J. Wang, H. Sheng, Z. Zhang, and S. X. Mao, Formation of monatomic metallic glasses through ultrafast liquid quenching. *Nature* **512**, 177 (2014).

[19] A. L. Greer, Diffusion and reactions in thin films. *Appl. Surf. Sci.* **86**, 329 (1995).

[20] J. Orava and A. L. Greer, Fast crystal growth in glass-forming liquids. *J. Non-Cryst. Solids* **451**, 94 (2016).

[21] W. H. Wang, Dynamic relaxations and relaxation-property relationships in metallic glasses. *Prog. Mater. Sci.* **106**, 100561 (2019).

[22] M. Wakeda, J. Saida, J. Li, Sand . Ogata, Controlled rejuvenation of amorphous metals with thermal processing. *Sci. Rep.* **5**, 10545 (2015).

[23] K. Ding, J. Wang, Y. Zhou, H. Tian, L. Lu, R. Mazzarello, C. Jia, W. Zhang, F. Rao, and E. Ma, Phase-change heterostructure enables ultralow noise and drift for memory operation. *Science* **366**, 210 (2019).

[24] K. H. Behrndt, Formation of amorphous films. *J. Vac. Sci. Technol.* **7**, 385 (1970).

[25] I. V. Okulov, I. V. Soldatov, M. F. Sarmanova, I. Kaban, T. Gemming, K. Edström, and J. Eckert, Flash Joule heating for ductilization of metallic glasses. *Nat. Commun.* **6**, 7932 (2015).

[26] Y. Sun, A. Concustell, and A. L. Greer, Thermomechanical processing of metallic glasses: extending the range of the glassy state. *Nat. Rev. Mater.* **1**, 16039 (2016).

[27] C. M. Meylan, J. Orava, and A. L. Greer, Rejuvenation through plastic deformation of a La-based metallic glass measured by fast-scanning calorimetry. *J. Non-Cryst. Solids X* **8**, 100051 (2020).

[28] C. M. Meylan, F. Papparotto, S. Nachum, J. Orava, M. Miglierini, V. Basykh, J. Ferenc, T. Kulik, and A. L. Greer, Stimulation of shear-transformation zones in metallic glasses by cryogenic thermal cycling. *J. Non-Cryst. Solids.* **548**, 120299 (2020).

[29] S. V. Ketov, A. S. Trifonov, Y. P. Ivanov, A. Yu. Churyumov, A. V. Lubenchenko, A. A. Batrakov, J. Jiang, D. V. Louzguine-Luzgin, J. Eckert, J. Orava, and A. L. Greer, On cryothermal cycling as a method for inducing structural changes in metallic glasses. *NPG Asia Mater.* **10**, 137 (2018).

[30] S. V. Ketov, Y. H. Sun, S. Nachum, Z. Lu, A. Checchi, A. R. Beraldin, H. Y. Bai, W. H. Wang, D. V. Louzguine-Luzgin, M. A. Carpenter, and A. L. Greer, Rejuvenation of metallic glasses by non-affine thermal strain. *Nature* **524**, 200 (2015)

[31] J. Pan, Yu. P. Ivanov, W. H. Zhou, Y. Li, and A. L. Greer, Strain-hardening and suppression of shear-banding in rejuvenated bulk metallic glass. *Nature* **578**, 559 (2020).

[32] D. Turnbull, Formation of crystal nuclei in liquid metals. *J. Appl. Phys.* **21**, 1022 (1950).

[33] C. V. Thompson and F. Spaepen, On the approximation of the free energy change on crystallization. *Acta Metall.* **27**, 1855 (1979).

[34] J. D. Hoffman, Thermodynamic driving force in nucleation and growth processes. *J. Chem. Phys.* **29**, 1192 (1958).

[35] R. W. Cahn and A. Greer, *Metastable States of Alloys.* in: *Physical Metallurgy* (R. W. Chang and P. Haasen, eds.), Elsevier, (1996), pp. 1723–1830.

[36] J. Orava and A. L. Greer, *Chalcogenides for Phase-Change Memory,* in: *Handbook of Thermal Analysis and Calorimetr*y (S. Vyazovkin, N. Koga, and C. Schick, eds.), Elsevier, Amsterdam, (2018), pp. 685–734.

[37] V. M. Fokin, M. L. F. Nascimento, and E. D. Zanotto, Correlation between maximum crystal growth rate and glass transition temperature of silicate glasses. *J. Non-Cryst. Solids.* **351**, 789 (2005).

[38] M. L. F. Nascimento and E. D. Zanotto, Does viscosity describe the kinetic barrier for crystal growth from the *liquidus* to the glass transition? *J. Chem. Phys.* **133**, 174701 (2010).

[39] M. D. Ediger, P. Harrowell, and L. Yu, Crystal growth kinetics exhibit a fragility-dependent decoupling from viscosity. *J. Chem. Phys.* **128**, 034709 (2008)–34709.

[40] D. M. Herlach, R. Kobold, and S. Klein, Crystal nucleation and growth in undercooled melts of pure Zr, binary Zr-based and ternary Zr-Ni-Cu glass-forming alloys. *JOM* **70**, 726 (2018).

[41] A. L. Greer, Grain refinement in rapidly solidified alloys. *Mater. Sci. Eng. A* **133**, 16 (1991).

[42] J. Orava and A. L. Greer, Classical-nucleation-theory analysis of priming in chalcogenide phase-change memory. *Acta Mater.* **139**, 226 (2017).

[43] J. H. Na, M. D. Demetriou, M. Floyd, A. Hoff, G. R. Garrett, and W. L. Johnson, Compositional landscape for glass formation in metal alloys. *Proc. Natl. Acad. Sci.* **111**, 9031 (2014).

[44] W. L. Johnson, J. H. Na, and M. D. Demetriou, Quantifying the origin of metallic glass formation. *Nat. Commun.* **7**, 10313 (2016).

[45] K. F. Kelton, A. L. Greer, and C. V. Thompson, Transient nucleation in condensed systems. *J. Chem. Phys.* **79**, 6261 (1983).

[46] K. F. Kelton, *Crystal Nucleation in Liquids and Glasses*, in: *Solid State Physics* (H. Ehrenreich and D. Turnbull, eds.), Academic Press, Boston, (1991), pp. 75–177.

[47] F. Spaepen, A structural model for the solid-liquid interface in monatomic systems. *Acta Metall.* **23**, 729 (1975).

[48] D. M. Herlach, Containerless undercooling and solidification of pure metals. *Annu. Rev. Mater. Sci.* **21**, 23 (1991).

[49] F. Spaepen and R. B. Meyer, The surface tension in a structural model for the solid-liquid interface. *Scr. Metall.* **10**, 257 (1976).

[50] F. Spaepen, The temperature dependence of the crystal-melt interfacial tension: A simple model. *Mater. Sci. Eng. A* **178**, 15 (1994).

[51] F. Spaepen, Effect of structural non-uniformity on the temperature dependence of the crystal-melt interfacial tension. *Mater. Sci. Eng. A* **226** , 129 (1997).

[52] A. L. Greer and K. F. Kelton, Nucleation in lithium disilicate glass: A test of classical theory by quantitative modeling, *J. Am. Ceram. Soc.* **74**, 1015 (1991).

[53] M. Volmer and A. Weber, Nuclei formation in supersaturated states. *Z Phys Chem.* **119**, 227 (1926).

[54] T. H. Lee, D. Loke, and S. R. Elliott, Microscopic mechanism of doping-induced kinetically constrained crystallization in phase-change materials. *Adv. Mater.* **27**, 5477 (2015).

[55] B.-S. Lee, S. G. Bishop, and J. R. Abelson, Fluctuation transmission electron microscopy: Detecting nanoscale order in disordered structures. *ChemPhysChem* **11**, 2311 (2010).

[56] J. W. P. Schmelzer, A. S. Abyzov, and V. G. Baidakov, Time of formation of the first supercritical nucleus, time-lag, and the steady-state nucleation rate. *Int. J. Appl. Glass Sci.* **8**, 48 (2017).

[57] H. W. Wilson, XX. On the velocity of solidification and viscosity of super-cooled liquids. *Phil. Mag.* **50**, 283 (1900).

[58] D. Valdes, S. Martinkova, J. Malek, and J. Bartak, Crystal growth in Ge-Sb-Se glass and its relation to viscosity and surface diffusion. *J. Non-Cryst. Solids.* **566**, 120865 (2021).

[59] J. Bartak, P. Kostal, and J. Málek, Analysis of crystal growth and viscosity in Ge-Sb-Se-Te undercooled melts, *J. Non-Cryst. Solids* **505**, 1 (2019).

[60] G. C. Sosso, J. Behler, and M. Bernasconi, Breakdown of Stokes-Einstein relation in the supercooled liquid state of phase change materials. *Phys. Stat. Sol. B* **249**, 1880 (2012).

[61] Y. Ashkenazy and R. S. Averback, Kinetic stages in the crystallization of deeply undercooled body-centered-cubic and face-centered-cubic metals, *Acta Mater.* **58**, 524 (2010).

[62] H. Xi, Y. Sun, and L. Yu, Diffusion-controlled and diffusionless crystal growth in liquid *o*-terphenyl near its glass transition temperature. *J. Chem. Phys.* **130**, 094508 (2009).

[63] A. L. Greer, New horizons for glass formation and stability, *Nat. Mater.* **14**, 542 (2015).

[64] M. H. Cohen and G. S. Grest, Liquid-glass transition, a free-volume approach. *Phys. Rev. B* **20**, 1077 (1979).

[65] M. H. Cohen and G. S. Grest, Erratum: Liquid-glass transition, a free-volume approach. *Phys. Rev. B* **26**, 6313 (1982).

[66] S. R. Coriell and D. Turnbull, Relative roles of heat transport and interface rearrangement rates in the rapid growth of crystals in undercooled melts. *Acta Metall.* **30**, 2135 (1982).

[67] J. Q. Broughton, G. H. Gilmer, and K. A. Jackson, Crystallization rates of a Lennard-Jones liquid. *Phys. Rev. Lett.* **49**, 1496 (1982).

[68] A. Schottelius, F. Mambretti, A. Kalinin, B. Beyersdorff, A. Rothkirch, C. Goy, J. Müller, N. Petridis, M. Ritzer, F. Trinter, J. M. Fernández, T. A. Ezquerra, D. E. Galli, R .E. Grisenti, Crystal growth rates in supercooled atomic liquid mixtures. *Nat. Mater.* **19**, 512 (2020).

[69] M. I. Mendelev, M. J. Rahman, J. J. Hoyt, and M. Asta, Molecular-dynamics study of solid–liquid interface migration in fcc metals. *Model. Simul. Mater. Sci. Eng.* **18**, 074002 (2010).

[70] M. Amini and B. Laird, Kinetic coefficient for hard-sphere crystal growth from the melt. *Phys. Rev. Lett.* **97**, 216102 (2006).

[71] D. Sun, M. Asta, and J. Hoyt, Kinetic coefficient of Ni solid-liquid interfaces from molecular-dynamics simulations. *Phys. Rev. B* **69**, 024108 (2004).

[72] Y. Sun, H. Xi, S. Chen, M. D. Ediger, and L. Yu, Crystallization near glass transition: Transition from diffusion-controlled to diffusionless crystal growth studied with seven polymorphs. *J. Phys. Chem. B* **112**, 5594 (2008).

[73] Y. Sun, H. Xi, M. D. Ediger, R. Richert, and L. Yu, Diffusion-controlled and "diffusionless" crystal growth near the glass transition temperature: Relation between liquid dynamics and growth kinetics of seven ROY polymorphs. *J. Chem. Phys.* **131**, 074506 (2009).

[74] C. T. Powell, H. Xi, Y. Sun, E. Gunn, Y. Chen, M. D. Ediger, and L. Yu, Fast crystal growth in *o*-terphenyl glasses: A possible role for fracture and surface mobility. *J. Phys. Chem. B* **119**, 10124 (2015).

[75] K. Paeng, C. T. Powell, L. Yu, and M. D. Ediger, Fast crystal growth induces mobility and tension in supercooled *o*-terphenyl. *J. Phys. Chem. Lett.* **3**, 2562 (2012).

[76] S. Martinkova, D. Valdes, S. Slang, K. Palka, and J. Bartak, Relationship between crystal growth and surface/volume mobilityies in $Se_{95}Te_5$ bulk glasses and thin films. *Acta Mater.* **213**, 116953 (2021).

[77] Z. P. L and C. T. Liu, A new glass-forming ability criterion for bulk metallic glasses. *Acta Mater.* **50**, 3501 (2002).

[78] D. Turnbull, Under what conditions can a glass be formed? *Contemp. Phys.* **10**, 473 (1969).

[79] L.-M. Wang, Y. Tian, and R. Liu, Dependence of glass forming ability on liquid fragility: Thermodynamics versus kinetics. *Appl. Phys. Lett.* **97**, 181901 (2010).

[80] Z. P. Lu, Y. Li, and S. C. Ng, Reduced glass transition temperature and glass forming ability of bulk glass forming alloys. *J. Non-Cryst. Solids* **270**, 103 (2000).

[81] S. Mukherjee, J. Schroers, Z. Zhou, W. L. Johnson, and W.-K. Rhim, Viscosity and specific volume of bulk metallic glass-forming alloys and their correlation with glass forming ability. *Acta Mater.* **52**, 3689 (2004).

[82] I. Douglass, T. Hudson, and P. Harrowell, Density and glass forming ability in amorphous atomic alloys: The role of the particle softness. *J. Chem. Phys.* **144**, 144502 (2016).

[83] J. C. Bendert and K. F. Kelton, Correlation between kinetic strength, volumetric properties, and glass forming ability in metallic liquids. *J. Non-Cryst. Solids* **376**, 205 (2013).

[84] O. Senkov, Correlation between fragility and glass-forming ability of metallic alloys. *Phys. Rev. B* **76**, 104202 (2007).

[85] J. Orava, A. L. Greer, B. Gholipour, D. W. Hewak, and C. E. Smith, Characterization of supercooled liquid $Ge_2Sb_2Te_5$ and its crystallization by ultrafast-heating calorimetry. *Nat. Mater.* **11**, 279 (2012).

[86] J. Orava, D. W. Hewak, and A. L. Greer, Fragile-to-strong crossover in supercooled liquid Ag-In-Sb-Te studied by ultrafast calorimetry. *Adv. Funct. Mater.* **25**, 4851 (2015).

[87] C. Schick and V. Mathot (Eds.), Fast Scanning Calorimetry. Springer, Cham, (2016).

[88] Q. Wang, L.-M. Wang, M. Z. Ma, S. Binder, T. Volkmann, D. M. Herlach, J. S. Wang, Q. G. Xue, Y. J. Tian, and R. P. Liu, Diffusion-controlled crystal growth in deeply undercooled melt on approaching the glass transition. *Phys. Rev. B* **83**, 014202 (2011).

[89] J. W. P. Schmelzer, A. S. Abyzov, V. M. Fokin, C. Schick, and E. D. Zanotto, Crystallization of glass-forming liquids: Maxima of nucleation, growth, and overall crystallization rates. *J. Non-Cryst. Solids.* **429**, 24 (2015).

[90] S. Pauly, J. Das, N. Mattern, D. H. Kim, and J. Eckert, Phase formation and thermal stability in Cu–Zr–Ti(Al) metallic glasses. *Intermetallics* **17**, 453 (2009).

[91] G. Sun, J. Xu, and P. Harrowell, The mechanism of the ultrafast crystal growth of pure metals from their melts. *Nat. Mater.* **17**, 881 (2018).

[92] J. Orava and A. L. Greer, Kissinger method applied to the crystallization of glass-forming liquids: Regimes revealed by ultra-fast-heating calorimetry. *Thermochimica Acta* **603**, 63 (2014).

[93] W.-L. Chan, R. S. Averback, and Y. Ashkenazy, Anisotropic atomic motion at undercooled crystal/melt interfaces. *Phys. Rev. B* **82**, 020201(R) (2010).

[94] D. W. Henderson, Thermal analysis of non-isothermal crystallization kinetics in glass forming liquids. *J. Non-Cryst. Solids* **30**, 301 (1979)–315.

[95] K. F. Kelton, Analysis of crystallization kinetics. *Mater Sci Eng A* **226–228**, 142 (1997).

[96] E. Zhuravlev, V. Madhavi, A. Lustiger, R. Androsch, and C. Schick, Crystallization of polyethylene at large undercooling. *ACS Macro Lett.* **5**, 365 (2016).

[97] B. Chen, J. Momand, P. A. Vermeulen, and B. J. Kooi, Crystallization kinetics of supercooled liquid Ge–Sb based on ultrafast calorimetry. *Cryst. Growth Des.* **16**, 242 (2016).

[98] M. Salinga, E. Carria, A. Kaldenbach, M. Bornhöfft, J. Benke, J. Mayer, and M. Wuttig, Measurement of crystal growth velocity in a melt-quenched phase-change material. *Nat. Commun.* **4**, 2371 (2013).

[99] P. Zalden, A. von Hoegen, P. Landreman, M. Wuttig, and A. M. Lindenberg, How supercooled liquid phase-change materials crystallize: Snapshots after femtosecond optical excitation. *Chem. Mater.* **27**, 5641 (2015).

[100] P. Zalden, F. Quirin, M. Schumacher, J. Siegel, S. Wei, A. Koc, M. Nicoul, M. Trigo, P. Andreasson, H. Enquist, M. J. Shu, T. Pardini, M. Chollet, D. Zhu, H. Lemke, I. Ronneberger, J. Larsson, A. M. Lindenberg, H. E. Fischer, S. Hau-Riege, D. A. Reis, R. Mazzarello, M. Wuttig, and K. Sokolowski-Tinten, Femtosecond x-ray diffraction reveals a liquid–liquid phase transition in phase-change materials. *Science* **364**, 1062 (2019).

[101] A. Sebastian, M. Le Gallo, and D. Krebs, Crystal growth within a phase change memory cell. *Nat. Commun.* **5**, 4314 (2014).

[102] R. Jeyasingh, S. W. Fong, J. Lee, Z. Li, K.-W. Chang, D. Mantegazza, M. Asheghi, K. E. Goodson, and H.-S. P. Wong, Ultrafast characterization of phase-change material crystallization properties in the melt-quenched amorphous phase. *Nano Lett.* **14**, 3419 (2014).

[103] D. Langstaff, M. Gunn, G. N. Greaves, A. Marsing, and F. Kargl, Aerodynamic levitator furnace for measuring thermophysical properties of refractory liquids. *Rev. Sci. Instrum.* **84**, 124901 (2013).

[104] M. K. Santala, S. Raoux, and G. H. Campbell, Kinetics of liquid-mediated crystallization of amorphous Ge from multi-frame dynamic transmission electron microscopy. *Appl. Phys. Lett.* **107**, 252106 (2015).

[105] M. K. Santala, B. W. Reed, T. Topuria, S. Raoux, S. Meister, Y. Cui, T. LaGrange, G. H. Campbell, and N. D. Browning, Nanosecond *in situ* transmission electron microscope studies of the reversible $Ge_2Sb_2Te_5$ crystalline ⇔ amorphous phase transformation. *J. Appl. Phys.* **111**, 024309 (2012).

[106] M. R. Armstrong, K. Boyden, N. D. Browning, G. H. Campbell, J. D. Colvin, W. J. DeHope, A. M. Frank, D. J. Gibson, F. Hartemann, J. S. Kim, W. E. King, T. B. LaGrange, B. J. Pyke, B. W. Reed, R. M. Shuttlesworth, B. C. Stuart, and B. R. Torralva, Practical considerations for high spatial and temporal resolution dynamic transmission electron microscopy. *Ultramicroscopy* **107**, 356 (2007).

[107] R. Pandian, B. J. Kooi, J. T. M. De Hosson, and A. Pauza, Influence of electron beam exposure on crystallization of phase-change materials. *J. Appl. Phys.* **101**, 053529 (2007).

[108] Yu. P. Ivanov, C. M. Meylan, N. T. Panagiotopoulos, K. Georgarakis, and A. L. Greer, In-situ TEM study of the crystallization sequence in a gold-based metallic glass. *Acta Mater.* **196**, 52 (2020).

[109] S. Vyazovkin, N. Koga, and C. Schick (Eds.), *Handbook of Thermal Analysis and Calorimetr*y. Elsevier, Amsterdam, (2018).

[110] R. Svoboda, D. Brandova, and J. Malek, Thermal behavior of $Ge_{20}Se_yTe_{80-y}$ infrared glasses (for *y* up to 8 at.%). *J. Alloys Compd.* **680**, 427 (2016).

[111] H. E. Kissinger, Reaction kinetics in differential thermal analysis. *Anal. Chem.* **29**, 1702 (1957).

[112] R. L. Blaine and H. E. Kissinger, Homer Kissinger and the Kissinger equation. *Thermochimica Acta* **540**, 1 (2012).

[113] J. Malek, Kinetic analysis of crystallization processes in amorphous materials. *Thermochimica Acta* **355**, 239 (2000).

[114] V. Weidenhof, I. Friedrich, S. Ziegler, and M. Wuttig, Laser induced crystallization of amorphous $Ge_2Sb_2Te_5$ films. *J. Appl. Phys.* **89**, 3168 (2001).

[115] S. Pogatscher, P. J. Uggowitzer, and J. F. Löffler, *In-situ* probing of metallic glass formation and crystallization upon heating and cooling via fast differential scanning calorimetry. *Appl. Phys. Lett.* **104**, 251908 (2014).

[116] W. L. Johnson, G. Kaltenboeck, M. D. Demetriou, J. P. Schramm, X. Liu, K. Samwer, C. P. Kim, and D. C. Hofmann, Beating crystallization in glass-forming metals by millisecond heating and processing. *Science* **332**, 828 (2011).

[117] J. Pries, S. Wei, M. Wuttig, and P. Lucas, Switching between crystallization from the glassy and the undercooled liquid phase in phase change material $Ge_2Sb_2Te_5$. *Adv. Mater.* **31**, 1900784 (2019).

[118] J. Pries, J. C. Sehringer, S. Wei, P. Lucas, and M. Wuttig, Glass transition of the phase change material AIST and its impact on crystallization. *Mater. Sci. Semicond. Process.* **134**, 105990 (2021).

[119] J. C. Mauro, Y. Yue, A. J. Ellison, P. K. Gupta, and D. C. Allan, Viscosity of glass-forming liquids. *Proc. Natl. Acad. Sci.* **106**, 19780 (2009)

[120] D. J. Plazek, C. A. Bero, and I.-C. Chay, The recoverable compliance of amorphous materials. *J. Non-Cryst. Solids* **172–174**, 181 (1994).

[121] G. Eising, T. Van Damme, and B. J. Kooi, Unraveling crystal growth in GeSb phase-change films in between the glass-transition and melting temperatures. *Cryst. Growth Des.* **14**, 3392 (2014).

[122] G. Wicker, A review of recent phase change memory developments. *Proceedings of the European Phase Change Ovonics Symposium* (E\PCOS), Cambridge, United Kingdom, September 4–6, (2016), p. 32.

[123] A. Chen, A review of emerging non-volatile memory (NVM) technologies and applications. *Solid-State Electron*. **125**, 25 (2016).

[124] D. Terebenec, N. Castellani, N. Bernier, V. Sever, P. Kowalczyk, M. Bernard, M.-C. Cyrille, N.-P. Tran, F. Hippert, and P. Noe, Improvement of phase-change memory performance by means of $GeTe/Sb_2Te_3$ superlattices. *Phys. Status Solidi RRL – Rapid Res. Lett.* **15**, 2000538 (2021).

[125] J. Tominaga, N. Miyata, S. Sumi, H. Awano, S. Murakami, Topologically protected spin diffusion and spin generator using chalcogenide superlattices. *npj 2D Mater. Appl.* **4**, 22 (2020).

[126] G. C. Sosso and M. Bernasconi, Harnessing machine learning potentials to understand the functional properties of phase-change materials. *MRS Bull.* **44**, 705 (2019).

[127] D. Loke, T. H. Lee, W. J. Wang, L. P. Shi, R. Zhao, Y. C. Yeo, T. C. Chong, and S. R. Elliott, Breaking the speed limits of phase-change memory. *Science* **336**, 1566 (2012).

[128] F. Rao, K. Ding, Y. Zhou, Y. Zheng, M. Xia, S. Lv, Z. Song, S. Feng, I. Ronneberger, R. Mazzarello, W. Zhang, and E. Ma, Reducing the stochasticity of crystal nucleation to enable subnanosecond memory writing. *Science* **358**, 1423 (2017).

[129] F. Pellizzer, Phase-change materials performances and applications from NOR replacement to storage class memory. *Proceedings of the European Phase Change Ovonics Symposium* (E\PCOS), Cambridge, United Kingdom, September 4–6, (2016), p. 37.

[130] Cisco Annual Internet Report (2018–2023) White Paper, https://www.cisco.com/c/en/us/solutions/collateral/executive-perspectives/annual-internet-report/white-paper-c11-741490.html (accessed on July 12, 2021).

[131] J. A. Kalb, F. Spaepen, and M. Wuttig, Kinetics of crystal nucleation in undercooled droplets of Sb- and Te-based alloys used for phase change recording. *J. Appl. Phys.* **98**, 054910 (2005).

[132] N. Ciocchini, M. Cassinerio, D. Fugazza, and D. Ielmini, Evidence for non-Arrhenius kinetics of crystallization in phase change memory devices. *IEEE Trans. Electron Devices* **60**, 3767 (2013).

[133] U. Russo, D. Ielmini, and A. L. Lacaita, Analytical modeling of chalcogenide crystallization for PCM data-retention extrapolation. *IEEE Trans. Electron Devices* **54**, 2769 (2007).

[134] J. Kalb, F. Spaepen, and M. Wuttig, Atomic force microscopy measurements of crystal nucleation and growth rates in thin films of amorphous Te alloys. *Appl. Phys. Lett.* **84**, 5240 (2004).

[135] J. Akola and R. Jones, Structural phase transitions on the nanoscale: The crucial pattern in the phase-change materials $Ge_2Sb_2Te_5$ and GeTe. *Phys. Rev. B* **76**, 235201 (2007).

[136] H. Neumann, F. Herwig, and W. Hoyer, The short range order of liquid eutectic A_{III}-Te and A_{IV}-Te alloys. *J. Non-Cryst. Solids* **205–207**, 438 (1996).

[137] J. Orava, A. L. Greer, B. Gholipour, D. W. Hewak, and C.E. Smith, Ultra-fast calorimetry study of $Ge_2Sb_2Te_5$ crystallization between dielectric layers. *Appl. Phys. Lett.* **101**, 091906 (2012).

[138] M. K. Santala, B. W. Reed, S. Raoux, T. Topuria, T. LaGrange, and G. H. Campbell, Irreversible reactions studied with nanosecond transmission electron microscopy movies: Laser crystallization of phase change materials. *Appl. Phys. Lett.* **102**, 174105 (2013).

[139] J. Orava, T. H. Lee, S. R. Elliott, and A. L. Greer, *Crystallization of Phase-Change Chalcogenides*, in: Volume 1: *Structure, Properties, Modeling and Applications of Amorphous Chalcogenides* (A. V. Kolobov and K. Shimakawa, eds.), World Scientific, New Jersey, (2021), pp. 367–402.

[140] J. Kalikka, J. Akola, and R. O. Jones, Crystallization processes in the phase change material $Ge_2Sb_2Te_5$: Unbiased density functional/molecular dynamics simulations. *Phys. Rev. B* **94**, 134105 (2016).

[141] I. Ronneberger, W. Zhang, H. Eshet, and R. Mazzarello, Crystallization properties of the $Ge_2Sb_2Te_5$ phase-change compound from advanced simulations. *Adv. Funct. Mater.* **25**, 6407 (2015).

[142] E. Cho, S. Han, D. Kim, H. Horii, and H.-S. Nam, *Ab initio* study on influence of dopants on crystalline and amorphous $Ge_2Sb_2Te_5$. *J. Appl. Phys.* **109**, 043705 (2011).

[143] J. M. Skelton and S. R. Elliott, *In silico* optimization of phase-change materials for digital memories: A survey of first-row transition-metal dopants for $Ge_2Sb_2Te_5$. *J. Phys. Condens. Matter.* **25**, 205801 (2013).

[144] J. Hegedüs and S. R. Elliott, Microscopic origin of the fast crystallization ability of Ge–Sb–Te phase-change memory materials. *Nat. Mater.* **7**, 399 (2008).

[145] T. H. Lee and S. R. Elliott, *Ab initio* computer simulation of the early stages of crystallization: application to $Ge_2Sb_2Te_5$ phase-change materials. *Phys. Rev. Lett.* **107**, 145702 (2011).

[146] T. H. Lee and S. R. Elliott, The relation between chemical bonding and ultrafast crystal growth. *Adv. Mater.* **29**, 1700814 (2017).

[147] M. Wuttig and M. Salinga, Phase-change materials: Fast transformers. *Nat. Mater.* **11**, 270 (2012).

[148] T. P. L. Pedersen, J. Kalb, W. K. Njoroge, D. Wamwangi, M. Wuttig, and F. Spaepen, Mechanical stresses upon crystallization in phase change materials. *Appl. Phys. Lett.* **79**, 3597 (2001).

[149] W. Chong and Z. Koon, Thickness dependent nano-crystallization in $Ge_2Sb_2Te_5$ films and its effect on devices. *Jpn. J. Appl. Phys.* **46**, 2211 (2007).

[150] H.-Y. Cheng, S. Raoux, and Y.-C. Chen, The impact of film thickness and melt-quenched phase on the phase transition characteristics of $Ge_2Sb_2Te_5$. *J. Appl. Phys.* **107**, 074308 (2010).

[151] S. Raoux, J. L. Jordan-Sweet, and A. J. Kellock, Crystallization properties of ultrathin phase change films. *J. Appl. Phys.* **103**, 114310 (2008).

[152] M. Zacharias and P. Streitenberger, Crystallization of amorphous superlattices in the limit of ultrathin films with oxide interfaces. *Phys. Rev. B* **62**, 8391 (2000).

[153] I. Friedrich, V. Weidenhof, W. Njoroge, P. Franz, and M. Wuttig, Structural transformations of $Ge_2Sb_2Te_5$ films studied by electrical resistance measurement. *J. Appl. Phys.* **87**, 4130 (2000).

[154] R. Pandian, B. J. Kooi, J. T. M. De Hosson, and A. Pauza, Influence of capping layers on the crystallization of doped Sb_xTe fast-growth phase-change films. *J. Appl. Phys.* **100**, 123511 (2006).

[155] J. A. Kalb, M. Wuttig, and F. Spaepen, Calorimetric measurements of structural relaxation and glass transition temperatures in sputtered films of amorphous Te alloys used for phase change recording. *J. Mater. Res.* **22**, 748 (2007).

[156] N. Amini, J. Pries, Y. Cheng, C. Persch, M. Wuttig, M. Stolpe, and S. Wei, Thermodynamics and kinetics of glassy and liquid phase-change materials. *Mater. Sci. Semicond. Process.* **135**, 106094 (2021).

[157] J. Kalb, F. Spaepen, T. P. Leervad Pedersen, and M. Wuttig, Viscosity and elastic constants of thin films of amorphous Te alloys used for optical data storage. *J. Appl. Phys.* **94**, 4908 (2003).

[158] B. Chen, Y. Chen, K. Ding, K. Li, F. Jiao, L. Wang, X. Zeng, J. Wang, X. Shen, W. Zhang, F. Rao, and E. Ma, Kinetics features conducive to cache-type nonvolatile phase-change memory. *Chem. Mater.* **31**, 8794 (2019).

[159] C. A. Angell, Water II is a "strong" liquid. *J. Phys. Chem.* **97**, 6339 (1993).

[160] C. Zhang, L. Hu, Y. Yue, and J. C. Mauro, Fragile-to-strong transition in metallic glass-forming liquids. *J. Chem. Phys.* **133**, 014508 (2010).

[161] J. Orava, H. Weber, I. Kaban, and A. L. Greer, Viscosity of liquid Ag–In–Sb–Te: Evidence of a fragile-to-strong crossover. *J. Chem. Phys.* **144**, 194503 (2016).

[162] B. Chen, G. H. ten Brink, G. Palasantzas, and B. J. Kooi, Crystallization kinetics of GeSbTe phase-change nanoparticles resolved by ultrafast calorimetry. *J. Phys. Chem. C* **121**, 8569 (2017).

[163] B. Chen, D. de Wal, G. H. ten Brink, G. Palasantzas, and B. J. Kooi, Resolving crystallization kinetics of GeTe phase-change nanoparticles by ultrafast calorimetry. *Cryst. Growth Des.* **18**, 1041 (2018).

[164] S. Wei, P. Lucas, and C. A. Angell, Phase change alloy viscosities down to T_g using Adam-Gibbs-equation fittings to excess entropy data: A fragile-to-strong transition. *J. Appl. Phys.* **118**, 034903 (2015).

[165] S. Wei, M. Stolpe, O. Gross, W. Hembree, S. Hechler, J. Bednarcik, R. Busch, and P. Lucas, Structural evolution on medium-range-order during the fragile-strong transition in $Ge_{15}Te_{85}$. *Acta Mater.* **129**, 259 (2017).

[166] H. Weber, J. Orava, I. Kaban, J. Pries, and A. L. Greer, Correlating ultrafast calorimetry, viscosity, and structural measurements in liquid GeTe and $Ge_{15}Te_{85}$. *Phys. Rev. Mater.* **2**, 093405 (2018).

[167] S. Stølen, T. Grande, and H.-B. Johnsen, Fragility transition in $GeSe_2$–Se liquids. *Phys. Chem. Chem. Phys.* **4**, 3396 (2002).

[168] Y. Gueguen, T. Rouxel, P. Gadaud, C. Bernard, V. Keryvin, and J.-C. Sangleboeuf, High-temperature elasticity and viscosity of Ge_xSe_{1-x} glasses in the transition range. *Phys. Rev. B* **84** 064201 (2011).

[169] C. Zhou, L. Hu, Q. Sun, H. Zheng, C. Zhang, and Y. Yue, Structural evolution during fragile-to-strong transition in CuZr(Al) glass-forming liquids. *J. Chem. Phys.* **142**, 064508 (2015).

[170] H. Laksmono, T. A. McQueen, J. A. Sellberg, N. D. Loh, C. Huang, D. Schlesinger, R. G. Sierra, C. Y. Hampton, D. Nordlund, M. Beye, A. V. Martin, A. Barty, M. M. Seibert, M. Messerschmidt, G. J. Williams, S. Boutet, K. Amann-Winkel, T. Loerting, L. G. M. Pettersson, M. J. Bogan, and A. Nilsson, Anomalous behavior of the homogeneous ice nucleation rate in "no-man's land". *J. Phys. Chem. Lett.* **6**, 2826 (2015).

[171] J. Kalb, F. Spaepen, and M. Wuttig, Calorimetric measurements of phase transformations in thin films of amorphous Te alloys used for optical data storage. *J. Appl. Phys.* **93**, 2389 (2003).

[172] W. K. Njoroge, H. Dieker, and M. Wuttig, Influence of dielectric capping layers on the crystallization kinetics of $Ag_5In_6Sb_{59}Te_{30}$ films. *J. Appl. Phys.* **96**, 2624 (2004).

[173] Y. Chen, G. Wang, L. Song, X. Shen, J. Wang, J. Huo, R. Wang, T. Xu, S. Dai, and Q. Nie, Unraveling the crystallization kinetics of supercooled liquid GeTe by ultrafast calorimetry. *Cryst. Growth Des.* **17**, 3687 (2017).

[174] I. Kaban, E. Dost, and W. Hoyer, Thermodynamic and structural investigations of heat-treated amorphous Ge–Te alloys. *J. Alloys Compd.* **379**, 166 (2004).

[175] W. Zhang, I. Ronneberger, P. Zalden, M. Xu, M. Salinga, M. Wuttig, and R. Mazzarello, How fragility makes phase-change data storage robust: Insights from ab initio simulations. *Sci. Rep.* **4**, 6529 (2014).

[176] J. Akola and R.O. Jones, Structure of liquid phase change material AgInSbTe from density functional/molecular dynamics simulations. *Appl. Phys. Lett.* **94**, 251905 (2009).

[177] S. Gruner and W. Hoyer, A statistical approach to estimate the experimental uncertainty of viscosity data obtained by the oscillating cup technique. *J. Alloys Compd.* **480**, 629 (2009).

[178] G. Adam and J. H. Gibbs, On the temperature dependence of cooperative relaxation properties in glass-forming liquids. *J. Chem. Phys.* **43**, 139 (1965).

[179] J. Rocca, M. Erazu, M. Fontana, and B. Arcondo, Crystallization process on amorphous GeTeSb samples near to eutectic point $Ge_{15}Te_{85}$. *J. Non-Cryst. Solids* **355**, 2068 (2009).

[180] Y. Tsuchiya, The anomalous negative thermal expansion and the compressibility maximum of molten Ge-Te Alloys. *J. Phys. Soc. Jpn.* **60**, 227 (2013).

[181] Y. Tsuchiya, AC calorimetry of the thermodynamic transition in liquid $Ge_{15}Te_{85}$. *J. Non-Cryst. Solids* **156–158**, 704 (1993).

[182] Y. Tsuchiya and H. Saitoh, Semiconductor-metal transition induced by the structural transition in liquid $Ge_{15}Te_{85}$. *J. Phys. Soc. Jpn.* **62**, 1272 (1993).

[183] L. Battezzati and A. L. Greer, Thermodynamics of $Te_{80}Ge_{20-x}Pb_x$ glass-forming alloys. *J. Mater. Res.* **3**, 570 (1988).

[184] J. P. deNeufville, Chemical aspects of glass formation in telluride systems. *J. Non-Cryst. Solids* **8–10**, 85 (1972).

[185] H. Neumann, W. Matz, W. Hoyee, and M. Wobst, Investigation of the structure of molten $Ge_{15}Te_{85}$ in dependence on temperature. *Phys. Status Solidi A* **90**, 489 (1985).

[186] Q. M. Lu and M. Libera, Microstructural measurements of amorphous GeTe crystallization by hot-stage optical microscopy. *J. Appl. Phys.* **77**, 517 (1995).

[187] H. Weber, M. Schumacher, P. Jovari, Y. Tsuchiya, W. Skrotzki, R. Mazzarello, and I. Kaban, Experimental and *ab initio* molecular dynamics study of the structure and physical properties of liquid GeTe. *Phys. Rev. B* **96**, 054204 (2017).

[188] F. Herwig and M. Wobst, Viskositätsuntersuchungen in System Germanium-Tellur. *Z Met.* **82**, 917 (1991).

[189] N. A. Mauro, M. Blodgett, M. L. Johnson, A. J. Vogt, and K. F. Kelton, A structural signature of liquid fragility. *Nat. Commun.* **5**, 4616 (2014).

[190] K. F. Kelton, Kinetic and structural fragility—a correlation between structures and dynamics in metallic liquids and glasses. *J. Phys. Condens. Matter.* **29**, 023002 (2017).

[191] A. A. Piarristeguy, M. Micoulaut, R. Escalier, P. Jovari, I. Kaban, J. van Eijk, J. Luckas, S. Ravindren, P. Boolchand, and A. Pradel, Structural singularities in Ge_xTe_{100-x} films. *J. Chem. Phys.* **143**, 074502 (2015).

[192] P. Jovari, I. Kaban, J. Steiner, B. Beuneu, A. Schöps, and A. Webb, 'Wrong bonds' in sputtered amorphous $Ge_2Sb_2Te_5$. *J. Phys. Condens. Matter.* **19**, 335212 (2007).

[193] Y. Tsuchiya, Thermodynamic evidence for a structural transition of liquid Te in the supercooled region. *J. Phys. Condens. Matter.* **3**, 3163 (1991).

[194] Y. Tsuchiya, K. Saitoh, and F. Kakinuma, Thermodynamics of structural changes in liquid Ge–Te alloys around the eutectic composition: Specific heat measurements and thermodynamic stability. *Monatshefte Für Chem. Chem. Mon.* **136**, 1963 (2005).

[195] I. Kaban, P. Jovari, W. Hoyer, R. G. Delaplane, and A. Wannberg, Structural studies on Te-rich Ge–Te melts. *J. Phys. Condens. Matter.* **18**, 2749 (2006).

[196] I. Kaban, W. Hoyer, A. Il'inskii, A. Shpak, and P. Jovari, Temperature-dependent structural changes in liquid $Ge_{15}Te_{85}$. *J. Non-Cryst. Solids* **353**, 1808 (2007).

[197] Y. Tsuchiya, Thermodynamics of the structural changes in the liquid Ge–Te system around the Te-rich eutectic composition. *J. Non-Cryst. Solids* **312–314**, 212 (2002).

[198] I. Kaban, P. Jovari, W. Hoyer, and E. Welter, Determination of partial pair distribution functions in amorphous $Ge_{15}Te_{85}$ by simultaneous RMC simulation of diffraction and EXAFS data. *J. Non-Cryst. Solids* **353**, 2474 (2007).

[199] M. Chen, K. A. Rubin, and R. W. Barton, Compound materials for reversible, phase-change optical data storage. *Appl. Phys. Lett.* **49**, 502 (1986).

[200] K. Georgarakis, L. Hennet, G. A. Evangelakis, J. Antonowicz, G. B. Bokas, V. Honkimaki, A. Bytchkov, M. W. Chen, and A. R. Yavari, Probing the structure of a liquid metal during vitrification. *Acta Mater.* **87**, 174 (2015).

[201] Y. Xu, N. G. Petrik, R. S. Smith, B. D. Kay, and G. A. Kimmel, Growth rate of crystalline ice and the diffusivity of supercooled water from 126 to 262 K. *Proc. Natl. Acad. Sci.* **113**, 14921 (2016).

[202] G.-F. Zhou, Materials aspects in phase change optical recording. *Mater. Sci. Eng. A* **304–306**, 73 (2001).

[203] S. Raoux, Phase change materials. *Annu. Rev. Mater. Res.* **39**, 25 (2009).

[204] D. Kuzum, S. Yu, and H.-S. Philip Wong, Synaptic electronics: Materials, devices and applications. *Nanotechnology* **24**, 382001 (2013).

[205] T. Ishikawa, P.-F. Paradis, J. T. Okada, and Y. Watanabe, Viscosity measurements of molten refractory metals using an electrostatic levitator. *Meas. Sci. Technol.* **23**, 025305 (2012).

[206] N. Yamada, E. Ohno, K. Nishiuchi, N. Akahira, and M. Takao, Rapid-phase transitions of GeTe-Sb_2Te_3 pseudobinary amorphous thin films for an optical disk memory. *J. Appl. Phys.* **69**, 2849 (1991).

[207] T. H. Lee, D. Loke, K.-J. Huang, W.-J. Wang, and S. R. Elliott, Tailoring transient-amorphous states: Towards fast and power-efficient phase-change memory and neuromorphic computing. *Adv. Mater.* **26**, 7493 (2014).

[208] K. Kohary and C. D. Wright, Modelling the phase-transition in phase-change materials. *Phys. Status Solidi B* **250**, 944 (2013).

[209] S. Senkader and C. D. Wright, Models for phase-change of $Ge_2Sb_2Te_5$ in optical and electrical memory devices. *J. Appl. Phys.* **95**, 504 (2004).

[210] T. Gille, K. D. Meyer, and D. J. Wouters, Amorphous-crystalline phase transitions in chalcogenide materials for memory applications. *Phase Transit.* **81**, 773 (2008).

[211] G. W. Burr, P. Tchoulfian, T. Topuria, C. Nyffeler, K. Virwani, A. Padilla, R. M. Shelby, M. Eskandari, B. Jackson, and B.-S. Lee, Observation and modeling of polycrystalline grain formation in $Ge_2Sb_2Te_5$. *J. Appl. Phys.* **111**, 104308 (2012).

[212] S. Privitera, C. Bongiorno, E. Rimini, and R. Zonca, Crystal nucleation and growth processes in $Ge_2Sb_2Te_5$. *Appl. Phys. Lett.* **84**, 4448 (2004).

[213] K. F. Kelton and A. L. Greer, Transient nucleation effects in glass formation. *J. Non-Cryst. Solids* **79**, 295 (1986).

[214] K. Matusita and M. Tashiro, Rate of homogeneous nucleation in alkali disilicate glasses. *J. Non-Cryst. Solids* **11**, 471 (1973).

[215] E. D. Zanotto, *Crystals in Glass: A Hidden Beauty*, John Wiley & Sons, New Jersey, (2013).

[216] B.-S. Lee, G. W. Burr, R. M. Shelby, S. Raoux, C. T. Rettner, S. N. Bogle, K. Darmawikarta, S. G. Bishop, and J. R. Abelson, Observation of the role of subcritical nuclei in crystallization of a glassy solid. *Science* **326**, 980 (2009).

[217] K. Darmawikarta, B.-S. Lee, R. M. Shelby, S. Raoux, S. G. Bishop, and J. R. Abelson, Quasi-equilibrium size distribution of subcritical nuclei in amorphous phase change AgIn-Sb_2Te. *J. Appl. Phys.* **114**, 034904 (2013).

[218] B.-S. Lee, R .M. Shelby, S. Raoux, C. T. Retter, G. W. Burr, S. N. Bogle, K. Darmawikarta, S. G. Bishop, and J. R. Abelson, Nanoscale nuclei in phase change materials: Origin of different crystallization mechanisms of $Ge_2Sb_2Te_5$ and AgInSbTe. *J. Appl. Phys.* **115**, 063506 (2014).

[219] G. Ruitenberg, A. K. Petford-Long, and R. C. Doole, Determination of the isothermal nucleation and growth parameters for the crystallization of thin $Ge_2Sb_2Te_5$ films. *J. Appl. Phys.* **92**, 3116 (2002).

[220] S. Privitera, S. Lombardo, C. Bongiorno, E. Rimini, and A. Pirovano, Phase change mechanisms in $Ge_2Sb_2Te_5$. *J. Appl. Phys.* **102**, 013516 (2007).

[221] B.-S. Lee, K. Darmawikarta, S. Raoux, Y.-H. Shih, Y. Zhu, S. G. Bishop, and J. R. Abelson, Distribution of nanoscale nuclei in the amorphous dome of a phase change random access memory. *Appl. Phys. Lett.* **104**, 071907 (2014).

[222] Y. Wang, F. Y. Zuo, H. Huang, F. X. Zhai, T. S. Lai, and Y. Q. Wu, Transient phase change in picosecond laser pulse-driven crystallization process. *Proc. SPIE* **7517**, 75170S (2009).

[223] E. G. Yeo, R. Zhao, L. P. Shi, K. G. Lim, T. C. Chong, and I. Adesida, Transient phase change effect during the crystallization process in phase change memory devices. *Appl. Phys. Lett.* **94**, 243504 (2009).

[224] R. E. Simpson, M. Krbal, P. Fons, A. V. Kolobov, J. Tominaga, T. Uruga, and H. Tanida, Toward the ultimate limit of phase change in $Ge_2Sb_2Te_5$. *Nano Lett.* **10**, 414 (2010).

[225] V. G. Karpov, Y. A. Kryukov, S. D. Savransky, and I. V. Karpov, Nucleation switching in phase change memory. *Appl. Phys. Lett.* **90**, 123504 (2007).

[226] I. Valov, R. Waser, J. R. Jameson, and M. N. Kozicki, Electrochemical metallization memories—fundamentals, applications, prospects. *Nanotechnology* **22**, 254003 (2011).

[227] J. Orava, M. N. Kozicki, S. N. Yannopoulos, and A. L. Greer, Reversible migration of silver on memorized pathways in Ag-$Ge_{40}S_{60}$ films. *AIP Adv.* **5**, 077134 (2015).

[228] J. Orava, Y. Wen, J. Prikryl, T. Wagner, N. A. Stelmashenko, M. Chen, and A. L. Greer, Preferred location for conducting filament formation in thin-film nano-ionic electrolyte: Study of microstructure by atom-probe tomography. *J. Mater. Sci. Mater. Electron.* **28**, 6846 (2017).

[229] M. Frumar and T. Wagner, Ag doped chalcogenide glasses and their applications. *Curr. Opin. Solid State Mater. Sci.* **7**, 117 (2003).

[230] B. Block, A. O. Thornton, J. Ingwersen, and W. Daschner, Gray scale mask and depth pattern transfer technique using inorganic chalcogenide glass. US6033766A, (2000).

[231] M. F. Ashby and A. L. Greer, Metallic glasses as structural materials. *Scr. Mater.* **54**, 321 (2006).

[232] J. M. Silveyra, E. Ferrara, D. L. Huber, and T. C. Monson, Soft magnetic materials for a sustainable and electrified world. *Science* **362**, eaao0195 (2018).

[233] P. Meagher, E. D. O'Cearbhaill, J. H. Byrne, and D. J. Browne, Bulk metallic glasses for implantable medical devices and surgical tools. *Adv. Mater.* **28**, 5755 (2016).

[234] D. C. Hofmann, L. Hamill, E. Christiansen, and S. Nutt, Hypervelocity impact testing of a metallic glass-stuffed Whipple shield. *Adv. Eng. Mater.* **17**, 1313 (2015).

[235] F. Spaepen, A microscopic mechanism for steady state inhomogeneous flow in metallic glasses, *Acta Metall.* **25**, 407 (1977).

[236] A. L. Greer, Y. Q. Cheng, and E. Ma, Shear bands in metallic glasses. *Mater. Sci. Eng. R Rep.* **74**, 71 (2013).

[237] F. Shimizu, S. Ogata, and J. Li, Yield point of metallic glass. *Acta Mater.* **54**, 4293 (2006).

[238] J. Orava, I. Kaban, M. Benkocka, X. Han, I. Soldatov, and A. L. Greer, Fast-heating-induced formation of metallic-glass/crystal composites with enhanced plasticity. *Thermochimica Acta* **677**, 198 (2019).

[239] S. Scudino, J. J. Bian, H. Shakur Shahabi, D. Şopu, J. Sort, J. Eckert, and G. Liu, Ductile bulk metallic glass by controlling structural heterogeneities. *Sci. Rep.* **8**, 9174 (2018).

[240] S. Pauly, S. Gorantla, G. Wang, U. Kühn, and J. Eckert, Transformation-mediated ductility in CuZr-based bulk metallic glasses. *Nat. Mater.* **9**, 473 (2010).

[241] A. L. Greer, *Metallic Glasses*, in: *Physical Metallurgy* (D.E. Laughlin and K. Hono, eds.), Elsevier, Oxford, (2014), pp. 305–385.

[242] Y. H. Liu, D. Wang, K. Nakajima, W. Zhang, A. Hirata, T. Nishi, A. Inoue, and M. W. Chen, Characterization of nanoscale mechanical heterogeneity in a metallic glass by dynamic force microscopy. *Phys. Rev. Lett.* **106**, 125504 (2011).

[243] J. Orava, S. Balachandran, X. Han, O. Shuleshova, E. Nurouzi, I. Soldatov, S. Oswald, O. Gutowski, O. Ivashko, A.-C. Dippel, M. v Zimmermann, Y. P. Ivanov, A. L. Greer, D. Raabe, M. Herbig, and I. Kaban, In situ correlation between metastable phase-transformation mechanism and kinetics in a metallic glass. *Nat. Commun.* **12**, 2839 (2021).

[244] J. Orava, K. Kosiba, X. Han, I. Soldatov, O. Gutowski, O. Ivashko, A.-C. Dippel, M. v. Zimmermann, A. Rothkirch, J. Bednarcik, U. Kühn, H. Siegel, S. Ziller, A. Horst, K. Peukert, R. Voigtländer, D. Lindackers, and I. Kaban, Fast-current-heating devices to study *in situ* phase formation in metallic glasses by using high-energy synchrotron radiation. *Rev. Sci. Instrum.* **91**, 073901 (2020).

[245] Q. Cheng, X. Han, I. Kaban, I. Soldatov, W. H. Wang, Y. H. Sun, and J. Orava, Phase transformations in a Cu–Zr–Al metallic glass. *Scr. Mater.* **183**, 61 (2020).

[246] T. Kozieł, Estimation of cooling rates in suction casting and copper-mould casting processes. *Arch. Metall. Mater.* **60**, 767 (2015).

[247] Y Y. Wu, H. Wang, H. H. Wu, Z. Y. Zhang, X. D. Hui, G. L. Chen, D. Ma, X. L. Wang, and Z. P. Lu, Formation of Cu–Zr–Al bulk metallic glass composites with improved tensile properties. *Acta Mater.* **59**, 2928 (2011).

[248] K. Kosiba, S. Scudino, R. Kobold, U. Kühn, A. L. Greer, J. Eckert, and S. Pauly, Transient nucleation and microstructural design in flash-annealed bulk metallic glasses. *Acta Mater.* **127**, *416* (2017).

[249] I. Kalay, M. J. Kramer, and R. E. Napolitano, High-accuracy X-ray diffraction analysis of phase evolution sequence during devitrification of $Cu_{50}Zr_{50}$ metallic glass. *Metall. Mater. Trans. A* **42**, 1144 (2011).

[250] I. Kalay, M. J. Kramer, and R. E. Napolitano, Crystallization kinetics and phase transformation mechanisms in $Cu_{56}Zr_{44}$ glassy alloy. *Metall. Mater. Trans. A* **46**, 3356.

[251] T. Cullinan, I. Kalay, Y. E. Kalay, M. Kramer, and R. Napolitano, Kinetics and mechanisms of isothermal devitrification in amorphous $Cu_{50}Zr_{50}$. *Metall. Mater. Trans. A* **46**, 600 (2015).

[252] K. Hajlaoui, A. R. Yavari, B. Doisneau, A. Lemoulec, W. J. F. Botta, G. Vaughan, A. L. Greer, A. Inoue, W. Zhang, and Å. Kvick, Shear delocalization and crack blunting of a metallic glass containing nanoparticles: In situ deformation in TEM analysis. *Scr. Mater.* **54**, 1829 (2006).

[253] K. Hajlaoui, N. Alsaleh, N. H. Alrasheedi, and A. R. Yavari, Coalescence and subsequent twinning of nanocrystals during deformation of CuZr-based metallic glasses: The grain size effect. *J. Non-Cryst. Solids* **464**, 39 (2017).

[254] F.-F. Wu, K. C. Chan, S.-S. Jiang, S.-H. Chen, and G. Wang, Bulk metallic glass composite with good tensile ductility, high strength and large elastic strain limit. *Sci. Rep.* **4**, 5302 (2015).

[255] D. Wang, J. Mu, Y. Chen, Y. Qi, W. Wu, Y. Wang, H. Xu, H. Zhang, and K. An, A study of stress-induced phase transformation and micromechanical behavior of CuZr-based alloy by in-situ neutron diffraction. *J. Alloys Compd.* **696**, 1096 (2017).

[256] Y. Feng, W. B. Liao, J. Zheng, L. W. Wang, Y. Zhang, J. Sun, and F. Pan, Nanocrystals generated under tensile stress in metallic glasses with phase selectivity. *Nanoscale* **9**, 15542 (2017).

[257] S. H. Hong, J. T. Kim, J. M. Park, G. Song, W. M. Wang, and K. B. Kim, Mechanical, deformation and fracture behaviors of bulk metallic glass composites reinforced by spherical B2 particles. *Prog. Nat. Sci. Mater. Int.* **28**, 704 (2018).

[258] X.-L. Wang, J. Almer, C. T. Liu, Y. D. Wang, J. K. Zhao, A. D. Stoica, D. R. Haeffner, and W. H. Wang, *In situ* synchrotron study of phase transformation behaviors in bulk metallic glass by simultaneous diffraction and small angle scattering. *Phys. Rev. Lett.* **91**, 265501 (2003).

[259] G. Song, C. Lee, S. H. Hong, K. B. Kim, S. Chen, D. Ma, K. An, and P. K. Liaw, Martensitic transformation in a B2-containing CuZr-based BMG composite revealed by *in situ* neutron diffraction. *J. Alloys Compd.* **723**, 714 (2017).

[260] D. M. Wang, Y. Chen, J. Mu, Z. W. Zhu, H. F. Zhang, Y. D. Wang, and K. An, An in situ neutron diffraction study of plastic deformation in a $Cu_{46.5}Zr_{46.5}Al_7$ bulk metallic glass composite. *Scr. Mater.* **153**, 118 (2018).

[261] P. Xue, Y. Huang, S. Jiang, and J. Sun, Cryogenic-temperature-induced phase transformation in a CuZr-based bulk metallic glass composite under tensile stress. *Mater. Lett.* **262**, 127065 (2020).

[262] V. M. Villapun, F. Esat, S. Bull, L. G. Dover, and S. Gonzalez, Tuning the mechanical and antimicrobial performance of a Cu-based metallic glass composite through cooling rate control and annealing. *Materials* **10**, 506 (2017).

[263] T. Gustmann, J. M. dos Santos, P. Gargarella, U. Kühn, J. Van Humbeeck, and S. Pauly, Properties of Cu-based shape-memory alloys prepared by selective laser melting. *Shape Mem. Superelasticity* **3**, 24 (2017).

[264] K. Kosiba, *Flash-Annealing of Cu-Zr-Al-based Bulk Metallic Glasses*, Ph.D. Thesis, TU Dresden, Germany, (2017).

[265] D. Lee, B. Zhao, E. Perim, H. Zhang, P. Gong, Y. Gao, Y. Liu, C. Toher, S. Curtarolo, J. Schroers, and J. J. Vlassak, Crystallization behavior upon heating and cooling in $Cu_{50}Zr_{50}$ metallic glass thin films. *Acta Mater.* **121**, 68 (2016).

[266] J. E. K. Schawe and J. F. Löffler, Existence of multiple critical cooling rates which generate different types of monolithic metallic glass. *Nat. Commun.* **10**, 1337 (2019).

[267] V. Kokotin, H. Hermann, and J. Eckert, Computer simulation of the matrix–inclusion interphase in bulk metallic glass based nanocomposites*. J. Phys. Condens. Matter.* **23**, 425403 (2011).

[268] R. Müller, E. D. Zanotto, and V. M. Fokin, Surface crystallization of silicate glasses: Nucleation sites and kinetics. *J. Non-Cryst. Solids* **274**, 208 (2000).

[269] J. Zheng, Y. Miao, H. Zhang, S. Chen, D. Lee, R. Arróyave, and J. J. Vlassak, Phase transformations in equiatomic CuZr shape memory thin films analyzed by differential nanocalorimetry. *Acta Mater.* **159**, 320 (2018).

[270] I. Kaban, P. Jovari, B. Escher, D. T. Tran, G. Svensson, M. A. Webb, T. Z. Regier, V. Kokotin, B. Beuneu, T. Gemming, and J. Eckert, Atomic structure and formation of CuZrAl bulk metallic glasses and composites. *Acta Mater.* **100**, 369 (2015).

[271] W. Guo, J. Saida, M. Zhao, S. Lü, and S. Wu, Non-thermal crystallization process in heterogeneous metallic glass upon deep cryogenic cycling treatment. *J. Mater. Sci.* **54**, 8778 (2019).

[272] V. Schmidt, H. Rösner, M. Peterlechner, G. Wilde, and P. M. Voyles, Quantitative measurement of density in a shear band of metallic glass monitored along its propagation direction. *Phys. Rev. Lett.* **115**, 035501 (2015).

[273] B. Huang, T. P. Ge, G. L. Liu, J. H. Luan, Q. F. He, Q. X. Yuan, W. X. Huang, K. Zhang, H. Y. Bai, C. H. Shek, C. T. Liu, Y. Yang, and W. H. Wang, Density fluctuations with fractal order in metallic glasses detected by synchrotron X-ray nano-computed tomography. *Acta Mater.* **155**, 69 (2018).

[274] V. Hieronymus-Schmidt, H. Rösner, G. Wilde, and A. Zaccone, Shear banding in metallic glasses described by alignments of Eshelby quadrupoles. *Phys. Rev. B* **95**, 134111 (2017).

[275] C. Liu, Z. Cai, X. Xia, V. Roddatis, R. Yuan, J. M. Zuo, and R. Maaß, Shear-band structure and chemistry in a Zr-based metallic glass probed with nano-beam x-ray fluorescence and transmission electron microscopy. *Scr. Mater.* **169**, 23 (2019).

[276] H. Rösner, M. Peterlechner, C. Kübel, V. Schmidt, and G. Wilde, Density changes in shear bands of a metallic glass determined by correlative analytical transmission electron microscopy. *Ultramicroscopy* **142**, 1 (2014).

[277] W. H. Jiang and M. Atzmon, The effect of compression and tension on shear-band structure and nanocrystallization in amorphous $Al_{90}Fe_5Gd_5$: A high-resolution transmission electron microscopy study. *Acta Mater.* **51**, 4095 (2003).

[278] H. Chen, Y. He, G. J. Shiflet, and S. J. Poon, Deformation-induced nanocrystal formation in shear bands of amorphous alloys. *Nature* **367**, 541 (1994).

[279] S. Balachandran, J. Orava, M. Köhler, A. J. Breen, I. Kaban, D. Raabe, and M. Herbig, Elemental re-distribution inside shear bands revealed by correlative atom-probe tomography and electron microscopy in a deformed metallic glass. *Scr. Mater.* **168**, 14 (2019).

[280] F. Kargl, H. Weis, T. Unruh, and A. Meyer, Self diffusion in liquid aluminium. *J. Phys. Conf. Ser.* **340**, 012077 (2012).

[281] J. Burke and T. R. Ramachandran, Self-diffusion in aluminum at low temperatures. *Metall. Mater. Trans. B* **3**, 147 (1972).

[282] M. R. Chellali, S. H. Nandam, and H. Hahn, Deformation-induced chemical inhomogeneity and short-circuit diffusion in shear bands of a bulk metallic glass. *Phys. Rev. Lett.* **125**, 205501 (2020).

[283] A. V. Kolobov (Ed.), *Photo-Induced Metastability in Amorphous Semiconductors*, Wiley-VCH, Weinheim, (2003).

[284] S. N. Yannopoulos, *Athermal Photoelectronic Effects in Non-Crystalline Chalcogenides: Current Status and Beyond*, in: *Volume 1: Structure, Properties, Modeling and Applications of Amorphous Chalcogenides* (A. V. Kolobov and K. Shimakawa, eds.), World Scientific, New Jersey, (2021), pp. 251–319.

[285] S. N. Yannopoulos and M. L. Trunov, Photoplastic effects in chalcogenide glasses: A review. *Phys. Status Solidi B Basic Res.* **246**, 1773 (2009).

[286] S. N. Yannopoulos, Structure and photo-induced effects in elemental chalcogens: A review on Raman scattering. *J. Mater. Sci. Mater. Electron.* **31**, 7565 (2020).

[287] M. Frumar, B. Frumarova, and T. Wagner, *Amorphous and Glassy Semiconducting Chalcogenides*, in: *Comprehensive Semiconductor Science and Technology* (P. Bhattacharya, R. Fornari, and H. Kamimura, eds.), Elsevier, Amsterdam, (2011), pp. 206–261.

[288] K. Tanaka, Photo-induced phenomena in chalcogenide glass: Comparison with those in oxide glass and polymer. *J. Non-Cryst. Solids* **352**, 2580 (2006).

[289] J. Singh and K. Shimakawa, *Advances in Amorphous Semiconductors*, Taylor&Francis, London, (2003).

[290] W. von Ammon, A. Sattler, and G. Kissinger, *Defects in Monocrystalline Silicon*, in: *Springer Handbook of Electronic and Photonic Materials* (S. Kasap and P. Capper, eds.), Springer International Publishing, Cham, (2017), pp. 111–132.

[291] P. Luo, C. R. Cao, F. Zhu, Y. M. Lv, Y. H. Liu, P. Wen, H. Y. Bai, G. Vaughan, M. di Michiel, B. Ruta, and W. H. Wang, Ultrastable metallic glasses formed on cold substrates. *Nat. Commun*. 9, 1389 (2018).

[292] H. Hisakuni and K. Tanaka, Optical microfabrication of chalcogenide glasses. *Science* **270**, 974 (1995).

[293] B. J. Eggleton, B. Luther-Davies, and K. Richardson, Chalcogenide photonics. *Nat Photon.* **5**, 141 (2011).

[294] S. Danto, P. Houizot, C. Boussard-Pledel, X.-H. Zhang, F. Smektala, and J. Lucas, A family of far-infrared-transmitting glasses in the Ga–Ge–Te system for space applications. *Adv. Funct. Mater.* **16**, 1847 (2006).

[295] K. Tanaka, *Optical Nonlinearity in Photonic Glasses*, in: *Springer Handbook of Electronic and Photonic Materials* (S. Kasap and P. Capper, eds.), Springer International Publishing, Cham, (2017), pp. 1081–1094.

[296] L. Strizik, J. Zhang, T. Wagner, J. Oswald, T. Kohoutek, B. M. Walsh, J. Prikryl, R. Svoboda, C. Liu, B. Frumarova, M. Frumar, M. Pavlista, W. J. Park, and J. Heo, Green, red and near-infrared photon up-conversion in Ga–Ge–Sb–S:Er^{3+} amorphous chalcogenides. *J. Lumin.* **147**, 209 (2014).

[297] A. Cornet, C. Martinet, V. Martinez, and D. de Ligny, Evidence of polyamorphic transitions during densified SiO_2 glass annealing. *J. Chem. Phys.* **151**, 164502 (2019).

[298] G. N. Greaves and S. Sen, Inorganic glasses, glass-forming liquids and amorphizing solids. *Adv. Phys.* **56**, 1 (2007).

[299] P. F. McMillan, G. N. Greaves, M. Wilson, M. C. Wilding, and D. Daisenberger, *Polyamorphism and Liquid–Liquid Phase Transitions in Amorphous Silicon and Supercooled Al_2O_3–Y_2O_3 Liquids*, in: *Liquid Polymorphism* (H. E. Stanley, ed.), John Wiley & Sons, New Jersey, (2013): pp. 309–353.

[300] H. W. Sheng, H. Z. Liu, Y. Q. Cheng, J. Wen, P. L. Lee, W. K. Luo, S. D. Shastri, and E. Ma, Polyamorphism in a metallic glass. *Nat. Mater.* **6**, 192 (2007).

[301] L. Belhadi, F. Decremps, S. Pascarelli, L. Cormier, Y. Le Godec, S. Gorsse, F. Baudelet, C. Marini, and G. Garbarino, Polyamorphism in cerium based bulk metallic glasses: Electronic and structural properties under pressure and temperature by x-ray absorption techniques. *Appl. Phys. Lett.* **103**, 111905 (2013).

[302] B. Kalkan, R. P. Dias, C.-S. Yoo, S. M. Clark, and S. Sen, Polyamorphism and pressure-induced metallization at the rigidity percolation threshold in densified $GeSe_4$ glass. *J. Phys. Chem. C* **118**, 5110 (2014).

[303] B. Kalkan, G. Okay, B. G. Aitken, S. M. Clark, and S. Sen, Unravelling the mechanism of pressure induced polyamorphic transition in an inorganic molecular glass. *Sci. Rep.* **10**, 5208 (2020).

[304] A. V. Kolobov, P. Fons, M. Krbal, and J. Tominaga, Amorphous phase of GeTe-based phase-change memory alloys: Polyvalency of Ge—Te bonding and polyamorphism. *Phys. Status Solidi A* **209**, 1031 (2012).

[305] B. Kalkan, S. Sen, J.-Y. Cho, Y.-C. Joo, S. M. Clark, Observation of polyamorphism in the phase change alloy $Ge_1Sb_2Te_4$. *Appl. Phys. Lett.* **101**, 151906 (2012).

[306] Y. Nguyen Thi, K. Rademann, and F. Emmerling, Direct evidence of polyamorphism in paracetamol. *CrystEngComm.* **17**, 9029 (2015).

[307] W. Tang and J. H. Perepezko, Polyamorphism and liquid-liquid transformations in D-mannitol. *J. Chem. Phys.* **149**, 074505 (2018).

[308] H. Tanaka, Liquid–liquid transition and polyamorphism. *J. Chem. Phys.* **153**, 130901 (2020).

[309] K. Shimakawa, A. Kolobov, and S. R. Elliott, Photoinduced effects and metastability in amorphous semiconductors and insulators. *Adv. Phys.* **44**, 475 (1995).

[310] F. Kyriazis and S. N. Yannopoulos, Colossal photostructural changes in chalcogenide glasses: Athermal photoinduced polymerization in As_xS_{100-x} bulk glasses revealed by near-bandgap Raman scattering. *Appl. Phys. Lett.* **94**, 101901 (2009).

[311] S. N. Yannopoulos, F. Kyriazis, and I. P. Chochliouros, Composition-dependent photosensitivity in As–S glasses induced by bandgap light: Structural origin by Raman scattering. *Opt. Lett.* **36**, 534 (2011).

[312] A. Siokou, M. Kalyva, S. N. Yannopoulos, M. Frumar, and P. Nemec, Photoemission studies of As_xSe_{100-x} (*x*: 0, 50, 100) films prepared by pulsed-laser deposition - The effect of annealing. *J. Phys. Condens. Matter.* **18**, 5525 (2006).

[313] M. Kalyva, A. Siokou, S. N. Yannopoulos, T. Wagner, M. Krbal, J. Orava, and M. Frumar, Soft x-ray induced Ag diffusion in amorphous pulse laser deposited $As_{50}Se_{50}$ thin films: An x-ray photoelectron and secondary ion mass spectroscopy study. *J. Appl. Phys.* **104**, 043704 (2008).

[314] V. A. Bershtein, L. M. Egorova, A. V. Kolobov, and V. A. Ryzhov, A differential scanning calorimetric study of structural changes in thin As-Se films. *Sov. J. Glass Phys. Chem.* **18**, 367 (1992).

[315] M. Kalyva, J. Orava, A. Siokou, M. Pavlista, T. Wagner, and S. N. Yannopoulos, Reversible amorphous-to-amorphous transitions in chalcogenide films: Correlating changes in structure and optical properties. *Adv. Funct. Mater.* **23**, 2052 (2013).

[316] J. Orava, T. Kohoutek, and T. Wagner, *Deposition Techniques for Chalcogenide Thin Films*, in: *Chalcogenide Glasses, Preparation, Properties and Applications* (J. L. Adam and X. Zhang, eds.), Woodhead Publishing Limited, Oxford, (2014), pp. 265–309.

[317] L. Cauchy, *Bull Sci Math*. **14**, 9 (1830).

[318] G. E. Jellison and F. A. Modine, Parameterization of the optical functions of amorphous materials in the interband region. *Appl. Phys. Lett.* **69**, 371 (1996).

[319] G. E. Jellison and F. A. Modine, Erratum: '"Parameterization of the optical functions of amorphous materials in the interband region"' [Appl. Phys. Lett. 69, 371 (1996)]. *Appl. Phys. Lett.* **69**, 2137 (1996).

[320] A. S. Ferlauto, G. M. Ferreira, J. M. Pearce, C. R. Wronski, R. W. Collins, X. Deng, and G. Ganguly, Analytical model for the optical functions of amorphous semiconductors from the near-infrared to ultraviolet: Applications in thin film photovoltaics. *J. Appl. Phys.* **92**, 2424 (2002).

[321] I. Ohlidal, D. Franta, M. Siler, F. Vizda, M. Frumar, J. Jedelsky, and J. Omasta, Comparison of dispersion models in the optical characterization of As–S chalcogenide thin films. *J. Non-Cryst. Solids* **352**, 5633 (2006).

[322] J. Orava, J. Sik, T. Wagner, and M. Frumar, Optical properties of $As_{33}S_{67-x}Se_x$ bulk glasses studied by spectroscopic ellipsometry. *J. Appl. Phys.* **103**, 083512 (2008).

[323] J. Sik, *Studium optických funkcí polovodičů pomocí spektroskopické elipsometrie*, Habilitation Thesis, Masaryk University, (2013).

[324] J. Orava, T. Wagner, J. Sik, J. Prikryl, M. Frumar, and L. Benes, Optical properties and phase change transition in $Ge_2Sb_2Te_5$ flash evaporated thin films studied by temperature dependent spectroscopic ellipsometry. *J. Appl. Phys.* **104**, 043523 (2008).

[325] M. I. Zavetova and I. Gregora, Refractive index of amorphous arsenic. *Phys. Status Solidi A* **43**, K109.

[326] T. S. Moss, *Optical Properties of Semiconductors*, Butterworths Scientific Publications, London, (1959).

[327] J. Mistrik, S. Kasap, H. E. Ruda, C. Koughia, and J. Singh, *Optical Properties of Electronic Materials: Fundamentals and Characterization*, in: *Springer Handbook of Electronic and Photonic Materials* (S. Kasap and P. Capper, eds.), Springer International Publishing, Cham, (2017), pp. 47–83.

[328] K. Tanaka and K. Shimakawa, *Amorphous Chalcogenide Semiconductors and Related Materials*, Springer, New York, (2011).

[329] K. Tanaka, Minimal Urbach energy in non-crystalline materials. *J. Non-Cryst. Solids* **389**, 35 (2014).

[330] A. Bernas, C. Ferradini, and J.-P. Jay-Gerin, On the electronic structure of liquid water: Facts and reflections. *Chem. Phys.* **222**, 151 (1997).

[331] M. Frumar, B. Frumarova, T. Wagner, and P. Nemec, *Photo-Induced Phenomena in Amorphous and Glassy Chalcogenides*, in: *Photo-Induced Metastability in Amorphous Semiconductors* (A. V. Kolobov, ed.), Wiley-VCH, Weinheim, (2003), pp. 23–44.

[332] P. Nemec and M. Frumar, Irreversible photoinduced changes in $As_{48}S_{52}$ amorphous thin films prepared by pulsed laser deposition. *Thin Solid Films* **517**, 3635 (2009).

[333] E. J. Evans, J. H. Helbers, and S. R. Ovshinsky, Reversible conductivity transformations in chalcogenide alloy films. *J. Non-Cryst. Solids* **2**, 334 (1970).

[334] A. Bienenstock, F. Betts, and S. R. Ovshinsky, Structural studies of amorphous semiconductors. *J. Non-Cryst. Solids* **2**, 347 (1970).

[335] J. E. Griffiths, G. P. Espinosa, J. P. Remeika, and J. C. Phillips, Reversible reconstruction and crystallization of $GeSe_2$ glass. *Solid State Commun.* **40**, 1077 (1981).

[336] J. E. Griffiths, G. P. Espinosa, J. P. Remeika, and J. C. Phillips, Reversible quasicrystallization in $GeSe_2$ glass. *Phys. Rev. B* **25**, 1272 (1982).

[337] M. Frumar, H. Ticha, M. Vlcek, J. Klikorka, and L. Tichy, Photostructural changes in some ternary Ge-Sb-S chalcogenide layers. Czechoslov. *J. Phys.* **31**, 441 (1981).

[338] S. R. Elliott and A. V. Kolobov, Athermal light-induced vitrification of $As_{50}Se_{50}$ films. *J. Non-Cryst. Solids* **128**, 216 (1991).

[339] R. Prieto-Alcon, E. Marquez, J. M. Gonzalez-Leal, R. Jimenez-Garay, A. V. Kolobov, and M. Frumar, Reversible and athermal photo-vitrification of $As_{50}Se_{50}$ thin films deposited onto silicon wafer and glass substrates. *Appl. Phys. A: Mater. Sci. Process.* **68**, 653 (1999).

[340] A. V. Kolobov, V. A. Bershtein, and S. R. Elliott, Athermal photo-amorphization of $As_{50}Se_{50}$ films. *J. Non-Cryst. Solids* **150**, 116 (1992).

[341] A. V. Kolobov and S. R. Elliott, Reversible photo-amorphization of crystalline films of $As_{50}Se_{50}$. *J. Non-Cryst. Solids* **189**, 297 (1995).

[342] A. V. Kolobov and S.R. Elliott, Reversible photo-amorphization of a crystallized $As_{50}Se_{50}$ alloy. *Philos. Mag. B* **71**, 1 (1995).

[343] E. Marquez, C. Corrales, J. B. Ramirez-Malo, J. Reyes, J. Fernandez-Pena, P. Villares, and R. Jimenez-Garay, On the reversible and athermal photo-vitrification phenomenon of $As_{50}Se_{50}$ chalcogenide thin films. *Mater. Lett.* **20**, 183 (1994).

[344] M. Frumar, A. P. Firth, and A. E. Owen, Optically induced crystal-to-amorphous-state transition in As_2S_3. *J. Non-Cryst. Solids* **192–193**, 447 (1995).

[345] V. Benekou, L. Strizik, T. Wagner, S. N. Yannopoulos, A. L. Greer, and J. Orava, In-situ study of athermal reversible photocrystallization in a chalcogenide glass. *J. Appl. Phys.* **122**, 173101 (2017).

[346] T. Petkova, B. Monchev, O. Kostadinova, P. Petkov, and S. N. Yannopoulos, Vibrational modes and structure of $(AgI)_x(GeS_{1.5})_{100-x}$ chalcohalide glasses. *J. Non-Cryst. Solids* **355**, 2063 (2009).

[347] J. Heo, J. Min Yoon, and S.-Y. Ryou, Raman spectroscopic analysis on the solubility mechanism of La^{3+} in GeS_2–Ga_2S_3 glasses. *J. Non-Cryst. Solids* **238**, 115 (1998).

[348] A. Chrissanthopoulos, P. Jovari, I. Kaban, S. Gruner, T. Kavetskyy, J. Borc, W. Wang, J. Ren, G. Chen, and S. N. Yannopoulos, Structure of AgI-doped Ge–In–S glasses: Experiment, reverse Monte Carlo modelling, and density functional calculations. *J. Solid State Chem.* **192**, 7 (2012).

[349] I. P. Kotsalas and C. Raptis, High-temperature structural phase transitions of Ge_xS_{1-x} alloys studied by Raman spectroscopy. *Phys. Rev. B* **64**, 125210 (2001).

[350] M. Frumar, T. Wagner, K. Shimakawa, and B. Frumarova, *Crystalline and Amorphous Chalcogenides, High-Tech Materials with Structural Disorder and Many Important Applications*, in: *Nanomaterials and Nanoarchitectures* (M. Bardosova and T. Wagner), Springer, Dordrecht, (2015), pp. 151–238.

[351] J. Chovanec, M. Chromcikova, M. Liska, J. Shanelova, and J. Malek, Thermodynamic model and viscosity of Ge–S glasses. *J. Therm. Anal. Calorim.* **116**, 581 (2013).

[352] J. Malek, L. Tichy, and J. Klikorka, Crystallization kinetics of Ge_xS_{1-x} glasses. *J. Therm. Anal.* **33**, 667 (1988).

[353] J. Malek, V. Podzemna, and J. Shanelova, Crystal growth kinetics in GeS_2 glass and viscosity of supercooled liquid. *J. Phys. Chem. B* **125**, 7515 (2021).

[354] J. Malek, The glass transition and crystallization of germanium-sulphur glasses. *J. Non-Cryst. Solids* **107**, 323 (1989).

[355] V. Podzemna, J. Bartak, and J. Malek, Crystal growth kinetics in GeS_2 amorphous thin films. *J. Therm. Anal. Calorim*. **118**, 775 (2014).

[356] M. A. Popescu, *Non-Crystalline Chalcogenides*, Kluwer, Dordrecht, (2002).

[357] Y. Wang, O. Matsuda, K. Inoue, and K. Murase, Photo-induced crystallization in amorphous $GeSe_2$ studied by Raman scattering. *J. Non-Cryst. Solids* **227–230**, 728 (1998).

[358] K. Sakai, K. Maeda, H. Yokoyama, and T. Ikari, Photo-enhanced crystallization by laser irradiation and thermal annealing in amorphous $GeSe_2$. *J. Non-Cryst. Solids* **320**, 223 (2003).

[359] K. Tanaka, Reversible photo-induced structural changes in chalcogenide glasses. *AIP Conf. Proc.* **31**, 148 (1976).

[360] D. K. Tagantsev and S. V. Nemilov Photoviscous effect in chalcogenide glasses. *Sov. J. Glass Phys. Chem.* **15**, 220 (1989).

[361] P. Khan, R. K. Yadav, and K. V. Adarsh, Ultrafast light-induced softening of chalcogenide thin films above the rigidity percolation transition. *J. Appl. Phys.* **124**, 125702 (2018).

[362] L. Calvez, Z. Yang, and P. Lucas, Reversible giant photocontraction in chalcogenide glass. *Opt. Express* **17**, 18581 (2009).

Appendix I

#1

J. Orava, A. L. Greer*, B. Gholipour, D. W. Hewak, and C. E. Smith, Characterization of supercooled liquid $Ge_2Sb_2Te_5$ and its crystallization by ultrafast-heating calorimetry. *Nat. Mater.* **11**, 279 (2012). https://doi.org/10.1038/nmat3275

ABSTRACT: Differential scanning calorimetry (DSC) is widely used to study the stability of amorphous solids, characterizing the kinetics of crystallization close to the glass-transition temperature T_g. We apply ultrafast DSC to the phase-change material $Ge_2Sb_2Te_5$ (GST) and show that if the range of heating rates is extended to more than 10^4 K s^{-1}, the analysis can cover a wider temperature range, up to the point where the crystal growth rate approaches its maximum. The growth rates that can be characterized are some four orders of magnitude higher than in conventional DSC, reaching values relevant for the application of GST as a data-storage medium. The kinetic coefficient for crystal growth has a strongly non-Arrhenius temperature dependence, revealing that supercooled liquid GST has a high fragility. Near T_g there is evidence for decoupling of the crystal-growth kinetics from viscous flow, matching the behaviour for a fragile liquid suggested by studies on oxide and organic systems.

#2

J. Orava, A. L. Greer*, B. Gholipour, D. W. Hewak, and C. E. Smith, Ultra-fast calorimetry study of $Ge_2Sb_2Te_5$ crystallization between dielectric layers. *Appl. Phys. Lett.* **101**, 091906 (2012). https://doi.org/10.1063/1.4748881

ABSTRACT: Phase changes in chalcogenides such as $Ge_2Sb_2Te_5$ can be exploited in non-volatile random-access memory, with fast crystallization crucial for device operation. Ultra-fast differential scanning calorimetry, heating at rates up to 40 000 K s^{-1}, has been used to study the crystallization of amorphous $Ge_2Sb_2Te_5$ with and without sandwich layers of ZnS-SiO_2. At heating rates up to 1000 K s^{-1}, the sandwich layers retard crystallization, an effect attributed to crystallization-induced stress. At greater heating rates (≥5000 K s^{-1}), and consequently higher crystallization temperatures, the stress is relaxed, and sandwich layers catalyze crystallization. Implications for memory-device performance are discussed.

#3

M. Kalyva[§], **J. Orava**[§], A. Siokou[*], M. Pavlista, T. Wagner, and S. N. Yannopoulos[*], Reversible amorphous-to-amorphous transitions in chalcogenide films: Correlation changes in structure and optical properties. *Adv. Funct. Mater.* **23**, 2052 (2013). https://doi.org/10.1002/adfm.201202461

ABSTRACT: Structural transitions in materials are accompanied by appreciable and exploitable changes in physical-chemical properties. Whereas reversible optically-driven atomistic changes in crystal-to-amorphous transitions are generally known and exploited in applications, the nature of the corresponding polyamorphic transitions between two structurally distinct meta-stable amorphous phases is an unexplored theme. Direct experimental evidence is reported for the nature of the atomistic changes during fully reversible amorphous-to-amorphous switching between two individual states in the non-crystalline $As_{50}Se_{50}$ films prepared by pulsed-laser deposition and consequent changes in optical properties. Combination of surface sensitive X-ray photoelectron spectroscopy and spectroscopic ellipsometry show that the near-bandgap energy illumination and annealing induce reversible switching in the material's structure by local bonding rearrangements. This is accompanied by switching in refractive index between two well-defined states. Exploiting the pluralism of distinct structural states in a disordered solid can provide new insights into the data storage in emerging optical memory and photonic applications.

#4

J. Orava and A. L. Greer[*], Fast and slow crystal growth kinetics in glass-forming melts. *J. Chem. Phys.* **140**, 214504 (2014). https://doi.org/10.1063/1.4880959

ABSTRACT: Published values of crystal growth rates are compared for supercooled glass-forming liquids undergoing congruent freezing at a planar crystal-liquid interface. For the purposes of comparison pure metals are considered to be glass-forming systems, using data from molecular-dynamics simulations. For each system, the growth rate has a maximum value $U_{\max}$ at a temperature $T_{\max}$ that lies between the glass-transition temperature T_{g} and the melting temperature T_{m}. A classification is suggested, based on the lability (specifically, the propensity for fast crystallization), of the liquid. High-lability systems show "fast" growth characterized by a high $U_{\max}$, a low $T_{\max}/T_{\mathrm{m}}$, and a very broad peak in U vs. T/T_{m}. In contrast, systems showing "slow" growth have a low $U_{\max}$, a high $T_{\max}/T_{\mathrm{m}}$, and a sharp peak in U vs. T/T_{m}. Despite the difference of more than 11 orders of magnitude in $U_{\max}$ seen in pure metals and in silica, the range of glass-forming systems surveyed fit into a common pattern in which the lability increases with lower reduced glass-transition temperature ($T_{\mathrm{g}}/T_{\mathrm{m}}$) and higher fragility of the liquid. A single parameter, a linear combination of $T_{\mathrm{g}}/T_{\mathrm{m}}$ and fragility, can show a good correlation with $U_{\max}$. For all the systems, growth at $U_{\max}$ is coupled to the atomic/molecular mobility in the liquid. It is found that, across the diversity of glass-forming systems, $T_{\max}/T = 1.48 \pm 0.15$.

#5

J. Orava, T. Kohoutek, and T. Wagner, Deposition techniques for chalcogenide thin films, in: *Chalcogenide Glasses: Preparation, Properties and Applications*, J. L. Adam & X. Zhang (Eds.), Woodhead Publishing Ltd., Cambridge, UK, 2014, pp. 265–309. https://doi.org/10.1533/9780857093561.1.265

ABSTRACT: The chapter describes details of deposition techniques, namely thermal evaporation, sputtering, pulsed-laser deposition, chemical vapour deposition and spin-coating for chalcogenide thin films. We discuss key issues, advantages and influence of different deposition techniques and experimental conditions on properties of as-prepared amorphous chalcogenide thin films. The final chemical composition, structure and physico-chemical properties of the prepared films predetermine their application and vice versa. Their applications are in many fields such as (nano)electronics, (nano)optics, information storage, security, health protection and alternative energy sources.

#6

J. Orava, D. W. Hewak, and A. L. Greer*, Fragile-to-strong crossover in supercooled liquid Ag-In-Sb-Te studied by ultrafast calorimetry. *Adv. Funct. Mater.* **25**, 4851 (2015). https://doi.org/10.1002/adfm.201501607

ABSTRACT: Phase-change random-access memory relies on the reversible crystalline-glassy phase change in chalcogenide thin films. In this application, the speed of crystallization is critical for device performance: there is a need to combine ultrafast crystallization for switching at high temperature with high resistance to crystallization for non-volatile data retention near to room temperature. In phase-change media such as nucleation-dominated $Ge_2Sb_2Te_5$, these conflicting requirements are met through the highly “fragile” nature of the temperature dependence of the viscosity of the supercooled liquid. The present study explores, using ultrafast-heating calorimetry, the equivalent temperature dependence for the growth-dominated medium Ag-In-Sb-Te. The crystallization shows (unexpectedly) Arrhenius temperature dependence over a wide intermediate temperature range. Here it is shown that this is evidence for a fragile-to-strong crossover on cooling the liquid. Such a crossover has many consequences for the interpretation and control of phase-change kinetics in chalcogenide media, helping to understand the distinction between nucleation- and growth-dominated crystallization, and offering a route to designing improved device performance.

#7

J. Orava[*] and A. L. Greer[*], Kissinger method applied to the crystallization of glass-forming liquids: Regimes revealed by ultra-fast-heating calorimetry. *Thermochimica Acta* **603**, 63 (2015). https://doi.org/10.1016/j.tca.2014.06.021

ABSTRACT: Numerical simulation of DSC traces is used to study the validity and limitations of the Kissinger method for determining the temperature dependence of the crystal-growth rate on continuous heating of glasses from the glass transition to the melting temperature. A particular interest is to use the wide range of heating rates accessible with ultra-fast DSC to study systems such as the chalcogenide $Ge_2Sb_2Te_5$ for which fast crystallization is of practical interest in phase-change memory. Kissinger plots are found to show three regimes: (i) at low heating rates the plot is straight, (ii) at medium heating rates the plot is curved as expected from the liquid fragility, and (iii) at the highest heating rates the crystallization rate is thermodynamically limited, and the plot has curvature of the opposite sign. The relative importance of these regimes is identified for different glass-forming systems, considered in terms of the liquid fragility and the reduced glass-transition temperature. The extraction of quantitative information on fundamental crystallization kinetics from Kissinger plots is discussed.

#8

J. Orava[*], M. N. Kozicki, S. N. Yannopoulos, and A. L. Greer, Reversible migration of silver on memorized pathways in Ag-$Ge_{40}S_{60}$ films. *AIP Advances* **5**, 077134 (2015). http://dx.doi.org/10.1063/1.4927006

ABSTRACT: Reversible and reproducible formation and dissolution of silver conductive filaments are studied in Ag-photodoped thin-film $Ge_{40}S_{60}$ subjected to electric fields. A tip-planar geometry is employed, where a conductive-atomic-force microscopy tip is the tip electrode and a silver patch is the planar electrode. We highlight an inherent “memory” effect in the amorphous chalcogenide solid-state electrolyte, in which particular silver-ion migration pathways are preserved “memorized” during writing and erasing cycles. The “memorized” pathways reflect structural changes in the photodoped chalcogenide film. Structural changes due to silver photodoping, and electrically-induced structural changes arising from silver migration, are elucidated using Raman spectroscopy. Conductive filament formation, dissolution, and electron (reduction) efficiency in a lateral device geometry are related to operation of the nano-ionic Programmable Metallization Cell memory and to newly emerging chalcogenide-based lateral geometry MEMS technologies. The methods in this work can also be used for qualitative multi-parameter sampling of metal/amorphous-chalcogenide combinations, characterizing the growth/dissolution rates, retention and endurance of fractal conductive filaments, with the aim of optimizing devices.

#9

J. Orava[*], H. Weber, I. Kaban, and A. L. Greer[*], Viscosity of liquid Ag–In–Sb–Te: Evidence of a fragile-to-strong crossover. *J. Chem. Phys.* **144**, 194503 (2016). https://doi.org/10.1063/1.4949526

ABSTRACT: The temperature-dependent viscosity $\eta(T)$ is measured for the equilibrium liquid of the chalcogenide Ag–In–Sb–Te (AIST), the first time this has been reported for a material of actual interest for phase-change memory. The measurements, in the range 829–1254 K, are made using an oscillating-crucible viscometer, and show a liquid with high fragility and low viscosity, similar to liquid pure metals. Combining the high-temperature viscosity measurements with values inferred from crystal growth rates in the supercooled liquid allows the form of $\eta(T)$ to be estimated over the entire temperature range from above the melting point down to the glass transition. It is then clear that $\eta(T)$ for liquid AIST cannot be described with a single fragility value, unlike other phase-change chalcogenides such as liquid Ge–Sb–Te. There is clear evidence for a fragile-to-strong crossover on cooling liquid AIST, similar to that analyzed in $Te_{85}Ge_{15}$. The change in fragility associated with the crossover in both these cases is rather weak, giving a broad temperature range over which $\eta(T)$ is near-Arrhenius. We discuss how such behavior may be beneficial for the performance of phase-change memory. Consideration of the fragile-to-strong crossover in liquid chalcogenides may be important in tuning compositions to optimize the device performance.

#10

J. Orava[*] and A. L. Greer[*], Fast crystal growth in glass-forming liquids, *J. Non-Cryst. Solids* **451**, 94 (2016). https://doi.org/10.1016/j.jnoncrysol.2016.06.007

ABSTRACT: In liquids of high glass-forming ability, in which crystal growth rates are low, the rates can be measured over the full range of supercooling from the liquidus temperature down to the glass transition. For systems of low glass-forming ability, growth rates are readily measured at small supercooling and at very large supercooling around the glass-transition temperature, but it is difficult to acquire data over the full range of intermediate supercooling, especially at the maximum in growth rate. Data at intermediate supercoolings are however of considerable interest for understanding glass formation in such systems as pure metals and chalcogenides for phase-change data storage. We will review the methods emerging for making such measurements, and will note that the fragility of the liquid (including possible crossover from 'fragile' to 'strong' liquid behaviour on cooling) is an important part of understanding fast crystal growth. We also note that there are deficiencies in existing theories of fast crystal growth.

#11

J. Orava[*] and A. L. Greer[*], Classical-nucleation-theory analysis of priming in chalcogenide phase-change memory. *Acta Mater.* **139**, 226 (2017). https://doi.org/10.1016/j.actamat.2017.08.013

ABSTRACT: The chalcogenide $Ge_2Sb_2Te_5$ (GST) is of interest for use in phase-change memory. Crystallization is the rate-limiting step for memory operation, and can be accelerated by the prior application of a "priming" heating pulse. There is characteristic fading of the priming effect if there is a time interval between the priming pulse and the main heating pulse to achieve crystallization. We apply classical nucleation theory to interpret these effects, based on a fitting of nucleation kinetics (steady-state and transient) over the full temperature range of the supercooled liquid. The input data come from both physical experiments and atomistic simulations. Prior studies of conventional glass-formers such as lithium disilicate preclude any possibility of fading; the present study shows, however, that fading can be expected with the particular thermodynamic parameters relevant for GST and, possibly, other phase-change chalcogenides. We also use the nucleation analysis to highlight the distinction between GST and the other archetypical chalcogenide system (Ag,In)-doped Sb_2Te. Classical nucleation theory appears to be applicable to phase-change chalcogenides, and to predict performance consistent with that of actual memory cells. Nucleation modeling may therefore be useful in optimizing materials selection and performance in device applications.

#12

V. Benekou[*], L. Strizik, T. Wagner, S. N. Yannopoulos, A. L. Greer, and **J. Orava**[*], *In-situ* study of athermal reversible photocrystallization in a chalcogenide glass. *J. Appl. Phys.* **122**, 173101 (2017). https://doi.org/10.1063/1.5003575

The time-resolved Raman measurements reveal a three-stage mechanism of the photostructural changes in $Ge_{25.0}Ga_{9.5}Sb_{0.5}S_{65.0}$ (containing 0.5 at. % of Er^{3+}) glass under continuous-above-bandgap illumination. These changes are reversible and effectively athermal, in that the local temperature rises to about 60% of the glass-transition temperature and the phase transitions take place in the glass/crystal and not in an equilibrium liquid. In the early stages of illumination, the glassy-network dimensionality changes from a predominantly 3-D to a mixture of 2-D/1-D represented by an increase in the fraction of edge-sharing tetrahedra and the emergence of homonuclear (semi)metallic bonds. This incubation period of the structural rearrangements, weakly thermally activated with an energy of ~0.16 eV, facilitates a reversible photocrystallization. The photocrystallization rate in the glass is comparable to that achieved by thermal crystallization from supercooled liquid at large supercooling. Almost complete re-amorphization can be achieved in about an hour by reducing the incident laser-power density by a factor of ten. Glass-ceramic composites—with varying glass-to-crystal fraction—can be obtained by ceasing the illumination during re-amorphization. Microstructural imaging reveals photoinduced mass transport and the formation of columnar-porous structures. This shows the potential for a bond-specific engineering of glassy structures for photonic applications with a spatial resolution unachievable by thermal annealing.

#13

J. Orava[*], Y. Wen, J. Prikryl, T. Wagner, N. A. Stelmashenko, M. W. Chen, and A. L. Greer[*], Preferred location for conducting filament formation in thin-film nano-ionic electrolyte: Study of microstructure by atom-probe tomography. *J. Mater. Sci.: Mater. Electron.* **28**, 6846 (2017). https://doi.org/10.1007/s10854-017-6383-y

ABSTRACT: Atom-probe tomography of Ag-photodoped amorphous thin-film $Ge_{40}S_{60}$, the material of interest in nano-ionic memory and lateral geometry MEMS technologies, reveals regions with two distinct compositions on a nanometer length-scale. One type of region is Ag-rich and of a size typically extending beyond the measured sample volume of ~40×40×80 nm^3. These type-I regions contain aligned nanocolumns, ~5 nm wide, that are the likely location for reversible diffusion of Ag^+ ions and associated growth/dissolution of conducting filaments. The nanocolumns become relatively Ag-rich during the photodoping, and the pattern of Ag enrichment originates from the columnar-porous structure of the as-deposited film that is to some extent preserved in the electrolyte after photodoping. Type-II regions have lower Ag content, are typically 10–20 nm across, and appear to conform to the usual description of the photoreaction products of the optically-induced dissolution and diffusion of silver in a thin-film chalcogenide. The microstructure, with two types of region and aligned nanocolumns, is present in the electrolyte after photodoping without any applied bias, and is important for understanding switching mechanisms, and writing and erasing cycles, in programmable-metallization-cell memory.

#14

H. Weber, **J. Orava**[*], I. Kaban[*], J. Pries, and A. L. Greer, Correlating ultrafast calorimetry, viscosity, and structural measurements in liquid GeTe and $Ge_{15}Te_{85}$. *Phys. Rev. Mater.* **2**, 093405 (2018). https://doi.org/10.1103/PhysRevMaterials.2.093405

ABSTRACT: Two distinct trends in the temperature dependence of viscosity, measured directly and inferred from calorimetry by analyzing crystallization kinetics, can be correlated with the temperature evolution of the height of the first peak of the x-ray total structure factor for liquid GeTe and $Ge_{15}Te_{85}$. The phase-change chalcogenide GeTe is a high-fragility liquid with the kinetic fragility value of 76, at the glass-transition temperature, being between those for liquid (Ag,In)-doped Sb_2Te and $Ge_2Sb_2Te_5$. The viscosity of the high-temperature liquid shows Arrhenius kinetics on cooling to the melting point, and the structure factor conforms to the fragile liquid. For liquid $Ge_{15}Te_{85}$, the temperature evolution of the structure factor suggests a transition in the temperature range of about 100 K above the melting. The crystallization shows a wide range of Arrhenius kinetics in the supercooled liquid region. This finding combined with the dynamic viscosity measurements is interpreted by invoking a weak fragile-to-strong crossover on cooling the liquid $Ge_{15}Te_{85}$. The differences in structures and dynamics of liquid GeTe and $Ge_{15}Te_{85}$ appear closely correlated to their distinctly different crystallization mechanisms.

#15

J. Orava and A. L. Greer, Chalcogenides for phase-change memory, in: *Handbook of Thermal Analysis and Calorimetry: Recent Advances, Techniques and Applications*, 2nd Edition, S. Vyazovkin, N. Koga & C. Schick (Eds.), Elsevier, Amsterdam, Netherlands, 2018, pp. 685–734. https://doi.org/10.1016/B978-0-444-64062-8.00014-0

ABSTRACT: Phase-change chalcogenides, specifically those containing tellurium, have amorphous/glassy phases that can undergo fast crystallization. The crystallization time is short, < 100 ns, challenging to measure, and it is the rate-limiting step of nonvolatile, low-power phase-change memory (PCM) operation. Reversible glassy-to-crystalline transitions are the key processes in writing (crystallization) and erasing (amorphization) steps in PCM devices. This chapter provides a basic overview of recent research on materials in PCM technology, describing developments in experimental techniques. The emphasis is on ultrafast calorimetry, and on how the data from this relatively novel technique can be used in modeling the transitions, particularly crystal growth rate and understanding the different crystallization mechanisms. Different forms of the temperature-dependent mobility in the supercooled liquid state are shown to have direct technological importance for memory operation.

#16

S. Balachandran*, **J. Orava**, M. Köhler, A. J. Breen, I. Kaban, D. Raabe, and M. Herbig, Elemental re-distribution inside shear bands revealed by correlative atom-probe tomography and electron microscopy in a deformed metallic glass. *Scr. Mater.* **168**, 14 (2019). https://doi.org/10.1016/j.scriptamat.2019.04.014

ABSTRACT: A density variation in shear bands visible by electron microscopy is correlated with compositionally altered locations measured by atom-probe tomography in plastically-deformed $Al_{85.6}Y_{7.5}Fe_{5.8}$ metallic-glass ribbons. Two compositionally distinct regions are identified along shear bands, one is Al-rich (~92 at.%), the other is Al-depleted (~82.5 at.%) and both regions show marginal concentration fluctuations of Y and Fe. The elemental re-distribution is observed within shear bands only, and no chemical exchange with the surrounding glassy matrix is observed.

#17

J. Orava[*], I. Kaban, M. Benkocka, X. Han, I. Soldatov, and A. L. Greer, Fast-heating-induced formation of metallic-glass/crystal composites with enhanced plasticity. *Thermochimica Acta* **677**, 198 (2019). https://doi.org/10.1016/j.tca.2019.03.029

ABSTRACT: Bulk metallic glasses are known to have poor plasticity which limits their application as structural materials. Due to the lack of atomic periodicity in metallic glasses, their mechanical properties cannot be controlled the same way as in crystalline materials. Fast-heating-induced, a heating rate of 10 K s^{-1} and higher, crystallization of ductile nanocrystalline phase(s) leads to enhanced plasticity of metallic-glass/crystal composites. Here, an overview of controlling the microstructure on fast heating, the suggested crystallization mechanism of metastable phases and the principle of enhanced plasticity of the composites is presented and discussed, with a special focus on Cu–Zr-based metallic glasses.

#18

J. Orava[*], K. Kosiba[*], X. Han, I. Soldatov, O. Gutowski, O. Ivashko, A.-C. Dippel, M. v. Zimmermann, A. Rothkirch, J. Bednarcik, U. Kühn, H. Siegel, S. Ziller, A. Horst, K. Peukert, R. Voigtländer, D. Lindackers, and I. Kaban, Fast-current-heating devices to study *in situ* phase formation in metallic glasses by using high-energy synchrotron radiation. *Rev. Sci. Instrum.* **91**, 073901 (2020). https://doi.org/10.1063/5.0005732

ABSTRACT: Details of fast-resistive-heating setups, controlled heating ranging from ~10^1 K s^{-1} to ~10^3 K s^{-1}, to study *in situ* phase transformations (on heating and on cooling) in metallic glasses by high-energy synchrotron x-ray diffraction are discussed. Both setups were designed and custom built at the Leibniz Institute for Solid State and Materials Research Dresden (IFW Dresden) and have been implemented at the P02.1 Powder Diffraction and Total Scattering Beamline and the P21.1 Swedish Materials Science Beamline at PETRA III storage ring, DESY, Hamburg. The devices are interchangeable at both beamlines. Joule heating is triggered automatically and is timed with the incident beam and detector. The crystallization process can be controlled via a feedback circuit by monitoring the change in the time-dependent resistivity and temperature of glasses. Different ambient atmospheres, such as vacuum and inert gases (He and Ar), can be used to control oxidation and cooling. The main focus of these devices is on understanding the crystallization mechanism and kinetics in metallic glasses, which are brittle and for which fast heating gives defined glass–crystal composites with enhanced plasticity. As an example, phase-transformation sequence(s) in a prototyped Cu–Zr-based metallic glass is described on heating, and a crystalline phase beneficial to the plasticity is identified.

#19

Q. Cheng, X. Han, I. Kaban, I. Soldatov, W. H. Wang, Y. H. Sun*, and **J. Orava***, Phase transformations in a Cu–Zr–Al metallic glass. *Scr. Mater.* **183**, 61 (2020). https://doi.org/10.1016/j.scriptamat.2020.03.028

ABSTRACT: A combination of conventional calorimetry, ultra-fast scanning calorimetry and resistive heating gives access to heating rates exceeding 6 orders of magnitude allowing to probe crystallization kinetics and mechanisms in a Cu-Zr-Al metallic glass. Continuous-heating-transformation and double-peak time-temperature-transformation diagrams are constructed and related to the formation of glass–crystal composites with enhanced ductility. The metastable B2-CuZr phase becomes dominantly formed at a heating rate of ~10^2 K s^{-1} and higher. A critical heating rate to bypass crystallization is ~10,000 K s^{-1}. For isothermal annealing at >850 K, only one crystallization event is detected; for lower temperatures, a complex two-step transformation occurs.

#20

Q. Cheng, P. F. Wang, H. Y. Jiang, L. Gu, **J. Orava***, Y. H. Sun*, H. Y. Bai, and W. H. Wang, Effect of high-temperature up-quenching on stabilizing off-eutectic metallic glasses. *Phys. Rev. B* **103**, L100302 (2021). https://doi.org/10.1103/PhysRevB.103.L100203

ABSTRACT: Fast-heating calorimetry is used to study *in operando* the vitrification mechanism of off-eutectic $Yb_{47}Mg_{31}Zn_{19}Cu_3$ liquid at a cooling rate of 10 000K s^{-1}. The glass forms only when it is quenched from between the melting and liquidus temperature, contradicting the need for full remelting. Zinc-rich precipitates, forming on quenching from above the liquidus, deteriorate vitrification—which also offers an alternative explanation to what has often been considered as liquid-liquid transition. Application of an up-quenching thermal protocol facilitates the glass formation by removing the precipitates *in situ*; it is generally applicable and may extend the glass-forming range of other off-eutectic glasses. This research demonstrates a strategy to develop bulk metallic glasses.

#21

J. Orava[*], S. Balachandran[*], X. Han[*], O. Shuleshova, E. Nurouzi, I. Soldatov, S. Oswald, O. Gutowski, O. Ivashko, A.-C. Dippel, M. v. Zimmermann, Y. P. Ivanov, A. L. Greer, D. Raabe, M. Herbig, and I. Kaban[*], *In situ* correlation between metastable phase-transformation mechanism and kinetics in a metallic glass. *Nat. Commun.* **12**, 2839 (2021). https://doi.org/10.1038/s41467-021-23028-9

ABSTRACT: A combination of complementary high-energy X-ray diffraction, containerless solidification during electromagnetic levitation and transmission electron microscopy is used to map in situ the phase evolution in a prototype Cu-Zr-Al glass during flash-annealing imposed at a rate ranging from 10^2 to 10^3 K s^{-1} and during cooling from the liquid state. Such a combination of experimental techniques provides hitherto inaccessible insight into the phase-transformation mechanism and its kinetics with high temporal resolution over the entire temperature range of the existence of the supercooled liquid. On flash-annealing, most of the formed phases represent transient (metastable) states – they crystallographically conform to their equilibrium phases but the compositions, revealed by atom probe tomography, are different. It is only the B2 CuZr phase which is represented by its equilibrium composition, and its growth is facilitated by a kinetic mechanism of Al partitioning; Al-rich precipitates of less than 10 nm in a diameter are revealed. In this work, the kinetic and chemical conditions of the high propensity of the glass for the B2 phase formation are formulated, and the multi-technique approach can be applied to map phase transformations in other metallic-glass-forming systems.

#22

J. Orava, T. H. Lee, S. R. Elliott, and A. L. Greer, Crystallization of phase-change chalcogenides, in: *The World Scientific Reference of Amorphous Materials, Volume 1: Amorphous Chalcogenides: Structure, Properties, Modeling and Applications*, K. Shimakawa & A. V. Kolobov (Volume Eds.), Elsevier, World Scientific, 2021, pp. 367–402. https://doi.org/10.1142/9789811215575_0012

ABSTRACT: not available

* Corresponding author(s)
§ These authors contributed equally to the work